

---

# Ultrafast Dynamics in Wide-bandgap (2D & 3D) Perovskite Semiconductor Thin Films

---

DISSERTATION

zur Erlangung des Doktorgrades

der Naturwissenschaften



Vorgelegt beim Fachbereich

Biochemie, Chemie und Pharmazie

der Johann Wolfgang Goethe-Universität

in Frankfurt am Main

von

**MAHMOUD MOHAMED MOHYELDIN MOSTAFA HASSAN**

(Wissenschaftlicher Name: Mahmoud M. Elshanawany)

Geboren in Asuit / Ägypten

Frankfurt am Main 2022

(D 30)

Vom Fachbereich Biochemie, Chemie und Pharmazie der  
Johann Wolfgang Goethe-Universität als Dissertation angenommen.

Dekan: Prof. Dr. Clemens Glaubitz

1. Gutachter: PD Dr. Markus Braun

2. Gutachter: Prof. Dr. Josef Wachtveitl

Datum der Disputation: 31.01.2023





وَمَا أُوتِيتُمْ بِهِ لَعَلَّكُمْ تَعْلَمُونَ إِلَّا قَلِيلًا

القرآن الكريم  
سورة الإسراء الآية

Holy Quran (Surah Al-Isra, Ayat 85)









## *List of Publications*

(# - These authors contributed equally to this work)

### **[I] Mechanism of Ultrafast Energy Transfer between the Organic-Inorganic Layers in Multiple-Ring Aromatic Spacers for 2D Perovskites**

**Mahmoud M. Elshanawany**, Antonio Gaetano Ricciardulli, Michael Saliba, Josef Wachtveitl and Markus Braun\*

Nanoscale, **2021**, 13, 15668-15676

DOI: 10.1039/D1NR04290D

### **[II] Ultrafast Carrier Dynamics in Wide Band Gap Mixed-Cation Perovskites: Influence of the Cs Cation**

**Mahmoud M. Elshanawany**, Antonio Gaetano Ricciardulli, Jose J. Jeronimo-Rendon, Michael Saliba, Josef Wachtveitl and Markus Braun\*

J. Phys. Chem. C **2022**, 126, 20, 8787–8793

DOI: 10.1021/acs.jpcc.2c02682

### **[III] Base-Free Synthesis and Photophysical Properties of New Schiff Bases Containing Indole Moiety**

Ahmed I. A. Soliman\*<sup>#</sup>, Mostafa Sayed<sup>#</sup>, **Mahmoud M. Elshanawany**<sup>#</sup>, Osama Younis, Mostafa Ahmed, Adel M. Kamal El-Dean, Aboel-Magd A. Abdel-Wahab, Josef Wachtveitl, Markus Braun\*, Pedram Fatehi, and Mahmoud S. Tolba

ACS Omega **2022**, 7, 12, 10178–10186

DOI: 10.1021/acsomega.1c06636

## *Conferences*

### **[I] International Conference on Photochemistry**

Presentation: Ultrafast energy transfer between the organic-inorganic layers in 2D perovskites

Geneva 18-23 July 2021

### **[II] IPTC Seminar**

Presentation: Ultrafast energy transfer between the organic-inorganic layers in 2D perovskites

Hirschegg, 21-25 March 2022

### **[III] Tandem PV Workshop**

Poster: Influence of Cs cation in ultrafast carrier dynamics of mixed-cation perovskites

**Mahmoud M. Elshanawany**, Antonio Gaetano Ricciardulli, Jose J. Jeronimo-Rendon,

Michael Saliba, Josef Wachtveitl and Markus Braun

Freiburg 30 May–1 June 2022

## Zusammenfassung

Diese kumulative Arbeit konzentriert sich auf die Untersuchung der zeitaufgelösten Dynamik in verschiedenen Perowskiten und neu synthetisierten Schiffbasen, die für optoelektronische Anwendungen wie Solarzellen und LEDs interessant sein könnten. Die gängigen Solarzellen und LEDs basieren aufgrund ihrer hohen Effizienz und Stabilität auf anorganischen Materialien wie Silizium. Die hohen Kosten für die Verarbeitung von reinem kristallinem Silizium veranlassen Forschungsgruppen, nach kostengünstigen Kandidaten mit vergleichbarer Effizienz und Stabilität zu suchen. Seitdem wurden umfangreiche Forschungsarbeiten zu 2D und 3D-Perowskiten für alternative Solarzellen und LEDs durchgeführt. Diese Perowskite könnten in naher Zukunft vielversprechende Ergebnisse als Ersatz für Silizium liefern, wenn einige Probleme, z. B. die Stabilität und die Verwendung von Blei, gelöst sind (siehe Kapitel 1).

Im ersten Projekt (Ref. 1) wurde die Ein-Schritt-Spin-Coating-Methode angewandt, um hochwertige Dünnschichten aus 2D-Perowskiten mit verschiedenen Chromophoren (Benzyl, Naphthyl und Pyrenyl) herzustellen. Hier wurden die Energietransfereigenschaften und Relaxationswege mit Hilfe von UV-Vis-Absorptions-, PL-, TCSPC- und transienten Absorptionsspektroskopietechniken (fs-TAS) unter ähnlichen experimentellen Bedingungen untersucht. Die Wahl des Chromophors in der organischen Schicht und der Halogenidgehalt sind entscheidende Faktoren bei der Kontrolle der elektronischen Eigenschaften von zweidimensionalen (2D) Materialien. Das Verständnis der Photophysik von 2D-Perowskit-Materialien ist für effiziente und stabile optoelektronische Geräte von großer Bedeutung. Diese Chromophore stellen drei verschiedene Energieniveauszenarien für die Studie dar. Ziel dieser Arbeit war es, den Einfluss der Größe der aromatischen Spacer der verschiedenen Chromophore zu visualisieren und zu untersuchen. Daher haben wir den Halogenidanteil in der anorganischen Schicht in allen Perowskitfilmen auf Br (70 %) und I (30 %) festgelegt. Die Verwendung von großen Chromophoren in 2D-Bleihalogenid-Perowskiten als Abstandshalter zeigte erfolgreiche Energieübertragungssysteme. Wir beobachteten den exzitonischen Absorptionspeak der Bleihalogenidschicht in  $(\text{BA})_2\text{Pb}(\text{Br}_{0,7}\text{I}_{0,3})_4$ ,  $(\text{NMA})_2\text{Pb}(\text{Br}_{0,7}\text{I}_{0,3})_4$  und  $(\text{PMA})_2\text{Pb}(\text{Br}_{0,7}\text{I}_{0,3})_4$  bei 402 nm, 417 nm bzw. 404 nm. In den Absorptionsspektren von  $(\text{NMA})_2\text{Pb}(\text{Br}_{0,7}\text{I}_{0,3})_4$  und  $(\text{PMA})_2\text{Pb}(\text{Br}_{0,7}\text{I}_{0,3})_4$  ist eine breite, rotverschobene Absorption zu erkennen, die auf Fallenzustände in beiden Proben zurückzuführen sein könnte. Das PL-Spektrum von  $(\text{BA})_2\text{Pb}(\text{Br}_{0,7}\text{I}_{0,3})_4$  zeigt ein schmales exzitonisches Emissionsverhalten der anorganischen Bleihalogenidschicht. Das Emissionsspektrum von  $(\text{NMA})_2\text{Pb}(\text{Br}_{0,7}\text{I}_{0,3})_4$  besteht aus zwei Komponenten: (1) einem leicht rotverschobenen exzitonischen Peak bei 440 nm aus der

anorganischen Schicht und (2) der Phosphoreszenz des Naphthylchromophors bei Raumtemperatur (eine strukturierte Emission mit Maxima bei 570 und 617 nm) aus der organischen Schicht. Das Emissionsspektrum von  $(\text{PMA})_2\text{Pb}(\text{Br}_{0,7}\text{I}_{0,3})_4$  stammt hauptsächlich aus der organischen Schicht und stellt die Fluoreszenz des Pyrenylchromophors dar.

Wir haben TCSPC verwendet, um die Lebensdauern dieser Emissionen mit der Anregung bei 320 nm zu untersuchen.  $(\text{NMA})_2\text{Pb}(\text{Br}_{0,7}\text{I}_{0,3})_4$  (0,6 ns) und  $(\text{BA})_2\text{Pb}(\text{Br}_{0,7}\text{I}_{0,3})_4$  (0,61 ns) haben Lebensdauer im Vergleich zu  $(\text{PMA})_2\text{Pb}(\text{Br}_{0,7}\text{I}_{0,3})_4$  (zwei Zerfallskomponenten 0,98 und 17 ns). In  $(\text{BA})_2\text{Pb}(\text{Br}_{0,7}\text{I}_{0,3})_4$  steht die Lebensdauer von 0,61 ns für die Relaxation der Exzitonen von der anorganischen Schicht zum Grundzustand. In  $(\text{NMA})_2\text{Pb}(\text{Br}_{0,7}\text{I}_{0,3})_4$  wurden zwei verschiedene Bereiche gemessen (vor und nach 530 nm). Im ersten Bereich (Wellenlänge < 530 nm) stellt die Lebensdauer die Relaxation von der anorganischen Schicht zum Grundzustand dar. Im zweiten Bereich (Wellenlänge > 530 nm) stellt die Lebensdauer die Relaxation vom organischen Triplett-Zustand zum Grundzustand dar. Die PL-Transiente von  $(\text{PMA})_2\text{Pb}(\text{Br}_{0,7}\text{I}_{0,3})_4$  wurde gut mit einer bi-exponentiellen Kurve angepasst. Die schnelle Komponente (0,98 ns) wird verschiedenen Relaxationsprozessen zugeordnet, z. B. Singulett-Singulett-Annihilation in der organischen Schicht. Die langsamere Komponente (17 ns) steht für die Lebensdauer des Pyrenyl-Singulettzustands. Aus den UV-Vis-Absorptions-, Photolumineszenz- und TCSPC-Messungen geht eindeutig hervor, dass jeder Chromophor ein völlig anderes Verhalten aufweist. In  $(\text{BA})_2\text{Pb}(\text{Br}_{0,7}\text{I}_{0,3})_4$  gibt es keine Wechselwirkung oder Energieübertragung zwischen den anorganischen und organischen Schichten, da die Singulett- und Triplett-Zustandsbanden des BA-Chromophors eine höhere Energie aufweisen als die Exzitonenbande. Bei  $(\text{NMA})_2\text{Pb}(\text{Br}_{0,7}\text{I}_{0,3})_4$  und  $(\text{PMA})_2\text{Pb}(\text{Br}_{0,7}\text{I}_{0,3})_4$  besteht jedoch eine starke Kopplung zwischen den Schichten. Bei  $(\text{NMA})_2\text{Pb}(\text{Br}_{0,7}\text{I}_{0,3})_4$  liegt die exzitonische Bande energetisch zwischen der Singulett- und Triplett-Zustandsbande des NMA-Chromophors. In  $(\text{PMA})_2\text{Pb}(\text{Br}_{0,7}\text{I}_{0,3})_4$  ist schließlich die exzitonische Bande energetisch höher als die Singulett- und Triplett-Zustandsbande des PMA-Chromophors.

Zur weiteren Untersuchung des Energietransfers haben wir fs-TAS-Experimente nach 387 nm Anregung für alle Perowskit-Proben durchgeführt. In  $(\text{BA})_2\text{Pb}(\text{Br}_{0,7}\text{I}_{0,3})_4$  beobachten wir nur das Bleihalogenid-Exziton-Signal bei 404 nm ohne jedes andere Signal aus der organischen Schicht, was mit den PL- und TCSPC-Messungen übereinstimmt. Die transienten Absorptionsspektren von  $(\text{NMA})_2\text{Pb}(\text{Br}_{0,7}\text{I}_{0,3})_4$  bestätigen den ultraschnellen Energietransfer von der anorganischen Schicht zur organischen Triplettsschicht innerhalb von 0,26 ps. Aufgrund unserer begrenzten experimentellen Auflösung konnten wir die Kinetik für den Energietransfer von der anorganischen Schicht zum organischen Singulett-Zustand des PMA Chromophors in

(PMA)<sub>2</sub>Pb(Br<sub>0,7</sub>I<sub>0,3</sub>)<sub>4</sub> nicht zeitlich auflösen, der Prozess läuft somit schneller als 150 fs ab. Die Erfassung von TA-Spektren für verschiedene Anregungsleistungen an allen Proben zeigt eine deutliche Abhängigkeit von der Pumpleistung. Mit abnehmender Anregungsleistung verlängern sich die Ladungsträgerabklingzeiten, und die jeweiligen Amplituden der schnellen Komponenten  $\tau_1$  und  $\tau_2$  werden enorm verringert. Der Methylspacer zwischen dem organischen Chromophor und der Ammonium-Ankergruppe ermöglicht einen engen Kontakt zwischen dem 2D-Exziton in der anorganischen Schicht und den organischen Chromophoren, was zu einem Energietransfermechanismus vom Dexter-Typ sowohl in (NMA)<sub>2</sub>Pb(Br<sub>0,7</sub>I<sub>0,3</sub>)<sub>4</sub> als auch in (PMA)<sub>2</sub>Pb(Br<sub>0,7</sub>I<sub>0,3</sub>)<sub>4</sub> führt. Das Verständnis der Wechselwirkung zwischen großen Chromophoren und Perowskit-Strukturen wird dazu beitragen, die Bauelemente für verschiedene Anwendungen zu optimieren, insbesondere für LEDs (hohe Emissionsquantenausbeute) und Solarzellen (hohe Ladungstrennungseffizienz).

Im zweiten Projekt (Ref. 2) haben wir 3D-Perowskite untersucht, bei denen die PbX<sub>6</sub> Oktaeder in allen drei Raumrichtungen verknüpft sind. Doppelkation-Perowskite könnten eine vielversprechende Verwendung als Solarzellen der nächsten Generation und in optoelektronischen Anwendungen haben. Ein Weg zur weiteren Verbesserung der Qualität und Stabilität dieser Materialien ist die Zugabe von Cäsium (Cs) als Dreifachkation zur A-Seite des Mischkations-Formamidinium (FA)/Methylammonium (MA) im Perowskit APbX<sub>3</sub>. Cs/FA/MA-Perowskite weisen einen hohen Wirkungsgrad, eine geringere Fallenbildung, erhöhte thermische Stabilität und eine verbesserte Stabilität gegenüber Feuchtigkeit auf. Die Perowskite auf Bromidbasis sind jedoch Halbleiter mit breiter Bandlücke (> 1,8 eV) im Vergleich zu Iodid-Perowskiten, die stabile Bauelemente für LEDs, Wasserspalter, Sensoren und Hochleistungs-SCs mit mehreren Übergängen darstellen könnten. Die ultraschnelle transiente Absorptionsspektroskopie wurde eingesetzt, um die Photophysik von Einzel- und Mischkation-Perowskiten zu verstehen. Während Cs als Dreifachkation den Wirkungsgrad verbessert, hat der Einfluss von Cs auf die Dynamik von FA/MA-Perowskiten bisher weniger Beachtung gefunden.

Wir haben durch die Ein-Schritt-Spin-Coating-Methode dünne Filme von FA<sub>0,83</sub>MA<sub>0,17</sub>PbBr<sub>3</sub> und Cs<sub>0,05</sub>(FA<sub>0,83</sub>MA<sub>0,17</sub>)<sub>0,95</sub>PbBr<sub>3</sub> auf einem Glassubstrat hergestellt. Wir verwenden zeitaufgelöste spektroskopische Techniken (stationäre Spektroskopie, zeitaufgelöste Emission und fs-TAS), um die Wirkung von Cs auf die Dynamik von Perowskiten auf Basis von Mischkationen mit breiter Bandlücke und Bromid zu untersuchen. Die Absorptionsspektren beider Filme sind ähnlich mit einem scharfen Peak bei 532 nm, was auf eine ähnliche Lokalisierung der Ladungsträger an der Bandkante hinweist. Die PL-Intensität von

## Zusammenfassung

$\text{Cs}_{0,05}(\text{FA}_{0,83}\text{MA}_{0,17})_{0,95}\text{PbBr}_3$  ist im Vergleich zu  $\text{FA}_{0,83}\text{MA}_{0,17}\text{PbBr}_3$  um das Vierfache erhöht, was auf eine Verringerung der nicht-radiativen Rekombinationsstellen im Perowskitfilm hinweist. Die Zugabe von Cs erhöht auch die Lebensdauer der photogenerierten Ladungsträger (von 291 auf 355 ns), indem die Fallendichte und die nicht-radiativen Rekombinationsstellen im Perowskitfilm reduziert werden.

Eine genauere Untersuchung der Dynamik und der Relaxationspfade beider Proben mittels fs-TAS im Spektralbereich von 400 bis 645 nm ergab nach einer Anregung bei 387 nm ähnliche Ergebnisse wie zuvor berichtet. In beiden Filmen beobachteten wir drei Signale, das negative Photobleach-Signal (PB), die positive photoinduzierte Absorption (PIA1) und (PIA2). Das PB bei 532 nm wird dem Band-Filling-Effekt zugeordnet, und stimmt mit dem stationären Absorptionsspektrum überein. Das kurzlebige PIA1-Signal (<1 ps) im Bereich von 539 bis 580 nm ist mit der transienten Elektroabsorption (Stark-Effekt) und der Renormierung der Bandlücke (BGR) verbunden. Das PIA2-Signal (Spektralbereich zwischen 400 und 520 nm), das nicht-exponentiell abklingt, wird der Relaxation freier Ladungsträger zugeordnet. Eine klare Abhängigkeit von der Pumpleistung ist in beiden Filmen zu erkennen, wenn man leistungsabhängige Experimente mit optischen Pumpimpulsen bei 387 nm durchführt. Bei niedriger Pumpleistung erscheint das PIA2-Signal bei frühen Verzögerungszeiten bei 520 nm, ohne sich auch bei längeren Verzögerungszeiten spektral zu verändern. Allerdings wird das PIA2-Signal bei hohen Pumpleistungen mit einer Verbreiterung und einer starken Blauverschiebung (bis 420 nm) beobachtet, was bedeutet, dass das PIA2-Signal ein empfindlicher Indikator für die thermische und Dichteverteilung der Ladungsträger in der Dünnschicht ist. In der  $\text{Cs}_{0,05}(\text{FA}_{0,83}\text{MA}_{0,17})_{0,95}\text{PbBr}_3$ -Schicht beobachteten wir eine Verbesserung des effizienten *hot-phonon-bottleneck* („Heiße-Phononen-Flaschenhals“) aufgrund der großen Masse und des kleinen Ionenradius von Cs mit einer längeren Lebensdauer im Vergleich zur  $\text{FA}_{0,83}\text{MA}_{0,17}\text{PbBr}_3$ -Schicht. Auf der Grundlage der Datenauswertung mit dem Softwarepaket Optimus stimmt die schnellste Komponente mit der Polaronbildungszeit überein. Die langsamste Komponente, die in unserem experimentellen Zeitfenster (1,5 ns) nicht abklingt, ist wahrscheinlich auf eine *non-geminate* („nicht paarweise“) Rekombination zurückzuführen. Unsere Ergebnisse zeigen, dass die Zugabe von Cs eine entspannte Form des Perowskit-Kristallgitters mit weniger Fallen und damit eine bessere Leistung der Bauelemente ermöglicht. Wir glauben, dass die Mischkation-Bleibromid-Perowskite mit breiter Bandlücke ein interessantes Zielmaterial für Solarzellen, Sensoren und Leistungselektronik sein werden.

Im dritten Projekt (Ref. 3) wurden Schiffbasen untersucht. Diese sind bemerkenswerte Kandidaten für zahlreiche Anwendungen wie antibakterielle, antivirale, antitumorale und

antimykotische biomedizinische Anwendungen, organische Leuchtdioden (OLED), Sensoren und photovoltaische Solarzellen, da sie in einem bestimmten Bereich emittieren können. Schiffsbasen werden durch Kondensationsreaktionen zwischen primären Aminen mit Aldehyden oder Ketonen in Gegenwart von homogenen oder heterogenen Katalysatoren unter optimierten Bedingungen synthetisiert. Heterogene Katalysatoren werden häufig in der organischen Synthese verwendet, da sie leicht zu gewinnen sind und eine hohe Effizienz aufweisen. Darüber hinaus wurden für einige Indolderivate und andere heterocyclische Verbindungen aggregationsinduzierte Emissionseigenschaften nachgewiesen. Daher können Schiffsbasen mit Indolanteilen einige interessante optische Eigenschaften aufweisen. Allerdings gibt es nur wenige Studien, die ausschließlich solche Materialien untersucht haben. Der Ersatz des giftigen Piperidin-Katalysators, der in der organischen Synthese verwendet wird, ist sehr wichtig.

Verglichen wurde die Produktausbeute bei der Synthese von sechs neuen, von Indol abgeleiteten Schiffbasen unter Verwendung des heterogenen Katalysators Au@TiO<sub>2</sub> und Piperidin als organischem Katalysator. Beide Katalysatoren zeigten vergleichbare Ergebnisse, aber Au@TiO<sub>2</sub> war leicht zu trennen und recycelbar. Unser Hauptbeitrag zu diesem Projekt ist die Untersuchung der photophysikalischen Eigenschaften der vier Materialien anhand von UV-Vis-Absorption, PL und TCSPC. Alle Lösungen wurden mit Dimethylsulfoxid (DMSO) als Lösungsmittel hergestellt. Die Lösungskonzentration für alle Proben beträgt  $1 \times 10^{-9}$  mol L<sup>-1</sup>, mit Ausnahme der Probe (E)-1-(4-(((3-Chlor-1H-indol-2-yl)methylen)amino)phenyl)ethan-1-on (3b), die eine schwache Absorption zeigt, daher wurde hier die Konzentrationen  $1 \times 10^{-7}$  mol L<sup>-1</sup> verwendet. Die Absorptionspeaks für alle Proben können  $\pi \rightarrow \pi^*$ -Übergängen zugeordnet werden. Erstens resultieren die Peaks bei 280-320 nm aus  $\pi \rightarrow \pi^*$ -Übergängen des aromatischen Kerns. Zweitens beziehen sich die Banden im Bereich 300-360 nm auf  $\pi \rightarrow \pi^*$ -Übergänge der C=N-Gruppen. Die längerwelligen Absorptionen schließlich spiegeln die erweiterte Konjugation im gesamten Molekül wider. Diese Proben weisen verschiedene Grundzustände für unterschiedliche Substituenten auf.

Die Emissionsspektren von (E)-1-(3-Chlor-1H-indol-2-yl)-N-(4-methoxyphenyl)methanimin (3a) (Methoxygruppe) und (3b) (Acetylgruppe) weisen keine Veränderung des Maximums (415 nm) auf; es wurde jedoch berichtet, dass diese Gruppen die Energielücke zwischen dem niedrigsten unbesetzten Molekülorbital (LUMO) und dem höchsten besetzten Molekülorbital (HOMO) beeinflussen können, so dass eine Blau- oder Rotverschiebung entsteht. Durch Ersetzen des Phenylrings von (3a) und (3b) durch Naphthyl in (E)-1-(3-Chlor-1H-indol-2-yl)-N-(naphthalen-1-yl)methanimin (3c) und Carbazolyl in (E)-1-(3-Chlor-1H-indol-2-yl)-N-(9-

## *Zusammenfassung*

ethyl-9H-carbazol-3-yl)methanimin (3f) wird das Emissionsmaximum auf 430 bzw. 450 nm rotverschoben. Dieses Ergebnis deutet auf die Möglichkeit hin, dass die Substituentengruppen die Energie  $E_{\text{HOMO}}$  in der Reihenfolge Carbazolyl > Naphthyl > Phenyl erhöhen.

Um die Lebensdauer dieser Emissionen weiter zu untersuchen, führten wir TCSPC-Messungen im Lösungszustand durch. Die untersuchten Schiffbasen zeigten gut angepasste biexponentielle Zerfallsprofile mit Emissionslebensdauern in der Größenordnung von Nanosekunden. Wir ordneten diese Zerfallszeiten der Fluoreszenz zu, die von angeregten Singulett-Zuständen emittiert wird. Bei der Bestimmung der Emissionsfarben mit der Commission Internationale de l'Éclairage (CIE) zeigten die (3b), (3c) und (3f) Proben eine tiefblaue Fluoreszenz mit CIE-Koordinaten von  $y < 0,1$ . Daher könnten diese Materialien für die Entwicklung neuer OLEDs mit geringerem Energieverbrauch interessant sein.

**Keywords:** Ultrafast spectroscopy, transient absorption spectroscopy, TCSPC, lead-halide perovskites, bromide-based perovskite, 2D perovskite, 3D perovskite, energy transfer, wide-bandgap semiconductor, benzyl ammonium (BA), 1-naphthyl methyl ammonium (NMA), 1-pyrene methyl ammonium (PMA), mixed-cation, triple-cation, Schiff base



# Table of Contents

<i>Chapter 1 Introduction</i> .....	1
1.1 Background and progress in perovskite research .....	2
<i>Chapter 2 Theoretical Framework and Spectroscopic Methods</i> .....	9
2.1 Basic concepts of semiconductors .....	9
2.1.1 Excitons and free charge carriers .....	9
2.1.2 Polarons.....	10
2.1.3 Low and high dimensional systems .....	11
2.1.4 Thin film deposition methods for semiconductor solutions.....	12
2.2 Spectroscopic background .....	13
2.2.1 UV-Vis spectroscopy .....	13
2.2.2 Steady-state photoluminescence spectra (PL).....	14
2.2.3 Relaxation processes .....	14
2.2.4 Time-correlated single photon counting (TCSPC) .....	16
2.2.5 Transient absorption spectroscopy (TAS).....	17
<i>Chapter 3 Ultrafast Dynamics in 2D &amp; 3D Perovskite Thin Films</i> .....	25
3.1 Ultrafast Dynamics in 2D perovskite thin films .....	25
3.1.1 Introduction.....	25
3.1.2 Dynamics of (BA) <sub>2</sub> Pb(Br <sub>0.7</sub> I <sub>0.3</sub> ) <sub>4</sub> thin film .....	26
3.1.3 Dynamics of (NMA) <sub>2</sub> Pb(Br <sub>0.7</sub> I <sub>0.3</sub> ) <sub>4</sub> thin film.....	27
3.1.4 Dynamics of (PMA) <sub>2</sub> Pb(Br <sub>0.7</sub> I <sub>0.3</sub> ) <sub>4</sub> thin film .....	28
3.2 Ultrafast Dynamics in 3D perovskite thin films .....	29
3.2.1 Introduction.....	29
3.2.2 Influence of the Cs as triple cation.....	30
<i>Chapter 4 Photophysical Properties of New Schiff Bases Containing an Indole Moiety</i> .....	33
4.1 Introduction.....	33

4.2 Photophysical behavior of the selected Schiff bases .....	33
<i>Chapter 5 Conclusion and Outlook</i> .....	37
5.1 Conclusion .....	37
5.2 Outlook .....	38
<i>Chapter 6 Bibliography</i> .....	39
<i>Chapter 7 List of Publications</i> .....	55
7.1 Declaration of the own contribution for each publication: .....	55
7.2 Elshanawany et al., <i>Nanoscale 2021, 13</i> .....	56
7.3 Elshanawany et al., <i>ACS.JPCC 2022, 126</i> .....	73
7.4 Soliman et al., <i>ACS Omega 2022, 7</i> .....	86
Abbreviations .....	115
Acknowledgements .....	117
Curriculum Vitae.....	121

## List of Figures

Figure 1.1. Perovskite crystal structure $ABX_3$ .	2
Figure 1.2. Recent progress in the perovskite solar cell.	3
Figure 1.3. Degradation scheme of $MAPbI_3$ .	5
Figure 1.4. Scheme of perovskite structure series from 2D to 3D showing the quasi 2D as intermediate of both structures.	6
Figure 2.1. The scheme shows the movement of the anions (large circles) and cations (small circles) in a lattice from their equilibrium positions (small and large open circles) to a new configuration (small and large filled circles), leading to producing a potential well for that self-trapped electron on a cation (hatched area). Readapted from ref. 102.	10
Figure 2.2. Examples of crystal structures of 0D ( $(CH_3NH_3)_4PbI_6 \cdot 2H_2O$ ), 1D ( $(NH_2C(I) = NH_2)_3PbI_5$ ), 2D ( $(C_9H_{19}NH_3)_2PbI_4$ ) and 3D ( $CH_3NH_3PbI_3$ ). The red spheres are Pb atoms, blue spheres I atoms, and black spheres are O, N and C atoms.	11
Figure 2.3. Absorption measurement setup.	13
Figure 2.4. Scheme of Jablonski diagram with different possible relaxation pathways.	14
Figure 2.5. Scheme of electron-hole recombination mechanism. (1) band-to-band recombination and (2) trap-assisted recombination and the electronic levels related to an exciton in a direct bandgap semiconductor.	15
Figure 2.6. Optical scheme of the femtosecond transient absorption spectrometer.	18
Figure 2.7. The scheme represents the three processes that can be observed in a transient absorption spectrum, e.g., ground state bleach (GSB), stimulated emission (SE) and excited state absorption (ESA).	19
Figure 2.8. The generation of different frequencies by two incident pulses in a non-linear crystal.	19
Figure 2.9. Phase matching direction in a uniaxial birefringent crystal.	21
Figure 2.10. Spectrum of white light continuum generated in $CaF_2$ crystal by excitation at 778 nm.	22
Figure 3.1. The chemical structure of the benzyl (left), naphthyl (middle), and pyrenyl (right) perovskite thin films. X = Br (70%) and I (30%).	26
Figure 3.2. (a) A schematic representation showing the energy levels of the organic and inorganic layers. (b) UV-vis absorption and normalized PL spectra (the excitation wavelength for the emission measurements was 320 nm) and (c) transient absorption data for $(BA)_2Pb(Br_{0.7}I_{0.3})_4$ thin films excited at 387 nm ( $81 \mu J/cm^2$ ) at room temperature.	27

Figure 3.3. (a) A schematic representation showing the energy levels of the organic and inorganic layers. (b) UV-vis absorption and normalized PL spectra (the excitation wavelength for the emission measurements was 320 nm) and (c) TA map for (NMA) <sub>2</sub> Pb(Br <sub>0.7</sub> I <sub>0.3</sub> ) <sub>4</sub> thin films excited at 387 nm (81 μJ/cm <sup>2</sup> ) at room temperature. ....	27
Figure 3.4. (a) A schematic representation showing the energy levels of the organic and inorganic layers. (b) UV-vis absorption and normalized PL spectra (the excitation wavelength for the emission measurements was 320 nm) and (c) TA map for (PMA) <sub>2</sub> Pb(Br <sub>0.7</sub> I <sub>0.3</sub> ) <sub>4</sub> thin films excited at 387 nm (146 μJ/cm <sup>2</sup> ) at room temperature. ....	29
Figure 3.5. (a) Steady-state absorption, (b) steady-state photoluminescence (PL) spectra with optical excitation at 362 nm, and (c) time-resolved (PL) decay with optical excitation at 387 nm of FA/MA (blue) and Cs/FA/MA (orange) thin films deposited on glass substrates at room temperature. ....	31
Figure 4.1. The chemical structure of 3a, 3b, 3c and 3f Schiff base derivatives. ....	33
Figure 4.2. Photophysical behavior of DMSO solutions of 3a, 3b, 3c, and 3f at room temperature: (a) UV-Vis absorption spectra (1×10 <sup>-7</sup> mol L <sup>-1</sup> for 3b and 1×10 <sup>-9</sup> mol L <sup>-1</sup> for 3a, 3c, and 3f). (b) Emission spectra with excitation at 320 nm (1×10 <sup>-7</sup> mol L <sup>-1</sup> ). (c) Photoluminescence decay profiles at 320 nm excitation. ....	34





## *Chapter 1 Introduction*

In the last twenty years, there has been splendid progress in energy conversion technologies to have sustainable energy sources. For example, solar cells contribute significantly to energy production as the sun is an enormous source for renewable energy. Currently, the most common commercialized photovoltaic devices are silicon-based. The scientists' main targets are high efficiency, low cost, environmentally friendly, and easy to synthesize new semiconductor materials to replace silicon. Furthermore, understanding the photophysical properties of these materials is very important for designing high efficient photoconversion systems.

This thesis investigates the photophysics of lead-based wide-bandgap perovskites with different dimensionality (2D, 3D) and how they can be optimized for optoelectronic applications. In chapter 1, we present the background and progress in perovskite research. The basic concepts of semiconductor and spectroscopic methods of the applied techniques in this work are discussed in chapter 2.

In the first project (chapter 3.1), we used our time-resolved techniques to study the ultrafast dynamics of energy transfer from the inorganic to the organic layer in a series of three lead-based mixed-halide 2D perovskites containing benzyl ammonium (BA), 1-naphthyl methyl ammonium (NMA), and 1-pyrene methyl ammonium (PMA) thin films.

In the second project (chapter 3.2), we used time-resolved spectroscopic techniques to study the effect of adding 5% of Cs on the dynamics of a mixed-cation wide bandgap bromide-based 3D perovskite.

In another side project (chapter 4), we present the photophysics properties of newly synthesized new Schiff bases containing indole moieties using piperidine as an organic base catalyst and Au@TiO<sub>2</sub> as a heterogeneous catalyst. Finally, the results of this work are summarized in Chapter 5 with an outlook and a discussion of open questions for further research.

## 1.1 Background and progress in perovskite research

Organic–inorganic metal halide perovskites with the general formula  $ABX_3$  (A can be an organic cation like  $CH_3NH_3^+$ ,  $CH(NH_2)_2^+$ , etc. or inorganic like  $Cs^+$ ,  $Rb^+$ ; B =  $Pb^{2+}$  or  $Sn^{2+}$ ; X =  $Cl^-$ ,  $Br^-$ ,  $I^-$ ) promise new semiconductor materials in the field of photovoltaics which could show long carrier lifetimes<sup>[1]</sup>, sharp band edges<sup>[2,3]</sup>, high absorption coefficients<sup>[4,5]</sup>, the flexibility of tuning optical band gaps from the visible to the near IR wavelength ranges<sup>[6,7]</sup>, large hole and electron mobilities<sup>[8]</sup>, low trap densities<sup>[9,10]</sup> and high photoluminescence quantum yields<sup>[11]</sup>.

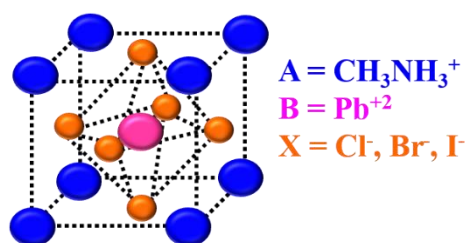


Figure 1.1. Perovskite crystal structure  $ABX_3$ .

Originally, perovskites as metal oxides were known as a class of compounds with the chemical structure  $ABO_3$ , most of which are classified as piezoelectric or ferroelectric materials. Gustav Rose was the first to discover perovskite in a piece of chlorite-rich skarn in 1839 ( $CaTiO_3$ )<sup>[12,13]</sup>. Cation A has 12-fold cuboctahedral coordination and sits at the cube corner positions. Cation B has 6-fold coordination surrounded by an octahedron of X anions. X anion occupying the face-centered positions. The hydrogen bonding among the  $A^+$  cations and halogen  $X^-$  anions, plus the electrostatic interactions, are helping to stabilize the 3D structure<sup>[14]</sup> (see Figure 1.1). By replacing oxygen with halide, Miyasaka's lab could show a photovoltaic function of the perovskite nanocrystalline particles self-organized on the  $TiO_2$  mesoporous layer with an efficiency of 3.8% on a  $CH_3NH_3PbI_3$ -based cell, and a high photovoltage of 0.96 V was obtained with a  $CH_3NH_3PbBr_3$ -based cell as an excellent start for other researchers<sup>[15,16]</sup>. The high electronegativity of the X anion increases the ionic character of the perovskite and highly influences the bandgap and the absorption spectra of the material. So, variation of the halogen ( $Cl^-$ ,  $Br^-$ ,  $I^-$ ) or using mixed halides enables tuning the bandgap (for solar cell or optoelectronic applications) as a unique point of halide perovskite semiconductors. The lowest bandgap energy (red-shift) can be achieved by the use of iodine (vice versa, adding chloride leads to a blue shift in the bandgap). From that time, many works have been published about the synthesis of new perovskites with promising efficiency and stability. The efficiency jumped from 3.8<sup>[15]</sup> to more than 25% during extensive work from many groups over thirteen years, which puts the perovskite competing with the best photovoltaic cell efficiency (PCE) of crystalline silicon solar cells (Figure 1.2 readapted from <https://www.nrel.gov/pv/cell-efficiency.html>).



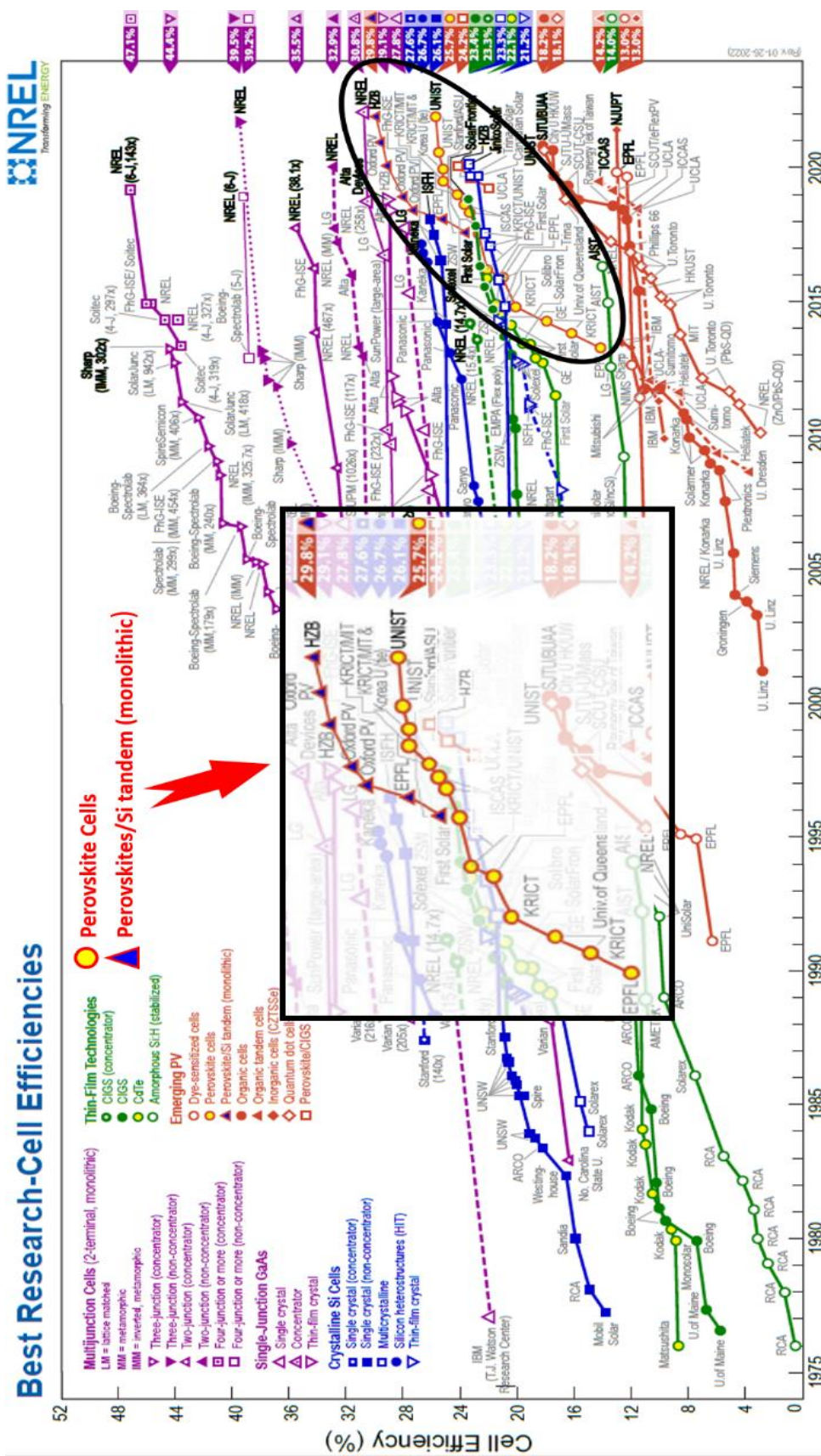
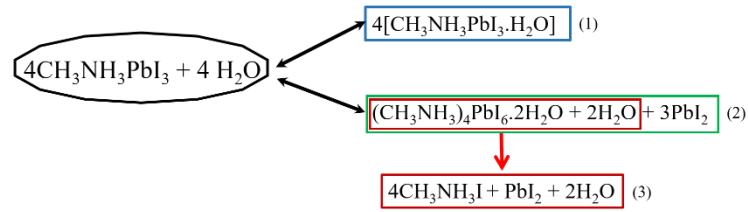


Figure 1.2. Recent progress in the perovskite solar cell.

## Introduction

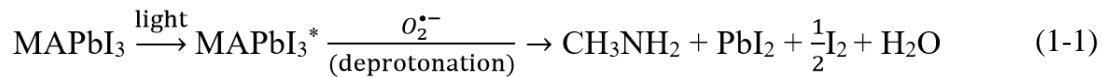
Halide perovskites are highly ionic crystals (ionic conductors) compared to oxide ones ( $ABO_3$ ). The solubility of lead halide perovskites in polar solvents (dimethylformamide, alcohol, etc.) opens the possibility of coating perovskite films in solar cell applications. However, halide perovskites have unique properties; there are many demands required from the industry, like stability and durability. The Photovoltaic (PV) community studied the solid-state physics of halide perovskites (charge recombination, mechanisms of carrier transport), especially three-dimensional (3D) perovskites, because of the isotropic carrier transport feature for power generation and long diffusion lengths for free carriers (Example:  $MAPbI_3$  (MA=methylammonium))<sup>[17,18]</sup>. Taking  $MAPbI_3$  as an example for 3D perovskites, the electronic structure of the valence band (VB) is 25% of ( $6s^2$ ) Pb orbital (lone pair) and 75% of (5p) I orbitals, while the conduction band is made of a mixture of (6p) Pb plus other orbitals with strong coupling between (5p) I and ( $6s^2$ ) Pb lone-pair<sup>[19]</sup>. There is a similar feature of  $MAPbI_3$ , GaAs and Si, the long carrier lifetime of hundreds of nanoseconds. Due to the help of the high ionic density of halides, the charge recombination is reduced by a charge-screening effect against Coulombic interactions<sup>[17,20,21]</sup>. Having all these unique features in the perovskite structure is not sufficient for industrial applications if the perovskite material is not stable. The target in the last few years was to improve the stability by replacing the A-site cation and the B-site anion with different inorganic or organic cations and halogen anions. The MA cation has a critical problem with thermal stability above 120 °C, so the direction is now to mix or replace it with other inorganic cations<sup>[22–24]</sup>. Replacing the MA with single cations like formamidinium (FA) cations or inorganic Cs yielded increased thermal stability with low energy of the bandgap<sup>[22,25–29]</sup>. Adding Cs as second cation to  $FAPbI_3$  ( $FA_xCs_{1-x}PbI_3$  film) showed devices with high performance (Efficiency > 20%)<sup>[30,31]</sup>. The key point of mixed cation perovskite samples is stabilizing the crystal structure with high symmetry (cubic). The mixed cation sample (FA/MA/Cs) is usually cubic, while the  $MAPbI_3$  is tetragonal, so it has the best stability. Nowadays, one of the best common options is triple-cation perovskite (Cs/FA/MA)Pb(I/Br)<sub>3</sub><sup>[32,33]</sup>. Saliba et al. reported that adding 5% Cs to the mixed cation sample (FA/MA) could improve the stability and efficiency of the device<sup>[32]</sup>.

External conditions such as air, heat, and moisture influence the intrinsic stability of perovskite structure. In other words, the device degrades as the perovskite is sensitive to water by forming hydrated compounds through hydrogen bonding. As shown in Figure 1.3, the loss of hydrated compounds can be reversed back to  $MAPbI_3$  (Eq. 1 and Eq. 2). On the other hand, complete segregation of the perovskite to  $CH_3NH_3I$  and other components (Eq. 3) with excess water might cause. Many ways have been developed to improve the moisture sensitivity and the



**Figure 1.5.** Degradation scheme of MAPbI<sub>3</sub>.

stability of the perovskite, such as the common polymer (spiro-OMeTAD)<sup>[34]</sup> as a hydrophobic layer or by modifying the surface with small molecules<sup>[35]</sup> or by mixing a small amount of two-dimensional (2D) perovskite containing hydrophobic organic cations<sup>[36–38]</sup>. Although the 2D perovskites usually have a high energy bandgap with negligible electron-transport features and narrow absorption bands, 2D perovskites could significantly improve the 3D perovskite's long-term stability and efficiency<sup>[39–43]</sup>. The researchers have found that the surface of a 3D perovskite film is affected by the atmosphere (O<sub>2</sub> and N<sub>2</sub>); however, the 2D perovskite has been used as a protective layer against humidity. The perovskite film is degraded by oxygen due to the formation of superoxide by electron transfer to O<sub>2</sub> from the photoexcited MAPbI<sub>3</sub><sup>\*</sup>, as shown in Eq. 1-1<sup>[44,45]</sup>.



Therefore, encapsulation methods would be the best solution against these stability challenges. In the last few years, low dimensional (LD) perovskite semiconductors attracted much attention due to their different optical and electronic properties compared to those of the bulk ones. Following the use of large cations, e.g., alkylammonium, to replace the small cation (MA, FA, Cs), lead to structure shifts from 3D to 2D as the organic ammonium cation layers separate the 2D (MX<sub>4</sub>)<sup>-2</sup> sheets consequently the structure regulates the connecting bonds via hydrogen bonding between the organic cation ammonium groups, via van der Waals interactions between adjacent organic tails and the inorganic sheet halogens. For this reason, the excitons are confined within the 2D inorganic layers since the interfaces between the organic and inorganic layers are flat<sup>[46,47]</sup>. Therefore, the width of the barrier layer in the 2D system is vital to the quantum confinement effect. Takeoka et al. reported the change in the quantum confinement structure with different halide species, well thickness, and barrier size of perovskite thin films with long-chain lengths<sup>[48]</sup>. In addition, there is another group of materials called quasi-2D perovskites structurally between the 2D and 3D systems, which are achieved by multi-sheet layers of MAPbX<sub>3</sub> perovskites sandwiched between organic ammonium layers with (n) number of inorganic monolayer sheets. As shown in Figure 1.4, increasing these inorganic monolayer sheets will produce a 3D structure. The general formula of the quasi-2D perovskites is A<sub>2</sub>B<sub>n-1</sub>M<sub>n</sub>X<sub>3n+1</sub> (A = CH<sub>3</sub>(CH<sub>2</sub>)<sub>n</sub>NH<sub>3</sub><sup>+</sup>; B = CH<sub>3</sub>NH<sub>3</sub><sup>+</sup>; M = Pb<sup>2+</sup> or Sn<sup>2+</sup>; X = I<sup>-</sup>, Br<sup>-</sup>, Cl<sup>-</sup>)<sup>[47–52]</sup>.

These materials are counted as Ruddlesden–Popper series. The quasi-2D perovskites could show a high performance in LEDs applications due to the large exciton binding energy and the high photoluminescence quantum yields (PLQYs)<sup>[53]</sup>. Many factors (the deposition method and the spacing cation) influence the 2D films during the fabrication process, e.g., crystallinity and film morphology, as they might lead to different phases<sup>[54,55]</sup>.

There is a quick jump in the field of 2D perovskite materials with a high interest in understanding the photophysics properties of these materials. After the material absorbs light (excitation), luminescence might arise from the organic or inorganic layers. The emission arising from the inorganic layer comes through radiative decay of the excited electron-hole pairs (excitons) or self-trapped excitons<sup>[56]</sup>. Emission come from the organic layer through excited molecules  $S_1$  or  $T_1$  states (Fluorescence or phosphorescence). The emission might also come from both layers due to the energy transfer from the inorganic to the organic layer. The history of these materials started in 1993; the first 2D mixed halide perovskites were synthesized with different organic cations by Papavassiliou<sup>[57–64]</sup> and later by Mitzi<sup>[51,65–68]</sup>. Mitzi and his co-

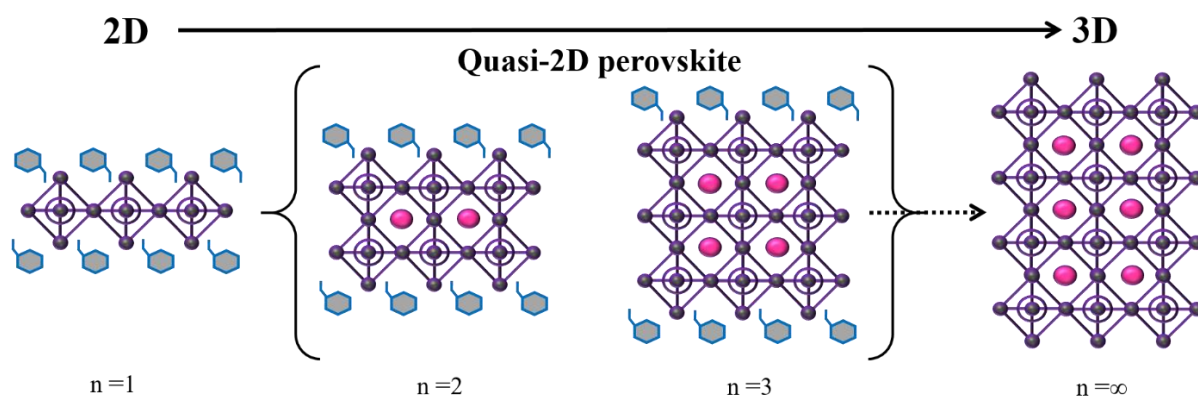


**Figure 1.6.** Scheme of perovskite structure series from 2D to 3D showing the quasi 2D as intermediate of both structures.

workers reported a promising series of Sn-I-based perovskites for thin film transistor application<sup>[69]</sup> based on the high electrical conductivity of these materials<sup>[51,70]</sup>. The first effort to investigate the photophysics of lead-based 2D perovskite was from Ishihara and his co-workers by visualizing the effects of the organic cations on the optical properties and their excitonic nature<sup>[71–74]</sup>. Even though the inorganic layer is the domain layer of luminescence properties for 2D halide perovskites, there is an opportunity for coupling the luminescent properties of both layers (inorganic with organic chromophores)<sup>[56]</sup>. A broad range of many chromophores like azobenzene<sup>[75]</sup>, naphthalene<sup>[75]</sup>, thiophene derivatives<sup>[66,76]</sup>, anthracene<sup>[77]</sup>, p-terphenyl<sup>[78]</sup>, pyrene<sup>[79]</sup>, and other groups<sup>[80,81]</sup> have been used as cations in 2D perovskite layers. There are two possibilities resulting from this mixture: weak or strong coupling between organic and inorganic layers. The weak coupling occurs as a result of no interaction between

the organic and inorganic sublattices; thus, the emission is an aggregate of the luminescence spectra of the individual components. For example, Cortecchia et al. reported that by using 4,4'-(1,1'-biphenyl-4,4'-diyl)di-aniline as an organic building block in 2D Cu–Cl perovskite: no emission was detected from Cu–Cl framework and the emission arises only from the organic chromophore<sup>[81]</sup>. The strong coupling between the excited state of the organic and inorganic layers will lead to the emission of the organic molecule due to energy transfer from the inorganic lattice to a lower state of the chromophore. In this case, the emission depends on the excitation wavelength (energy) and the tuning of the inorganic layer energy. Braun et al. reported different Pb–Cl perovskites containing benzyl ammonium, phenethyl, 2-naphthyl methyl, and 2-anthryl methyl cations with different energy levels<sup>[77]</sup>. To better understand the energy transfer mechanism, Era et al. synthesized a series of alkylammonium-linked naphthalene molecules to study the influence of the alkyl chain length on the energy transfer efficiency. They reported that perovskites formed from naphthalene derivatives with shorter alkyl chains showed that energy transfer becomes highly efficient as the chromophore is moved close to the inorganic lattice<sup>[82]</sup>. Furthermore, that energy transfer can be stated as Dexter charge transfer mechanism<sup>[83]</sup> or Förster resonance energy transfer (FRET) mechanism<sup>[84]</sup>. The main difference between both mechanisms is the length scale. When the distance between two parties decreases, the reaction rate constant of Dexter energy transfer rises. Ema et al. studied an example of a Dexter energy transfer from the inorganic layer to naphthalene molecules in the organic layer investigated by temperature-dependent measurements<sup>[85]</sup>. Braun and co-workers were the first group to study the packing effect arrangement of organic chromophores (pyrene-methyl ammonium cation (PMA)) with different halides (Cl and Br)<sup>[79]</sup>. In (PMA)<sub>2</sub>PbCl<sub>4</sub>, the perovskite displayed only monomeric fluorescence from pyrene. However, in (PMA)<sub>2</sub>PbBr<sub>4</sub>, there is energy transfer from the inorganic excitonic band (Pb–Br) to the excited singlet state of pyrene, leading to excimer formation and for iodide pure phosphorescence is observed<sup>[79]</sup>. Furthermore, Kagan and co-workers studied the energetic effect of the excitonic band energy by changing the halide side (Cl, Br, I) in the perovskite containing the organic chromophore AEQT (5,5'' bis(ethylammonium)-2,2':5',2'':5'',2'''-quaterthiophene<sup>[66]</sup>). In their study, they found that by shifting the VB to higher energy in the iodide perovskite, the photoluminescence is quenched due to trapping the holes in the inorganic layers concurrently with the electrons migrating to the LUMO of the organic layer. However, (AEQT)PbCl<sub>4</sub> showed radiative recombination since electrons and holes migrate into the LUMO and HOMO<sup>[56,66]</sup>. These materials have other applications beside the solar cell and LEDs such as scintillators<sup>[86,87]</sup> and phosphors (using the narrow<sup>[88,89]</sup> and broad<sup>[88]</sup> emission feature).



# *Chapter 2 Theoretical Framework and Spectroscopic Methods*

This chapter is divided into two sections. In the first section, basic concepts of semiconductors related to the results of this work are discussed. The second section presents the spectroscopic background of the applied techniques in this thesis.

## **2.1 Basic concepts of semiconductors**

The classic definition of a semiconductor is a crystalline solid characterized by a forbidden gap separating two bands of states; the occupied valence band (VB) and the empty conduction band (at low temperatures). There are two classes of semiconductors: direct and indirect bandgaps with different optical properties. When the energetic maximum of the valence band and the energetic minimum of the conduction band occur at the same point in the Brillouin zone, it is called a direct bandgap. When it occurs at different points, it is called an indirect bandgap. A direct bandgap leads to allowed electronic transitions between VB and CB.

### **2.1.1 Excitons and free charge carriers**

Excitation creates an electron-hole pair when electrons get excited to the CB, they leave holes in the VB. These missing electrons (holes) are treated in solid state physics as quasi-particles with positive elementary charge  $+e$  and effective mass  $m_h$ . The pair consists of free carriers if the electron and hole interaction is negligible. On the other hand, due to an electrostatic Coulomb interaction (quasi-particles) between an electron and hole, an exciton can be formed as a bound state of an electron and a hole with a total charge of zero. Excitons can be formed by direct photoexcitation or a combination of free carriers. The binding energy of these excitons can play an essential role in different applications. In the first scenario, they get separated after the photoexcitation to free carriers, and fits well for the photovoltaic devices, meaning low binding energy. In the second scenario, the exciton binding energy is high, so the exciton remains bound and emits light. This feature can be used for laser media and light-emitting diode technologies. The electron-hole interaction must be considered to describe the exciton after the excitation. An exciton's binding energy ( $E_b$ ) and size significantly influences the exciton dynamics from optical absorption to equilibration before the photoluminescence emission<sup>[90]</sup>. The dielectric constant defines the exciton binding energy as it balances the electron-hole interactions or protects the electron-electron repulsions. Usually, compared to thermal energy at room temperature ( $k_B T \sim 25$  meV), the exciton binding energy is small in the bulk

semiconductor with a high dielectric constant and lower bandgap; subsequently, the exciton is not a unique feature in these materials. For example, the exciton binding energy is 4.9 meV for GaAs, ~10 meV for 3D perovskites<sup>[91,92]</sup>, 15 meV for CdSe, 27 meV for CdS but > 150 meV in 2D perovskites with n=1<sup>[72,93–96]</sup>. Some 3D perovskites like CH<sub>3</sub>NH<sub>3</sub>PbBr<sub>3</sub> and CH<sub>3</sub>NH<sub>3</sub>PbI<sub>3</sub>, showed temperature dependence of exciton binding energy<sup>[97]</sup>. The exciton binding energy has to be measured at low temperatures due to the phase transition at 160 K, as it will be different compared to measuring at room temperature<sup>[91,98–100]</sup>. The 2D perovskite structure contains the inorganic layer as the well and the organic spacer as the barrier. The exciton binding energy of 2D perovskite is higher than the 3D one because the inorganic layer usually has a higher dielectric constant than the organic spacer. The E<sub>b</sub> of 2D perovskite can be calculated by,

$$E_b = 4\left(\frac{\epsilon_w}{\epsilon_b}\right)^2 E_b^{3D} \quad (2-1)$$

Where  $\epsilon_w$  and  $\epsilon_b$  are the dielectric constants of the well and barrier, respectively, and  $E_b^{3D}$  is the exciton binding energy of the corresponding 3D perovskite<sup>[55]</sup>.

## 2.1.2 Polarons

Polarons are quasi-particles that result from the strong coupling of electrons or holes with ionic vibrations in polarizable materials. The term "polaron" was termed by Pekar<sup>[101]</sup> and generally refers to an electronic charge carrier in a solid-state material, which alters the atomic motions of this material, as illustrated in Figure 2.1. So if the electronic carriers are self-trapped, they can be treated as strong-coupling polarons. On the other hand, it is called week-coupling polarons if the electronic carriers are not self-trapped. The quasi-particle is called small polaron (strong coupling) or large polaron (weak coupling) based on the intensity of the electron-phonon coupling<sup>[102]</sup>. The small polarons have many features like incoherent motion, mobility

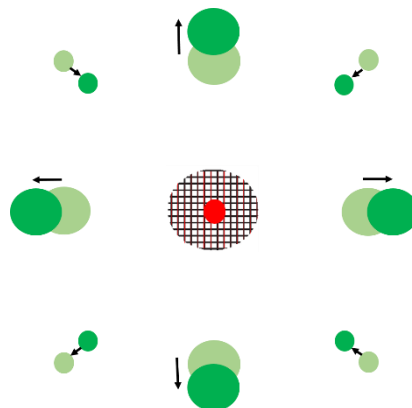


**Figure 2.1.** The scheme shows the movement of the anions (large circles) and cations (small circles) in a lattice from their equilibrium positions (small and large open circles) to a new configuration (small and large filled circles), leading to producing a potential well for that self-trapped electron on a cation (hatched area). Readapted from ref 102.



increasing with temperature, polaron radius being almost the same as the lattice parameter, narrow mid-gap electronic states, and short-range electron-phonon interaction<sup>[103]</sup>. By contrast, large polarons show coherent motion, mobility decreasing with temperature, a polaron radius larger than the lattice parameter, shallow electronic states, and long-range electron-phonon interaction.

### 2.1.3 Low and high dimensional systems

The synthesis of semiconductor materials with different dimensionality, e.g., zero-dimensional (0D), one-dimensional (1D), two-dimensional (2D), or high dimensional, e.g., three-dimensional (3D), opened many applications due to the possibility of having different physical properties like dielectric quantum confinement of the exciton, excitonic absorption, and photoluminescence. For example, the synthesis of 2D systems showed enhancement in the oscillator strength and higher excitonic binding energy  $E_b$  ( $\sim 360$  meV)<sup>[104]</sup>, which was early applied to light-emitting devices and affordable transistors<sup>[105–108]</sup>. By taking the building block  $MX_6$  octahedron ( $M = \text{Pb}$  or  $\text{Sn}$  and  $X = \text{Cl}$ ,  $\text{Br}$  or  $\text{I}$ ) as an example, the 0D system has isolated octahedral crystallized with no interaction Ex:  $(\text{CH}_3\text{NH}_3)_4\text{PbI}_6 \cdot 2\text{H}_2\text{O}$ <sup>[109]</sup>. In the 1D system, each octahedron shares two opposite corners forming separate infinite chains with linear arrangement (Ex:  $(\text{NH}_2\text{C}(\text{I}) = \text{NH}_2)_3\text{PbI}_5$ )<sup>[61,110]</sup>. In the case of each octahedron sharing four coplanar corners lead to 2D system formation. So the 2D material has separate layers that come from the long carbon amine part (Ex:  $(\text{C}_9\text{H}_{19}\text{NH}_3)_2\text{MX}_4$ )<sup>[59,111]</sup>. In the 3D system, each octahedron shares all its corners to connect from all directions to form the 3D network (Ex:  $(\text{CH}_3\text{NH}_3\text{MX}_3)$ <sup>[112]</sup>. In semiconductor thin films, by lower the system's dimensionality, the

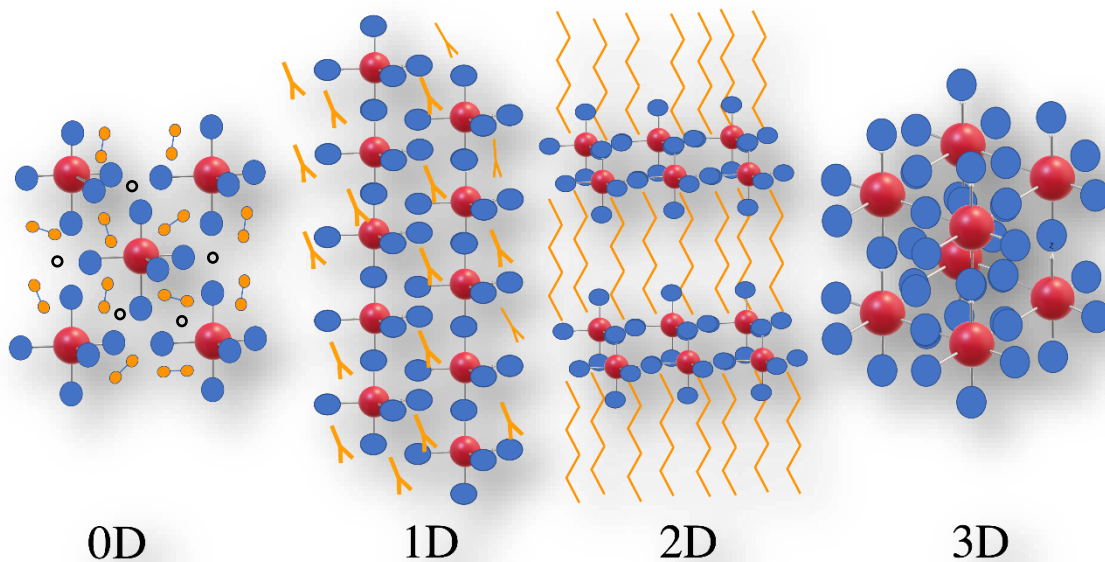


**Figure 2.2.** Examples of crystal structures of 0D  $(\text{CH}_3\text{NH}_3)_4\text{PbI}_6 \cdot 2\text{H}_2\text{O}$ , 1D  $(\text{NH}_2\text{C}(\text{I}) = \text{NH}_2)_3\text{PbI}_5$ , 2D  $(\text{C}_9\text{H}_{19}\text{NH}_3)_2\text{PbI}_4$  and 3D  $(\text{CH}_3\text{NH}_3\text{PbI}_3)$ . The red spheres are Pb atoms, blue spheres I atoms, and black spheres are O, N and C atoms.

quantum mechanical wave functions of the electron and hole are confined within the materials, leading to so-called quantum confinement effects<sup>[73,113]</sup>. In other words, the characteristic semiconductor dimension ( $L$ ) has to be much longer than the effective de Broglie wavelength ( $\lambda_D$ ) of a thermal electron or hole to behave as a classical particle ( $L \gg \lambda_D$ ). In case of  $L \approx \lambda_D$ , the electron wave must be taken into account since the electrons become confined. Particularly, when the electron motion is confined in three dimensions its forms 0D nanocrystals or quantum dots. Confinement in one or two dimensions forms 1D quantum wires or creates 2D quantum wells<sup>[104]</sup>. Since the inorganic layers are higher polarizable than the organic layers<sup>[74]</sup>, the dielectric confinement comes from the poor screening of the Coulombic attraction between the electron and hole by the organic layers<sup>[93,114,115]</sup>.

#### **2.1.4 Thin film deposition methods for semiconductor solutions**

The typical coating method used in industry is vacuum deposition, as it offers stable and highly uniform films with the option to perform multilayer deposition methods. However, this method requires large material consumption and expensive steps. On the other hand, the solution processes have many advantages like less material use, low cost, and compatibility. For high-quality film formation, choosing the coating method depends on the characteristics of the material, and the solvent used is essential. The method that we have used for this work is the spin coating method. In principle, we mixed a lead halide (inorganic) solution with organic ammonium hydrohalide with a specific molar ratio (1:2 for 2D perovskite or 1:1 in 3D perovskite) and spin-coated that mixture on a substrate. Dimethylformamide (DMF) and dimethylsulfoxide (DMSO) proved to be the most common solvents for this process. The thin film thickness could be controlled by the rotational speed of the spin coater and the concentration of the perovskite precursor.

## 2.2 Spectroscopic background

In this section, the theoretical background and the general principles of optical spectroscopy techniques are discussed. To investigate the relaxation process of charge carriers and excitons in the perovskite samples, we used UV-Vis absorption spectroscopy, steady-state photoluminescence spectroscopy (PL), time-correlated single photon counting (TCSPC), and femtosecond transient absorption spectroscopy (fs-TAS). UV-Vis absorption spectroscopy is discussed in subsection 2.2.1, and PL spectroscopy is discussed in subsection 2.2.2. Finally, in subsections 2.2.3, 2.2.4 and 2.2.5, we discuss relaxation processes and the time-resolved techniques (TCSPC and TAS).

### 2.2.1 UV-Vis spectroscopy

Absorption spectroscopy is a helpful tool for estimating allowed molecular transitions and the nature of semiconductors. It is used to investigate the electronic states of atoms, molecules or solid-state materials by measuring the absorption of radiation as a function of wavelength or energy in the ultraviolet ( $\lambda \leq 400 \text{ nm}$ ,  $\Delta E \geq 3.1 \text{ eV}$ ) and visible ( $\lambda = 400 - 760 \text{ nm}$ ,  $\Delta E \sim 1.6 - 3.1 \text{ eV}$ ) to the IR ( $\lambda \geq 700 \text{ nm}$ ,  $\Delta E \leq 1.6 \text{ eV}$ ) spectral ranges. By measuring the ratio of the transmitted light and the incident light intensity, the absorption of radiation can be determined. Beer-Lambert's law gives the absorbance of a sample in Eq (2.2).

$$I = I_0 e^{-\sigma l N} \quad (2-2)$$

The intensity of the transmitted light ( $I$ ) depends on the initial incident light ( $I_0$ ), the absorption cross-section ( $\sigma$ ), the path length ( $l$ ), and the number of absorbing molecules ( $N$ ). The absorption edge determines the semiconductor's bandgap. We used a commercial UV/Vis spectrophotometer SPECORD S600 (Analytik Jena, Jena, Germany) for all the measurements. The determination of the unknown concentration of an analyte molecule or atom can be done by measuring the amount of light that is absorbed by a sample. The non-linearity of Beer-Lambert law includes many causes like stray light, scattering of light because of particles in the sample, or fluorescence or phosphorescence.

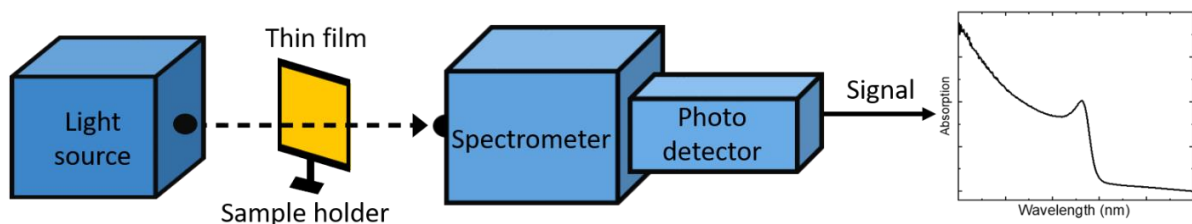


**Figure 2.3.** Absorption measurement setup.

## 2.2.2 Steady-state photoluminescence spectra (PL)

PL spectra result when the sample is constantly illuminated with a specific wavelength. Then the electrons are excited to higher energy levels by photons. These electrons, after some time, relax from the excited state to the ground state and emit light. PL is the emission of light resulting from the absorption of photons. Measuring the luminescence spectrum over a broad electromagnetic range gives information about the materials' impurities and morphology. In this thesis, the measurements were done using an FP-8500 spectrofluorometer (Jasco, Groß-Umstadt, Germany). We also applied bandpass filters for spectral cleaning depending on the excitation wavelengths used for the excitation pass and a long pass filter for the emission path. For example, for an excitation wavelength of  $\lambda = 320$  nm, we have used a UV bandpass filter for 280–370 nm (UG11, Schott Glas) for the excitation path and a long pass filter of 360 nm (WG360, Schott Glas) for the emission path. Routinely, the data were corrected for the wavelength-dependent instrument sensitivity and the baseline.

## 2.2.3 Relaxation processes

The Jablonski diagram is normally used to understand the relaxation processes that occur between absorption and emission in the excited states of molecular systems. As shown in Figure 2.4<sup>[116]</sup>,  $S_0$ ,  $S_1$ , and  $S_2$  represent the ground, first, and second electronic states. The fluorophores can exist in several vibrational energy levels ( $V_0$ ,  $V_1$ ,  $V_2$ , ...,  $V_n$ ) at each electronic energy

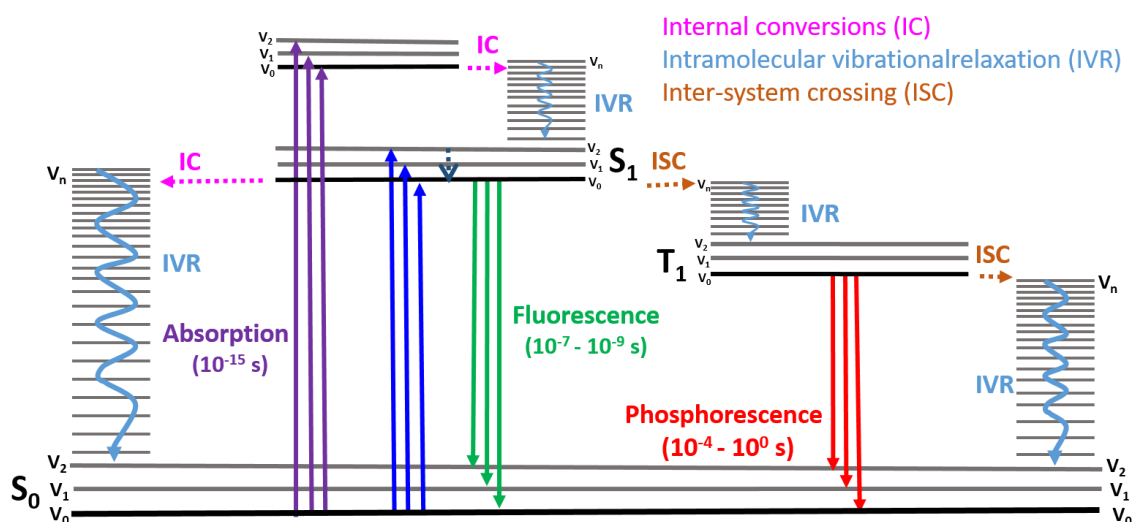


**Figure 2.4.** Scheme of Jablonski diagram with different possible relaxation pathways.

level. Absorption and emission usually occur from the lowest vibrational state. In the shown Jablonski diagram, various processes usually occur after the material absorbs light. Usually, the excitation of the fluorophore leads to some higher vibrational levels of  $S_1$  or  $S_2$ . Then the molecules relax to an energetic vibrational level of  $S_1$  within  $10^{-12}$ s or less; this process is called

internal conversion (IC). The relaxation to the ground state occurs to higher excited vibrational ground state levels in  $10^{-12}$ s for reaching the thermal equilibrium. The electronic excitation does

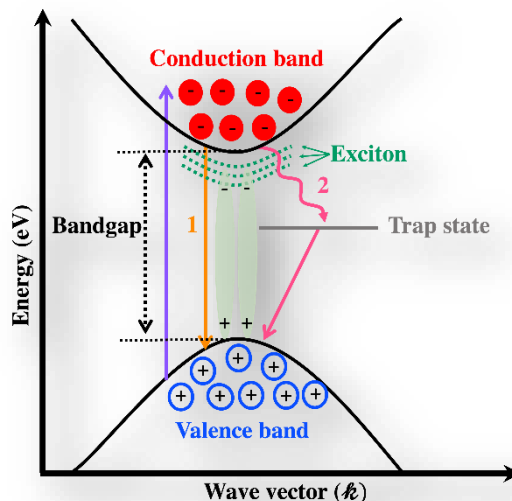


**Figure 2.5.** Scheme of electron-hole recombination mechanism. (1) band-to-band recombination and (2) trap-assisted recombination and the electronic levels related to an exciton in a direct bandgap semiconductor.

not change the nuclear geometry, so the emission spectrum typically is a mirror image of the  $S_0$  to  $S_1$  transition absorption spectrum. Often, the spacing of the vibrational energy levels of the ground state is similar to that of the excited states. Another possibility for molecules in the  $S_1$  state is to go through a spin conversion to the first triplet state  $T_1$  a so-called intersystem crossing process (ISC). The emission from  $T_1$  is called phosphorescence which is generally shifted to lower energy (longer wavelengths). The rate constants for triplet emission are smaller than those for fluorescence since the transition from  $T_1$  to the singlet ground state is forbidden. The molecules with heavy atoms facilitate intersystem crossing (Ex: bromine and iodine) by increased spin-orbital coupling<sup>[116]</sup>.

In Figure 2.5, the carrier recombination mechanisms for a direct bandgap semiconductor are shown. Firstly, a radiative transition (path 1) in direct bandgap (band to band transition) occurs when an electron falls from its state in the CB into the empty state in the VB, which is associated with the hole. The other possibility (path 2) is that an electron falls into a trap at an energy level within the bandgap caused by the presence of a structural defect or a foreign atom. Once the trap is filled, it can not accept another electron. The electron occupying of the trapped energy can then move to the VB's empty state. This process is called Shockley-Read-Hall (SRH) recombination.

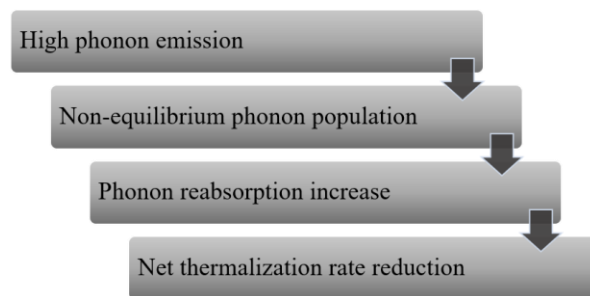
### 2.2.3.1 Bandgap renormalization (BGR)

After intense semiconductor excitation, the charge carrier's dynamic is affected by the state-filling and many-body effects. The system minimizes its total energy by reducing the

fundamental bandgap energy, leading to a red shift of the band edge. Due to the Coulombic repulsion between the carriers in the conduction band, a density-dependent renormalization of the fundamental bandgap of the semiconductor because of a quantum mechanical effect occurs from the Pauli repulsion<sup>[117,118]</sup>. This change in the bandgap is called BGR, and this phenomenon is short-lived ( $\sim 1$  ps) in perovskite (MAPbI<sub>3</sub>)<sup>[119]</sup>.

### 2.2.3.2 Phonon bottleneck

Photovoltaic devices lose much energy, which can not be converted to electricity as heat. The phonon bottleneck process retards the relaxation cooling due to an inefficient coupling and energy transfer between acoustic and optical phonons in the conduction band<sup>[120]</sup>. The excess hot optical phonons raise the phonon reabsorption and decrease the overall thermalization rate leading to a delay in the recombination of the carriers. The transient absorption spectroscopy technique observes this phenomenon at the sub picosecond time frame in the lead halide perovskites<sup>[92,119,121]</sup>.



### 2.2.4 Time-correlated single photon counting (TCSPC)

This technique is used in many analyses to investigate excited state or charge carrier relaxation processes, which happen at the nano to picosecond time ranges. By exciting the sample with a pulsed laser, the fluorescence can be collected by detecting the arrival time of individual photons and constructing the decay curves from the individual time measurement. In principle, the emission time signal of single photons is repeated. The excitation pulse duration is used as the reference for timing. In this dissertation, we have used two different excitation sources. Firstly, the thin films were excited using a sub-ns pulsed LED PLS320 at 325 nm, and the PL of the sample was detected using a photomultiplier detector (PMA 182, PicoQuant). The repetition rate of the pulsed LED was adjusted to  $10^7$  Hz (a time window of 100 ns). The Rayleigh scattered light on a pure quartz substrate was used to determine the temporal instrument response function (IRF) of the TCSPC system (full width at half maximum (FWHM) of  $\sim 800$  ps in this setup).

Secondly, a mode-locked titanium-doped sapphire (Ti:Sa) laser (Tsunami 3941-X3BB, Spectra-Physics, Darmstadt, Germany) was pumped by an 8 W continuous-wave diode-pumped solid-state laser (Millennia eV, Spectra-Physics, 532 nm) for the excitation of the samples. The Ti:Sa Laser allowed tuning the fundamental wavelength within the range from 700 to 1000 nm at a repetition rate of 80 MHz. The acousto-optic modulator assisted in reducing the repetition rate to 800 kHz. By tuning the fundamental to 775 nm, the excitation wavelength of 387 nm was obtained by SHG in a BBO crystal (frequency doubler and pulse selector, Model 3980, Spectra-Physics). The instrument response function (IRF, FWHM 200 ps) was obtained using an empty glass substrate as a scattering sample. A photomultiplier tube (PMT, PMA-C 182-M, PicoQuant, Berlin, Germany) and a TimeHarp 260 PICO Single PCIe card (PicoQuant) were used for single-photon detection with 25 ps time resolution.

### 2.2.5 Transient absorption spectroscopy (TAS)

TAS is a valuable technique for understanding solid-phase dynamics<sup>[122–124]</sup>. In this method, we use two different pulses: pump and probe. The pump pulse is used to excite the sample at a time delay ( $\Delta\tau = 0$ ), and the pulse must be shorter than the investigated species' lifetime. The probe pulse (which has to be low intensity) is used to reveal the non-equilibrium dynamics of the system. By temporally delaying one of both beams (using the delay stage), the changes in the system can be measured at different time delays. The probe signal  $\Delta A(\lambda, \tau)$  is derived by subtracting the absorption spectrum after the excitation and the absorption spectrum before the excitation ( $\Delta A$ ) at different time delays  $\Delta\tau$  using the Beer-Lambert law. Based on that, the absorbance difference is collected according to

$$\Delta A(\lambda) = -\log \frac{I(\lambda)_{pumped}}{I(\lambda)_{unpumped}} \quad (2-3)$$

$I(\lambda)_{unpumped}$  is the transmitted intensity through the sample before excitation, and  $I(\lambda)_{pumped}$  is the transmitted intensity through the sample after the sample was excited. For the time being, many laboratories prefer to use a rotating optical chopper or a mechanical shutter to block the excitation pump (every second pulse) for shot-to-shot detection (Figure 2.6).

Therefore, the absorbance change is averaged  $n$  times for each single delay time  $\tau$ . The difference in absorbance is calculated for two subsequent averaged sequences of  $S$  probe pulses with the corresponding pump pulses unblocked or blocked. Therefore, for each  $\tau$ , the detected pulse number is  $i = 2nS$ . The averaging of the change in absorbance is repeated for  $t$  time delays  $\tau$ , forming a transient map. The signal-to-noise ratio can further get better by averaging  $N$  individual successful transient measurements. Figure 2.7. shows the signals which can be

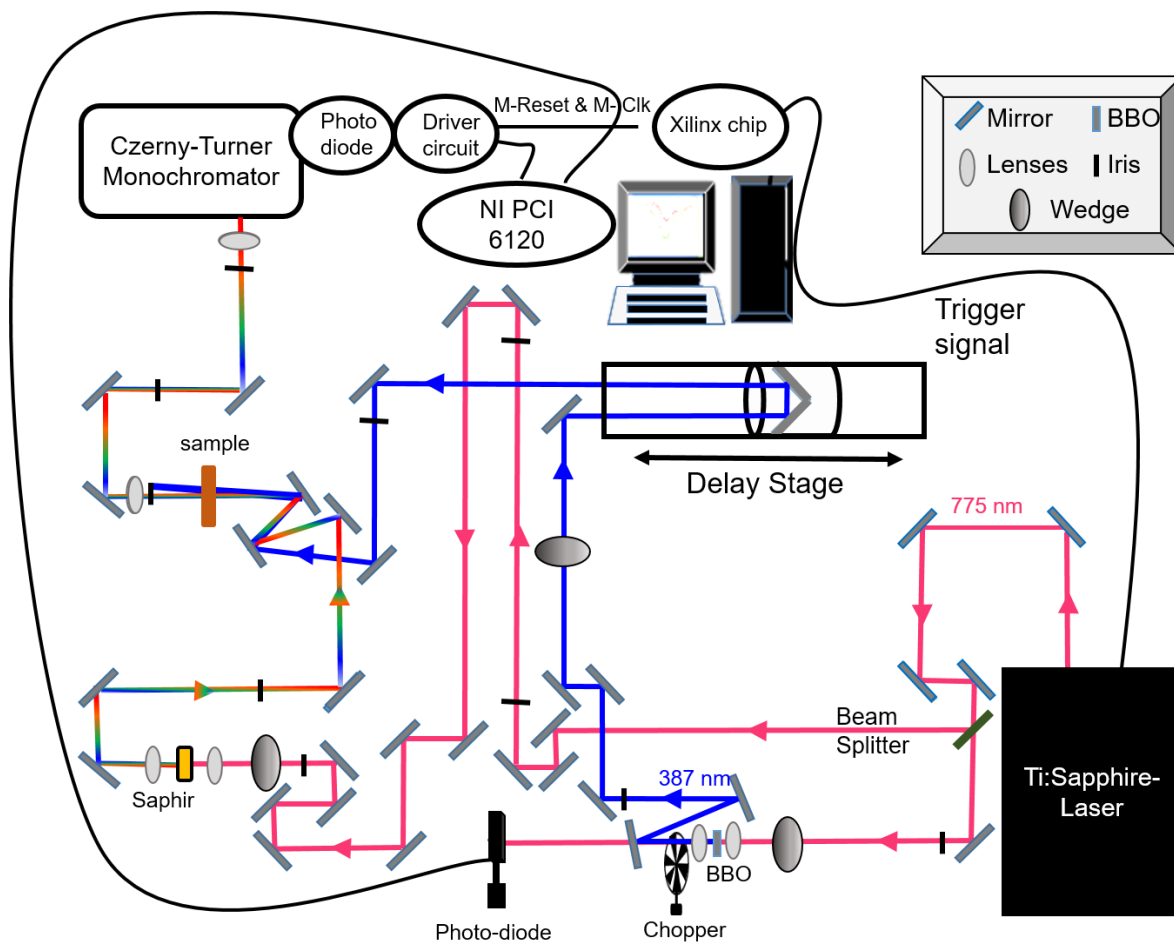


**Figure 2.6.** Optical scheme of the femtosecond transient absorption spectrometer.

observed in a transient absorption spectrum, i.e., ground-state bleach (GSB), stimulated emission (SE), and excited state absorption (ESA) in condensed matter. GSB is a negative signal in the  $\Delta A$  spectrum due to the decreased number of molecules after the excitation in the ground state, which is observed in the wavelength region of ground state absorption. The negative signal (SE) occurs only for optically allowed transitions due to a photon from the probe pulse prompting the emission of another photon from the excited state, which drops to the ground state. The SE signal results in Stokes shift with regard to the ground-state bleach, and sometimes it overlaps with the ground-state bleach. The third signal (ESA) is positive and comes from the absorption of the excited sample in higher excited states. During the excitation of the sample, we have to use lower probe pulse intensity to avoid affecting the excited state population<sup>[124]</sup>.



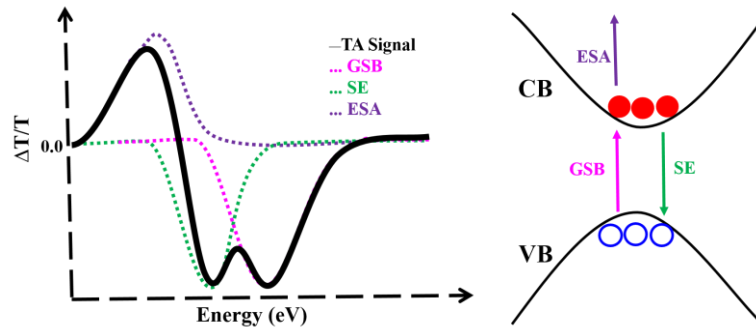


**Figure 2.7.** The scheme represents the three processes that can be observed in a transient absorption spectrum, e.g., ground state bleach (GSB), stimulated emission (SE) and excited state absorption (ESA).

## Frequency-mixing processes and non-linear crystals

The phenomena of non-linear optics have an essential role in developing many fields like femtosecond laser chemistry, laser spectroscopy, and photochemistry. Non-linear effects require light intensities that high-power lasers can produce. Introducing high-intensity pulses with different frequencies to crystals leads to the creation of new pulses with different wavelengths resulting in the generation of e.g. the second and the third harmonic or sum and difference frequency. When we focus an intense pulse of frequency  $\Omega$  onto a crystal, two pulses are generated: one with the incident frequency  $\Omega$  and the second pulse has the double frequency  $2\Omega$  (called second harmonic). When the light of a pulsed laser is directed onto a non-linear crystal, by tuning the angle ( $\Theta$ ) between the direction of the crystal optic axis and the direction of the laser beam, at certain angles, the output pulse from the crystal has two components as shown in Figure 2.8. Many effects can occur like e.g. second harmonic generation (SHG)<sup>[125]</sup>

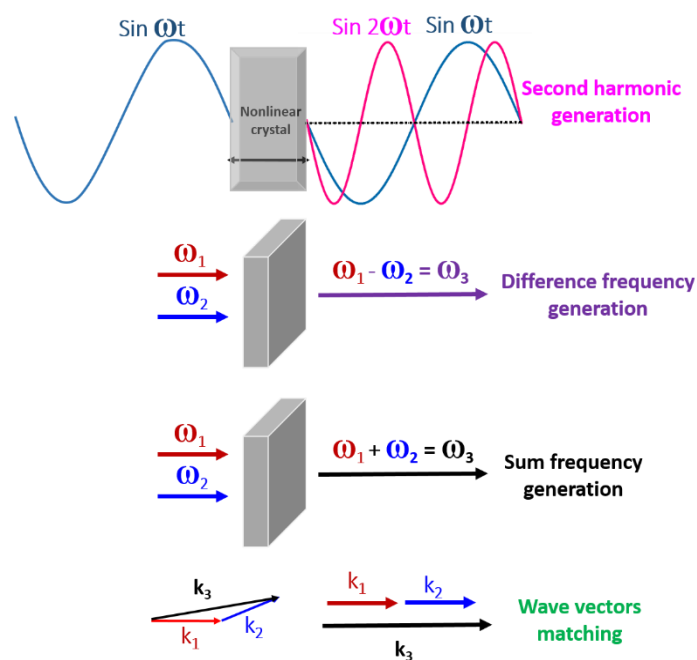


**Figure 2.8.** The generation of different frequencies by two incident pulses in a non-linear crystal.

difference frequency generation ( $\omega_1 - \omega_2$ ) and the sum frequency generation ( $\omega_1 + \omega_2$ ), third harmonic generation  $3\omega$ , self-phase modulation, self-focusing, two-photon absorption, stimulated Raman scattering and four-wave mixing.

The short laser pulses with an electric field (about  $> 10^{12}$  V/cm<sup>2</sup>) in a matter can change the microscopic properties of the non-linear crystal. The electric induction  $D$  depends on the medium polarization  $P$ , the electric permittivity of free space  $\epsilon_0$  and electric field  $E$

$$D = \epsilon_0 E + P, \quad (2-4)$$

For a small intensity of light, the polarization induced in the materials depends linearly on the electric field  $E$

$$P(t) = \chi^{(1)} E(t), \quad (2-5)$$

Where  $\chi^{(1)}$  is the electronic susceptibility of the first order and represents the linear response. If the electric field  $E$  of the incident light increases, the polarization of the medium is not linearly dependent on  $E$ . It can be expanded in a power series, and each term is based on the susceptibility of the  $n$ -th order.

$$P(t) = \epsilon_0 (\chi^{(1)} E(t) + \chi^{(2)} E^2(t) + \chi^{(3)} E^3(t) + \dots) \quad (2-6)$$

The electron in the material might move in the  $x$ ,  $y$ , or  $z$  direction. The form should be written

$$P_i = \epsilon_0 (\chi_{ij}^{(1)} E_j + \chi_{ijk}^{(2)} E_j E_k + \chi_{ijkl}^{(3)} E_j E_k E_l + \dots) \quad (2-7)$$

where  $i, j, k$  identify the  $x, y, z$  Cartesian components.

Assume the electric field  $E$  of the incident wave is a plane wave with frequency component  $\omega$  and wave vector  $\vec{k}$  travelling in  $z$ -direction

$$E = E_0 \cos(\omega t - \vec{k} \cdot \vec{z}) \quad (2-8)$$

the polarization  $P^{(1)}$  in case of first order susceptibility will be

$$P^{(1)}(t) = \chi^{(1)} E_0 \cos(\omega t - \vec{k} \cdot \vec{z}) \quad (2-9)$$

Obviously in linear optics an incident wave of frequency  $\omega$  induces in a material a polarization wave of the same frequency.

And in the nonlinear second order polarization case  $P^{(2)}$  the polarization yields

$$P^{(2)}(t) = \chi^{(2)} E_0^2 (\cos(\omega t - \vec{k} \cdot \vec{z}))^2 \quad (2-10)$$

$$\begin{aligned} &= \epsilon_0 \chi^{(2)} E_0^2 \frac{1 + \cos(2\omega t - 2\vec{k} \cdot \vec{z})}{2} \\ &= \frac{\epsilon_0 \chi^{(2)} E_0^2}{2} + \frac{\epsilon_0 \chi^{(2)} E_0^2}{2} \cos(2\omega t - 2\vec{k} \cdot \vec{z}) \end{aligned} \quad (2-11)$$

Eq (2-11) shows that in the second order polarization, there is a new wave with double frequency ( $2\omega$ ) and a new wave vector  $2\vec{k}_1$ , which is called second harmonic generation (SHG). Additionally, in the first term of  $P^{(2)}(t)$  a constant nonlinear polarization is seen, which does not depend on the frequency  $\omega$  and is called optical rectification.

## Phase matching condition

Phase-matching condition ( $\Delta\vec{k} = 0$ ) is achieved when the phase velocity of the nonlinear polarization wave travelling through the material is the same as the phase velocity of the primary refracted wave<sup>[126]</sup>. The phase velocity  $v_{ph}$  is the speed at which a plane wave propagates in a medium with a reflection index  $n(\omega)$  and it can be written

$$v_{ph} = \frac{\omega}{k} = \frac{c}{n(\omega)} \quad (2-12)$$

The incident wave with the frequency  $\Omega_1$  and the wave vector  $\vec{k}_1$  generates a non-linear polarization wave at the wave vector  $2\vec{k}_1$  and the frequency  $2\Omega_1$ . In this case, the SHG wave frequency is  $\Omega_2 = 2\Omega_1$ , and the wave vector  $\vec{k}_2$  is not equal to  $2\vec{k}_1$ , because in general the refractive index  $n(\Omega_1)$  is not equal to  $n(\Omega_2)$ . Therefore, the polarization wave ( $\vec{k}_{SHG}$ ) phase velocity in the material is different and the phase matching condition is carried out only when:

$$n(\Omega_1) = n(\Omega_2) \quad (2-13)$$

This condition is not fulfilled in the isotropic media but can be obtained in birefringent crystals. These crystals have different refractive indices for ordinary ( $n_o$ ) and extraordinary ( $n_e$ ) waves (see Figure 2.9). The question will now be written as

$$n_e(\Omega_1) = n_o(\Omega_2) \quad (2-14)$$

It guarantees a highly efficient conversion of the fundamental frequency to its second harmonic. There are many commonly used crystals like beta-barium borate (BBO), lithium triborate (LBO), KDP (potassium dihydrogen phosphate), and Potassium titanyl phosphate (KTP). In this work, we have used BBO crystal.

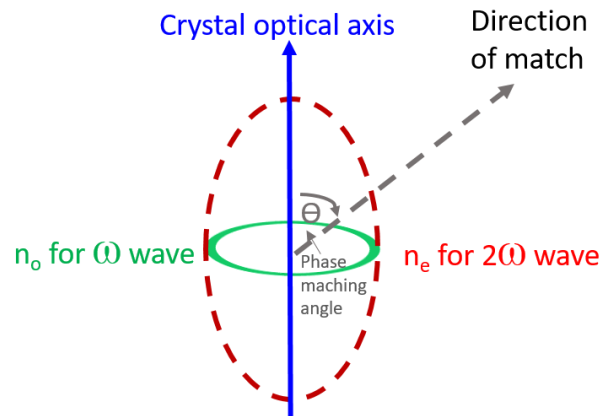


**Figure 2.9.** Phase matching direction in a uniaxial birefringent crystal.

Another nonlinear effect of second order is the so-called parametric process, where a high energetic photon is split up into a signal and an idler photon. Also this process is very efficient if phase matching is obtained, and by a non-collinear arrangement (see Fig 2.8, below) also the

group velocities can be matched. This leads to a phase-matching condition over the whole spectral range of the pulse. Thus the pulse duration will become shorter. This process is called non-collinear parametric amplification (NOPA).

### **White-light supercontinuum generation (SCG)**

This process was discovered by Alfano and Shapiro<sup>[127]</sup>. By focusing a high-peak-intensity pulse with narrow spectral bandwidth into a medium, the output will be a pulse with a very broad spectral bandwidth. The spectral broadening, which leads to the self-focusing (SF) and generation of the new frequencies, mainly comes from the non-linear optical effects of self-phase modulation (SPM). The most common crystals are sapphire (aluminum oxide  $\alpha\text{-Al}_2\text{O}_3$ ) and calcium fluoride  $\text{CaF}_2$ . In this work, we have used  $\text{CaF}_2$  as it performs better in the investigated spectrum region (see Figure 2.10).

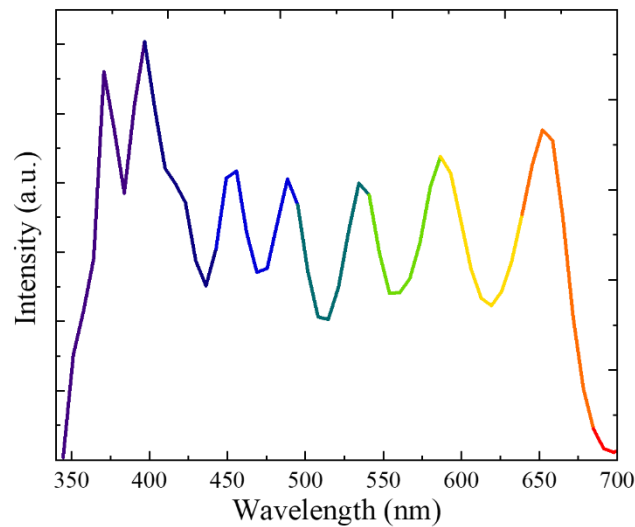


**Figure 2.10.** Spectrum of white light continuum generated in  $\text{CaF}_2$  crystal by excitation at 778 nm.





# *Chapter 3 Ultrafast Dynamics in 2D & 3D Perovskite Thin Films*

This chapter is based on the works published in *Nanoscale* 2021 (Ref.1)<sup>[128]</sup> and the *Journal of Physical Chemistry C* 2022 (Ref. 2)<sup>[129]</sup>. The chapter is divided into two sections. The first section discusses ultrafast energy transfer between organic-inorganic layers in 2D perovskite thin films. In the second section, the influence of Cs cation in wide-bandgap mixed-cation 3D Perovskites is discussed.

## **3.1 Ultrafast Dynamics in 2D perovskite thin films**

### **3.1.1 Introduction**

Recently, many researchers are trying to improve the properties of the two-dimensional (2D) organic-inorganic perovskites with large size organic spacers as they are structurally and photochemically very stable because of the hydrophobicity of these organic layers compared with the 3D perovskites.<sup>[130–134]</sup> About 20 years ago, some groups started to use the organic cations in this material class to determine the structure of the inorganic semiconductor material and to become the electronically active component. The introduction of large chromophores in 2D lead halides leads to effective low-dimensional energy transfer systems, including organic singlet states<sup>[77,79]</sup>, organic triplet states<sup>[77,79,82,135]</sup> and organic charge-transfer states (pyrene-TCNQ)<sup>[136,137]</sup>. Efficient energy transfer between the inorganic layers (lead chloride) and organic layers (benzyl, naphthyl, anthryl) could be achieved<sup>[77]</sup> by tuning the inorganic excitonic states to high transition energies in the  $(R-CH_2-NH_3)_2PbCl_4$  system. This was interpreted for benzyl and naphthyl chromophores by an efficient energy transfer process from the inorganic excitonic band to the triplet state of the organic layer via a Dexter energy transfer mechanism<sup>[77]</sup> due to a strong coupling between the lead chloride excitonic band and the triplet state of the chromophore. Ema et al. reported for lead bromides that the energy transfer efficiency to the organic naphthyl triplet system increases with decreasing the alkyl chain length between the  $NH_3$  anchor group and the aromatic naphthyl system<sup>[85]</sup>. Pyrene-based halide perovskites were also studied with different lead halides as a promising material for efficient energy transfer and light-emitting applications<sup>[79]</sup>. 2D perovskites showed progress in power conversion efficiency (PCE) from 4.02%<sup>[37]</sup> to 12.4% by employing quasi-2D perovskites, which consist of alternating naphthylmethylamine and formamidinium cations<sup>[138]</sup> and even solar cells with naphthyl and anthryl groups were realized<sup>[139]</sup>. Many studies have reported the possibility of tuning the

excitonic band by replacing or mixing halide crystals, which facilitates the fabrication of LEDs from blue to green region<sup>[140–144]</sup>.

Based on that, the choice of the chromophore in the organic layer and the halide content are critical factors in monitoring the electronic properties of 2D materials. Understanding the photophysics of 2D perovskite materials is significant for efficient and stable optoelectronic devices. The one-step spin coating method was applied to fabricate high-quality thin films of 2D perovskites with different chromophores (benzyl, naphthyl, and pyrenyl) to study the role of the energy transfer properties and relaxation pathways by using UV-Vis absorption, PL, TCSPC, and transient absorption spectroscopy techniques under similar experimental conditions (Figure 3.1). These chromophores represent three different energy level scenarios for the study (see Figure 3.2).

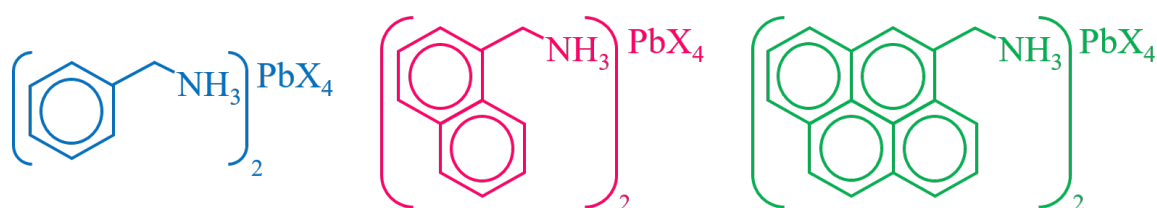


**Figure 3.1.** The chemical structure of the benzyl (left), naphthyl (middle), and pyrenyl (right) perovskite thin films. X = Br (70%) and I (30%).

This work aimed to visualize and investigate the influence of the size of the aromatic spacers of the different chromophores, so we fixed the halide percentage in the inorganic layer to Br (70%) and I (30%) in all perovskite films. Using large chromophores in 2D lead halide perovskites as a spacer showed successful energy transfer systems<sup>[77,79,82,135–137]</sup>.

### 3.1.2 Dynamics of (BA)<sub>2</sub>Pb(Br<sub>0.7</sub>I<sub>0.3</sub>)<sub>4</sub> thin film

In the BA-based perovskite, the singlet (at about 260 nm) and the triplet (at about 360 nm) excited state of the BA chromophore are higher in energy than (402 nm) the excitonic lead halide state (see Figure 3.2a). The excitonic absorption peak of the (BA)<sub>2</sub>Pb(Br<sub>0.7</sub>I<sub>0.3</sub>)<sub>4</sub> film is observed at 402 nm (3.09 eV) with a red-shifted extinction tail due to scattering. The PL spectrum of (BA)<sub>2</sub>Pb(Br<sub>0.7</sub>I<sub>0.3</sub>)<sub>4</sub> after excitation at 320 nm shows the typical emission behavior for the 2D exciton confined in the inorganic lead halide layer at 405 nm without fine spectral structure<sup>[77,79]</sup> (see Figure 3.2b). By performing TCSPC with excitation at 320 nm, the exciton relaxation lifetime from the inorganic layer is determined to 0.61 ns. To collect deep information on the excited state and mechanism of energy transfer, we performed fs-TAS experiments. As expected, only the exciton dynamics from the inorganic layer are observed without any relaxation channels provided by singlet or triplet states of the organic cation<sup>[145]</sup>.



The wavelength and time-dependent TA map of BA perovskite thin film is shown in Figure 3.2c.

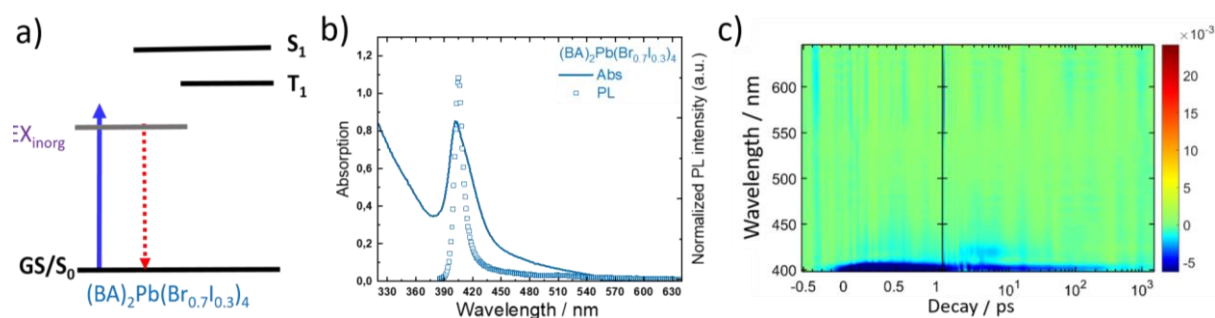


**Figure 3.2.** (a) A schematic representation showing the energy levels of the organic and inorganic layers. (b) UV-vis absorption and normalized PL spectra (the excitation wavelength for the emission measurements was 320 nm) and (c) transient absorption data for  $(\text{BA})_2\text{Pb}(\text{Br}_{0.7}\text{I}_{0.3})_4$  thin films excited at 387 nm ( $81 \mu\text{J}/\text{cm}^2$ ) at room temperature.

A clear pump power dependence is observed and with increasing power (from  $81$  to  $146 \mu\text{J cm}^{-2}$ ) the exciton relaxation time decreases from  $506$  to  $32$  ps, respectively, and the amplitude of the fast component  $\tau_1$  strongly increases by comparing the TA spectra of different excitation power densities.

### 3.1.3 Dynamics of $(\text{NMA})_2\text{Pb}(\text{Br}_{0.7}\text{I}_{0.3})_4$ thin film

In the NMA-based perovskite, the excitonic lead halide state energy at  $417$  nm is in between the singlet and the triplet excited state energies (see Figure 3.3a)<sup>[77]</sup>. In this case, an efficient energy transfer occurs from the excitonic lead halide band to the organic triplet state due to strong coupling between the layers<sup>[85]</sup>. As shown in Figure 3.3b, the excitonic absorption is observed at  $417$  nm ( $2.98$  eV) with a weak broad red-shifted absorption plateau that extends until  $570$  nm due to trap states<sup>[145]</sup>. The emission spectrum of the  $(\text{NMA})_2\text{Pb}(\text{Br}_{0.7}\text{I}_{0.3})_4$  consists of two parts: an excitonic peak at  $440$  nm, which is slightly red-shifted to the excitonic absorption maximum of the film and structured emission with maxima at  $570$  and  $617$  nm which can be assigned to the phosphorescence of the naphthyl chromophore at room temperature<sup>[85,146]</sup>. These two emission parts have different decay times. The exciton peak has a slightly shorter decay ( $0.6$  ns) than NMA phosphorescence ( $0.67$  ns).

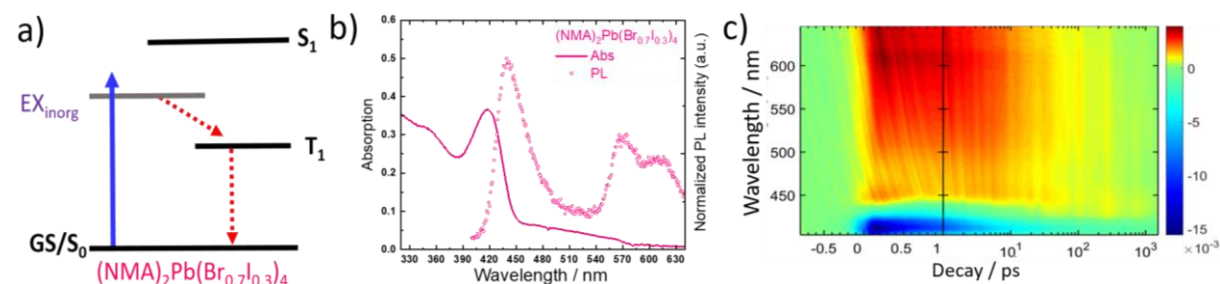


**Figure 3.3.** (a) A schematic representation showing the energy levels of the organic and inorganic layers. (b) UV-vis absorption and normalized PL spectra (the excitation wavelength for the emission measurements was 320 nm) and (c) TA map for  $(\text{NMA})_2\text{Pb}(\text{Br}_{0.7}\text{I}_{0.3})_4$  thin films excited at 387 nm ( $81 \mu\text{J}/\text{cm}^2$ ) at room temperature.

For further inspection of energy transfer, we performed fs-TAS experiments after 387 nm excitation. In the TA map (Figure 3.3c), the peak position of the negative signal (blue signal at 420 nm) is in good agreement with the excitonic peak in the absorption spectrum assigned to the state filling signal contributed by both band-edge electrons and holes. The positive feature (around 440 nm) which appears around 0.5 ps after the optical excitation pulse, might be due to the naphthalene monomer triplet-triplet absorption<sup>[146–148]</sup>. The broad positive peak (red signal at 600 nm) is assigned to triplet-triplet absorption of the intramolecular triplet excimer of NMA<sup>[138,146,148]</sup>, which forms due to the high density of naphthalene chromophores in the organic layer. As discussed in detail (Ref.1), the transient absorption spectra of (NMA)<sub>2</sub>Pb(Br<sub>0.7</sub>I<sub>0.3</sub>)<sub>4</sub> confirmed ultrafast energy transfer from the inorganic layer to the triplet organic layer within 0.26 ps<sup>[77,85]</sup>. The long-lived signal consists of a negative signal at 420 nm (bleach of exciton signal from inorganic layer) and positive signals at 435 nm (triplet-triplet absorption of naphthalene chromophore<sup>[149]</sup>) and at 600 nm (triplet-triplet absorption of naphthalene excimer<sup>[149]</sup>). By comparing the TA spectra at different excitation power densities, it is observed that exciton relaxation times become faster, and the respective amplitudes become larger with increasing pump power.

### 3.1.4 Dynamics of (PMA)<sub>2</sub>Pb(Br<sub>0.7</sub>I<sub>0.3</sub>)<sub>4</sub> thin film

In the PMA-based perovskite, the excitonic band is higher in energy than the singlet and triplet excited states of the chromophore<sup>[150,151]</sup>. The excitonic peak of (PMA)<sub>2</sub>Pb(Br<sub>0.7</sub>I<sub>0.3</sub>)<sub>4</sub> is found at 404 nm (3.07 eV) and has a weak red-shifted absorption at about 453 nm (2.74 eV), most likely due to trap states<sup>[145]</sup> (see Figure 3.4a). The PL spectrum shows a broad, fine structured emission with maxima at 403, 428, and 460 nm that extends until 600 nm (excited at 320 nm). This can be assigned to the fluorescence of the pyrenyl chromophore in this film<sup>[152,153]</sup>. The PMA perovskite has two decay components. The fast component (0.98 ns) may represent different relaxation processes like singlet-singlet annihilation in the organic layer, while the slow component (17 ns) shows the lifetime of the pyrenyl singlet state<sup>[150]</sup>. The wavelength and time-dependent TA map of PMA perovskite thin film is shown in Figure. 3.4c. The peak position of the negative signal at 418 nm is in good agreement with the excitonic absorption peak in the steady-state spectrum assigned to the state filling signal. The spectrally broad positive feature in the visible range with a maximum around 575 nm can be assigned to excited singlet state absorption of the PMA chromophore<sup>[152,154]</sup>. The excited-state absorption appears within about 0.4 ps and does not decay until 1 ns (time window of the experiment), suggesting a long-lived singlet state which match the observed long-lived fluorescence decay from TCPSC measurement. The comparison of the TA spectra at different excitation power densities shows

that carrier relaxation times become faster with increasing power. Due to our limited experimental resolution, we could not detect the energy transfer kinetics from the inorganic layer to the organic singlet state of the PMA chromophore.

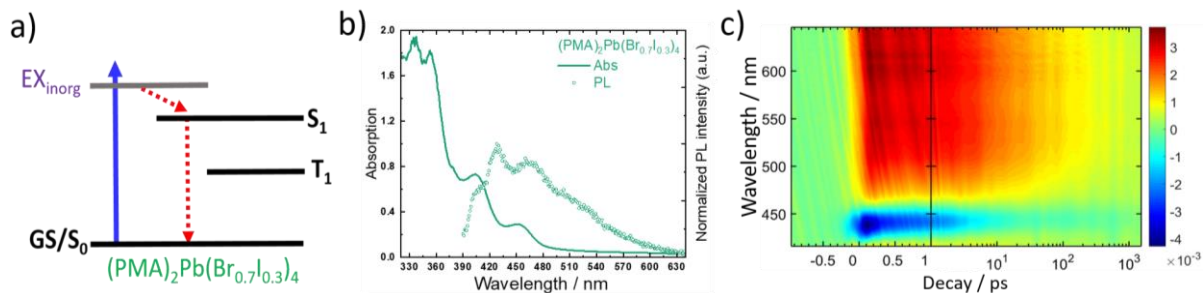


**Figure 3.4.** (a) A schematic representation showing the energy levels of the organic and inorganic layers. (b) UV-vis absorption and normalized PL spectra (the excitation wavelength for the emission measurements was 320 nm) and (c) TA map for  $(\text{PMA})_2\text{Pb}(\text{Br}_{0.7}\text{I}_{0.3})_4$  thin films excited at 387 nm ( $146 \mu\text{J}/\text{cm}^2$ ) at room temperature.

### Energy transfer mechanisms of $(\text{NMA})_2\text{Pb}(\text{Br}_{0.7}\text{I}_{0.3})_4$ and $(\text{PMA})_2\text{Pb}(\text{Br}_{0.7}\text{I}_{0.3})_4$

The methyl spacer between the organic chromophore and the ammonium anchor group allows for close contact between 2D exciton in the inorganic layer and organic chromophores leading to a Dexter-type energy transfer mechanism in both  $(\text{NMA})_2\text{Pb}(\text{Br}_{0.7}\text{I}_{0.3})_4$  and  $(\text{PMA})_2\text{Pb}(\text{Br}_{0.7}\text{I}_{0.3})_4$ <sup>[77,85,138,155]</sup>. Our study aimed to show how the choice of the organic chromophores concerning the singlet and triplet states simplifies the energetic alignment of the 2D confined exciton in the lead halide layer. Understanding the interaction of large chromophores with perovskite structures will help to optimize the devices for different applications, especially LEDs (high emission quantum yield) and solar cells (high charge separation efficiency).

## 3.2 Ultrafast Dynamics in 3D perovskite thin films

### 3.2.1 Introduction

Double-cation perovskites showed promising device performance as next-generation solar cells and in optoelectronic applications. One pathway to further increase the quality and stability of these materials is adding cesium (Cs) as a triple cation to the A-site of mixed-cation formamidinium (FA)/ methylammonium (MA) in the perovskite  $\text{APbX}_3$ <sup>[32,156–159]</sup>. Cs/FA/MA perovskites exhibit high efficiencies<sup>[32]</sup>, decrease trap state formation<sup>[145]</sup>, thermal stability<sup>[160,161]</sup>, and improved stability against humidity<sup>[162,163]</sup>. Bromide-based perovskites are wide-bandgap semiconductors ( $> 1.8 \text{ eV}$ )<sup>[157,164–166]</sup> compared to iodide perovskites, which could display stable devices for LEDs, water splitters, sensors, and multi-junctions high-performance SCs<sup>[167–169]</sup>. Ultrafast transient absorption spectroscopy (TAS) has been used to understand the photophysics of single<sup>[92,118,119,121,145,170–176]</sup> and mixed<sup>[137,177–184]</sup> cation

perovskites. Ghosh et.al, reported the separation time of the initial photo-excited excitons into free charge carriers (20 fs), which is followed by charge carrier thermalization (sub-100 fs time range)<sup>[175]</sup>. Polaron formation occurs depending on the used cations (0.3 ps in the case of MAPbBr<sub>3</sub> and 0.7 ps in CsPbBr<sub>3</sub>)<sup>[185]</sup>. The time constant for subsequent carrier cooling was determined to be 230 fs for low carrier densities, which is slowed down to 770 fs for higher carrier densities due to the hot phonon bottleneck effect<sup>[119]</sup>. Finally, the later signal decay extending to the nanosecond time scale obeys second-order kinetics due to charge recombination<sup>[173]</sup>. Reducing recombination losses before carrier extraction is critical for enhancing the efficiency of perovskite SCs<sup>[186]</sup>. While Cs as a triple cation exhibits improvement in efficiency, the influence of Cs in FA/MA perovskite dynamics has attracted less attention until now.

### 3.2.2 Influence of the Cs as triple cation

In this project, by the one-step spin-coating method, we fabricated FA<sub>0.83</sub>MA<sub>0.17</sub>PbBr<sub>3</sub> and Cs<sub>0.05</sub>(FA<sub>0.83</sub>MA<sub>0.17</sub>)<sub>0.95</sub>PbBr<sub>3</sub> thin films on a glass substrate as reported elsewhere<sup>[32,187]</sup>. We use time-resolved spectroscopic techniques (steady-state spectroscopy, time-resolved emission, and fs-TAS) to study the effect of Cs on the dynamics of mixed-cation wide bandgap bromide-based perovskite. The absorption spectra of both films are similar with a sharp peak at 532 nm, indicating a similar localization of the charge carriers at the band edge (see Figure 3.5a). The PL intensity of Cs<sub>0.05</sub>(FA<sub>0.83</sub>MA<sub>0.17</sub>)<sub>0.95</sub>PbBr<sub>3</sub> is enhanced by a factor of four compared to FA<sub>0.83</sub>MA<sub>0.17</sub>PbBr<sub>3</sub>, which refers to a reduction of non-radiative recombination sites in the perovskite film (see Figure 3.5b). Adding Cs increases the lifetime of the photogenerated charge carriers (from 291 to 355 ns) by reducing trap density and non-radiative recombination sites in the perovskite film (See Figure 3.5c).

A closer look at both samples' dynamics and relaxation pathways by fs-TAS after excitation at 387 nm in the probe spectral region from 400 to 645 nm showed similar results reported previously<sup>[178,188]</sup>. In both films, we observed three signals, negative Photobleach signal (PB), positive photoinduced absorption (PIA1), and (PIA2). PB at 532 nm is assigned to the band-filling effect<sup>[173]</sup>, which matches the steady-state absorption spectrum. The short-lived PIA1 (<1 ps) signal in the 539 to 580 nm region is linked to transient electroabsorption (Stark effect) and band gap renormalization (BGR)<sup>[119,178,188–190]</sup>. PIA2 signal (spectral range between 400 and

520 nm), which decayed non-exponentially, is assigned to the relaxation of free charge carriers.

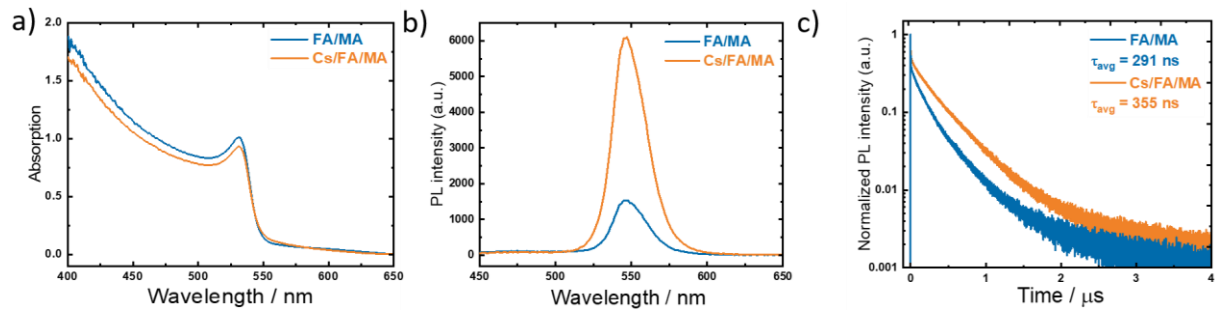


**Figure 3.5.** (a) Steady-state absorption, (b) steady-state photoluminescence (PL) spectra with optical excitation at 362 nm, and (c) time-resolved (PL) decay with optical excitation at 387 nm of FA/MA (blue) and Cs/FA/MA (orange) thin films deposited on glass substrates at room temperature.

A clear pump power dependence is seen in both films by performing power-dependent experiments with optical pump pulses at 387 nm. For low pump power, the PIA2 signal appears at early delay times at 520 nm without spectral changes also for longer delay times. However, the PIA2 signal is observed with a broadening and a strong blue shift (up to 420 nm) for high pump powers, which means that the PIA2 signal is a sensitive indicator for the thin film's thermal and density distribution of charge carriers. In  $\text{Cs}_{0.05}(\text{FA}_{0.83}\text{MA}_{0.17})_{0.95}\text{PbBr}_3$  film, we observed an enhancement in the efficient hot-phonon bottleneck due to the large mass and small ionic radius of Cs with a longer lifetime compared to  $\text{FA}_{0.83}\text{MA}_{0.17}\text{PbBr}_3$  film<sup>[92,119,121]</sup>. Based on the data evaluation by the software package Optimus<sup>[191]</sup>, the fastest component agrees with the polaron formation time<sup>[185]</sup>. The slowest component, which does not decay in our experimental time window (1.5 ns), is likely due to non-geminate recombination. Our results showed that the addition of Cs allows a relaxed form of the perovskite crystal lattice with less traps and, therefore, better device performance. We believe that the wide band gap mixed-cation lead bromide perovskites will be an exciting target material for solar cells, sensors, and power electronics.



# Chapter 4 Photophysical Properties of New Schiff Bases Containing an Indole Moiety

## 4.1 Introduction

This chapter is based on the work published in ACS Omega 2022 (Ref. 3)<sup>[192]</sup>. Schiff bases are a remarkable candidate for many applications such as antibacterial<sup>[193]</sup>, antiviral<sup>[193]</sup>, antitumor<sup>[194]</sup>, antifungal<sup>[195]</sup> biomedical, organic light emitting diode (OLED)<sup>[196]</sup>, sensors<sup>[197]</sup>, and photovoltaic solar cell applications<sup>[198–200]</sup>, owing to the possibility of emitting in a specific range. Schiff bases are synthesized through condensation reactions between primary amines with aldehydes or ketones in the presence of homogeneous or heterogeneous catalysts under optimized conditions. Heterogeneous catalysts are often used in organic synthesis as they are easy to recover and have high efficiency<sup>[201–203]</sup>. In addition, some indole derivatives and other heterocyclic compounds have shown aggregation-induced emission properties<sup>[198,204–206]</sup>. Thus, Schiff bases with indole moieties may have some interesting optical properties. However, only a few studies have exclusively examined such materials. Replacing the toxic piperidine catalyst that is used in organic synthesis is very important.

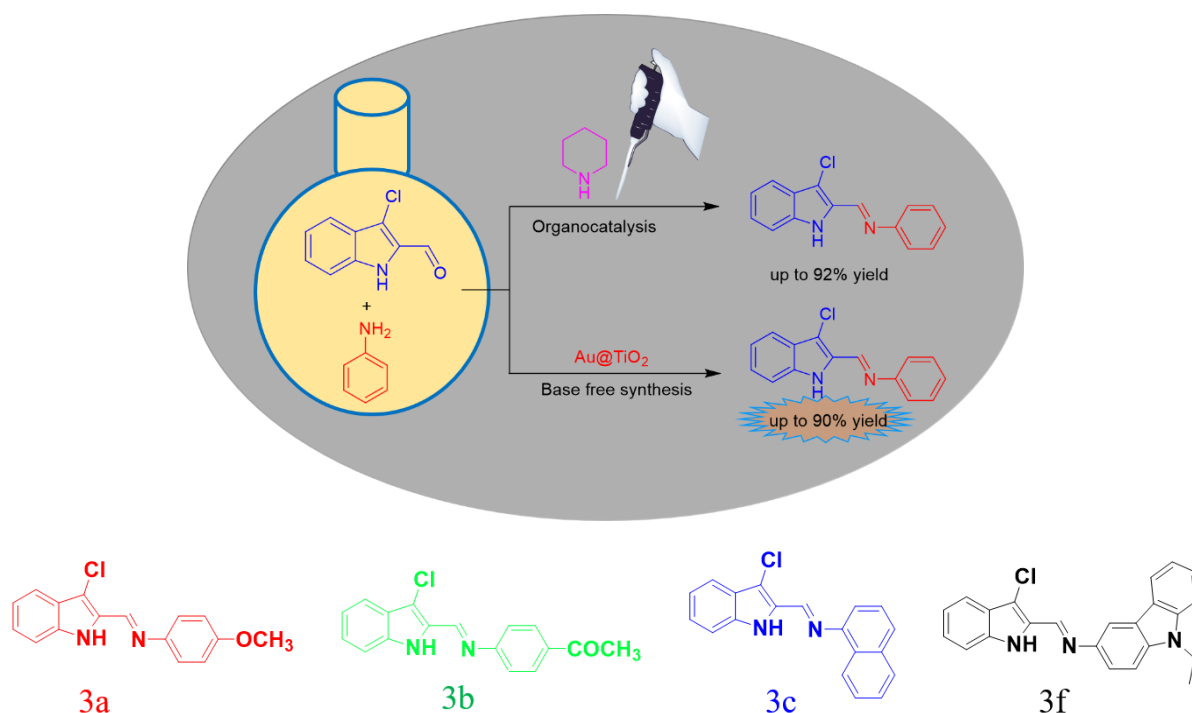


**Figure 4.1.** The chemical structure of 3a, 3b, 3c and 3f Schiff base derivatives.

## 4.2 Photophysical behavior of the selected Schiff bases

In this project, we compared the synthesized product yield of six new Schiff bases derived from indole using the heterogenous catalyst Au@TiO<sub>2</sub> and piperidine as an organic catalyst. Both

catalysts showed comparable results, but the Au@TiO<sub>2</sub> was easy to separate and recyclable. Our main contribution to this project is studying the photophysics properties of four materials using UV–Vis absorption, PL, and TCSPC. All solutions have been prepared using dimethyl sulfoxide (DMSO) as solvent. The solution concentration for all samples is 1×10<sup>-9</sup> mol L<sup>-1</sup>, except for sample (E)-1-(4-(((3-chloro-1H-indol-2-yl)methylene)amino)phenyl)ethan-1-one (**3b**) where it is 1×10<sup>-7</sup> mol L<sup>-1</sup> as it shows a weak absorption. The absorption peaks for all samples can be assigned to the π→π\* transitions. Firstly, the peaks at 280–320 nm resulted from π→π\* transitions of the aromatic core. Secondly, the bands in the 300–360 nm range refer to π→π\* transitions of the C=N groups. Finally, the longer wavelength absorptions reflect the extended conjugation in the whole molecule. These samples have various ground states for different substituents.

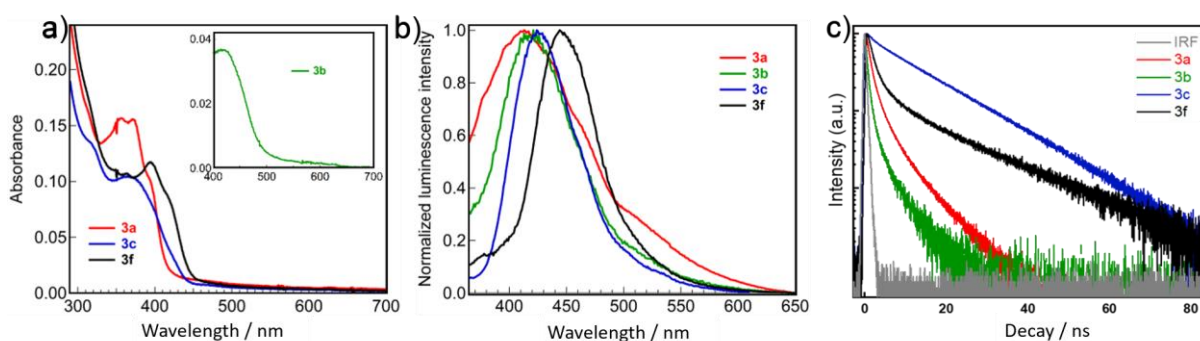


**Figure 4.2.** Photophysical behavior of DMSO solutions of **3a**, **3b**, **3c**, and **3f** at room temperature: (a) UV-Vis absorption spectra (1×10<sup>-7</sup> mol L<sup>-1</sup> for **3b** and 1×10<sup>-9</sup> mol L<sup>-1</sup> for **3a**, **3c**, and **3f**). (b) Emission spectra with excitation at 320 nm (1×10<sup>-7</sup> mol L<sup>-1</sup>). (c) Photoluminescence decay profiles at 320 nm excitation.

The emission spectra of (E)-1-(3-chloro-1H-indol-2-yl)-N-(4-methoxyphenyl)methanimine (**3a**) (methoxy group) and (**3b**) (acetyl group) have no change in the λ<sub>max</sub> (415 nm); however, it has been reported that these groups can affect the energy gap between the lowest unoccupied molecular orbital (LUMO) and the highest occupied molecular orbital (HOMO) to produce a blue or red shift<sup>[207]</sup>. The emission maximum is red-shifted by replacing the phenyl ring of (**3a**) and (**3b**) with naphthyl in (E)-1-(3-chloro-1H-indol-2-yl)-N-(naphthalen-1-yl)methanimine (**3c**) and carbazolyl in (E)-1-(3-chloro-1H-indol-2-yl)-N-(9-ethyl-9H-carbazol-3-yl)methanimine (**3f**) rings to 430 and 450 nm, respectively. This result signifies the possibility of the substituent groups increasing E<sub>HOMO</sub> in the order carbazolyl > naphthyl > phenyl.

For further investigation of the lifetime of these emissions, we performed TCSPC measurements in the solution state. The studied Schiff bases showed well-fitted biexponential decay profiles with emission lifetimes on the order of nanoseconds. We assigned these decay's lifetimes to fluorescence emitted from singlet excited states. By detecting the emission colors with the Commission Internationale de l'Éclairage (CIE), the (**3b**), (**3c**) and (**3f**) samples



showed a deep blue fluorescence with CIE coordinates of  $y < 0.1$ <sup>[208]</sup>. Based on that, these materials might be interesting for designing new OLEDs with reduced energy consumption.



# *Chapter 5 Conclusion and Outlook*

## **5.1 Conclusion**

In summary, this cumulative thesis focuses on investigating the time-resolved dynamics in different perovskites and new synthesized Schiff base materials that might be interesting for optoelectronic applications like solar cells and LEDs. The common solar cell and LEDs devices are based on inorganic materials like silicon because of their high efficiency and stability. The high cost of processing pure-crystalline silicon encourages researchers to find low-cost candidates with comparable efficiency and stability. Since then, extensive research has been done on 2D and 3D perovskites for alternative solar cells and LEDs. These perovskites could show promising results in replacing silicon in the near future when some issues, e.g., stability and the presence of lead are fixed (discussed in chapter 1).

In chapter 3, we studied the energy transfer from the inorganic to the organic layer in three lead-based mixed-halide perovskite thin films containing BA, NMA, and PMA cations. The selection of the organic chromophores makes it easier for the 2D confined exciton in the lead halide layer to align energetically with the singlet and triplet states of the organic layer. Our studies provide insight into how large chromophores affect perovskite photophysical properties. In the visible spectral range, fs-TAS on  $(\text{BA})_2\text{Pb}(\text{Br}_{0.7}\text{I}_{0.3})$ ,  $(\text{NMA})_2\text{Pb}(\text{Br}_{0.7}\text{I}_{0.3})$ , and  $(\text{PMA})_2\text{Pb}(\text{Br}_{0.7}\text{I}_{0.3})_4$  thin films revealed the ultrafast Dexter-type energy transfer channel between the donating 2D-confined exciton and the accepting chromophore under spin conservation.

In chapter 4, we used fs-TAS and time-resolved spectroscopic techniques (steady-state spectroscopy and TCSPC) to study the effect of Cs on the dynamics of a mixed-cation (FA/MA) wide band gap bromide-based perovskite. Adding 5% of Cs increased the average lifetime of the photogenerated charge carriers due to less non-radiative recombination channels and reduced trap density. Investigating the mechanism of charge dynamics in mixed cation perovskite thin films is essential for fabricating high-performance and stable devices. Recent interest in 2D and 3D perovskite systems is coupled with frequently complementary demands for optimization in various applications, including LEDs and solar cells.

In chapter 5, our study showed that using  $\text{Au}@\text{TiO}_2$  as a heterogeneous catalyst for synthesizing six new Schiff bases derived from indole facilitates the procedure with high yield and reusability of the used catalyst. In addition, the photophysical properties of these new dyes exhibit

interesting luminescence behaviors, such as the dependence of the spectral shape on the substituent group and the emission of deep-blue fluorescence with CIE coordinates of  $y < 0.1$ . Based on that, these dyes may help in designing new OLEDs because they decrease the emitting devices' energy consumption.

## 5.2 Outlook

Perovskite material with different dimensionality could show outstanding improvement in the past few years for making a further step from lab to industry. The efforts to understand the photochemical and photophysical properties of 2D halide perovskites will push this field further. Choosing suitable spacers, especially those with heavily conjugated rings, open many doors for the use and suitability of these materials for specific applications. However, many still open questions about these materials, such as the impact of spacer on film properties, limitation of layer numbers, device stability, mixing of different cations and the photophysical properties, need to be studied and resolved.

## Chapter 6 Bibliography

- [1] C. Wehrenfennig, G. E. Eperon, M. B. Johnston, H. J. Snaith, L. M. Herz, *Adv. Mater.* **2014**, *26*, 1584–1589.
- [2] S. De Wolf, J. Holovsky, S.-J. Moon, P. Löper, B. Niesen, M. Ledinsky, F.-J. Haug, J.-H. Yum, C. Ballif, *J. Phys. Chem. Lett.* **2014**, *5*, 1035–1039.
- [3] N.-G. Park, *Mater. Today* **2015**, *18*, 65–72.
- [4] Y. Kanemitsu, *J. Mater. Chem. C* **2017**, *5*, 3427–3437.
- [5] J. Maes, L. Balcaen, E. Drijvers, Q. Zhao, J. De Roo, A. Vantomme, F. Vanhaecke, P. Geiregat, Z. Hens, *J. Phys. Chem. Lett.* **2018**, *9*, 3093–3097.
- [6] Y. Ogomi, A. Morita, S. Tsukamoto, T. Saitho, N. Fujikawa, Q. Shen, T. Toyoda, K. Yoshino, S. S. Pandey, T. Ma, S. Hayase, *J. Phys. Chem. Lett.* **2014**, *5*, 1004–1011.
- [7] M. Lyu, M. Zhang, N. A. Cooling, Y. Jiao, Q. Wang, J.-H. Yun, B. Vaughan, G. Triani, P. Evans, X. Zhou, K. Feron, A. Du, P. Dastoor, L. Wang, *Sci. Bull.* **2016**, *61*, 1558–1562.
- [8] T. Leijtens, S. D. Stranks, G. E. Eperon, R. Lindblad, E. M. J. Johansson, I. J. McPherson, H. Rensmo, J. M. Ball, M. M. Lee, H. J. Snaith, *ACS Nano* **2014**, *8*, 7147–7155.
- [9] G. Xing, N. Mathews, S. Sun, S. S. Lim, Y. M. Lam, M. Grätzel, S. Mhaisalkar, T. C. Sum, *Science*. **2013**, *342*, 344 LP – 347.
- [10] D. Qingfeng, F. Yanjun, S. Yuchuan, M. Padhraic, Q. Jie, C. Lei, H. Jinsong, *Science*. **2015**, *347*, 967–970.
- [11] J. Woo Choi, H. C. Woo, X. Huang, W.-G. Jung, B.-J. Kim, S.-W. Jeon, S.-Y. Yim, J.-S. Lee, C.-L. Lee, *Nanoscale* **2018**, *10*, 13356–13367.
- [12] A. R. Chakhmouradian, P. M. Woodward, *Phys. Chem. Miner.* **2014**, *41*, 387–391.
- [13] A. K. Jena, A. Kulkarni, T. Miyasaka, *Chem. Rev.* **2019**, *119*, 3036–3103.
- [14] W. A. Dunlap-Shohl, Y. Zhou, N. P. Padture, D. B. Mitzi, *Chem. Rev.* **2019**, *119*, 3193–3295.

- [15] A. Kojima, K. Teshima, Y. Shirai, T. Miyasaka, *J. Am. Chem. Soc.* **2009**, *131*, 6050–6051.
- [16] T. Miyasaka, A. K. Jena, in *Perovskite Photovoltaics Optoelectron.*, John Wiley & Sons, Ltd, **2022**, pp. 1–60.
- [17] S. D. Stranks, G. E. Eperon, G. Grancini, C. Menelaou, M. J. P. Alcocer, T. Leijtens, L. M. Herz, A. Petrozza, H. J. Snaith, *Science*. **2013**, *342*, 341–344.
- [18] Q. Dong, Y. Fang, Y. Shao, P. Mulligan, J. Qiu, L. Cao, J. Huang, *Science*. **2015**, *347*, 967–970.
- [19] W.-J. Yin, T. Shi, Y. Yan, *J. Phys. Chem. C* **2015**, *119*, 5253–5264.
- [20] D. W. de Quilettes, S. M. Vorpahl, S. D. Stranks, H. Nagaoka, G. E. Eperon, M. E. Ziffer, H. J. Snaith, D. S. Ginger, *Science*. **2015**, *348*, 683–686.
- [21] S. D. Stranks, H. J. Snaith, *Nat. Nanotechnol.* **2015**, *10*, 391–402.
- [22] E. Smecca, Y. Numata, I. Deretzis, G. Pellegrino, S. Boninelli, T. Miyasaka, A. La Magna, A. Alberti, *Phys. Chem. Chem. Phys.* **2016**, *18*, 13413–13422.
- [23] S.-H. Turren-Cruz, A. Hagfeldt, M. Saliba, *Science*. **2018**, *362*, 449–453.
- [24] T. Miyasaka, A. Kulkarni, G. M. Kim, S. Öz, A. K. Jena, *Adv. Energy Mater.* **2020**, *10*, 1902500.
- [25] G. E. Eperon, G. M. Paternò, R. J. Sutton, A. Zampetti, A. A. Haghighirad, F. Cacialli, H. J. Snaith, *J. Mater. Chem. A* **2015**, *3*, 19688–19695.
- [26] C. C. Stoumpos, C. D. Malliakas, M. G. Kanatzidis, *Inorg. Chem.* **2013**, *52*, 9019–9038.
- [27] A. Binek, F. C. Hanusch, P. Docampo, T. Bein, *J. Phys. Chem. Lett.* **2015**, *6*, 1249–1253.
- [28] G. E. Eperon, S. D. Stranks, C. Menelaou, M. B. Johnston, L. M. Herz, H. J. Snaith, *Energy Environ. Sci.* **2014**, *7*, 982–988.
- [29] G. Niu, W. Li, J. Li, X. Liang, L. Wang, *RSC Adv.* **2017**, *7*, 17473–17479.
- [30] Z. Li, M. Yang, J.-S. Park, S.-H. Wei, J. J. Berry, K. Zhu, *Chem. Mater.* **2016**, *28*, 284–292.
- [31] C. Yi, J. Luo, S. Meloni, A. Boziki, N. Ashari-Astani, C. Grätzel, S. M. Zakeeruddin, U.

- Röthlisberger, M. Grätzel, *Energy Environ. Sci.* **2016**, *9*, 656–662.
- [32] M. Saliba, T. Matsui, J.-Y. Seo, K. Domanski, J.-P. Correa-Baena, M. K. Nazeeruddin, S. M. Zakeeruddin, W. Tress, A. Abate, A. Hagfeldt, M. Grätzel, *Energy Environ. Sci.* **2016**, *9*, 1989–1997.
- [33] W. S. Yang, B.-W. Park, E. H. Jung, N. J. Jeon, Y. C. Kim, D. U. Lee, S. S. Shin, J. Seo, E. K. Kim, J. H. Noh, S. Il Seok, *Science*. **2017**, *356*, 1376–1379.
- [34] S. N. Habisreutinger, T. Leijtens, G. E. Eperon, S. D. Stranks, R. J. Nicholas, H. J. Snaith, *Nano Lett.* **2014**, *14*, 5561–5568.
- [35] G. Abdelmageed, H. R. Sully, S. Bonabi Naghadeh, A. El-Hag Ali, S. A. Carter, J. Z. Zhang, *ACS Appl. Energy Mater.* **2018**, *1*, 387–392.
- [36] I. C. Smith, E. T. Hoke, D. Solis-Ibarra, M. D. McGehee, H. I. Karunadasa, *Angew. Chemie Int. Ed.* **2014**, *53*, 11232–11235.
- [37] D. H. Cao, C. C. Stoumpos, O. K. Farha, J. T. Hupp, M. G. Kanatzidis, *J. Am. Chem. Soc.* **2015**, *137*, 7843–7850.
- [38] F. Zhang, H. Lu, J. Tong, J. J. Berry, M. C. Beard, K. Zhu, *Energy Environ. Sci.* **2020**, *13*, 1154–1186.
- [39] N. Li, Z. Zhu, C.-C. Chueh, H. Liu, B. Peng, A. Petrone, X. Li, L. Wang, A. K.-Y. Jen, *Adv. Energy Mater.* **2017**, *7*, 1601307.
- [40] Z. Wang, Q. Lin, F. P. Chmiel, N. Sakai, L. M. Herz, H. J. Snaith, *Nat. Energy* **2017**, *2*, 17135.
- [41] H. Xu, Y. Sun, H. Zheng, G. Liu, X. Xu, S. Xu, L. Zhang, X. Chen, X. Pan, *J. Mater. Chem. C* **2019**, *7*, 15276–15284.
- [42] R. Hu, Y. Zhang, S. Paek, X.-X. Gao, X. Li, M. K. Nazeeruddin, *J. Mater. Chem. A* **2020**, *8*, 8058–8064.
- [43] A. Krishna, S. Gottis, M. K. Nazeeruddin, F. Sauvage, *Adv. Funct. Mater.* **2019**, *29*, 1806482.
- [44] N. Aristidou, I. Sanchez-Molina, T. Chotchuangchutchaval, M. Brown, L. Martinez, T. Rath, S. A. Haque, *Angew. Chemie Int. Ed.* **2015**, *54*, 8208–8212.

## Bibliography

- [45] W. Kong, A. Rahimi-Iman, G. Bi, X. Dai, H. Wu, *J. Phys. Chem. C* **2016**, *120*, 7606–7611.
- [46] K. Tanaka, F. Sano, T. Takahashi, T. Kondo, R. Ito, K. Ema, *Solid State Commun.* **2002**, *122*, 249–252.
- [47] Y. Takeoka, D. B. Mitzi, in *Perovskite Photovoltaics Optoelectron.*, John Wiley & Sons, Ltd, **2022**, pp. 61–79.
- [48] Y. Takeoka, K. Asai, M. Rikukawa, K. Sanui, *Bull. Chem. Soc. Jpn.* **2006**, *79*, 1607–1613.
- [49] J. Calabrese, N. L. Jones, R. L. Harlow, N. Herron, D. L. Thorn, Y. Wang, *J. Am. Chem. Soc.* **1991**, *113*, 2328–2330.
- [50] G. C. Papavassiliou, I. B. Koutselas, D. J. Lagouvardos, J. Kapoutsis, A. Terzis, G. J. Papaioannou, *Mol. Cryst. Liq. Cryst. Sci. Technol. Sect. A. Mol. Cryst. Liq. Cryst.* **1994**, *253*, 103–112.
- [51] D. B. Mitzi, C. A. Feild, W. T. A. Harrison, A. M. Guloy, *Nature* **1994**, *369*, 467–469.
- [52] Z. Cheng, J. Lin, *CrystEngComm* **2010**, *12*, 2646–2662.
- [53] L. Zhang, C. Sun, T. He, Y. Jiang, J. Wei, Y. Huang, M. Yuan, *Light Sci. Appl.* **2021**, *10*, 61.
- [54] R. Quintero-Bermudez, A. Gold-Parker, A. H. Proppe, R. Munir, Z. Yang, S. O. Kelley, A. Amassian, M. F. Toney, E. H. Sargent, *Nat. Mater.* **2018**, *17*, 900–907.
- [55] X. Li, J. M. Hoffman, M. G. Kanatzidis, *Chem. Rev.* **2021**, *121*, 2230–2291.
- [56] M. D. Smith, B. A. Connor, H. I. Karunadasa, *Chem. Rev.* **2019**, *119*, 3104–3139.
- [57] G. C. Papavassiliou, A. P. Patsis, D. J. Lagouvardos, I. B. Koutselas, *Synth. Met.* **1993**, *57*, 3889–3894.
- [58] G. C. Papavassiliou, J. B. Koutselas, D. J. Lagouvardos, *Zeitschrift für Naturforsch. B* **1993**, *48*, 1013–1014.
- [59] G. C. Papavassiliou, I. B. Koutselas, A. Terzis, M.-H. Whangbo, *Solid State Commun.* **1994**, *91*, 695–698.



- [60] G. C. Papavassiliou, I. B. Koutselas, *Synth. Met.* **1995**, *71*, 1713–1714.
- [61] I. B. Koutselas, L. Ducasse, G. C. Papavassiliou, *J. Phys. Condens. Matter* **1996**, *8*, 1217–1227.
- [62] G. A. Mousdis, V. Gionis, G. C. Papavassiliou, C. P. Raptopoulou, A. Terzis, *J. Mater. Chem.* **1998**, *8*, 2259–2262.
- [63] G. C. Papavassiliou, G. A. Mousdis, I. B. Koutselas, *Adv. Mater. Opt. Electron.* **1999**, *9*, 265–271.
- [64] G. A. Mousdis, G. C. Papavassiliou, C. P. Raptopoulou, A. Terzis, *J. Mater. Chem.* **2000**, *10*, 515–518.
- [65] D. B. Mitzi, *Chem. Mater.* **1996**, *8*, 791–800.
- [66] D. B. Mitzi, K. Chondroudis, C. R. Kagan, *Inorg. Chem.* **1999**, *38*, 6246–6256.
- [67] D. B. Mitzi, *J. Chem. Soc., Dalton Trans.* **2001**, 1–12.
- [68] J. L. Knutson, J. D. Martin, D. B. Mitzi, *Inorg. Chem.* **2005**, *44*, 4699–4705.
- [69] D. B. Mitzi, C. D. Dimitrakopoulos, L. L. Kosbar, *Chem. Mater.* **2001**, *13*, 3728–3740.
- [70] D. B. Mitzi, S. Wang, C. A. Feild, C. A. Chess, A. M. Guloy, *Science*. **1995**, *267*, 1473 LP – 1476.
- [71] T. Ishihara, J. Takahashi, T. Goto, *Phys. Rev. B* **1990**, *42*, 11099–11107.
- [72] X. Hong, T. Ishihara, A. V Nurmikko, *Phys. Rev. B* **1992**, *45*, 6961–6964.
- [73] T. Ishihara, *J. Lumin.* **1994**, *60–61*, 269–274.
- [74] E. A. Muljarov, S. G. Tikhodeev, N. A. Gippius, T. Ishihara, *Phys. Rev. B* **1995**, *51*, 14370–14378.
- [75] M. Era, K. Maeda, T. Tsutsui, *Chem. Lett.* **1997**, *26*, 1235–1236.
- [76] X.-H. Zhu, N. Mercier, P. Frère, P. Blanchard, J. Roncali, M. Allain, C. Pasquier, A. Riou, *Inorg. Chem.* **2003**, *42*, 5330–5339.
- [77] M. Braun, W. Tuffentsammer, H. Wachtel, H. C. Wolf, *Chem. Phys. Lett.* **1999**, *303*, 157–164.

## Bibliography

- [78] K. Sakai, T. Sonoyama, T. Tsuzuki, M. Ichikawa, Y. Taniguchi, *Chem. Lett.* **2005**, *34*, 212–213.
- [79] M. Braun, W. Tuffentsammer, H. Wachtel, H. C. Wolf, *Chem. Phys. Lett.* **1999**, *307*, 373–378.
- [80] M. Era, A. Shimizu, *Mol. Cryst. Liq. Cryst. Sci. Technol. Sect. A. Mol. Cryst. Liq. Cryst.* **2001**, *371*, 199–202.
- [81] D. Cortecchia, C. Soci, M. Cametti, A. Petrozza, J. Martí-Rujas, *Chempluschem* **2017**, *82*, 681–685.
- [82] M. Era, K. Maeda, T. Tsutsui, *Chem. Phys. Lett.* **1998**, *296*, 417–420.
- [83] D. L. Dexter, *J. Chem. Phys.* **1953**, *21*, 836–850.
- [84] T. Förster, *Ann. Phys.* **1948**, *437*, 55–75.
- [85] K. Ema, M. Inomata, Y. Kato, H. Kunugita, M. Era, *Phys. Rev. Lett.* **2008**, *100*, 257401.
- [86] K. Shibuya, M. Koshimizu, Y. Takeoka, K. Asai, *Nucl. Instruments Methods Phys. Res. Sect. B Beam Interact. with Mater. Atoms* **2002**, *194*, 207–212.
- [87] K. Shibuya, M. Koshimizu, H. Murakami, Y. Muroya, Y. Katsumura, K. Asai, *Jpn. J. Appl. Phys.* **2004**, *43*, L1333–L1336.
- [88] J. Silver, R. Withnall, in *Lumin. Mater. Appl.*, John Wiley & Sons, Ltd, **2008**, pp. 75–109.
- [89] S. Ye, F. Xiao, Y. X. Pan, Y. Y. Ma, Q. Y. Zhang, *Mater. Sci. Eng. R Reports* **2010**, *71*, 1–34.
- [90] G. D. Scholes, G. Rumbles, *Nat. Mater.* **2006**, *5*, 683–696.
- [91] A. Miyata, A. Mitioglu, P. Plochocka, O. Portugall, J. T.-W. Wang, S. D. Stranks, H. J. Snaith, R. J. Nicholas, *Nat. Phys.* **2015**, *11*, 582–587.
- [92] Y. Yang, D. P. Ostrowski, R. M. France, K. Zhu, J. van de Lagemaat, J. M. Luther, M. C. Beard, *Nat. Photonics* **2016**, *10*, 53–59.
- [93] L. V Keldysh, *Sov. J. Exp. Theor. Phys. Lett.* **1979**, *29*, 658.
- [94] M. Kumagai, T. Takagahara, *Phys. Rev. B* **1989**, *40*, 12359–12381.

- [95] T. Ishihara, X. Hong, J. Ding, A. V Nurmikko, *Surf. Sci.* **1992**, *267*, 323–326.
- [96] D. B. Straus, C. R. Kagan, *J. Phys. Chem. Lett.* **2018**, *9*, 1434–1447.
- [97] T. C. Sum, S. Chen, G. Xing, X. Liu, B. Wu, *Nanotechnology* **2015**, *26*, 342001.
- [98] N. Onoda-Yamamuro, T. Matsuo, H. Suga, *J. Phys. Chem. Solids* **1990**, *51*, 1383–1395.
- [99] J. Even, L. Pedesseau, C. Katan, *J. Phys. Chem. C* **2014**, *118*, 11566–11572.
- [100] Y. Yamada, T. Nakamura, M. Endo, A. Wakamiya, Y. Kanemitsu, *J. Am. Chem. Soc.* **2014**, *136*, 11610–11613.
- [101] S. Pekar, M. F. Deigen, **1948**.
- [102] D. Emin, Ed. , in *Polarons*, Cambridge University Press, Cambridge, **2012**, pp. i–ii.
- [103] C. Franchini, M. Reticcioli, M. Setvin, U. Diebold, *Nat. Rev. Mater.* **2021**, *6*, 560–586.
- [104] H. von Känel, *Adv. Mater.* **1992**, *4*, 448.
- [105] X. Hong, T. Ishihara, A. V Nurmikko, *Solid State Commun.* **1992**, *84*, 657–661.
- [106] K. Chondroudis, D. B. Mitzi, *Chem. Mater.* **1999**, *11*, 3028–3030.
- [107] C. R. Kagan, D. B. Mitzi, C. D. Dimitrakopoulos, *Science.* **1999**, *286*, 945–947.
- [108] D. B. Mitzi, K. Chondroudis, C. R. Kagan, *IBM J. Res. Dev.* **2001**, *45*, 29–45.
- [109] B. R. Vincent, K. N. Robertson, T. S. Cameron, O. Knop, *Can. J. Chem.* **1987**, *65*, 1042–1046.
- [110] S. Wang, D. B. Mitzi, C. A. Feild, A. M. Guloy, *J. Am. Chem. Soc.* **1995**, *117*, 5297–5302.
- [111] S. S. "Nagapetyan, E. R. "Arakelova, E. A. "Ziger, V. M. "Koshkin, Y. T. "Struchkov, V. E. [AN S. "Shklover Moscow (USSR). Inst. Ehlementoorganicheskikh Soedinenij Khar'kovskij Politekhnikeskij Inst., Kharkov (Ukrainian SSR)]," **1989**, *34*:9, DOI <https://doi.org/>.
- [112] A. Poglitsch, D. Weber, *J. Chem. Phys.* **1987**, *87*, 6373–6378.
- [113] S. Masaki, S. Satoru, *J. Phys. Soc. Japan* **1966**, *21*, 1936–1946.

## Bibliography

- [114] E. Hanamura, N. Nagaosa, M. Kumagai, T. Takagahara, *Mater. Sci. Eng. B* **1988**, *1*, 255–258.
- [115] D. B. Tran Thoai, R. Zimmermann, M. Grundmann, D. Bimberg, *Phys. Rev. B* **1990**, *42*, 5906–5909.
- [116] J. R. Lakowicz, *Principles of Fluorescence Spectroscopy*, Springer New York, NY, **2006**.
- [117] C. F. Klingshirn, in (Ed.: C.F. Klingshirn), Springer Berlin Heidelberg, Berlin, Heidelberg, **2012**, pp. 507–560.
- [118] L. M. Herz, *Annu. Rev. Phys. Chem.* **2016**, *67*, 65–89.
- [119] M. B. Price, J. Butkus, T. C. Jellicoe, A. Sadhanala, A. Briane, J. E. Halpert, K. Broch, J. M. Hodgkiss, R. H. Friend, F. Deschler, *Nat. Commun.* **2015**, *6*, 8420.
- [120] S. Chung, S. Shrestha, X. Wen, Y. Feng, N. Gupta, H. Xia, P. Yu, J. Tang, G. Conibeer, *IOP Conf. Ser. Mater. Sci. Eng.* **2014**, *68*, 12002.
- [121] J. Yang, X. Wen, H. Xia, R. Sheng, Q. Ma, J. Kim, P. Tapping, T. Harada, T. W. Kee, F. Huang, Y.-B. Cheng, M. Green, A. Ho-Baillie, S. Huang, S. Shrestha, R. Patterson, G. Conibeer, *Nat. Commun.* **2017**, *8*, 14120.
- [122] A. H. Zewail, *J. Phys. Chem.* **1996**, *100*, 12701–12724.
- [123] A. H. Zewail, *J. Phys. Chem. A* **2000**, *104*, 5660–5694.
- [124] R. Berera, R. van Grondelle, J. T. M. Kennis, *Photosynth. Res.* **2009**, *101*, 105–118.
- [125] D. Meschede, *Optics, Light and Lasers: The Practical Approach to Modern Aspects of Photonics and Laser Physics*, Wiley-VCH, **1999**.
- [126] A. Halina, *Introduction to Laser Spectroscopy*, Elsevier B.V., **2005**.
- [127] R. R. Alfano, S. L. Shapiro, *Phys. Rev. Lett.* **1970**, *24*, 592–594.
- [128] M. M. Elshanawany, A. G. Ricciardulli, M. Saliba, J. Wachtveitl, M. Braun, *Nanoscale* **2021**, DOI 10.1039/D1NR04290D.
- [129] M. M. Elshanawany, A. G. Ricciardulli, J. J. Jeronimo-Rendon, M. Saliba, J. Wachtveitl, M. Braun, *J. Phys. Chem. C* **2022**, *126*, 8787–8793.

- [130] L. Mao, C. C. Stoumpos, M. G. Kanatzidis, *J. Am. Chem. Soc.* **2019**, *141*, 1171–1190.
- [131] L. N. Quan, M. Yuan, R. Comin, O. Voznyy, E. M. Beauregard, S. Hoogland, A. Buin, A. R. Kirmani, K. Zhao, A. Amassian, D. H. Kim, E. H. Sargent, *J. Am. Chem. Soc.* **2016**, *138*, 2649–2655.
- [132] H. Tsai, W. Nie, J.-C. Blancon, C. C. Stoumpos, R. Asadpour, B. Harutyunyan, A. J. Neukirch, R. Verduzco, J. J. Crochet, S. Tretiak, L. Pedesseau, J. Even, M. A. Alam, G. Gupta, J. Lou, P. M. Ajayan, M. J. Bedzyk, M. G. Kanatzidis, A. D. Mohite, *Nature* **2016**, *536*, 312–316.
- [133] A. G. Ricciardulli, S. Yang, J. H. Smet, M. Saliba, *Nat. Mater.* **2021**, DOI 10.1038/s41563-021-01029-9.
- [134] A. G. Ricciardulli, B. van der Zee, K. Philipps, G. A. H. Wetzelaer, R.-Q. Png, P. K. H. Ho, L.-L. Chua, P. W. M. Blom, *APL Mater.* **2020**, *8*, 21101.
- [135] S. Yang, D. Wu, W. Gong, Q. Huang, H. Zhen, Q. Ling, Z. Lin, *Chem. Sci.* **2018**, *9*, 8975–8981.
- [136] W. T. M. Van Gompel, R. Herckens, K. Van Hecke, B. Ruttens, J. D’Haen, L. Lutsen, D. Vanderzande, *Chem. Commun.* **2019**, *55*, 2481–2484.
- [137] M. C. Gélvez-Rueda, W. T. M. Van Gompel, R. Herckens, L. Lutsen, D. Vanderzande, F. C. Grozema, *J. Phys. Chem. Lett.* **2020**, *11*, 824–830.
- [138] C. Qin, T. Matsushima, W. J. Potscavage, A. S. D. Sandanayaka, M. R. Leyden, F. Bencheikh, K. Goushi, F. Mathevet, B. Heinrich, G. Yumoto, Y. Kanemitsu, C. Adachi, *Nat. Photonics* **2020**, *14*, 70–75.
- [139] Z. Xu, D. Lu, F. Liu, H. Lai, X. Wan, X. Zhang, Y. Liu, Y. Chen, *ACS Nano* **2020**, *14*, 4871–4881.
- [140] N. Kitazawa, *Jpn. J. Appl. Phys.* **1996**, *35*, 6202–6207.
- [141] N. Kitazawa, *Mater. Sci. Eng. B* **1997**, *49*, 233–238.
- [142] N. Kitazawa, *Jpn. J. Appl. Phys.* **1997**, *36*, 6876–6879.
- [143] N. Kitazawa, *Jpn. J. Appl. Phys.* **1997**, *36*, 2272–2276.
- [144] J. Cho, J. T. DuBose, A. N. T. Le, P. V. Kamat, *ACS Mater. Lett.* **2020**, *2*, 565–570.

- [145] X. Wu, M. T. Trinh, D. Niesner, H. Zhu, Z. Norman, J. S. Owen, O. Yaffe, B. J. Kudisch, X.-Y. Zhu, *J. Am. Chem. Soc.* **2015**, *137*, 2089–2096.
- [146] Y. Tian, Y. Li, B. Chen, R. Lai, S. He, X. Luo, Y. Han, Y. Wei, K. Wu, *J. Phys. Chem. Lett.* **2020**, *11*, 2247–2255.
- [147] Y. Han, X. Luo, R. Lai, Y. Li, G. Liang, K. Wu, *J. Phys. Chem. Lett.* **2019**, *10*, 1457–1463.
- [148] P. Avakian, E. Abramson, *J. Chem. Phys.* **1965**, *43*, 821–823.
- [149] X. Wang, W. G. Kofron, S. Kong, C. S. Rajesh, D. A. Modarelli, E. C. Lim, *J. Phys. Chem. A* **2000**, *104*, 1461–1465.
- [150] T. Takaya, T. Oda, Y. Shibazaki, Y. Hayashi, H. Shimomoto, E. Ihara, Y. Ishibashi, T. Asahi, K. Iwata, *Macromolecules* **2018**, *51*, 5430–5439.
- [151] O. L. J. Gijzeman, W. H. van Leeuwen, J. Langelaar, J. D. W. van Voorst, *Chem. Phys. Lett.* **1971**, *11*, 532–534.
- [152] P. Trojanowski, J. Plötner, C. Grünwald, F. F. Graupner, C. Slavov, A. J. Reuss, M. Braun, J. W. Engels, J. Wachtveitl, *Phys. Chem. Chem. Phys.* **2014**, *16*, 13875–13888.
- [153] A. G. Crawford, A. D. Dwyer, Z. Liu, A. Steffen, A. Beeby, L.-O. Pålsson, D. J. Tozer, T. B. Marder, *J. Am. Chem. Soc.* **2011**, *133*, 13349–13362.
- [154] M. Raytchev, E. Pandurski, I. Buchvarov, C. Modrakowski, T. Fiebig, *J. Phys. Chem. A* **2003**, *107*, 4592–4600.
- [155] H. Hu, D. Zhao, Y. Gao, X. Qiao, T. Salim, B. Chen, E. E. M. Chia, A. C. Grimsdale, Y. M. Lam, *Chem. Mater.* **2019**, *31*, 2597–2602.
- [156] E. H. Jung, N. J. Jeon, E. Y. Park, C. S. Moon, T. J. Shin, T.-Y. Yang, J. H. Noh, J. Seo, *Nature* **2019**, *567*, 511–515.
- [157] Q. Jiang, Y. Zhao, X. Zhang, X. Yang, Y. Chen, Z. Chu, Q. Ye, X. Li, Z. Yin, J. You, *Nat. Photonics* **2019**, *13*, 460–466.
- [158] X. Zheng, Y. Hou, C. Bao, J. Yin, F. Yuan, Z. Huang, K. Song, J. Liu, J. Troughton, N. Gasparini, C. Zhou, Y. Lin, D.-J. Xue, B. Chen, A. K. Johnston, N. Wei, M. N. Hedhili, M. Wei, A. Y. Alsalloum, P. Maity, B. Turedi, C. Yang, D. Baran, T. D. Anthopoulos,

- Y. Han, Z.-H. Lu, O. F. Mohammed, F. Gao, E. H. Sargent, O. M. Bakr, *Nat. Energy* **2020**, *5*, 131–140.
- [159] P. Ferdowsi, E. Ochoa-Martinez, U. Steiner, M. Saliba, *Chem. Mater.* **2021**, *33*, 3971–3979.
- [160] B. Conings, J. Drijkoningen, N. Gauquelin, A. Babayigit, J. D’Haen, L. D’Olieslaeger, A. Ethirajan, J. Verbeeck, J. Manca, E. Mosconi, F. De Angelis, H.-G. Boyen, *Adv. Energy Mater.* **2015**, *5*, 1500477.
- [161] R. K. Misra, S. Aharon, B. Li, D. Mogilyansky, I. Visoly-Fisher, L. Etgar, E. A. Katz, *J. Phys. Chem. Lett.* **2015**, *6*, 326–330.
- [162] W. Li, J. Li, L. Wang, G. Niu, R. Gao, Y. Qiu, *J. Mater. Chem. A* **2013**, *1*, 11735–11740.
- [163] M. Li, H. Li, J. Fu, T. Liang, W. Ma, *J. Phys. Chem. C* **2020**, *124*, 27251–27266.
- [164] Q. Chen, N. De Marco, Y. (Michael) Yang, T.-B. Song, C.-C. Chen, H. Zhao, Z. Hong, H. Zhou, Y. Yang, *Nano Today* **2015**, *10*, 355–396.
- [165] M. Kulbak, S. Gupta, N. Kedem, I. Levine, T. Bendikov, G. Hodes, D. Cahen, *J. Phys. Chem. Lett.* **2016**, *7*, 167–172.
- [166] C. A. López, M. V. Martínez-Huerta, M. C. Alvarez-Galván, P. Kayser, P. Gant, A. Castellanos-Gomez, M. T. Fernández-Díaz, F. Fauth, J. A. Alonso, *Inorg. Chem.* **2017**, *56*, 14214–14219.
- [167] Z. (Jason) Yu, M. Leilaeioun, Z. Holman, *Nat. Energy* **2016**, *1*, 16137.
- [168] T. Leijtens, K. A. Bush, R. Prasanna, M. D. McGehee, *Nat. Energy* **2018**, *3*, 828–838.
- [169] J. Xu, C. C. Boyd, Z. J. Yu, A. F. Palmstrom, D. J. Witter, B. W. Larson, R. M. France, J. Werner, S. P. Harvey, E. J. Wolf, W. Weigand, S. Manzoor, M. F. A. M. van Hest, J. J. Berry, J. M. Luther, Z. C. Holman, M. D. McGehee, *Science*. **2020**, *367*, 1097–1104.
- [170] D. W. deQuilettes, K. Frohna, D. Emin, T. Kirchartz, V. Bulovic, D. S. Ginger, S. D. Stranks, *Chem. Rev.* **2019**, *119*, 11007–11019.
- [171] C. Li, A. Wang, X. Deng, S. Wang, Y. Yuan, L. Ding, F. Hao, *ACS Photonics* **2020**, *7*, 1893–1907.
- [172] X. Guichuan, M. Nripan, S. Shuangyong, L. S. Sien, L. Y. Ming, G. Michael, M. Subodh,

- S. T. Chien, *Science*. **2013**, *342*, 344–347.
- [173] J. S. Manser, P. V Kamat, *Nat. Photonics* **2014**, *8*, 737–743.
- [174] K. G. Stampelcoskie, J. S. Manser, P. V Kamat, *Energy Environ. Sci.* **2015**, *8*, 208–215.
- [175] T. Ghosh, S. Aharon, L. Etgar, S. Ruhman, *J. Am. Chem. Soc.* **2017**, *139*, 18262–18270.
- [176] J. Shi, Y. Li, Y. Li, D. Li, Y. Luo, H. Wu, Q. Meng, *Joule* **2018**, *2*, 879–901.
- [177] I. Minda, J. Horn, E. Ahmed, D. Schlettwein, H. Schworer, *ChemPhysChem* **2018**, *19*, 3010–3017.
- [178] H. Tan, F. Che, M. Wei, Y. Zhao, M. I. Saidaminov, P. Todorović, D. Broberg, G. Walters, F. Tan, T. Zhuang, B. Sun, Z. Liang, H. Yuan, E. Fron, J. Kim, Z. Yang, O. Voznyy, M. Asta, E. H. Sargent, *Nat. Commun.* **2018**, *9*, 3100.
- [179] M. I. Saidaminov, K. Williams, M. Wei, A. Johnston, R. Quintero-Bermudez, M. Vafaie, J. M. Pina, A. H. Proppe, Y. Hou, G. Walters, S. O. Kelley, W. A. Tisdale, E. H. Sargent, *Nat. Mater.* **2020**, *19*, 412–418.
- [180] J. C. Brauer, D. Tsokkou, S. Sanchez, N. Droseros, B. Roose, E. Mosconi, X. Hua, M. Stolterfoht, D. Neher, U. Steiner, F. De Angelis, A. Abate, N. Banerji, *J. Chem. Phys.* **2020**, *152*, 104703.
- [181] T. Baumeler, N. Arora, A. Hinderhofer, S. Akin, A. Greco, M. Abdi-Jalebi, R. Shivanna, R. Uchida, Y. Liu, F. Schreiber, S. M. Zakeeruddin, R. H. Friend, M. Graetzel, M. I. Dar, *J. Phys. Chem. Lett.* **2020**, *11*, 10188–10195.
- [182] H. P. Pasanen, P. Vivo, L. Canil, H. Hempel, T. Unold, A. Abate, N. V Tkachenko, *J. Phys. Chem. Lett.* **2020**, *11*, 445–450.
- [183] T. Wang, L. Jin, J. Hidalgo, W. Chu, J. M. Snider, S. Deng, T. Zhu, B. Lai, O. Prezhdo, J.-P. Correa-Baena, L. Huang, *Sci. Adv.* **2020**, *6*, eabb1336.
- [184] D. Catone, G. Ammirati, P. O’Keeffe, F. Martelli, L. Di Mario, S. Turchini, A. Paladini, F. Toschi, A. Agresti, S. Pescetelli, A. Di Carlo, *Energies* **2021**, *14*, DOI 10.3390/en14030708.
- [185] M. Kiyoshi, M. Daniele, T. M. Tuan, J. P. P., M. Edoardo, J. S. C., D. A. Filippo, Z. X.-Y., *Sci. Adv.* **2021**, *3*, e1701217.



- [186] S. Kahmann, M. A. Loi, *J. Mater. Chem. C* **2019**, *7*, 2471–2486.
- [187] M. Saliba, J.-P. Correa-Baena, C. M. Wolff, M. Stollerfoht, N. Phung, S. Albrecht, D. Neher, A. Abate, *Chem. Mater.* **2018**, *30*, 4193–4201.
- [188] N. Mondal, A. Samanta, *Nanoscale* **2017**, *9*, 1878–1885.
- [189] M. T. Trinh, X. Wu, D. Niesner, X.-Y. Zhu, *J. Mater. Chem. A* **2015**, *3*, 9285–9290.
- [190] J. Chen, M. E. Messing, K. Zheng, T. Pullerits, *J. Am. Chem. Soc.* **2019**, *141*, 3532–3540.
- [191] C. Slavov, H. Hartmann, J. Wachtveitl, *Anal. Chem.* **2015**, *87*, 2328–2336.
- [192] A. I. A. Soliman, M. Sayed, M. M. Elshanawany, O. Younis, M. Ahmed, A. M. Kamal El-Dean, A.-M. A. Abdel-Wahab, J. Wachtveitl, M. Braun, P. Fatehi, M. S. Tolba, *ACS Omega* **2022**, *7*, 10178–10186.
- [193] A. A. Hamed, I. A. Abdelhamid, G. R. Saad, N. A. Elkady, M. Z. Elsabee, *Int. J. Biol. Macromol.* **2020**.
- [194] D. Sinha, A. K. Tiwari, S. Singh, G. Shukla, P. Mishra, H. Chandra, A. K. Mishra, *Eur. J. Med. Chem.* **2008**, *43*, 160–165.
- [195] R. Reshma, R. S. Joseyphus, A. Dasan, L. John, *J. Coord. Chem.* **2019**, *72*, 3326–3337.
- [196] S. Kagatkar, D. Sunil, *J. Electron. Mater.* **2021**, *50*, 6708–6723.
- [197] A. L. Berhanu, Gaurav, I. Mohiuddin, A. K. Malik, J. S. Aulakh, V. Kumar, K.-H. Kim, *TrAC Trends Anal. Chem.* **2019**, *116*, 74–91.
- [198] O. Younis, E. A. Orabi, A. M. Kamal, M. Sayed, R. Hassanien, R. L. Davis, O. Tsutsumi, M. Ahmed, *Opt. Mater. (Amst)*. **2020**, *100*, 109713.
- [199] O. Younis, E. E. El-Katori, R. Hassanien, A. S. Abousalem, O. Tsutsumi, *Dye. Pigment.* **2020**, *175*, 108146.
- [200] S. M. Gomha, H. A. Ahmed, M. Shaban, T. Z. Abolibda, M. S. Khushaim, K. A. Alharbi, *Materials (Basel)*. **2021**, *14*.
- [201] J. N. Appaturi, R. Ratti, B. L. Phoon, S. M. Batagarawa, I. Ud Din, M. Selvaraj, R. Jothi Ramalingam, *Dalt. Trans.* **2021**, *50*, 5370.
- [202] M. Aqeel Ashraf, Z. Liu, Y.-Y. Li, C. Li, D. Zhang, *Synth. Commun.* **2021**, *51*, 37–56.

## *Bibliography*

- [203] R. He, J. Zhou, W. Mao, *Synth. Commun.* **2021**, *51*, 1478–1495.
- [204] M. Sayed, O. Younis, R. Hassanien, M. Ahmed, A. A. K. Mohammed, A. M. Kamal, O. Tsutsumi, *J. Photochem. Photobiol. A Chem.* **2019**, *383*, 111969.
- [205] O. Younis, M. S. Tolba, E. A. Orabi, A. M. Kamal, R. Hassanien, O. Tsutsumi, M. Ahmed, *J. Photochem. Photobiol. A Chem.* **2020**, *400*, 112642.
- [206] M. Ahmed, O. Younis, E. A. Orabi, A. M. Sayed, A. M. Kamal El-Dean, R. Hassanien, R. L. Davis, O. Tsutsumi, M. S. Tolba, *ACS Omega* **2020**, *5*, 29988–30000.
- [207] K. Wang, H. Su, P. Wang, W. Wang, H. Li, *RSC Adv.* **2019**, *9*, 14268–14275.
- [208] Z. Q. Gao, Z. H. Li, P. F. Xia, M. S. Wong, K. W. Cheah, C. H. Chen, *Adv. Funct. Mater.* **2007**, *17*, 3194–3199.





## Chapter 7 List of Publications

(# - These authors contributed equally to this work)

### 7.1 Declaration of the own contribution for each publication:

#### Reference [1] Mechanism of Ultrafast Energy Transfer between the Organic-Inorganic Layers in Multiple-Ring Aromatic Spacers for 2D Perovskites

Mahmoud M Elshanawany, Antonio Gaetano Ricciardulli, Michael Saliba, Josef Wachtveitl and Markus Braun\*  
Nanoscale, **2021**, 13, 15668-15676

DOI: 10.1039/D1NR04290D

- Fabricate the thin films.
- Measuring and analyzing steady-state spectroscopy, time-resolved emission, and transient absorption experiments.
- Interpretation of the data together with co-authors.
- Writing the first draft of the manuscript.

#### Reference [2] Ultrafast Carrier Dynamics in Wide Band Gap Mixed-Cation Perovskites: Influence of the Cs Cation

Mahmoud M. Elshanawany, Antonio Gaetano Ricciardulli, Jose J. Jeronimo-Rendon, Michael Saliba, Josef Wachtveitl and Markus Braun\*

J. Phys. Chem. C **2022**, 126, 20, 8787–8793

DOI: 10.1021/acs.jpcc.2c02682

- Measuring and analyzing steady-state spectroscopy, time-resolved emission, and transient absorption experiments.
- Interpretation of the data together with co-authors.
- Writing the first draft of the manuscript.

#### Reference [3] Base-Free Synthesis and Photophysical Properties of New Schiff Bases Containing Indole Moiety

Ahmed I. A. Soliman\*<sup>#</sup>, Mostafa Sayed<sup>#</sup>, Mahmoud M. Elshanawany<sup>#</sup>, Osama Younis, Mostafa Ahmed, Adel M. Kamal El-Dean, Aboel-Magd A. Abdel-Wahab, Josef Wachtveitl, Markus Braun\*, Pedram Fatehi, and Mahmoud S. Tolba

ACS Omega **2022**, 7, 12, 10178–10186

DOI: 10.1021/acsomega.1c06636

- Measuring and analyzing steady-state spectroscopy and time-resolved emission experiments.
- Interpretation of the data together with co-authors.
- Writing the photophysical part of the manuscript in coordination with co-authors.

## 7.2 Elshanawany et al., *Nanoscale* 2021, 13

### **Mechanism of Ultrafast Energy Transfer between the Organic-Inorganic Layers in Multiple-Ring Aromatic Spacers for 2D Perovskites**

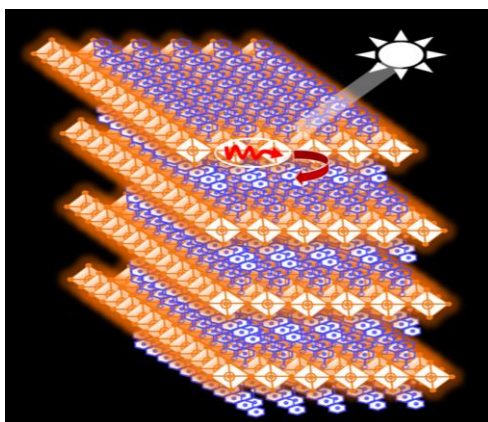
Mahmoud M. Elshanawany, Antonio Gaetano Ricciardulli, Michael Saliba, Josef Wachtveitl and Markus Braun\*

*Nanoscale*, 2021, 13, 15668-15676

**Publication Date:** September 7, 2021

**DOI:** 10.1039/D1NR04290D

Reprinted with permission from the Royal Society of Chemistry





Cite this: *Nanoscale*, 2021, **13**, 15668

## Mechanism of ultrafast energy transfer between the organic–inorganic layers in multiple-ring aromatic spacers for 2D perovskites†

Mahmoud M. Elshanawany,<sup>a</sup> Antonio Gaetano Ricciardulli,<sup>b</sup> Michael Saliba,<sup>c,d</sup> Josef Wachtveitl<sup>a</sup> and Markus Braun<sup>a\*</sup>

Lead halide based perovskite semiconductors self-assemble with distinct organic cations in natural multi-quantum-well structures. The emerging electronic properties of these two-dimensional (2D) materials can be controlled by the combination of the halide content and choice of chromophore in the organic layer. Understanding the photophysics of the perovskite semiconductor materials is critical for the optimization of stable and efficient optoelectronic devices. We use femtosecond transient absorption spectroscopy (fs-TAS) to study the mechanism of energy transfer between the organic and inorganic layers in a series of three lead-based mixed-halide perovskites such as benzylammonium (BA), 1-naphthylmethylammonium (NMA), and 1-pyrenemethylammonium (PMA) cations in 2D-lead-based perovskite thin films under similar experimental conditions. After optical excitation of the 2D-confined exciton in the lead halide layer, ultrafast energy transfer is observed to organic singlet and triplet states of the incorporated chromophores. This is explained by an effective Dexter energy transfer, which operates *via* a correlated electron exchange between the donating 2D-confined exciton and the accepting chromophore under spin conservation.

Received 2nd July 2021,  
 Accepted 6th September 2021

DOI: 10.1039/d1nr04290d

rsc.li/nanoscale

### Introduction

Perovskites are promising semiconductor materials for efficient solar cells (SCs) or light-emitting diodes (LEDs) because of their high quantum efficiencies, optical and electrical properties, tunability, and their low cost. Three-dimensional (3D) perovskite solar cells showed outstanding progress in the power conversion efficiency from 3.8%<sup>1</sup> to 25.2%<sup>2</sup> within 11 years. To date, many researchers are trying to improve the properties of the two-dimensional (2D) organic–inorganic perovskites with large size organic spacers as they are photochemically and structurally very stable because of the hydrophobicity of these organic layers compared with the 3D perovskites.<sup>3–7</sup> Besides, for 2D perovskites, important optoelectronic applications<sup>8</sup> like LEDs,<sup>9–11</sup> transistors,<sup>12</sup> solar cells,

photodetectors, scintillators,<sup>13</sup> phosphors,<sup>13</sup> and photonic devices<sup>14</sup> were demonstrated.

Lead halide perovskites consist of inorganic PbX<sub>6</sub> octahedrons, where X is Cl, Br, or I. Depending on the choice of the organic cations, these PbX<sub>6</sub> units crystallize isolated (0D), linearly arranged (1D), layered (2D), or connected in all directions (3D). This allows the control of the dimensionality of the inorganic semiconductor material.<sup>15–24</sup> The chemical formula of 2D perovskites (see scheme in Fig. S1†) is known for more than 30 years as (R–CH<sub>2</sub>–NH<sub>3</sub>)<sub>2</sub>(A)<sub>n–1</sub>BX<sub>3n+1</sub>, where A and B are cations. R–CH<sub>2</sub>–NH<sub>3</sub> is a primary aliphatic or an aromatic alkyl-ammonium group working as a spacer between the layers, X is a halide anion, and n refers to the number of metal halide octahedral layers.<sup>21</sup>

About 20 years ago, some groups started to use the organic cations in this material class not only to determine the structure of the inorganic semiconductor material but moreover to become the electronically active component. The introduction of large chromophores in 2D lead halides leads to effective low-dimensional energy transfer systems, including organic triplet states,<sup>25–28</sup> organic singlet states<sup>26,27</sup> and organic charge-transfer states (pyrene-TCNQ).<sup>29,30</sup> By tuning the inorganic excitonic states to high transition energies in the (R–CH<sub>2</sub>–NH<sub>3</sub>)<sub>2</sub>PbCl<sub>4</sub> system, efficient energy transfer between the inorganic layers (lead chloride) and organic layers (benzyl, naphthyl, anthryl) could be achieved.<sup>26</sup> For benzyl and

<sup>a</sup>Institute of Physical and Theoretical Chemistry, Goethe University, Frankfurt am Main, Germany. E-mail: braun@theochem.uni-frankfurt.de; Tel: +49 (0)69 798 29711

<sup>b</sup>Institute of Materials Science, Technische Universität Darmstadt, Germany

<sup>c</sup>Institute of Photovoltaics (ipv), University of Stuttgart, Stuttgart, Germany

<sup>d</sup>Helmholtz Young Investigator Group FRONTRUNNER, Forschungszentrum Jülich, Jülich, Germany

†Electronic supplementary information (ESI) available. See DOI: 10.1039/d1nr04290d

naphthyl chromophores, a strong coupling between the lead chloride excitonic band and the triplet state of the chromophore is monitored by a strong phosphorescence signal from the organic triplet state. This was interpreted by an efficient energy transfer process from the inorganic excitonic band to the triplet state of the organic layer *via* a Dexter energy transfer mechanism.<sup>26</sup> Ema *et al.* reported for lead bromides that the energy transfer efficiency to the organic naphthyl triplet system decreases with increasing the alkyl chain length between the NH<sub>3</sub> anchor group and the aromatic naphthyl system.<sup>31</sup> Pyrene-based halide perovskites were also studied with different lead halides (chloride, bromide, and iodide) as a promising material for light-emitting applications and efficient energy transfer to the organic singlet and triplet system.<sup>27</sup> 2D perovskites were not applied in solar cell devices until Cao *et al.* could achieve 4.02% power conversion efficiency.<sup>32</sup> Recently, efficiencies as high as 12.4% have been obtained by employing quasi-2D perovskites, which consist of alternating naphthylmethylamine and formamidinium cations<sup>33</sup> and even solar cells with naphthyl and anthryl groups were realized.<sup>34</sup> Many studies have reported the possibility of tuning the excitonic band by halide replacement and the improved stability of these mixed halide (Cl, Br, and I) crystals due to their flexibility, which facilitates the fabrication of LEDs from blue to the green region.<sup>35–39</sup> Those mixed halide perovskites are referred to as (R-CH<sub>2</sub>-NH<sub>3</sub>)<sub>2</sub>Pb(Br<sub>x</sub>I<sub>4-x</sub>) with the aromatic chromophore R. Here the parameter *x* determines the relative content of Br and I and for *e.g.* a ratio of Br:I of 0.7 : 0.3, this can also be written as (R-CH<sub>2</sub>-NH<sub>3</sub>)<sub>2</sub>Pb(Br<sub>0.7</sub>I<sub>0.3</sub>)<sub>4</sub>.

In this work, we present time-resolved spectral studies of different chromophores like benzylammonium (BA), 1-naphthylmethylammonium (NMA), and 1-pyrenemethylammonium (PMA) cations in 2D-lead based perovskite thin films using steady-state UV-Vis, steady-state PL spectroscopy, time-resolved emission, and ultrafast femtosecond transient absorption spectroscopy. These experiments are performed on all investigated samples under similar experimental conditions to elucidate the energy transfer and relaxation pathways.

## Experimental section

The one-step spin-coating method was applied to fabricate thin films of microcrystalline (BA)<sub>2</sub>Pb(Br<sub>0.7</sub>I<sub>0.3</sub>)<sub>4</sub>, (NMA)<sub>2</sub>Pb(Br<sub>0.7</sub>I<sub>0.3</sub>)<sub>4</sub>, and (PMA)<sub>2</sub>Pb(Br<sub>0.7</sub>I<sub>0.3</sub>)<sub>4</sub> on quartz glass substrates. We used mixed halide lead-based Pb(Br<sub>0.7</sub>I<sub>0.3</sub>)<sub>4</sub> for all samples to tune the excitonic transition energy of the inorganic part and visualize the influence of the different chromophores.

### Preparation of the substrates

The 25.4 mm × 25.4 mm quartz substrates of 1 mm thickness were cleaned with soapy water and then washed with deionized water after ultrasonication for 45 min in a mixture of acetone and isopropyl alcohol (1:1). Afterwards, the glass was dried with a nitrogen blower. Before the spin coating, the substrates were subsequently exposed to O<sub>2</sub> plasma for 15 min (Plasma cleaner Zepto, Diener electronic) to remove organic residues.

### Preparation of perovskite precursors for the thin films

Firstly, benzylammonium bromide (C<sub>7</sub>H<sub>7</sub>NH<sub>3</sub>Br), was synthesized *via* the reaction of benzylamine (C<sub>7</sub>H<sub>9</sub>N, 3 mL, Alfa Aesar) with hydrobromic acid (HBr, 48% in water, ACROS ORGANICS) and stirred at 0 °C for 30 min. The C<sub>7</sub>H<sub>7</sub>NH<sub>3</sub>Br powder was washed three times with petroleum ether and dried in a vacuum pump for two days before use. Benzylammonium iodide (C<sub>7</sub>H<sub>7</sub>NH<sub>3</sub>I) was synthesized *via* the reaction of benzylamine (C<sub>7</sub>H<sub>9</sub>N, 3 mL, Alfa Aesar) with hydroiodic acid (HI, 55–58 mass% in water, Fluka) by the same process. (BA)<sub>2</sub>PbBr<sub>4</sub> and (BA)<sub>2</sub>PbI<sub>4</sub> precursor solutions (the concentration of solute was fixed at 0.3 M for all samples) were prepared in *N,N*-dimethyl formamide (DMF, anhydrous, Aldrich, 1 mL). (BA)<sub>2</sub>Pb(Br<sub>0.7</sub>I<sub>0.3</sub>)<sub>4</sub> solution was mixed from 0.7 ml of (BA)<sub>2</sub>PbBr<sub>4</sub> and 0.3 ml of (BA)<sub>2</sub>PbI<sub>4</sub>. The solution was stirred at 50 °C for 1 day before use in the spin-coating process.

We have used the analogue procedure to prepare (NMA)<sub>2</sub>Pb(Br<sub>0.7</sub>I<sub>0.3</sub>)<sub>4</sub> (except that 1-naphthylmethylammonium bromide and 1-naphthylmethylammonium iodide powders were washed with diethyl ether). The procedure prepared the salts 1-pyrenemethylammonium bromide, and 1-pyrenemethylammonium iodide described elsewhere<sup>27</sup> and in the ESI.†

Finally, transparent and homogeneous solutions of (BA)<sub>2</sub>Pb(Br<sub>0.7</sub>I<sub>0.3</sub>)<sub>4</sub>, (NMA)<sub>2</sub>Pb(Br<sub>0.7</sub>I<sub>0.3</sub>)<sub>4</sub>, and (PMA)<sub>2</sub>Pb(Br<sub>0.7</sub>I<sub>0.3</sub>)<sub>4</sub> without the formation of any precipitates were obtained. Using these solutions at 50 °C, spin-coating was carried out at 4000 rpm for 50 s. After the spin-coating, the films were annealed at 100 °C for 10 min. As shown in Fig. S1,† the SEM and XRD spectra of all samples exhibit high crystallinity of the films.

### Optical measurements

**Steady-state spectroscopy.** Absorption spectra of the spin-coated films on a quartz substrate (thickness 1 mm) were recorded with the UV/Vis spectrophotometer SPECORD S600 (Analytik Jena, Jena, Germany). Photoluminescence (PL) spectra were collected by an FP-8500 spectrofluorometer (Jasco, Groß-Umstadt, Germany). The excitation wavelength was 320 nm with a bandwidth of 5 nm. We additionally applied an UV band pass filter for 280–370 nm (UG11, Schott Glas) for the excitation path and a long pass filter of 360 nm (WG360, Schott Glas) for the emission path. The PMT voltage was set to 950 V. The wavelength-dependent instrument sensitivity and the baseline were corrected routinely.

**Time-correlated single photon counting (TCSPC).** Nanosecond time-resolved emission measurements were performed using a TCSPC system (Fluo Time 100, PicoQuant) and counting card with 25 ps channel width. The thin films were excited using a sub-ns pulsed LED PLS320 at 325 nm, and the PL of the sample was detected using a photomultiplier detector (PMA 182, PicoQuant). The repetition rate of the pulsed LED was 10<sup>7</sup> Hz (time window of 100 ns). The Rayleigh scattered light on a pure quartz substrate was used to determine the temporal instrument response function (IRF) of the TCSPC system (full width at half maximum (FWHM) of ~800 ps). This



IRF was considered in the fitting of the transient traces. For all measurements, a long pass filter at 390 nm was inserted routinely to block stray light from the excitation source. Various detection wavelength ranges were selected using combinations of long pass and band pass filters.

**Femtosecond transient absorption spectroscopy measurements (fs-TAS).** We used a home-built pump-probe setup<sup>40</sup> for fs-TAS to investigate the ultrafast exciton dynamics, energy transfer, and recombination processes in the 2D perovskite systems. The pulsed laser system ran at a central wavelength of 775 nm and a repetition rate of 1 kHz (Clark-MXR, Dexter, MI, USA, pulse duration of 180 fs). Excitation pulses were applied with a central wavelength of 387 nm (after second harmonic generation of the laser fundamental). We adjusted the pump pulse energy to obtain an excitation density of  $162 \mu\text{J cm}^{-2}$  at the sample position. The probe white light covering a spectral range of 360–645 nm was generated by focusing a part of the laser fundamental onto a 5 mm thick calcium fluoride crystal. The white light was transmitted through the sample and subsequently detected *via* an HR320 spectrograph (Horiba, Kyoto, Japan). The detection system is consisting of a signal processing chip (S8865-128) with 128 channel photodiode arrays (PDA), a C9118 driver circuit (Hamamatsu Photonics) and a data acquisition card that digitizes the analog PDA signals at 16 bits (National Instruments, NI6120). The sample was continuously moved in the plane perpendicular to the direction of probe pulse propagation. By varying the time delay between the excitation and the probe pulses *via* a stepping translational stage (delay line), we obtained a three-dimensional transient absorption profile ( $\Delta\text{OD}$  vs.  $\lambda$  and  $t$ ).<sup>41</sup> All spectra presented here were chirp-corrected, and the instrumental resolution was  $\sim 200$  fs. The decay-associated spectra (DAS) resulted from the global lifetime analysis (GLA) discussed in detail elsewhere.<sup>42</sup> All TA measurements were performed up to 1.5 ns delay time.

## Results and discussion

The benzyl, naphthyl and pyrenyl chromophores, which are incorporated as an organic layer in the lead halide perovskite films, were chosen because the energetic position of their first

excited singlet and triplet states allows for different scenarios of energy transfer. The fluorescence and phosphorescence of these chromophores cover transition wavelengths from the UV to the red spectral range. The halide mixture of Br and I in the ratio 0.7:0.3 shifts the transition wavelength of the 2D lead halide exciton to about 400 nm.

It is worth noting that a paper by Wu *et al.* reporting the triplet excimer formation with NMA cations has been recently published during the preparation of our manuscript.<sup>43</sup> However, our study mainly focuses on the energy transfer mechanism between the inorganic and organic layers in 2D perovskite thin films.<sup>33</sup>

### UV-vis absorption and fluorescence spectroscopy of the thin film samples

Absorption spectroscopy is a unique tool for the estimation of optical bandgap and the nature of semiconductors, but also of allowed molecular transitions. The absorption spectra of thin semiconductor films show a sharp enhancement at wavelength regions larger than or close to the bandgap if the material is excitonic. As shown in (Fig. 1a–c), this excitonic absorption peak of the  $(\text{BA})_2\text{Pb}(\text{Br}_{0.7}\text{I}_{0.3})_4$  film is observed at 402 nm (3.09 eV) with a red-shifted extinction tail due to scattering. The  $(\text{NMA})_2\text{Pb}(\text{Br}_{0.7}\text{I}_{0.3})_4$  film shows excitonic absorption at 417 nm (2.98 eV) with a weak broad red-shifted absorption plateau that extends until 570 nm, most likely due to trap states.<sup>44</sup> The excitonic peak of  $(\text{PMA})_2\text{Pb}(\text{Br}_{0.7}\text{I}_{0.3})_4$  is found at 404 nm (3.07 eV) and has a weak red-shifted absorption at about 453 nm (2.74 eV), most likely due to trap states.<sup>44</sup> The PL spectrum of  $(\text{BA})_2\text{Pb}(\text{Br}_{0.7}\text{I}_{0.3})_4$  after excitation at 320 nm shows a spectrally narrow excitonic emission peak at 405 nm without spectral fine structure. This is the typical emission behaviour for the 2D exciton confined in the inorganic lead halide layer.<sup>26,27</sup> The emission spectrum of the  $(\text{NMA})_2\text{Pb}(\text{Br}_{0.7}\text{I}_{0.3})_4$  after excitation at 320 nm film consists of two components: an excitonic peak at 440 nm is observed, which is slightly red-shifted to the excitonic absorption maximum of the film; also a structured emission with maxima at 570 and 617 nm is observed, that can be assigned to the phosphorescence of the naphthyl chromophore at room temperature.<sup>31,43</sup> The PL spectrum of  $(\text{PMA})_2\text{Pb}$

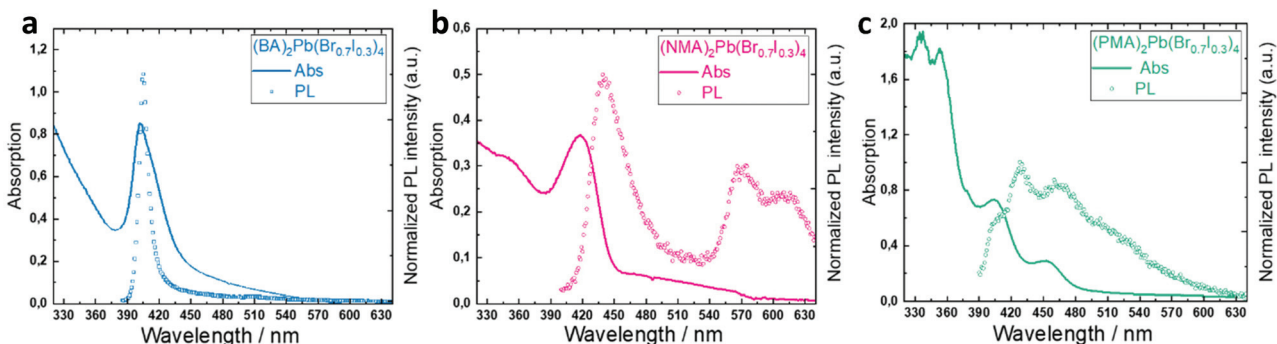


**Fig. 1** UV-vis absorption and normalized PL spectra of (a)  $(\text{BA})_2\text{Pb}(\text{Br}_{0.7}\text{I}_{0.3})_4$  (b)  $(\text{NMA})_2\text{Pb}(\text{Br}_{0.7}\text{I}_{0.3})_4$  and (c)  $(\text{PMA})_2\text{Pb}(\text{Br}_{0.7}\text{I}_{0.3})_4$  thin films at room temperature. The excitation wavelength for the emission measurements was 320 nm.

(Br<sub>0.7</sub>I<sub>0.3</sub>)<sub>4</sub> excited at 320 nm shows a broad, fine structured emission with maxima at 403, 428, and 460 nm that extends until 600 nm. This can be assigned to the fluorescence of the pyrenyl chromophore in this film, as these emission characteristics are well-known for 1-substituted pyrene chromophores.<sup>40,45</sup>

Altogether the 2D perovskite samples with the selected three different organic chromophores show an absorption behaviour which is dominated by the lead halide based 2D confined exciton of the inorganic layer while the emission behaviour is either due to the 2D inorganic exciton or the organic triplet state or the organic singlet state, depending on the chosen organic chromophore.

### Time-resolved fluorescence measurements

To investigate the mechanisms of energy relaxation pathways and lifetimes, PL decay measurements were performed using the TCSPC technique. TCSPC decay profiles of (BA)<sub>2</sub>Pb(Br<sub>0.7</sub>I<sub>0.3</sub>)<sub>4</sub>, (NMA)<sub>2</sub>Pb(Br<sub>0.7</sub>I<sub>0.3</sub>)<sub>4</sub>, and (PMA)<sub>2</sub>Pb(Br<sub>0.7</sub>I<sub>0.3</sub>)<sub>4</sub> thin films are shown in (Fig. S2†). It is evident from the figure that (PMA)<sub>2</sub>Pb(Br<sub>0.7</sub>I<sub>0.3</sub>)<sub>4</sub> has the longest lifetimes with two decay components of 0.98 ns and 17 ns, followed by (NMA)<sub>2</sub>Pb(Br<sub>0.7</sub>I<sub>0.3</sub>)<sub>4</sub> (0.60 ns) and (BA)<sub>2</sub>Pb(Br<sub>0.7</sub>I<sub>0.3</sub>)<sub>4</sub> (0.61 ns) samples. The detailed parameters are summarized in Table S1.†

In BA perovskite, the lifetime of 0.61 ns represents the exciton relaxation in the inorganic layer. In NMA perovskite, the lifetime component monitored at the exciton peak (440 nm) represents the relaxation of the 2D exciton to the ground state and the triplet state of the naphthyl chromophore at room temperature, while the slower decay monitored at the naphthyl phosphorescence (wavelength > 530 nm) shows the decay of the organic triplet state.<sup>31</sup> The PMA perovskite has two components. The fast component (0.98 ns) may represent different relaxation processes like singlet–singlet annihilation in the organic layer, while the slow component (17 ns) shows the lifetime of the pyrenyl singlet state.<sup>46</sup> The observed average PL lifetimes ( $\tau_{\text{avg}}$ ) of NMA and PMA chromophores are close to the reported values of different groups.<sup>31,46</sup>

### Transient absorption

By performing fs-TAS experiments, it is possible to monitor the dynamics of transiently created excited states, excitons or charge carriers. This provides insight into the mechanisms of exciton cooling processes, energy transfer or charge carrier transfer in these thin-film samples. The used approach is a pump–probe experiment, where the sample is excited by an ultrashort laser pulse.<sup>47–49</sup> The ensuing non-equilibrium dynamics of the system can be detected *via* the transmission of delayed probe pulses. The samples were pumped at 387 nm, and the spectrally broad probe pulse revealed the changes in the absorption spectrum ( $\Delta A$ ) as a function of time. The samples were measured from the sample side at room temperature. The films were stable during the measurements, and repeated measurements at identical sample positions showed no difference in the magnitude of the recovery kinetics of the signals.

### Ultrafast dynamics of (BA)<sub>2</sub>Pb(Br<sub>0.7</sub>I<sub>0.3</sub>)<sub>4</sub>

In the BA-based perovskite, thin-film absorption and emission are dominated by the 2D Pb-mixed halide excitonic state. It is expected that energy transfer between the organic and inorganic layers is absent after excitation at 387 nm, as the excitonic lead halide state at 406 nm is lower in energy than both the singlet (at about 260 nm) and the triplet (at about 360 nm)<sup>26</sup> excited state of the BA chromophore.

The wavelength and time-dependent TA map of BA perovskite thin film is shown in Fig. 2a. The ground state bleach GSB at 404 nm (3.09 eV) is close to the bandgap of the material. The excitonic band of the inorganic part is lower in energy than the singlet and the triplet states of the organic part, thus only the exciton dynamics from the inorganic layer is observed without any relaxation channels provided by singlet or triplet states of the organic cation.<sup>44</sup>

The absorption changes of the sample at 406 nm for different delay times are shown in Fig. 2b. The decay-associated spectra (DAS) resulting from the global lifetime analysis (GLA)<sup>42</sup> are composed of two lifetimes (Fig. 2c). The dominant bleach signal due to the lead halide exciton is long-lived and decays with a time constant of 506 ps.

By comparing the TA spectra of different excitation power densities, a clear pump power dependence is observed. With increasing power (from 81 to 146  $\mu\text{J cm}^{-2}$ ) the exciton relaxation time decreases from 506 to 32 ps, respectively, and the amplitude of the fast component  $\tau_1$  strongly increases (Fig. S3 and Table S2†). The excitation power-dependence is directly correlated to the exciton density in the sample. Therefore, the fast time constant  $\tau_1$  is assigned to the exciton–exciton annihilation process (EEA), whereas the time constant  $\tau_2$  is indicative for the relaxation of the 2D confined exciton to the ground state.

### Ultrafast dynamics of (NMA)<sub>2</sub>Pb(Br<sub>0.7</sub>I<sub>0.3</sub>)<sub>4</sub>

In the NMA-based perovskite thin-film, the excitonic band (at 417 nm) is lower in energy than the singlet excited state (at 290 nm) though it is higher in energy than the triplet excited state (at 470 nm) of the NMA chromophore.<sup>26</sup> In this case, a strong coupling between the layers leads to an energy transfer from the excitonic lead halide band to the organic triplet state.<sup>31</sup> The wavelength and time-dependent TA map are shown in Fig. 3a. In the transient absorption spectra of the NMA perovskite, the peak position of the negative signal (blue signal) at about 420 nm is in good agreement with the excitonic peak in the absorption spectrum (Fig. 1b). Thus it can be assigned to the state filling signal contributed by both band-edge electrons and holes of the lead halide exciton. The positive feature around 440 nm, which appears around 0.5 ps after the optical excitation pulse (see Fig. 3b and d), might be due to the naphthalene monomer triplet–triplet absorption.<sup>43,50,51</sup> The broad positive peak (red signal) around 600 nm is assigned to triplet–triplet absorption of the intramolecular triplet excimer of NMA,<sup>33,43,51</sup> which forms due to the high density of naphthalene chromophores in the organic layer.

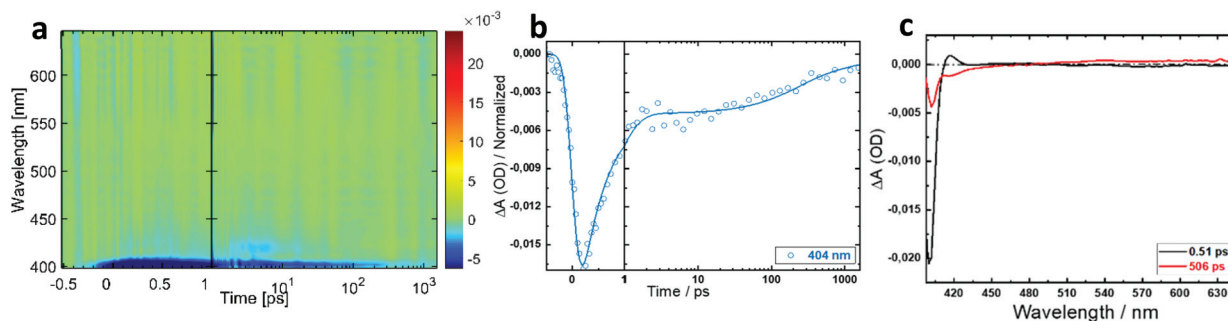


Fig. 2 Transient absorption data for  $(\text{BA})_2\text{Pb}(\text{Br}_{0.7}\text{I}_{0.3})_4$  thin films excited at 387 nm ( $81 \mu\text{J cm}^{-2}$ ). (a) Wavelength and time dependent TA map. (b) Kinetic profile at 404 nm. (c) Decay associated spectra (DAS) derived from kinetic fitting with two time constants.

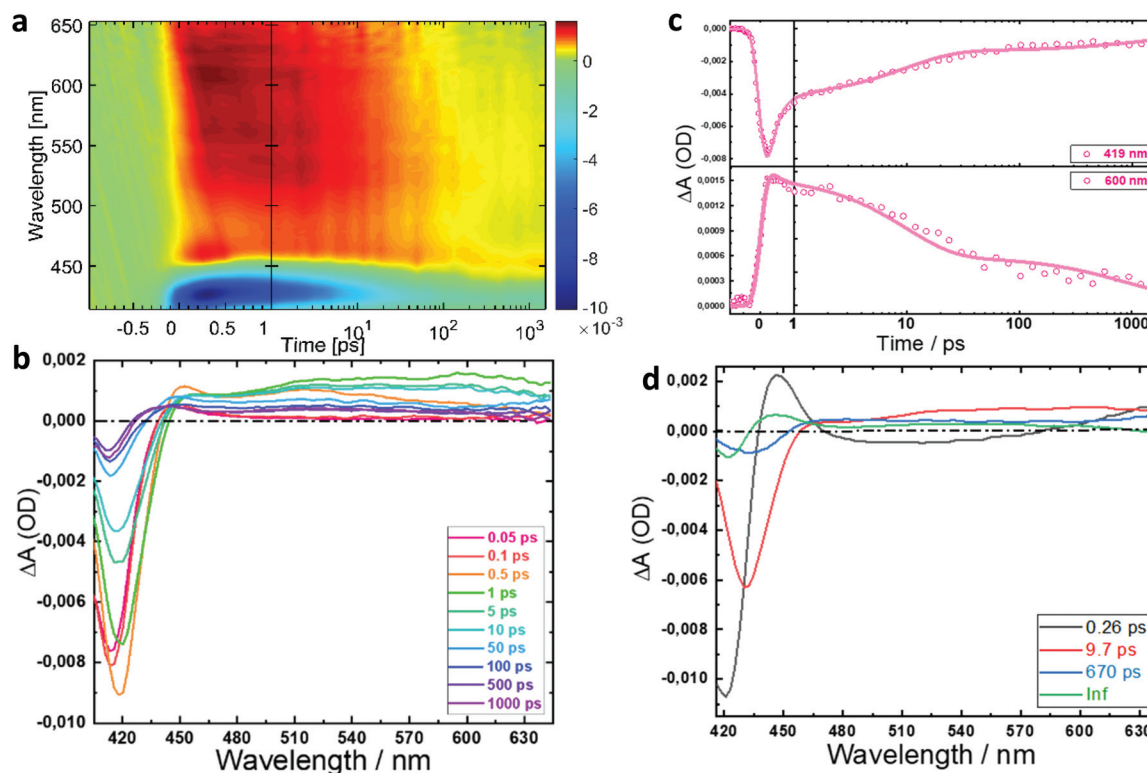


Fig. 3 Transient absorption data for  $(\text{NMA})_2\text{Pb}(\text{Br}_{0.7}\text{I}_{0.3})_4$  thin films excited at 387 nm ( $81 \mu\text{J cm}^{-2}$ ). (a) Wavelength and time dependent TA map. (b) Transient spectra at different time delay times. (c) Kinetic traces at 419 and 600 nm. (d) Decay associated spectra (DAS) from kinetic fitting with three time constants and slow component that does not decay (Inf).

The changes in the absorption spectrum of the sample at different delay times are shown in Fig. 3b. The respective recombination kinetics probed at 419 and 600 nm were plotted in Fig. 3c. The (DAS) is composed of three lifetimes and a long-lived component (inf) (Fig. 3d). It worth noting that the dominant bleach signal due to the lead halide exciton at 417 nm decays fast with  $\tau_1$  of 0.26 ps,  $\tau_2$  of 9.7 ps and  $\tau_3$  of 670 ps. This result is in agreement with the Ema work.<sup>31</sup>

By comparing the TA spectra at different excitation power densities (Fig. S4 and Table S3<sup>†</sup>), it is observed that exciton relaxation times become faster, and the respective amplitudes become larger with increasing pump power. Further, by

increasing the power from 81 to  $162 \mu\text{J cm}^{-2}$ , the exciton relaxation time decreases. Thus, the fast time constants  $\tau_1$  (0.26 ps) and  $\tau_2$  (9.7 ps) have strong contributions to the exciton-exciton annihilation process. The DAS of the time constant  $\tau_1$  also shows a negative amplitude in a spectrally broad range between 450 to 600 nm, and the DAS of the time constant  $\tau_2$  has a negative component at 430 nm, which both is indicative for the rise of triplet-triplet absorption signals of the naphthalene chromophore (Fig. 3d). Therefore, the energy transfer to the organic naphthalene layer is observed in this ultrafast time range. The transient absorption spectrum at the longest experimental delay time is identical with the DAS of the infinity

decay component  $\tau_4$ . This long-lived signal consists of a negative signal at 420 nm (bleach of lead halide based exciton signal) and positive signals at 435 nm (triplet–triplet absorption of naphthalene chromophore<sup>52</sup>) and at 600 nm (triplet–triplet absorption of naphthalene excimer.<sup>52</sup>)

#### Ultrafast dynamics of $(\text{PMA})_2\text{Pb}(\text{Br}_{0.7}\text{I}_{0.3})_4$

In the PMA-based perovskite, the excitonic band is higher in energy than the singlet and triplet excited states of the chromophore.<sup>46,53</sup> The wavelength and time-dependent TA map of PMA perovskite thin film is shown in Fig. 4a. The peak position of the negative signal (blue signal) at 418 nm is in good agreement with the excitonic absorption peak in the steady-state spectrum (Fig. 1c). This can be assigned to the state filling signal contributed by both band-edge electrons and holes. The spectrally broad positive feature in the visible range with a maximum around 575 nm can be assigned to excited singlet state absorption of the PMA chromophore.<sup>40,54</sup> The excited-state absorption appears within about 0.4 ps and does not decay until 1 ns, suggesting a long-lived singlet state. This is in line with the observed long-lived fluorescence decay (biexponential decay with 0.98 ns and 17.1 ns) as shown in Fig. S5 and Table S4.†

The absorption changes of the sample at different delay times are shown in Fig. 4b, and kinetics at selected probe wavelengths (420 nm, 473 nm and 584 nm) are plotted in Fig. 4c. The DAS is composed of three lifetimes and a long-

lived component (inf) (Fig. 4d). The dominant bleach signal due to the lead halide exciton probed at 420 nm decays fast with two time constants ( $\tau_1 = 0.2$  ps and  $\tau_2 = 8.6$  ps).

The comparison of the TA spectra at different excitation power densities shows that carrier relaxation times become faster with increasing power (Fig. S5 and Table S4†). By increasing the power density from 81 to 146  $\mu\text{J cm}^{-2}$ , the carrier relaxation time  $\tau_1$  of 0.36 ps decreases to 0.2 ps and the decay time  $\tau_2$  of 14 ps decreases to 8.6 ps. Moreover, the respective amplitudes of the fast components  $\tau_1$  and  $\tau_2$  are strongly increased. Thus these time constants are assigned to the exciton–exciton annihilation process. The DAS for all decay times lacks a negative amplitude between 450 and 620 nm, which was assigned to the ESA signal of the pyrene singlet state. Thus the energy transfer process from the lead halide based exciton to the organic pyrene layer occurs ultrafast beyond our experimental time resolution. The long-lived excited singlet state of the pyrene chromophore is also seen in the DAS of the time constant  $\tau_3$  and the infinity time constant  $\tau_4$ .

#### Differences between $(\text{NMA})_2\text{Pb}(\text{Br}_{0.7}\text{I}_{0.3})_4$ and $(\text{PMA})_2\text{Pb}(\text{Br}_{0.7}\text{I}_{0.3})_4$ thin films

$(\text{NMA})_2\text{Pb}(\text{Br}_{0.7}\text{I}_{0.3})_4$  triplet state and  $(\text{PMA})_2\text{Pb}(\text{Br}_{0.7}\text{I}_{0.3})_4$  singlet state both are lower in energy than the inorganic lead halide exciton band, yet the transient data monitoring the energy transfer processes exhibit different results. For the NMA chromophore, an ultrafast population time of 0.26 ps

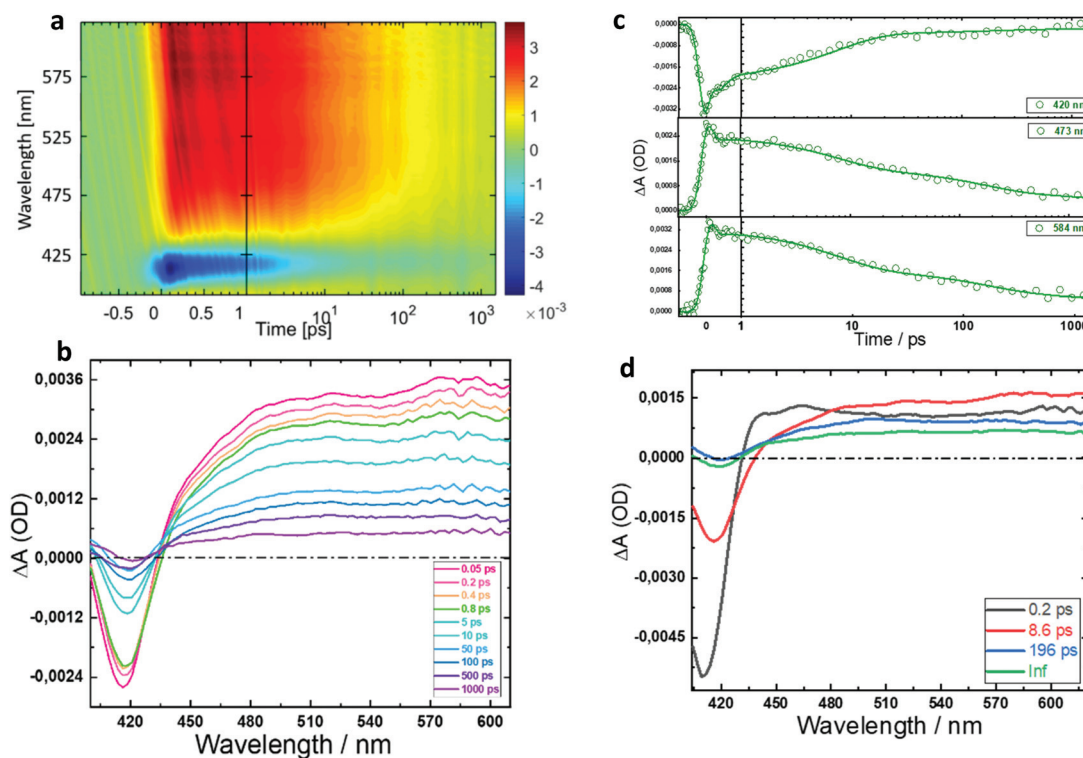


Fig. 4 Transient absorption data for  $(\text{PMA})_2\text{Pb}(\text{Br}_{0.7}\text{I}_{0.3})_4$  thin films excited at 387 nm ( $146 \mu\text{J cm}^{-2}$ ). (a) Wavelength and time dependent TA map. (b) Transient spectra at different time delay times. (c) Kinetic traces at 420 and 584 nm. (d) Decay associated spectra (DAS) from kinetic fitting with three time constants and slow component that does not decay (Inf).

could be resolved (negative amplitude of the respective DAS in the visible range between 450 and 600 nm). On the other hand, a similarly negative amplitude in the DAS of the PMA perovskite is not resolved. Instead, the transient absorption spectrum, which is characteristic for the pyrene singlet state is observed directly after optical excitation and remains to the nanosecond time regime. Therefore, the energy transfer from the lead halide exciton to the organic singlet state occurred faster than the time-resolution of our experiment (about 200 fs). For the PMA chromophore absorption, the negligible spectral overlap with the lead halide excitonic emission spectrum does not support the FRET process as a possible transfer mechanism. FRET is excluded as an explanation also for the energy transfer for the NMA chromophore as the accepting triplet state would be optically forbidden. Instead for both chromophores, a Dexter-type mechanism seems to be more reasonable. This was also discussed before by several research groups on comparable systems<sup>26,33,55</sup> and especially the work of Ema *et al.*,<sup>31</sup> where the energy transfer in dependence of the distance between the chromophore and lead halide layer was studied in detail. Therefore, a correlated two-fold charge transfer (electron and hole) from the lead halide exciton to the organic acceptor chromophore explains the observed ultrafast transfer time. The short methyl spacer between the organic chromophore and the ammonium anchor group to the halide allows for the necessary contact interaction between the 2D exciton in the inorganic layer and the organic chromophores. A recent theoretical study for the perovskite system  $(R-CH_2-NH_3)_2(A)_{n-1}BX_{3n+1}$  investigated the excitonic interaction of lead halide layers separated by organic spacer layers with respect to exciton delocalization.<sup>56</sup> Especially for the case of single lead halide layers ( $n = 1$ ) a very strong delocalization of electron and hole density was calculated, which results in Dexter-type energy transfer processes in the range of a few to tens of femtoseconds. This exciton delocalization effect also enables efficient energy transfer to suitable organic chromophores by this mechanism in the same time-range. Because the Dexter mechanism conserves the spin state, the ultrafast transfer to singlet and triplet states is feasible.

Besides the ultrafast energy transfer dynamics, as summarized in Fig. 5, an excitation density dependent decay is observed for all investigated samples. The samples showed exciton–exciton annihilation in the sub-ps and few-ps range for both chromophores t, which is effective due to the reduced

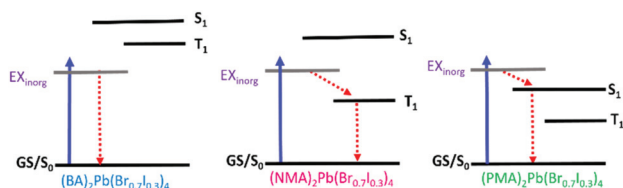


Fig. 5 A schematic representation showing the energy transfer dynamics of  $(BA)_2Pb(Br_{0.7}I_{0.3})_4$ ,  $(NMA)_2Pb(Br_{0.7}I_{0.3})_4$  and  $(PMA)_2Pb(Br_{0.7}I_{0.3})_4$  thin films.

dimensionality of the crystalline structure. These exciton–exciton annihilation processes are non-exponential by nature, which is reflected by the approximated parametrization *via* multi-exponential fit models as seen in the respective DAS<sup>57–59</sup> (Fig. 3 and 4).

## Conclusions

A series of three lead-based mixed-halide perovskites containing BA, NMA, and PMA thin films have been fabricated to study the ultrafast dynamics of energy transfer from the inorganic to the organic layer. The choice of the organic chromophores facilitates the relative energetic alignment of the 2D confined exciton in the lead halide layer with respect to the singlet and triplet states of the organic layer. Femtosecond transient absorption spectroscopy on  $(BA)_2Pb(Br_{0.7}I_{0.3})_4$ ,  $(NMA)_2Pb(Br_{0.7}I_{0.3})_4$ , and  $(PMA)_2Pb(Br_{0.7}I_{0.3})_4$  nanocrystalline thin films in the visible spectral region showed the ultrafast Dexter-type energy transfer path to the organic singlet/triplet states. The presented spectral studies help to understand the interaction of large chromophores with perovskite structures and how it can be optimized for different optoelectronic devices, where the recent interest in 2D and 3D perovskite systems is combined with often complementary demands for the optimization in different applications ranging from LEDs (high emission quantum yield) to solar cells (high charge separation efficiency). The implementation of large organic chromophores with well-defined spacers between the lead halide layer and the organic pi-electron system enables more flexibility in the design of those devices.

## Conflicts of interest

There are no conflicts to declare.

## Acknowledgements

This work has been funded by the German Research Foundation DFG (WA 1850/6-2). M. S. also acknowledges funding from the DFG (GRK 2642). We would like to thank Dr Jörn Plackmeyer for the synthesis of the PMAI and PMABr salts. Profound thanks to Dr Christos Karathanasis for his assistance with the plasma cleaner and Dr Lothar Fink for XRD measurements. Deep thanks to Dr Ahmed A. Farghaly (Argonne National Lab), Dr Ahmed Esmail Shalan (University of the Basque Country), Dr Ahmed M. El-Zohry (Stockholm University), Dr Yasser Hassan (University of Oxford) and Ahmed Gamal Abu-El-soud (Assuit University) for helpful discussions.

## Notes and references

- 1 A. Kojima, K. Teshima, Y. Shirai and T. Miyasaka, *J. Am. Chem. Soc.*, 2009, **131**, 6050–6051.

- 2 NREL, <https://www.nrel.gov/pv/cell-efficiency.html>.
- 3 L. Mao, C. C. Stoumpos and M. G. Kanatzidis, *J. Am. Chem. Soc.*, 2019, **141**, 1171–1190.
- 4 L. N. Quan, M. Yuan, R. Comin, O. Voznyy, E. M. Beauregard, S. Hoogland, A. Buin, A. R. Kirmani, K. Zhao, A. Amassian, D. H. Kim and E. H. Sargent, *J. Am. Chem. Soc.*, 2016, **138**, 2649–2655.
- 5 H. Tsai, W. Nie, J.-C. Blancon, C. C. Stoumpos, R. Asadpour, B. Harutyunyan, A. J. Neukirch, R. Verduzco, J. J. Crochet, S. Tretiak, L. Pedesseau, J. Even, M. A. Alam, G. Gupta, J. Lou, P. M. Ajayan, M. J. Bedzyk, M. G. Kanatzidis and A. D. Mohite, *Nature*, 2016, **536**, 312–316.
- 6 A. G. Ricciardulli, S. Yang, J. H. Smet and M. Saliba, *Nat. Mater.*, 2021, DOI: 10.1038/s41563-021-01029-9.
- 7 A. G. Ricciardulli, B. van der Zee, K. Philipps, G. A. H. Wetzelaer, R.-Q. Png, P. K. H. Ho, L.-L. Chua and P. W. M. Blom, *APL Mater.*, 2020, **8**, 21101.
- 8 J. Hu, L. Yan and W. You, *Adv. Mater.*, 2018, **30**, 1802041.
- 9 H. Cho, S.-H. Jeong, M.-H. Park, Y.-H. Kim, C. Wolf, C.-L. Lee, J. H. Heo, A. Sadhanala, N. Myoung, S. Yoo, S. H. Im, R. H. Friend and T.-W. Lee, *Science*, 2015, **350**, 1222–1225.
- 10 Y. Cao, N. Wang, H. Tian, J. Guo, Y. Wei, H. Chen, Y. Miao, W. Zou, K. Pan, Y. He, H. Cao, Y. Ke, M. Xu, Y. Wang, M. Yang, K. Du, Z. Fu, D. Kong, D. Dai, Y. Jin, G. Li, H. Li, Q. Peng, J. Wang and W. Huang, *Nature*, 2018, **562**, 249–253.
- 11 K. Lin, J. Xing, L. N. Quan, F. P. G. de Arquer, X. Gong, J. Lu, L. Xie, W. Zhao, D. Zhang, C. Yan, W. Li, X. Liu, Y. Lu, J. Kirman, E. H. Sargent, Q. Xiong and Z. Wei, *Nature*, 2018, **562**, 245–248.
- 12 T. Matsushima, S. Hwang, A. S. D. Sandanayaka, C. Qin, S. Terakawa, T. Fujihara, M. Yahiro and C. Adachi, *Adv. Mater.*, 2016, **28**, 10275–10281.
- 13 M. D. Smith, B. A. Connor and H. I. Karunadasa, *Chem. Rev.*, 2019, **119**, 3104–3139.
- 14 X. Qi, Y. Zhang, Q. Ou, S. T. Ha, C.-W. Qiu, H. Zhang, Y.-B. Cheng, Q. Xiong and Q. Bao, *Small*, 2018, **14**, 1800682.
- 15 M. Hirasawa, T. Ishihara and T. Goto, *J. Phys. Soc. Jpn.*, 1994, **63**, 3870–3879.
- 16 G. C. Papavassiliou, I. B. Koutselas, D. J. Lagouvardos, J. Kapoutsis, A. Terzis and G. J. Papaioannou, *Mol. Cryst. Liq. Cryst. Sci. Technol., Sect. A*, 1994, **253**, 103–112.
- 17 G. C. Papavassiliou and I. B. Koutselas, *Synth. Met.*, 1995, **71**, 1713–1714.
- 18 I. B. Koutselas, L. Ducasse and G. C. Papavassiliou, *J. Phys.: Condens. Matter*, 1996, **8**, 1217–1227.
- 19 G. C. Papavassiliou, *Mol. Cryst. Liq. Cryst. Sci. Technol., Sect. A*, 1996, **286**, 231–238.
- 20 I. B. Koutselas, D. B. Mitzi, G. C. Papavassiliou, G. J. Papaioannou and H. Krautscheid, *Synth. Met.*, 1997, **86**, 2171–2172.
- 21 J. Calabrese, N. L. Jones, R. L. Harlow, N. Herron, D. L. Thorn and Y. Wang, *J. Am. Chem. Soc.*, 1991, **113**, 2328–2330.
- 22 D. B. Mitzi, C. A. Feild, W. T. A. Harrison and A. M. Guloy, *Nature*, 1994, **369**, 467–469.
- 23 D. B. Mitzi, S. Wang, C. A. Feild, C. A. Chess and A. M. Guloy, *Science*, 1995, **267**, 1473–1476.
- 24 J. Cho, J. T. DuBose and P. V. Kamat, *J. Phys. Chem. Lett.*, 2020, **11**, 2570–2576.
- 25 M. Era, K. Maeda and T. Tsutsui, *Chem. Phys. Lett.*, 1998, **296**, 417–420.
- 26 M. Braun, W. Tuffentsammer, H. Wachtel and H. C. Wolf, *Chem. Phys. Lett.*, 1999, **303**, 157–164.
- 27 M. Braun, W. Tuffentsammer, H. Wachtel and H. C. Wolf, *Chem. Phys. Lett.*, 1999, **307**, 373–378.
- 28 S. Yang, D. Wu, W. Gong, Q. Huang, H. Zhen, Q. Ling and Z. Lin, *Chem. Sci.*, 2018, **9**, 8975–8981.
- 29 W. T. M. Van Gompel, R. Herckens, K. Van Hecke, B. Ruttens, J. D'Haen, L. Lutsen and D. Vanderzande, *Chem. Commun.*, 2019, **55**, 2481–2484.
- 30 M. C. Gélvez-Rueda, W. T. M. Van Gompel, R. Herckens, L. Lutsen, D. Vanderzande and F. C. Grozema, *J. Phys. Chem. Lett.*, 2020, **11**, 824–830.
- 31 K. Ema, M. Inomata, Y. Kato, H. Kunugita and M. Era, *Phys. Rev. Lett.*, 2008, **100**, 257401.
- 32 D. H. Cao, C. C. Stoumpos, O. K. Farha, J. T. Hupp and M. G. Kanatzidis, *J. Am. Chem. Soc.*, 2015, **137**, 7843–7850.
- 33 C. Qin, T. Matsushima, W. J. Potscavage, A. S. D. Sandanayaka, M. R. Leyden, F. Bencheikh, K. Goushi, F. Mathevet, B. Heinrich, G. Yumoto, Y. Kanemitsu and C. Adachi, *Nat. Photonics*, 2020, **14**, 70–75.
- 34 Z. Xu, D. Lu, F. Liu, H. Lai, X. Wan, X. Zhang, Y. Liu and Y. Chen, *ACS Nano*, 2020, **14**, 4871–4881.
- 35 N. Kitazawa, *Jpn. J. Appl. Phys.*, 1996, **35**, 6202–6207.
- 36 N. Kitazawa, *Mater. Sci. Eng., B*, 1997, **49**, 233–238.
- 37 N. Kitazawa, *Jpn. J. Appl. Phys.*, 1997, **36**, 6876–6879.
- 38 N. Kitazawa, *Jpn. J. Appl. Phys.*, 1997, **36**, 2272–2276.
- 39 J. Cho, J. T. DuBose, A. N. T. Le and P. V. Kamat, *ACS Mater. Lett.*, 2020, **2**, 565–570.
- 40 P. Trojanowski, J. Plötnner, C. Grünwald, F. F. Graupner, C. Slavov, A. J. Reuss, M. Braun, J. W. Engels and J. Wachtveitl, *Phys. Chem. Chem. Phys.*, 2014, **16**, 13875–13888.
- 41 R. Berera, R. van Grondelle and J. T. M. Kennis, *Photosynth. Res.*, 2009, **101**, 105–118.
- 42 C. Slavov, H. Hartmann and J. Wachtveitl, *Anal. Chem.*, 2015, **87**, 2328–2336.
- 43 Y. Tian, Y. Li, B. Chen, R. Lai, S. He, X. Luo, Y. Han, Y. Wei and K. Wu, *J. Phys. Chem. Lett.*, 2020, **11**, 2247–2255.
- 44 X. Wu, M. T. Trinh, D. Niesner, H. Zhu, Z. Norman, J. S. Owen, O. Yaffe, B. J. Kudisch and X.-Y. Zhu, *J. Am. Chem. Soc.*, 2015, **137**, 2089–2096.
- 45 A. G. Crawford, A. D. Dwyer, Z. Liu, A. Steffen, A. Beeby, L.-O. Pålsson, D. J. Tozer and T. B. Marder, *J. Am. Chem. Soc.*, 2011, **133**, 13349–13362.
- 46 T. Takaya, T. Oda, Y. Shibazaki, Y. Hayashi, H. Shimomoto, E. Ihara, Y. Ishibashi, T. Asahi and K. Iwata, *Macromolecules*, 2018, **51**, 5430–5439.

- 47 A. Mokhtari, P. Cong, J. L. Herek and A. H. Zewail, *Nature*, 1990, **348**, 225–227.
- 48 A. H. Zewail, *J. Phys. Chem.*, 1996, **100**, 12701–12724.
- 49 A. H. Zewail, *J. Phys. Chem. A*, 2000, **104**, 5660–5694.
- 50 Y. Han, X. Luo, R. Lai, Y. Li, G. Liang and K. Wu, *J. Phys. Chem. Lett.*, 2019, **10**, 1457–1463.
- 51 P. Avakian and E. Abramson, *J. Chem. Phys.*, 1965, **43**, 821–823.
- 52 X. Wang, W. G. Kofron, S. Kong, C. S. Rajesh, D. A. Modarelli and E. C. Lim, *J. Phys. Chem. A*, 2000, **104**, 1461–1465.
- 53 O. L. J. Gijzeman, W. H. van Leeuwen, J. Langelaar and J. D. W. van Voorst, *Chem. Phys. Lett.*, 1971, **11**, 532–534.
- 54 M. Raytchev, E. Pandurski, I. Buchvarov, C. Modrakowski and T. Fiebig, *J. Phys. Chem. A*, 2003, **107**, 4592–4600.
- 55 H. Hu, D. Zhao, Y. Gao, X. Qiao, T. Salim, B. Chen, E. E. M. Chia, A. C. Grimsdale and Y. M. Lam, *Chem. Mater.*, 2019, **31**, 2597–2602.
- 56 D. Giovanni, S. Ramesh, M. Righetto, J. W. Melvin Lim, Q. Zhang, Y. Wang, S. Ye, Q. Xu, N. Mathews and T. C. Sum, *Nano Lett.*, 2021, **21**, 405–413.
- 57 D. Sun, Y. Rao, G. A. Reider, G. Chen, Y. You, L. Brézin, A. R. Harutyunyan and T. F. Heinz, *Nano Lett.*, 2014, **14**, 5625–5629.
- 58 S. Sim, D. Lee, J. Lee, M. Cha, S. Cha, W. Heo, S. Cho, W. Shim, K. Lee, J. Yoo, R. P. Prasankumar, H. Choi and M.-H. Jo, *Phys. Rev. B*, 2020, **101**, 174309.
- 59 A. Burgos-Caminal, E. Socie, M. E. F. Bouduban and J.-E. Moser, *J. Phys. Chem. Lett.*, 2020, **11**, 7692–7701.

## Supporting Information for

### **Mechanism of Ultrafast Energy Transfer between the Organic-Inorganic Layers in Multiple-Ring Aromatic Spacers for 2D Perovskites**

*Mahmoud M. Elshanawany<sup>1</sup>, Antonio Gaetano Ricciardulli<sup>2</sup>, Michael Saliba<sup>3,4</sup>, Josef Wachtveitl<sup>1</sup> and Markus Braun<sup>1\*</sup>*

- 1- Institute of Physical and Theoretical Chemistry, Goethe University, Frankfurt am Main.
- 2- Institute of Materials Science, Technische Universität Darmstadt.
- 3- Institute of Photovoltaics (ipv), University of Stuttgart, Stuttgart.
- 4- Helmholtz Young Investigator Group FRONTRUNNER, Forschungszentrum Jülich, Jülich.

E-mail: braun@theochem.uni-frankfurt.de



**Preparation of 1-pyrenyl-methylammonium bromide:**

1-Pyrenyl-methylamine were dissolved in the required amount of isopropanol and stirred about 30 min at room temperature. Then hydrobromic (47%) were added in one portion, whereupon the hydrobromide precipitates immediately. There was still 30 min stirred, and the precipitate formed was filtered off, washed with isopropanol and finally with diethyl ether and dried in vacuum.

**Preparation of 1-pyrenyl-methylammonium iodide:**

1-Pyrenylmethylamine were dissolved in the required amount of isopropanol (approx. 40 mL). For a complete solution, about 30 min. be stirred at room temperature. Then 0.183 mL (1.38 mmol) HI (57%) were added in one portion, whereupon the hydroiodide precipitates immediately. (The hydriodic acid was present as a 57% aqueous solution, which was stabilized with 1.5% hypophosphorous acid and was therefore freshly distilled shortly before use. After the distillation, the acid changes colour very quickly due to light and small amounts of dust or the like red-brown.) Another 30 min stirred, and the precipitate formed was filtered off, washed with isopropanol and finally with diethyl ether and dried in vacuum. During all manipulations, care was taken to ensure that there was only a little incidence of light.

SEM, Schemes and XRD spectra of  $(\text{BA})_2\text{Pb}(\text{Br}_{0.7}\text{I}_{0.3})_4$ ,  $(\text{NMA})_2\text{Pb}(\text{Br}_{0.7}\text{I}_{0.3})_4$  and  $(\text{PMA})_2\text{Pb}(\text{Br}_{0.7}\text{I}_{0.3})_4$  thin films:

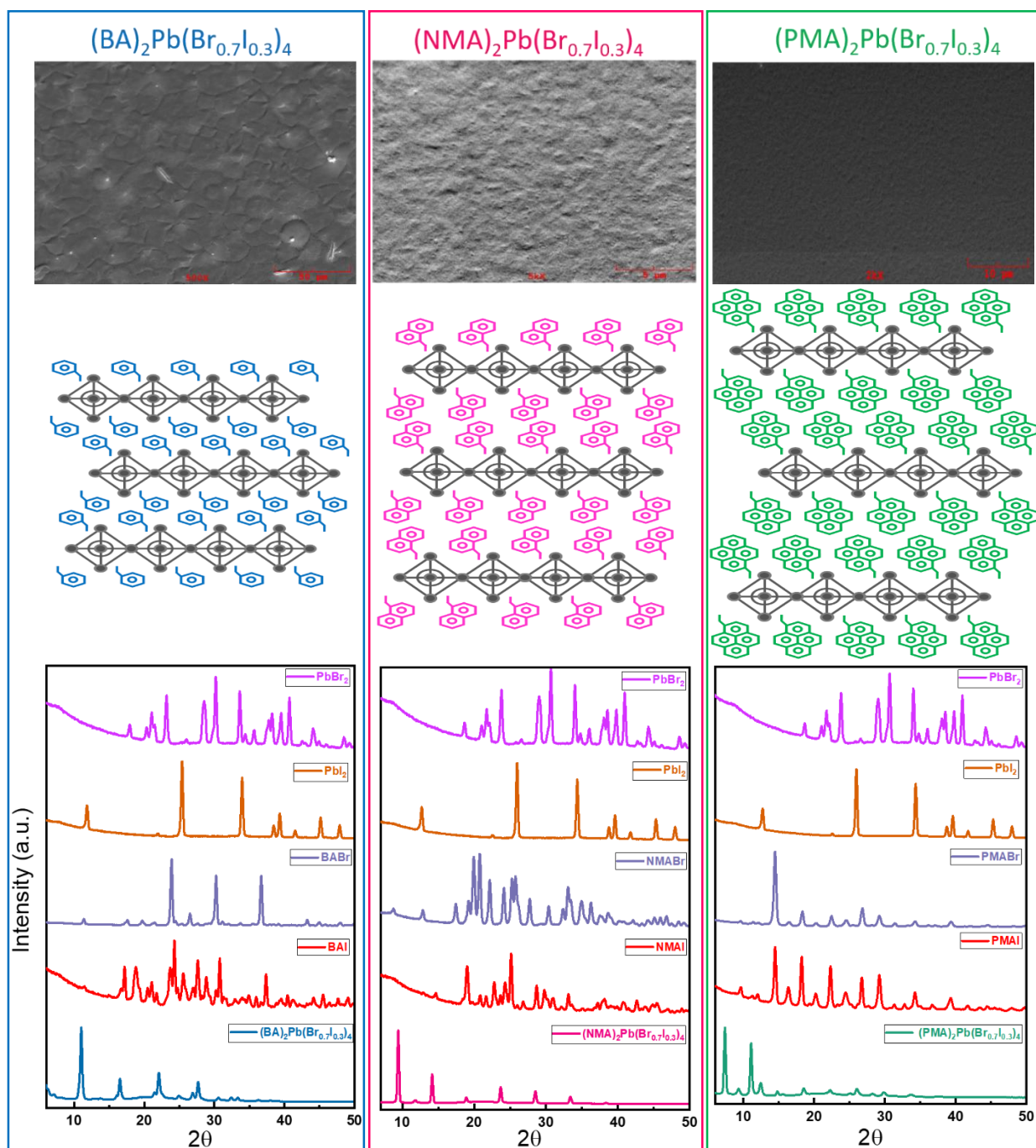


**Fig. S1** Scanning-electron Microscope images of all films. XRD patterns of  $\text{PbBr}_2$  and  $\text{PbI}_2$  powders (the same for all samples). Benzylammonium bromide, benzylammonium iodide powders, and  $(\text{BA})_2\text{Pb}(\text{Br}_{0.7}\text{I}_{0.3})_4$  film in the left panel; 1-naphthylmethylammonium bromide, 1-naphthylmethylammonium iodide powders, and  $(\text{NMA})_2\text{Pb}(\text{Br}_{0.7}\text{I}_{0.3})_4$  film in the middle panel; 1-pyrenemethylammonium bromide and 1-pyrenemethylammonium iodide powders and  $(\text{PMA})_2\text{Pb}(\text{Br}_{0.7}\text{I}_{0.3})_4$  film in the right panel. All powders exposed in ambient air.

## TCSPC measurements:

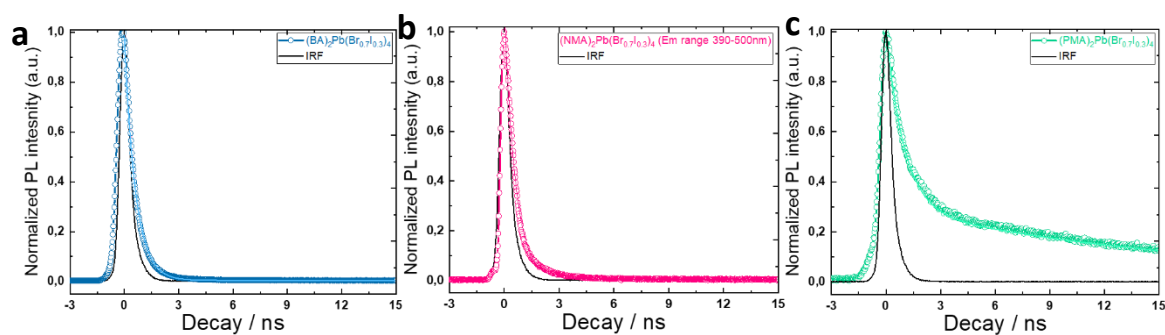


**Fig. S2** Photoluminescence (PL) decay of (a)  $(\text{BA})_2\text{Pb}(\text{Br}_{0.7}\text{I}_{0.3})_4$ , (b)  $(\text{NMA})_2\text{Pb}(\text{Br}_{0.7}\text{I}_{0.3})_4$  and (c)  $(\text{PMA})_2\text{Pb}(\text{Br}_{0.7}\text{I}_{0.3})_4$  thin films deposited on quartz substrates with excitation at 320 nm at room temperature measured by TCSPC.

Table S1. Photoluminescence (PL) decay time coefficients of all samples. Values in parentheses give the relative amplitude.

Films	$\tau_1$ (ns) ( $A_1$ )	$\tau_2$ (ns) ( $A_2$ )
$(\text{BA})_2\text{Pb}(\text{Br}_{0.7}\text{I}_{0.3})_4$	0.61 (100%)	
$(\text{NMA})_2\text{Pb}(\text{Br}_{0.7}\text{I}_{0.3})_4$ (390-500 nm)	0.60 (100%)	
$(\text{PMA})_2\text{Pb}(\text{Br}_{0.7}\text{I}_{0.3})_4$	0.98 (72%)	17.1 (28%)

### Excitation density-dependent measurements:

OPTIMUS ([www.optimusfit.org](http://www.optimusfit.org)) has been used to perform the global lifetime analysis for these measurements<sup>1</sup>. The samples were pumped by 387 nm and probed by a white-light continuum to reveal the transient changes in absorption ( $\Delta A$ ). The samples were measured at room temperature.

For  $(\text{BA})_2\text{Pb}(\text{Br}_{0.7}\text{I}_{0.3})_4$ , a bi-exponential decay function was sufficient to obtain a satisfactory global fit between 400 and 650 nm. In Fig. S3, the bleach signal of the lead halide-based exciton bleach at 404 nm is shown, exemplarily.

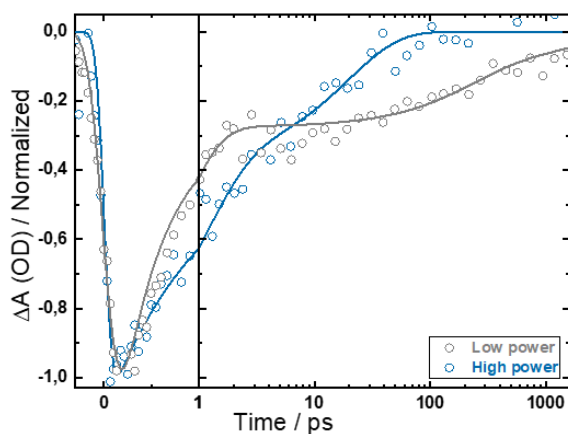


**Fig. S3**  $(\text{BA})_2\text{Pb}(\text{Br}_{0.7}\text{I}_{0.3})_4$  kinetic traces excited by 387 nm and probed at 404 nm at two different pump pulse energies.

Table S2. Time constants in ps resulting from the global fit analysis for different excitation densities of  $(\text{BA})_2\text{Pb}(\text{Br}_{0.7}\text{I}_{0.3})_4$  probed at 404 nm.

Power ( $\mu\text{J}/\text{cm}^2$ )	$\tau_1$ (ps) ( $A_1$ )	$\tau_2$ (ps) ( $A_2$ )
146	1 (70 %)	32 (30%)
81	0.52 (70%)	506 (30%)

For  $(\text{NMA})_2\text{Pb}(\text{Br}_{0.7}\text{I}_{0.3})_4$ , a tri-exponential decay function and signal offset ( $\tau_4 = \text{infinity}$ ) was required to obtain a satisfactory global fit between 400 and 650 nm. In Fig S4, the bleach signal of the lead halide-based exciton bleach at 419 nm is shown, exemplarily.

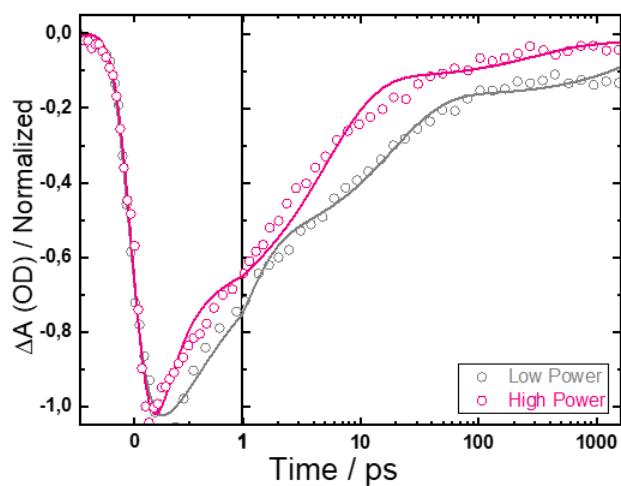


**Fig. S4**  $(\text{NMA})_2\text{Pb}(\text{Br}_{0.7}\text{I}_{0.3})_4$  kinetic traces excited by 387 nm and probed at 419 nm at two different pump pulse energies.

Table S3. Time constants in ps resulting from the global fit analysis for different excitation densities of  $(\text{NMA})_2\text{Pb}(\text{Br}_{0.7}\text{I}_{0.3})_4$ .

Power ( $\mu\text{J}/\text{cm}^2$ )	$\tau_1$ (ps) ( $A_1$ )	$\tau_2$ (ps) ( $A_2$ )	$\tau_3$ (ps) ( $A_3$ )	$\tau_4$ (ps)
162	0.20 (30%)	5 (48%)	288 (15%)	Infinity (7%)
81	0.26 (27%)	9.7 (48%)	670 (13%)	Infinity (12%)

For  $(\text{PMA})_2\text{Pb}(\text{Br}_{0.7}\text{I}_{0.3})_4$ , a tri-exponential decay function and signal offset ( $\tau_4 = \text{infinity}$ ) was required to obtain a satisfactory global fit between 400 and 650 nm. In Fig. S5, the bleach signal of the lead halide-based exciton bleach at 418 nm is shown, exemplarily.

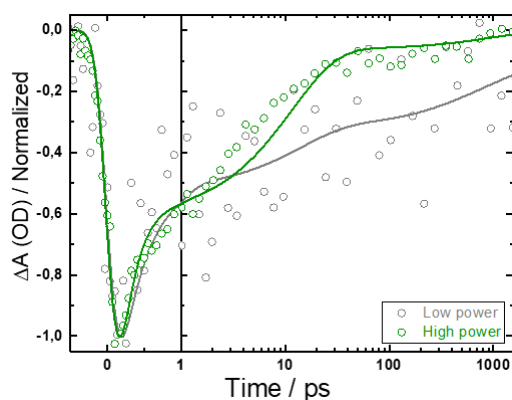


**Fig. S5**  $(\text{PMA})_2\text{Pb}(\text{Br}_{0.7}\text{I}_{0.3})_4$  kinetic traces excited by 387 nm and probed at 418 nm at two different pump pulse energies.

Table S4. Time constants in ps resulting from the global fit analysis for different excitation densities of  $(\text{PMA})_2\text{Pb}(\text{Br}_{0.7}\text{I}_{0.3})_4$ .

Power ( $\mu\text{J}/\text{cm}^2$ )	$\tau_1$ (ps)	$\tau_2$ (ps)	$\tau_3$ (ps)	$\tau_4$ (ps)
146	0.2 (40%)	8.6 (45%)	196 (10%)	Infinity (5%)
81	0.36 (40%)	14 (25%)	500 (19%)	Infinity (17%)

## SI References

- (1) Slavov, C.; Hartmann, H.; Wachtveitl, J. Implementation and Evaluation of Data Analysis Strategies for Time-Resolved Optical Spectroscopy. *Anal. Chem.* **2015**, *87* (4), 2328–2336. <https://doi.org/10.1021/ac504348h>.

### 7.3 Elshanawany et al., *ACS.JPCC* 2022, 126

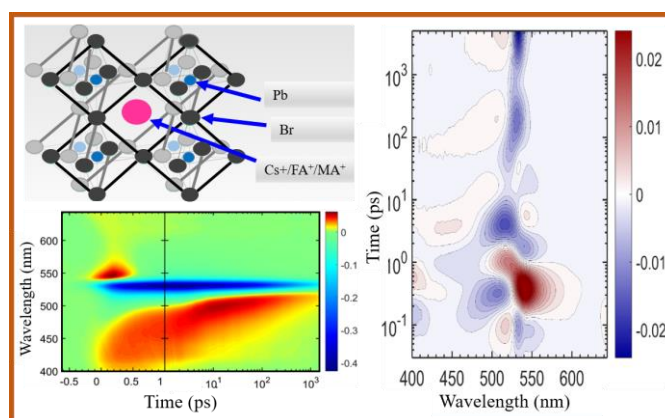
**Mahmoud M. Elshanawany**, Antonio Gaetano Ricciardulli, Jose J. Jeronimo-Rendon, Michael Saliba, Josef Wachtveitl and Markus Braun\*

*J. Phys. Chem. C* **2022**, 126, 20, 8787–8793

**Publication Date:** May 17, 2022

**DOI:** 10.1021/acs.jpcc.2c02682

Reprinted with permission from the American Chemical Society



# Ultrafast Carrier Dynamics in Wide Band Gap Mixed-Cation Perovskites: Influence of the Cs Cation

Mahmoud M. Elshanawany, Antonio Gaetano Ricciardulli, Jose J. Jeronimo-Rendon, Michael Saliba, Josef Wachtveitl, and Markus Braun\*



Cite This: *J. Phys. Chem. C* 2022, 126, 8787–8793



Read Online

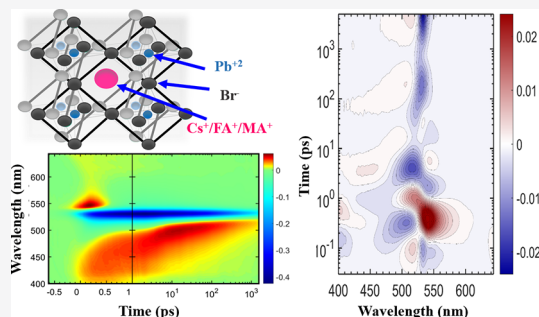
ACCESS |

Metrics & More

Article Recommendations

Supporting Information

**ABSTRACT:** Mixed-cation perovskites exhibit outstanding performance as next-generation solar cells and for optoelectronic applications. One pathway to increase the quality and stability of these materials is adding Cs to the A-site of mixed-cation formamidinium/methylammonium in the perovskite  $\text{APbX}_3$ . Here, we use femtosecond transient absorption spectroscopy to study the effect of Cs on the dynamics of a mixed-cation wide band gap bromide-based perovskite. Negligible changes in the optical spectra are observed between the two films, indicating a similar localization of the charge carriers at the band edge. However, adding Cs reduces the non-radiative recombination sites and increases the lifetime of the photogenerated charge carriers in the perovskite film (from 291 to 355 ns). Furthermore, the Cs cation slows down the cooling of hot carriers through an efficient hot-phonon bottleneck, which is observed by increasing the excitation power from 9.7 to 648  $\mu\text{J}/\text{cm}^2$  [the lifetime of the fast component ( $\tau_1$ ) increases from 0.21 to 0.91 ps]. Understanding the mechanism of charge dynamics in perovskite thin films is critical for the fabrication of high-performance devices.



## INTRODUCTION

Hybrid organic–inorganic lead halide perovskite solar cells (PSCs) have attracted much attention over the past 10 years as a pre-eminent candidate for the next generation of solar cells (SCs) due to their excellent optoelectronic properties, simple fabrication, and low-cost processing.<sup>1–3</sup> The possibility of changing the cation A, metal B, or halide X in the perovskite structure ( $\text{ABX}_3$ ) opened many opportunities for novel material synthesis with power conversion efficiencies of more than 25%<sup>1,2</sup> using  $\text{FAPbI}_3$ -rich perovskites with a band gap close to 1.5 eV.

A is a monovalent cation such as methylammonium ( $\text{MA}^+$ ), formamidinium ( $\text{FA}^+$ ), or the inorganic cation  $\text{Cs}^+$ , B is a divalent metal cation such as lead ( $\text{Pb}^{2+}$ ) or tin ( $\text{Sn}^{2+}$ ), and X is a halide anion ( $\text{Cl}^-$ ,  $\text{Br}^-$ , and  $\text{I}^-$ ). Triple cation PSCs with a Cs/FA/MA mixture at the A-site exhibit promising results toward an efficient and stable SC.<sup>4–8</sup> In addition, Cs/FA/MA perovskites show high efficiencies,<sup>2,9</sup> thermal stability,<sup>10,11</sup> improved stability against humidity,<sup>12,13</sup> increased reproducibility, and decreased trap state formation.<sup>14</sup> Replacing iodide with bromide leads to perovskite materials with increased stability against air, but it is less efficient for single-junction SCs due to its high band gap  $>1.8$  eV.<sup>8,15–17</sup> As wide band gap semiconductors, bromide-based perovskites offer promising possibilities for optoelectronic applications such as sensors, water splitters, light-emitting diodes (LEDs), and multi-junction high-performance SCs.<sup>7,17–20</sup>

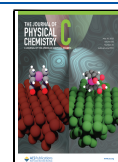
Much effort has been made to understand the dynamics of the single-cation perovskite photophysics using ultrafast transient absorption spectroscopy (TAS).<sup>14,21–27</sup> TAS is a powerful technique to visualize carrier excitation, recombination, relaxation, and energy transfer on a subpicosecond time scale.<sup>28–31</sup> Ghosh et al. reported the separation time of the initial photo-excited excitons into free charge carriers (20 fs) by performing a 10 fs resolution experiment,<sup>32</sup> which is followed by charge carrier thermalization (sub-100 fs time range).<sup>32</sup> Polaron formation occurs between 0.3 and 0.7 ps depending on the used cations (0.3 ps in the case of  $\text{MAPbBr}_3$  and 0.7 ps in  $\text{CsPbBr}_3$ ).<sup>33</sup> The time constant for subsequent carrier cooling was determined to be 230 fs for low carrier densities, which is slowed down to 770 fs for higher carrier densities.<sup>25</sup> This behavior is attributed to a hot-phonon bottleneck effect. Later signal decay extending to the nanosecond time scale obeys second-order kinetics due to charge recombination.<sup>21</sup>

Typically, charge carrier extraction in SCs is assisted by electron or hole transport layers. Reducing recombination

Received: April 19, 2022

Revised: April 29, 2022

Published: May 17, 2022





losses before carrier extraction is critical for enhancing the efficiency of perovskite SCs.<sup>34</sup> Recently, some dynamics studies on mixed-cation halide perovskite have been reported.<sup>35–43</sup> However, the role of Cs in FA/MA hybrid perovskite has received less attention so far.

In this work, we used time-resolved spectroscopic techniques [steady-state spectroscopy, time-resolved emission, and ultrafast femtosecond TAS (fs-TAS)] to study the excited-state dynamics of  $\text{FA}_{0.83}\text{MA}_{0.17}\text{PbBr}_3$  with or without 5% Cs to elucidate the underlying mechanism and relaxation pathways.

## EXPERIMENTAL SECTION

The one-step spin-coating method was applied to fabricate thin films of microcrystalline  $\text{FA}_{0.83}\text{MA}_{0.17}\text{PbBr}_3$  and  $\text{Cs}_{0.05}(\text{FA}_{0.83}\text{MA}_{0.17})_{0.95}\text{PbBr}_3$  on a glass substrate as reported elsewhere.<sup>7,44</sup> For the sake of simplicity, we will name these perovskite samples as FA/MA and Cs/FA/MA films in the following.

**Materials.** The chemicals used to fabricate perovskite films are commercially available from the specified suppliers. *N,N*-dimethylformamide (DMF), dimethyl sulfoxide (DMSO), and anisole were purchased from Acros Organics. Caesium bromide (CsBr, ultradry (99.998%)) was bought from abcr GmbH. Formamidinium bromide (FABr) and methylammonium bromide (MABr) were purchased from Greatcell solar. Lead bromide ( $\text{PbBr}_2$ ) was bought from Tokyo Chemical Industry (TCI) Co.

**Preparation of Perovskite Thin Films.** The perovskite films of Cs/FA/MA and FA/MA lead bromide were prepared by spin coating via the antisolvent method on glass substrates. First, glass substrates were cleaned in 2% Hellmanex deionized water solution with the assistance of an ultrasonic bath. Subsequently, the substrates were further cleaned with acetone, 2-propanol, and UV ozone treatment for 15 min. The perovskite solution was prepared following a triple cation process.<sup>44</sup> The  $\text{FAPbBr}_3$  precursor solution was prepared by dissolving FABr and  $\text{PbBr}_2$  (molar ratio 1:1.1) in anhydrous DMF/DMSO 4:1 (v/v). In contrast,  $\text{MAPbBr}_3$  solution was prepared by dissolving the precursors, MABr (1 M) and  $\text{PbBr}_2$  (1.1 M), dissolved in the DMF/DMSO solvent mixture. Furthermore, the double cation perovskite (FA/MA) was prepared by mixing the solutions of  $\text{FAPbBr}_3$  and  $\text{MAPbBr}_3$ , respectively, with an 83:17 volume ratio. To obtain the triple cation perovskite, 5 vol % solution of the inorganic salt CsBr (1.5 M) in DMSO was added to the double cation perovskite precursor.<sup>8</sup> Finally, 100  $\mu\text{L}$  of the perovskite solution was deposited using spin coating in one step (30 s at 3000 rpm and 2000 rpm/s). Ten seconds before the end of the process, 200  $\mu\text{L}$  of anisole, an antisolvent, was poured on the spinning substrate. Then, the substrates were annealed at 100 °C for 45 min. The entire process was carried out in a nitrogen-filled glovebox. As shown in Figures S1 and S2, the X-ray diffraction (XRD) spectra and scanning electron microscopy (SEM) images of both films exhibit high crystallinity and morphology of these films, respectively.

**Steady-State Spectroscopy.** Absorption spectra of the spin-coated films on a glass substrate (thickness 1 mm) were recorded with the SPECORD S600 UV/vis spectrophotometer (Analytik Jena, Jena, Germany). PL spectra were collected with an FP-8500 spectrofluorometer (Jasco, Groß-Umstadt, Germany). The excitation wavelength was 362 nm with a bandwidth of 5 nm. For additional spectral cleaning, we applied a UV band-pass filter between 280 and 370 nm

(UG11, Schott Glas) for the excitation path and a long pass filter at 360 nm (WG360, Schott Glas) for the emission path, respectively. The PMT voltage was set to 650 V. The wavelength-dependent instrument sensitivity and the baseline were corrected routinely. All measurements were performed at room temperature under ambient conditions.

**Time-Correlated Single-Photon Counting.** We used our home-built time-correlated single-photon counting (TCSPC) setup with a counting card for recording time-resolved PL data.<sup>45,46</sup> Briefly, the thin films were excited using a mode-locked titanium-doped sapphire (Ti/Sa) laser (Tsunami 3941-X3BB, Spectra-Physics, Darmstadt, Germany), which was pumped by a 8 W continuous wave diode pumped solid-state laser (Millennia eV, Spectra-Physics, 532 nm). The Ti/Sa laser allowed the tuning of the excitation wavelength to 775 nm with a pulse width of 100 fs at a repetition rate of 80 MHz. The acoustooptic modulator assisted to reduce the repetition rate to 160 kHz. The excitation wavelength of 387 nm was obtained by second harmonic generation (SHG) in a BBO crystal (frequency doubler and pulse selector, model 3980, Spectra-Physics). We used excitation filters (UG11, BG38, Schott AG, Mainz, Germany) to block remaining fundamental light from the SHG excitation pulses. The instrument response function (IRF, FWHM 200 ps) was obtained without emission filters using an empty glass substrate as a scattering sample. A photomultiplier tube (PMT, PMA-C 182-M, PicoQuant, Berlin, Germany) and a TimeHarp 260 PICO Single PCIe card (PicoQuant) were used for single-photon detection (channel width adjusted to 400 ps). Long-pass filters at 400 and 470 nm were inserted routinely to block stray light from the excitation pulses for both samples.

**Femtosecond Transient Absorption Spectroscopy Measurements.** We used fs-TAS to investigate the ultrafast excited-state dynamics and the recombination processes in the mixed cation perovskite systems using a home-built pump–probe setup.<sup>47</sup> Briefly, the excitation pump pulses were applied at a central wavelength of 387 nm (SHG of the laser fundamental). The pulsed laser system was running at 775 nm central wavelength and 1 kHz repetition rate (Clark-MXR, Dexter, MI, USA) with a pulse duration of 150 fs. The excitation power was adjusted between 9.7 and 648  $\mu\text{J cm}^{-2}$  at the sample position. The probe white light covering a spectral range of 400–645 nm was generated by focusing a part of the laser fundamental onto a 5 mm thick calcium fluoride crystal. The white light was transmitted through the sample and subsequently detected via an HR320 spectrograph (Horiba, Kyoto, Japan). The detection system consists of a signal-processing chip (S8865-128) with 128 channel photodiode arrays (PDA), a C9118 driver circuit (Hamamatsu Photonics), and a data acquisition card that digitizes the analogue PDA signals at 16 bits (National Instruments, NI6120). The sample was continuously moved in the plane perpendicular to the direction of probe pulse propagation. The measurements for both samples were performed at room temperature under ambient conditions.

Data evaluation of the transient absorption data was performed by the software package Optimus.<sup>48</sup> The data sets were fitted via a GLA to a multiexponential model with decay times  $\tau_i$  and related decay-associated spectra (DAS). Additionally, the data sets were converted by a model-free method, the so-called lifetime density analysis (LDA), which is a numerical variant of the Laplace transformation.

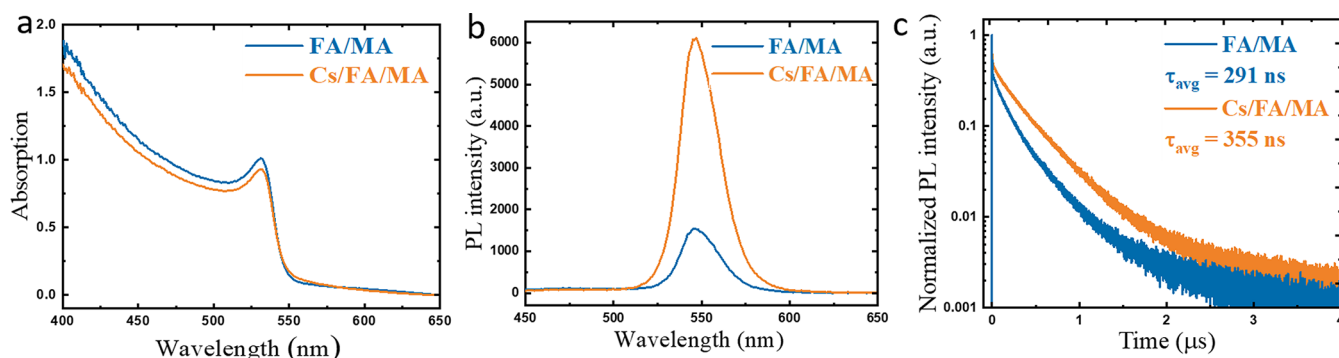


**Figure 1.** (a) Steady-state absorption, (b) steady-state photoluminescence (PL) spectra with optical excitation at 362 nm, and (c) time-resolved (PL) decay with optical excitation at 387 nm of FA/MA (blue) and Cs/FA/MA (orange) thin films deposited on glass substrates at room temperature.

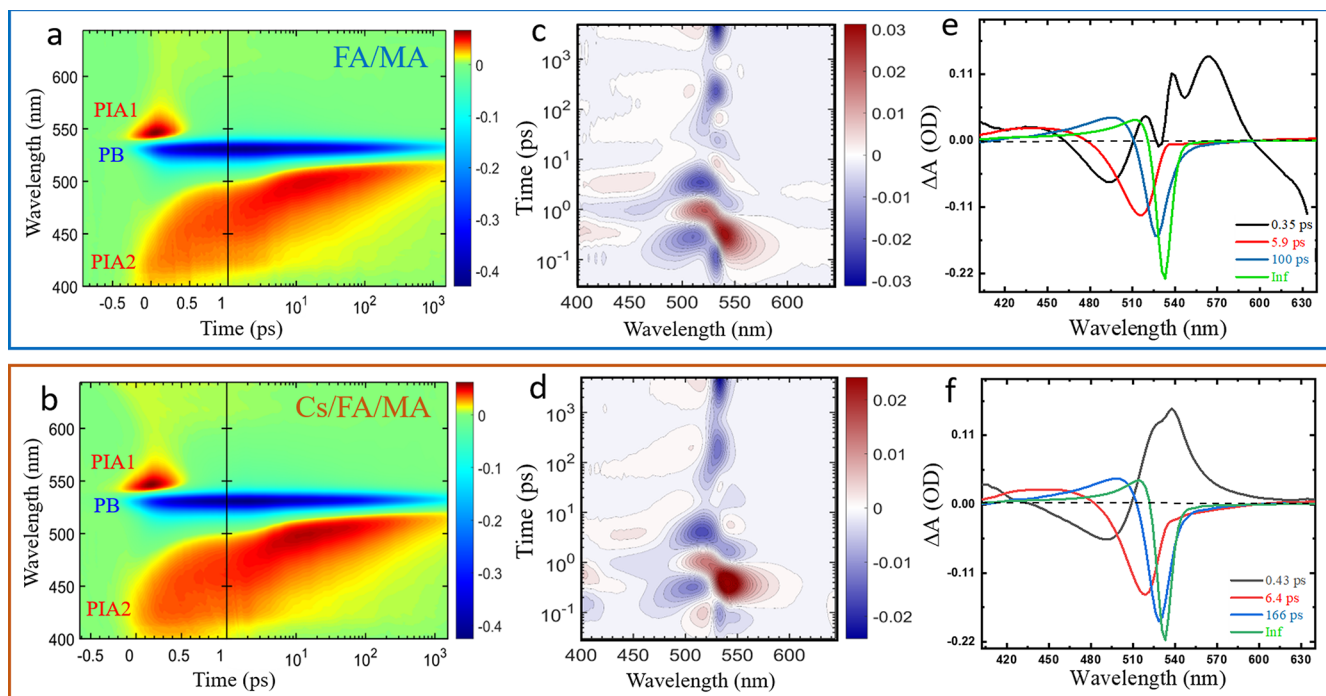


**Figure 2.** (a,b) Wavelength and time-dependent TA map of FA/MA (upper panel) and Cs/FA/MA (lower panel) films, (c,d) corresponding lifetime density maps (LDM) obtained from the lifetime distribution analysis of the TA data displayed in (a,b). (e,f) Decay-associated spectra (DAS) from a global lifetime analysis (GLA) to a sequential model with three exponential decay components and a remaining spectrum at the end of the experimental time window (inf). Both films were excited with a laser pulse of 387 nm and a fluence of  $324 \mu\text{J cm}^{-2}$ .

## RESULTS AND DISCUSSION

Here, we present the optical properties of the spin-coated  $\text{FA}_{0.83}\text{MA}_{0.17}\text{PbBr}_3$  thin films with and without 5% Cs on a glass substrate. As shown in Figure 1a, the absorption spectra of both samples are identical. Both compositions show a broad continuum with a sharp absorption peak at 532 nm (2.33 eV), the excitonic absorption of the materials. The emission spectra of both films have a maximum at 546 nm (2.2 eV), but the addition of Cs enhances the PL intensity by a factor of four (shown in Figure 1b), which indicates a reduction of the non-radiative recombination sites in the perovskite film. Moreover, we investigated the dynamics of the charge carrier relaxation by time-resolved PL with the TCSPC method. As shown in Figure 1c, the Cs/FA/MA film has a longer average lifetime (355 ns) than the FA/MA film (291 ns), which is also in agreement with fewer non-radiative recombination channels and a reduced trap density in the triple cation sample.

A closer look is taken at the photophysics of both thin films using fs-TAS after photoexcitation at 387 nm and in a probing spectral region between 400 and 645 nm. Both samples showed transient spectral features similar to those reported in previously published work.<sup>36,49</sup>

The TAS results of both thin films excited with an excitation density of  $324 \mu\text{J}/\text{cm}^2$  are shown in Figure 2. The wavelength and time-dependent TA maps are shown in Figure 2a for the FA/MA film and Figure 2b for the Cs/FA/MA film. In both samples, the photobleaching (PB) of the excitonic ground-state absorption centered at 532 nm (2.33 eV) is observed in accordance with the steady-state absorption spectrum. Slightly red-shifted to this signal a photoinduced absorption (PIA1) signal is observed at 539 nm (2.30 eV) for early delay times. This is related to a transient Stark shift of the excitonic transition due to charge carriers, after exciton dissociation. In the spectral range between 400 and 520 nm, a photoinduced

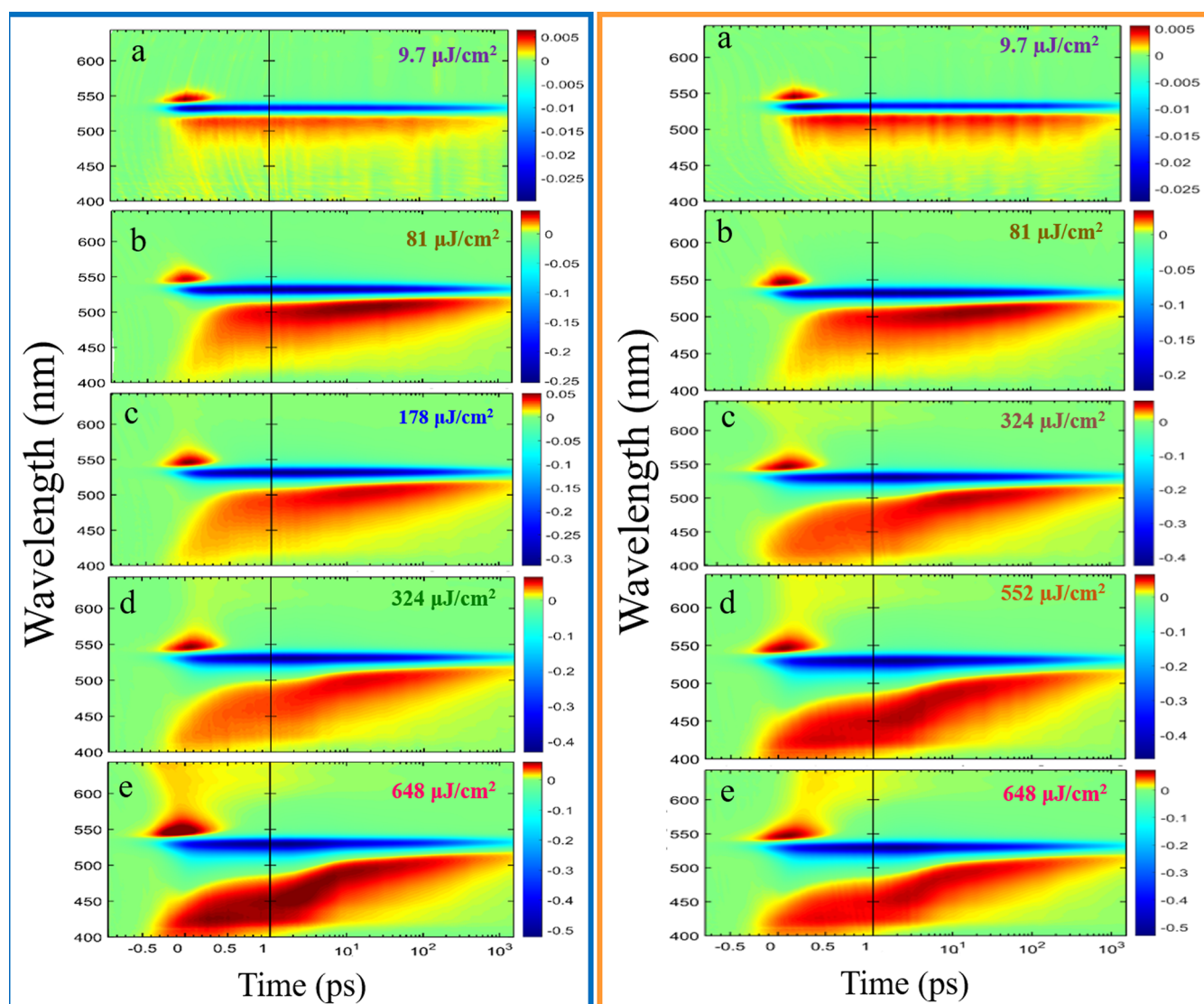


**Figure 3.** TA measurement on the FA/MA film up to 1.5 ns at (a) 9.7, (b) 81, (c) 178, (d) 324, and (e) 648  $\mu\text{J}/\text{cm}^2$  for different excitation powers (left panel). TA measurement on the Cs/FA/MA film at (a) 9.7, (b) 81, (c) 324, (d) 552, and (e) 648  $\mu\text{J}/\text{cm}^2$  for different excitation powers up to 1.5 ns (right panel). Both films were excited by optical pump pulses at 387 nm. A quantitative evaluation of these datasets was done by GLA and is presented in Tables S1 and S2. An evaluation of these data sets by LDA is presented in Figure S7.

absorption (PIA2) signal with a non-exponential dynamic spectral shift is monitored, which can be assigned to the relaxation of free charge carriers. The origin of this signal was first ascribed to intraband transitions,<sup>50</sup> but a recent study, which combined transient absorption with transient reflectance data, attributed this signal to increased sample reflectivity due to a photoinduced change of the refractive index.<sup>25</sup>

The LDMs of both samples are shown in Figure 2c (FA/MA film) and Figure 2d (Cs/FA/MA film) (see also Figure S7 for all powers). The positive LDM signal at 539 nm (PIA1) assigns a decay time of 0.2 ps to the PIA1 signal decay. At a wavelength of 532 nm (PB), the LDM plot shows an extended negative range between 5 ps and 3 ns. This illustrates that the PB signal of the samples decays via non-exponential decay kinetics. In the spectral range between 400 and 520 nm (PIA2), several tilted negative and positive areas are seen in the LDM plot between 1 and 100 ps. This shows that the PIA2 signal decays non-exponentially combined with a transient spectral shift from 400 to 520 nm.

In the following, the transient data set will be parametrized by a set of exponential decay components. This GLA<sup>48</sup> of the transient data yields DAS related to three lifetimes, and an infinity lifetime accounts for the transient spectrum at the end of our experimental time window [Figure 2e (FA/MA film) and Figure 2f (Cs/FA/MA film)]. The long-lived positive signal (PIA 2) in the region from 400 to 520 nm shows a dynamic red shift, which is assigned to the cooling of free charge carriers. The negative PB signal at 532 nm is assigned to the band-filling effect.<sup>51</sup> The stimulated emission and PB are possibly overlapped in the same transient feature. In the region from 540 to 580 nm, there is a positive feature (PIA1), below the band gap energy only at short delay times (<1 ps). It was also observed in single-cation perovskites such as MAPbI<sub>3</sub> and was associated with band gap renormalization (BGR) and transient electroabsorption (Stark effect).<sup>25,36,49–51</sup>

By performing experiments with different excitation power densities in both films, a clear pump power dependence is seen (Figure 3). For high pump powers, we observe a strong blue shift (up to 420 nm) and a broadening of the PIA2 signal at

early delay times, which red-shifts for longer delay times to 520 nm and becomes spectrally narrow. However, for very low pump power, the PIA2 signal appears at early delay times at 520 nm and remains spectrally unchanged also for longer delay times. This indicates that the PIA2 signal is a sensitive indicator for the density and thermal distribution of charge carriers in the thin film.<sup>52</sup> In the FA/MA film, by increasing the power from 9.7 to 648  $\mu\text{J}/\text{cm}^2$ , the slowest carrier relaxation time ( $\tau_3$ ) decreases from 500 to 85 ps, respectively [Figure 3 and Table S1 (Supporting Information)]. The excitation power dependence is directly correlated with the exciton density in the sample. In the Cs/FA/MA film, by increasing the power from 9.7 to 648  $\mu\text{J}/\text{cm}^2$ , the carrier relaxation time ( $\tau_3$ ) decreases from 905 to 124 ps, and the cooling process of the fast component ( $\tau_1$ ) is directly affected by the phonon bottleneck, which slows down the cooling of charge carriers with increasing carrier density.<sup>22,25,26</sup> This phenomenon is observed as well in the FA/MA film with shorter lifetimes (see Figure 3 and Table S2).

Therefore, the fast component  $\tau_1$  is compatible with polaron formation.<sup>33</sup> In the case of Cs, increasing the excitation power delays the polaron formation from 0.21 to 0.91 ps; however, in the case of absence of Cs, it delays the polaron formation from 0.2 to 0.84 ps. This excitation density-dependent slowdown in the polaron formation time ( $\tau_1$ ) together with the increase in the decay rate ( $\tau_2$  and  $\tau_3$ ) is an indication for the phonon bottleneck.<sup>22</sup> For the perovskite film with an addition of 5% Cs, this effect is slightly enhanced.

Considering the striking linearity of  $\Delta A^{-1}$  as a function of time for the PB signal (532 nm) for all excitation densities, we could conclude that the recombination mechanism occurs via second-order kinetics. This non-exponential mechanism is approximated in the GLA mainly by the second ( $\tau_2$ ) and third time constant ( $\tau_3$ ) (see Supporting Information, Figures S4 and S6).<sup>21</sup> The fourth time constant ( $\tau_4$ ) for the slowest component, which does not decay in our experimental time window (1.5 ns), is likely due to non-geminate recombination. For a stable fitting process of the data sets, it was set to infinity value.

In a former study, adding 5% of Cs to the perovskite material enabled a relative improvement of 17% in power conversion efficiency (PCE) (16.3 to 19.2%).<sup>7</sup> The present study shows that the main characteristics of ultrafast charge carrier dynamics exhibit only slight changes between the perovskite material with and without addition of Cs. However, the higher fluorescence signal is a clear indication for reduced trap state density. Our observation of the increase in the fluorescence lifetime from 291 to 355 ns after addition of 5% Cs to the perovskite corresponds to a relative increase in the lifetime of 18%. This coincides with the improvement in device performance, mentioned above. This unusual long fluorescence lifetime in the microsecond time range monitors the diffusion of screened charge carriers (polarons) in the perovskite film. If this perovskite material is incorporated in a photovoltaic device between hole- or electron-extracting layers in a typical sandwich geometry, the enlarged charge carrier lifetime would directly improve device performance. The incorporation of a small amount of non-polar Cs cation does not change the polar surrounding dominated by polar MA and FA cations in the perovskite lattice, but obviously the third cation allows a relaxed formation of the perovskite crystal lattice with less traps and therefore better device performance.

A similar observation was reported<sup>36</sup> for photovoltaic devices based on lead halides with a chloride/iodide mixture and a Cs/FA mixture on the A-site. Here, the introduction of polar MA as the third cation type resulted in a more defect-tolerant material with an increased fluorescence intensity and lifetime, which was explained by a reduction of trap-assisted recombination.

## CONCLUSIONS

In summary, we compared the excited-state properties of FA/MA and Cs/FA/MA mixture perovskite films using fs-TAS upon photoexcitation at 3.2 eV in the visible region ( $\sim 1.9$ – $3.1$  eV) to identify the role of Cs in carrier recombination paths. Adding 5% of Cs showed significant features in their photophysics. The steady-state spectra did not show any apparent change between the two materials, indicating a similar degree of localization of the charge carriers at the band edge (2.33 eV). Moreover, the addition of Cs reduced trap density and terminated non-radiative recombination channels as well as increased the average lifetime of the photogenerated charge carriers from 291 to 355 ns. In the Cs/FA/MA film, we observed the enhancement in the efficient hot-phonon bottleneck due to the large mass and small ionic radius of Cs. Our study suggests that triple-cation lead bromide perovskites will be an exciting target materials for designing photoconversion systems that use slow carrier relaxation for high-efficiency solar energy conversion.

## ASSOCIATED CONTENT

### Supporting Information

The Supporting Information is available free of charge at <https://pubs.acs.org/doi/10.1021/acs.jpcc.2c02682>.

XRD spectra; SEM images; kinetic profiles; results from global fitting; time constants; and lifetime density maps of  $\text{FA}_{0.83}\text{MA}_{0.17}\text{PbBr}_3$  and  $\text{Cs}_{0.05}(\text{FA}_{0.83}\text{MA}_{0.17})_{0.95}\text{PbBr}_3$  thin films on glass (PDF)

## AUTHOR INFORMATION

### Corresponding Author

Markus Braun – Institute of Physical and Theoretical Chemistry, Goethe University, Frankfurt am Main 60438, Germany; [orcid.org/0000-0002-7891-6954](https://orcid.org/0000-0002-7891-6954); Email: [braun@theochem.uni-frankfurt.de](mailto:braun@theochem.uni-frankfurt.de)

### Authors

Mahmoud M. Elshanawany – Institute of Physical and Theoretical Chemistry, Goethe University, Frankfurt am Main 60438, Germany; [orcid.org/0000-0001-9013-1263](https://orcid.org/0000-0001-9013-1263)

Antonio Gaetano Ricciardulli – Institute of Materials Science, Technische Universität Darmstadt, Darmstadt 64289, Germany; [orcid.org/0000-0003-2688-9912](https://orcid.org/0000-0003-2688-9912)

Jose J. Jeronimo-Rendon – Institute of Photovoltaics (ipv), University of Stuttgart, Stuttgart 70569, Germany

Michael Saliba – Institute of Photovoltaics (ipv), University of Stuttgart, Stuttgart 70569, Germany; Helmholtz Young Investigator Group FRONTRUNNER, Forschungszentrum Jülich, Jülich 52428, Germany; [orcid.org/0000-0002-6818-9781](https://orcid.org/0000-0002-6818-9781)

Josef Wachtveitl – Institute of Physical and Theoretical Chemistry, Goethe University, Frankfurt am Main 60438, Germany; [orcid.org/0000-0002-8496-8240](https://orcid.org/0000-0002-8496-8240)

Complete contact information is available at:

<https://pubs.acs.org/10.1021/acs.jpcc.2c02682>

## Notes

The authors declare no competing financial interest.

## ACKNOWLEDGMENTS

This work has been funded by the German Research Foundation DFG (WA 1850/6-2, SPP 2196, GRK 2642). We would like to thank Dr Lothar Fink for XRD measurements and Terfort group for SEM measurements. Deep thanks to Mostafa Sayed (University of Science and Technology of China, New Valley University), Metwally Ezzat (Ghent University), Dr. Christoph Kaiser, and Tobias Fischer (Goethe University) for helpful discussions.

## REFERENCES

- (1) National Renewable Energy Laboratory. Best Research-Cell Efficiencies. 2020, <https://www.nrel.gov/pv/cell-efficiency.html>.
- (2) Kojima, A.; Teshima, K.; Shirai, Y.; Miyasaka, T. Organometal Halide Perovskites as Visible-Light Sensitizers for Photovoltaic Cells. *J. Am. Chem. Soc.* **2009**, *131*, 6050–6051.
- (3) Gil-Escrig, L.; Dreesen, C.; Palazon, F.; Hawash, Z.; Moons, E.; Albrecht, S.; Sessolo, M.; Bolink, H. J. Efficient Wide-Bandgap Mixed-Cation and Mixed-Halide Perovskite Solar Cells by Vacuum Deposition. *ACS Energy Lett.* **2021**, *6*, 827–836.
- (4) Jung, E. H.; Jeon, N. J.; Park, E. Y.; Moon, C. S.; Shin, T. J.; Yang, T.-Y.; Noh, J. H.; Seo, J. Efficient, Stable and Scalable Perovskite Solar Cells Using Poly(3-Hexylthiophene). *Nature* **2019**, *567*, 511–515.
- (5) Jiang, Q.; Zhao, Y.; Zhang, X.; Yang, X.; Chen, Y.; Chu, Z.; Ye, Q.; Li, X.; Yin, Z.; You, J. Surface Passivation of Perovskite Film for Efficient Solar Cells. *Nat. Photonics* **2019**, *13*, 460–466.
- (6) Zheng, X.; Hou, Y.; Bao, C.; Yin, J.; Yuan, F.; Huang, Z.; Song, K.; Liu, J.; Troughton, J.; Gasparini, N.; Zhou, C.; Lin, Y.; Xue, D.-J.; Chen, B.; Johnston, A. K.; Wei, N.; Hedhili, M. N.; Wei, M.; Alsalloum, A. Y.; Maity, P.; Turedi, B.; Yang, C.; Baran, D.; Anthopoulos, T. D.; Han, Y.; Lu, Z.-H.; Mohammed, O. F.; Gao, F.; Sargent, E. H.; Bakr, O. M. Managing Grains and Interfaces via Ligand Anchoring Enables 22.3%-Efficiency Inverted Perovskite Solar Cells. *Nat. Energy* **2020**, *5*, 131–140.
- (7) Saliba, M.; Matsui, T.; Seo, J.-Y.; Domanski, K.; Correa-Baena, J.-P.; Nazeeruddin, M. K.; Zakeeruddin, S. M.; Tress, W.; Abate, A.; Hagfeldt, A.; Grätzel, M. Cesium-Containing Triple Cation Perovskite Solar Cells: Improved Stability, Reproducibility and High Efficiency. *Energy Environ. Sci.* **2016**, *9*, 1989–1997.
- (8) Ferdowsi, P.; Ochoa-Martinez, E.; Steiner, U.; Saliba, M. One-Step Solvent-Free Mechanochemical Incorporation of Insoluble Cesium Salt into Perovskites for Wide Band-Gap Solar Cells. *Chem. Mater.* **2021**, *33*, 3971–3979.
- (9) Lee, M. M.; Teuscher, J.; Miyasaka, T.; Murakami, T. N.; Snaith, H. J. Efficient Hybrid Solar Cells Based on Meso-Superstructured Organometal Halide Perovskites. *Science* **2012**, *338*, 643–647.
- (10) Conings, B.; Drijkoningen, J.; Gauquelin, N.; Babayigit, A.; D'Haen, J.; D'Olieslaeger, L.; Ethirajan, A.; Verbeeck, J.; Manca, J.; Mosconi, E.; Angelis, F. D.; Boyen, H.-G. Intrinsic Thermal Instability of Methylammonium Lead Trihalide Perovskite. *Adv. Energy Mater.* **2015**, *5*, 1500477.
- (11) Misra, R. K.; Aharon, S.; Li, B.; Mogilyansky, D.; Visoly-Fisher, I.; Etgar, L.; Katz, E. A. Temperature- and Component-Dependent Degradation of Perovskite Photovoltaic Materials under Concentrated Sunlight. *J. Phys. Chem. Lett.* **2015**, *6*, 326–330.
- (12) Li, W.; Li, J.; Wang, L.; Niu, G.; Gao, R.; Qiu, Y. Post Modification of Perovskite Sensitized Solar Cells by Aluminum Oxide for Enhanced Performance. *J. Mater. Chem. A* **2013**, *1*, 11735–11740.
- (13) Li, M.; Li, H.; Fu, J.; Liang, T.; Ma, W. Recent Progress on the Stability of Perovskite Solar Cells in a Humid Environment. *J. Phys. Chem. C* **2020**, *124*, 27251–27266.
- (14) Wu, X.; Trinh, M. T.; Niesner, D.; Zhu, H.; Norman, Z.; Owen, J. S.; Yaffe, O.; Kudisch, B. J.; Zhu, X.-Y. Trap States in Lead Iodide Perovskites. *J. Am. Chem. Soc.* **2015**, *137*, 2089–2096.
- (15) Chen, Q.; De Marco, N.; Yang, Y.; Song, T.-B.; Chen, C.-C.; Zhao, H.; Hong, Z.; Zhou, H.; Yang, Y. Under the Spotlight: The Organic–Inorganic Hybrid Halide Perovskite for Optoelectronic Applications. *Nano Today* **2015**, *10*, 355–396.
- (16) Kulbak, M.; Gupta, S.; Kedem, N.; Levine, I.; Bendikov, T.; Hodes, G.; Cahen, D. Cesium Enhances Long-Term Stability of Lead Bromide Perovskite-Based Solar Cells. *J. Phys. Chem. Lett.* **2016**, *7*, 167–172.
- (17) López, C. A.; Martínez-Huerta, M. V.; Alvarez-Galván, M. C.; Kayser, P.; Gant, P.; Castellanos-Gomez, A.; Fernández-Díaz, M. T.; Fauth, F.; Alonso, J. A. Elucidating the Methylammonium (MA) Conformation in MAPbBr<sub>3</sub> Perovskite with Application in Solar Cells. *Inorg. Chem.* **2017**, *56*, 14214–14219.
- (18) Yu, Z.; Leilaieoun, M.; Holman, Z. Selecting Tandem Partners for Silicon Solar Cells. *Nat. Energy* **2016**, *1*, 16137.
- (19) Leijtens, T.; Bush, K. A.; Prasanna, R.; McGehee, M. D. Opportunities and Challenges for Tandem Solar Cells Using Metal Halide Perovskite Semiconductors. *Nat. Energy* **2018**, *3*, 828–838.
- (20) Xu, J.; Boyd, C. C.; Yu, Z. J.; Palmstrom, A. F.; Witter, D. J.; Larson, B. W.; France, R. M.; Werner, J.; Harvey, S. P.; Wolf, E. J.; Weigand, W.; Manzoor, S.; van Hest, M. F. A. M.; Berry, J. J.; Luther, J. M.; Holman, Z. C.; McGehee, M. D. Triple-Halide Wide-Band Gap Perovskites with Suppressed Phase Segregation for Efficient Tandems. *Science* **2020**, *367*, 1097–1104.
- (21) Manser, J. S.; Kamat, P. V. Band Filling with Free Charge Carriers in Organometal Halide Perovskites. *Nat. Photonics* **2014**, *8*, 737–743.
- (22) Yang, Y.; Ostrowski, D. P.; France, R. M.; Zhu, K.; van de Lagemaat, J.; Luther, J. M.; Beard, M. C. Observation of a Hot-Phonon Bottleneck in Lead-Iodide Perovskites. *Nat. Photonics* **2016**, *10*, 53–59.
- (23) Herz, L. M. Charge-Carrier Dynamics in Organic-Inorganic Metal Halide Perovskites. *Annu. Rev. Phys. Chem.* **2016**, *67*, 65–89.
- (24) Stamplecoskie, K. G.; Manser, J. S.; Kamat, P. V. Dual Nature of the Excited State in Organic–Inorganic Lead Halide Perovskites. *Energy Environ. Sci.* **2015**, *8*, 208–215.
- (25) Price, M. B.; Butkus, J.; Jellicoe, T. C.; Sadhanala, A.; Briane, A.; Halpert, J. E.; Broch, K.; Hodgkiss, J. M.; Friend, R. H.; Deschler, F. Hot-Carrier Cooling and Photoinduced Refractive Index Changes in Organic–Inorganic Lead Halide Perovskites. *Nat. Commun.* **2015**, *6*, 8420.
- (26) Yang, J.; Wen, X.; Xia, H.; Sheng, R.; Ma, Q.; Kim, J.; Tapping, P.; Harada, T.; Kee, T. W.; Huang, F.; Cheng, Y.-B.; Green, M.; Ho-Baillie, A.; Huang, S.; Shrestha, S.; Patterson, R.; Conibeer, G. Acoustic-Optical Phonon up-Conversion and Hot-Phonon Bottleneck in Lead-Halide Perovskites. *Nat. Commun.* **2017**, *8*, 14120.
- (27) Xing, G.; Mathews, N.; Sun, S.; Lim, S. S.; Lam, Y. M.; Grätzel, M.; Mhaisalkar, S.; Sum, T. C. Long-Range Balanced Electron- and Hole-Transport Lengths in Organic-Inorganic CH<sub>3</sub>NH<sub>3</sub>PbI<sub>3</sub>. *Science* **2013**, *342*, 344–347.
- (28) Shi, J.; Li, Y.; Li, Y.; Li, D.; Luo, Y.; Wu, H.; Meng, Q. From Ultrafast to Ultra-slow: Charge-Carrier Dynamics of Perovskite Solar Cells. *Joule* **2018**, *2*, 879–901.
- (29) deQuilettes, D. W.; Frohna, K.; Emin, D.; Kirchartz, T.; Bulovic, V.; Ginger, D. S.; Stranks, S. D. Charge-Carrier Recombination in Halide Perovskites. *Chem. Rev.* **2019**, *119*, 11007–11019.
- (30) Li, C.; Wang, A.; Deng, X.; Wang, S.; Yuan, Y.; Ding, L.; Hao, F. Insights into Ultrafast Carrier Dynamics in Perovskite Thin Films and Solar Cells. *ACS Photonics* **2020**, *7*, 1893–1907.
- (31) Elshanawany, M. M.; Ricciardulli, A. G.; Saliba, M.; Wachtveitl, J.; Braun, M. Mechanism of Ultrafast Energy Transfer between the Organic–Inorganic Layers in Multiple-Ring Aromatic Spacers for 2D Perovskites. *Nanoscale* **2021**, *13*, 15668–15676.
- (32) Ghosh, T.; Aharon, S.; Etgar, L.; Ruhman, S. Free Carrier Emergence and Onset of Electron–Phonon Coupling in Methyl-

ammonium Lead Halide Perovskite Films. *J. Am. Chem. Soc.* **2017**, *139*, 18262–18270.

(33) Miyata, K.; Meggiolaro, D.; Trinh, M. T.; Joshi, P. P.; Mosconi, E.; Jones, S. C.; De Angelis, F.; Zhu, X.-Y. Large Polarons in Lead Halide Perovskites. *Sci. Adv.* **2017**, *3*, No. e1701217.

(34) Kahmann, S.; Loi, M. A. Hot Carrier Solar Cells and the Potential of Perovskites for Breaking the Shockley–Queisser Limit. *J. Mater. Chem. C* **2019**, *7*, 2471–2486.

(35) Minda, I.; Horn, J.; Ahmed, E.; Schlettwein, D.; Schwoerer, H. Ultrafast Charge Dynamics in Mixed Cation – Mixed Halide Perovskite Thin Films. *ChemPhysChem* **2018**, *19*, 3010–3017.

(36) Tan, H.; Che, F.; Wei, M.; Zhao, Y.; Saidaminov, M. I.; Todorović, P.; Broberg, D.; Walters, G.; Tan, F.; Zhuang, T.; Sun, B.; Liang, Z.; Yuan, H.; Fron, E.; Kim, J.; Yang, Z.; Voznyy, O.; Asta, M.; Sargent, E. H. Dipolar Cations Confer Defect Tolerance in Wide-Bandgap Metal Halide Perovskites. *Nat. Commun.* **2018**, *9*, 3100.

(37) Saidaminov, M. I.; Williams, K.; Wei, M.; Johnston, A.; Quintero-Bermudez, R.; Vafaie, M.; Pina, J. M.; Proppe, A. H.; Hou, Y.; Walters, G.; Kelley, S. O.; Tisdale, W. A.; Sargent, E. H. Multi-Cation Perovskites Prevent Carrier Reflection from Grain Surfaces. *Nat. Mater.* **2020**, *19*, 412–418.

(38) Gélvez-Rueda, M. C.; Van Gompel, W. T. M.; Herckens, R.; Lutsen, L.; Vanderzande, D.; Grozema, F. C. Inducing Charge Separation in Solid-State Two-Dimensional Hybrid Perovskites through the Incorporation of Organic Charge-Transfer Complexes. *J. Phys. Chem. Lett.* **2020**, *11*, 824–830.

(39) Brauer, J. C.; Tsokkou, D.; Sanchez, S.; Droseros, N.; Roose, B.; Mosconi, E.; Hua, X.; Stolterfoht, M.; Neher, D.; Steiner, U.; De Angelis, F.; Abate, A.; Banerji, N. Comparing the Excited-State Properties of a Mixed-Cation–Mixed-Halide Perovskite to Methylammonium Lead Iodide. *J. Chem. Phys.* **2020**, *152*, 104703.

(40) Baumeler, T.; Arora, N.; Hinderhofer, A.; Akin, S.; Greco, A.; Abdi-Jalebi, M.; Shivanna, R.; Uchida, R.; Liu, Y.; Schreiber, F.; Zakeeruddin, S. M.; Friend, R. H.; Graetzel, M.; Dar, M. I. Minimizing the Trade-Off between Photocurrent and Photovoltage in Triple-Cation Mixed-Halide Perovskite Solar Cells. *J. Phys. Chem. Lett.* **2020**, *11*, 10188–10195.

(41) Pasanen, H. P.; Vivo, P.; Canil, L.; Hempel, H.; Unold, T.; Abate, A.; Tkachenko, N. V. Monitoring Charge Carrier Diffusion across a Perovskite Film with Transient Absorption Spectroscopy. *J. Phys. Chem. Lett.* **2020**, *11*, 445–450.

(42) Wang, T.; Jin, L.; Hidalgo, J.; Chu, W.; Snaider, J. M.; Deng, S.; Zhu, T.; Lai, B.; Prezhdo, O.; Correa-Baena, J.-P.; Huang, L. Protecting Hot Carriers by Tuning Hybrid Perovskite Structures with Alkali Cations. *Sci. Adv.* **2020**, *6*, No. eabb1336.

(43) Catone, D.; Ammirati, G.; O’Keeffe, P.; Martelli, F.; Di Mario, L.; Turchini, S.; Paladini, A.; Toschi, F.; Agresti, A.; Pescetelli, S.; Di Carlo, A. Effects of Crystal Morphology on the Hot-Carrier Dynamics in Mixed-Cation Hybrid Lead Halide Perovskites. *Energies* **2021**, *14*, 708.

(44) Saliba, M.; Correa-Baena, J.-P.; Wolff, C. M.; Stolterfoht, M.; Phung, N.; Albrecht, S.; Neher, D.; Abate, A. How to Make over 20% Efficient Perovskite Solar Cells in Regular (n–i–p) and Inverted (p–i–n) Architectures. *Chem. Mater.* **2018**, *30*, 4193–4201.

(45) Reuss, A. J.; Grünwald, C.; Braun, M.; Engels, J. W.; Wachtveitl, J. The Three Possible 2-(Pyrenylethynyl) Adenosines: Rotameric Energy Barriers Govern the Photodynamics of These Structural Isomers. *ChemPhysChem* **2016**, *17*, 1369–1376.

(46) Gustmann, H.; Lefrancois, D.; Reuss, A. J.; Gophane, D. B.; Braun, M.; Dreu, A.; Sigurdsson, S. T.; Wachtveitl, J. Spin the Light off: Rapid Internal Conversion into a Dark Doublet State Quenches the Fluorescence of an RNA Spin Label. *Phys. Chem. Chem. Phys.* **2017**, *19*, 26255–26264.

(47) Trojanowski, P.; Plötner, J.; Grünwald, C.; Graupner, F. F.; Slavov, C.; Reuss, A. J.; Braun, M.; Engels, J. W.; Wachtveitl, J. Photo-Physical Properties of 2-(1-Ethynylpyrene)-Adenosine: Influence of Hydrogen Bonding on Excited State Properties. *Phys. Chem. Chem. Phys.* **2014**, *16*, 13875–13888.

(48) Slavov, C.; Hartmann, H.; Wachtveitl, J. Implementation and Evaluation of Data Analysis Strategies for Time-Resolved Optical Spectroscopy. *Anal. Chem.* **2015**, *87*, 2328–2336.

(49) Mondal, N.; Samanta, A. Complete Ultrafast Charge Carrier Dynamics in Photo-Excited All-Inorganic Perovskite Nanocrystals (CsPbX<sub>3</sub>). *Nanoscale* **2017**, *9*, 1878–1885.

(50) Trinh, M. T.; Wu, X.; Niesner, D.; Zhu, X.-Y. Many-Body Interactions in Photo-Excited Lead Iodide Perovskite. *J. Mater. Chem. A* **2015**, *3*, 9285–9290.

(51) Chen, J.; Messing, M. E.; Zheng, K.; Pullerits, T. Cation-Dependent Hot Carrier Cooling in Halide Perovskite Nanocrystals. *J. Am. Chem. Soc.* **2019**, *141*, 3532–3540.

(52) Chen, K.; Barker, A. J.; Morgan, F. L. C.; Halpert, J. E.; Hodgkiss, J. M. Effect of Carrier Thermalization Dynamics on Light Emission and Amplification in Organometal Halide Perovskites. *J. Phys. Chem. Lett.* **2015**, *6*, 153–158.

## Recommended by ACS

### Fine Structure of the Optical Absorption Resonance in Cs<sub>2</sub>AgBiBr<sub>6</sub> Double Perovskite Thin Films

Alexander Schmitz, Gerd Bacher, *et al.*

JANUARY 22, 2020  
ACS ENERGY LETTERS

READ 

### Two-Dimensional Cs<sub>2</sub>AgBiBr<sub>6</sub>/WS<sub>2</sub> Heterostructure-Based Photodetector with Boosted Detectivity via Interfacial Engineering

Feier Fang, Yumeng Shi, *et al.*

FEBRUARY 18, 2022  
ACS NANO

READ 

### Charge Injection from Excited Cs<sub>2</sub>AgBiBr<sub>6</sub> Quantum Dots into Semiconductor Oxides

Junsang Cho, Prashant V. Kamat, *et al.*

DECEMBER 10, 2019  
CHEMISTRY OF MATERIALS

READ 

### Role of the A-Site Cation in Low-Temperature Optical Behaviors of APbBr<sub>3</sub> (A = Cs, CH<sub>3</sub>NH<sub>3</sub>)

Hongsun Ryu, Joon I. Jang, *et al.*

JANUARY 27, 2021  
JOURNAL OF THE AMERICAN CHEMICAL SOCIETY

READ 

Get More Suggestions >

Supporting Information for

# **Ultrafast Carrier Dynamics in Wide Band Gap Mixed-Cation Perovskites: Influence of the Cs Cation**

Mahmoud M. Elshanawany<sup>a</sup>, Antonio Gaetano Ricciardulli<sup>b</sup>, Jose J. Jeronimo-Rendon<sup>c</sup>, Michael Saliba<sup>c,d</sup>, Josef Wachtveitl<sup>a</sup> and Markus Braun<sup>a,\*</sup>

<sup>a</sup> Institute of Physical and Theoretical Chemistry, Goethe University, 60438 Frankfurt am Main, Germany.

<sup>b</sup> Institute of Materials Science, Technische Universität Darmstadt, 64289 Darmstadt, Germany.

<sup>c</sup> Institute of Photovoltaics (ipv), University of Stuttgart, 70569 Stuttgart, Germany.

<sup>d</sup> Helmholtz Young Investigator Group FRONTRUNNER, Forschungszentrum Jülich, 52428 Jülich, Germany.

E-mail: braun@theochem.uni-frankfurt.de

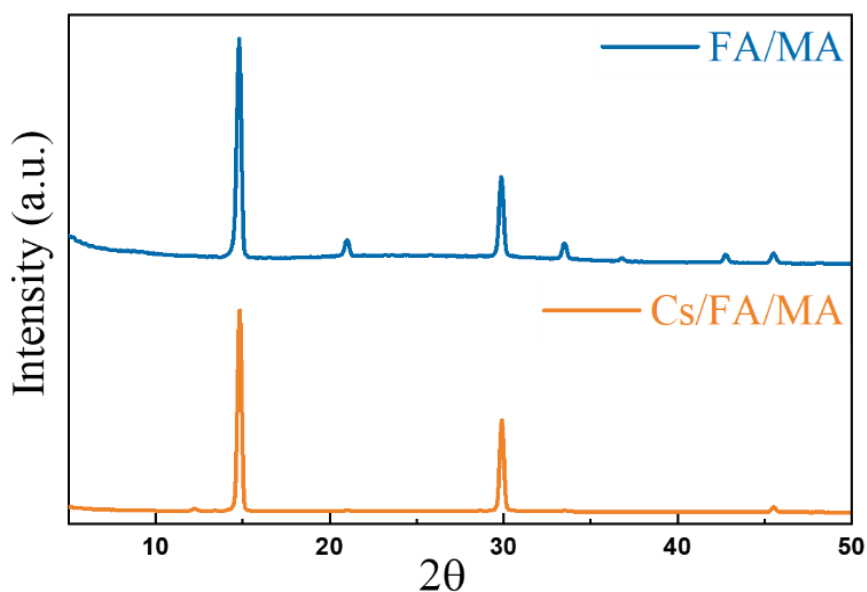


Figure S1. XRD spectra of  $\text{FA}_{0.83}\text{MA}_{0.17}\text{PbBr}_3$  and  $\text{Cs}_{0.05}(\text{FA}_{0.83}\text{MA}_{0.17})_{0.95}\text{PbBr}_3$  collected at room temperature. Data were collected in a D8 Advance Bruker  $2\theta$ - $\Omega$  diffractometer, with copper radiation ( $\text{Cu K}\alpha 1$ ,  $\lambda = 1.5406 \text{ \AA}$ ) and a secondary monochromator, operated at 40 kV and 30 mA.

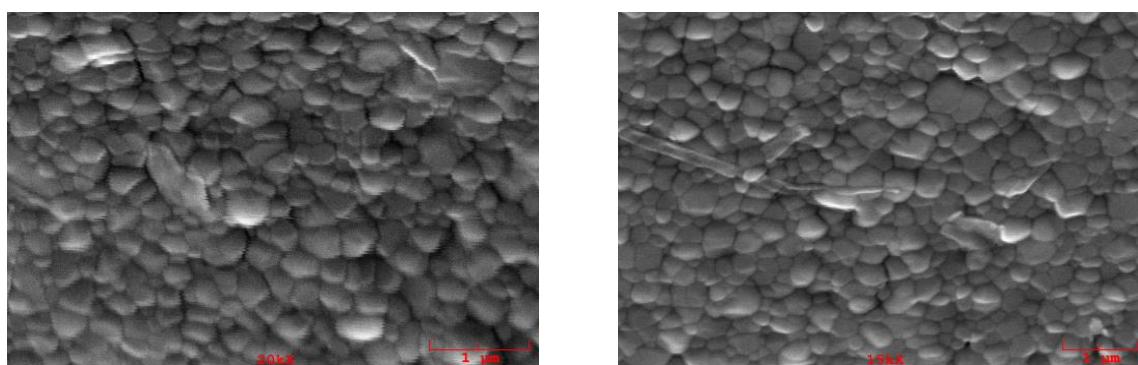


Figure S2. Top view scanning electron microscopy (SEM) images of FA/MA (left image) and Cs/FA/MA (right image) thin films deposited on glass substrates.



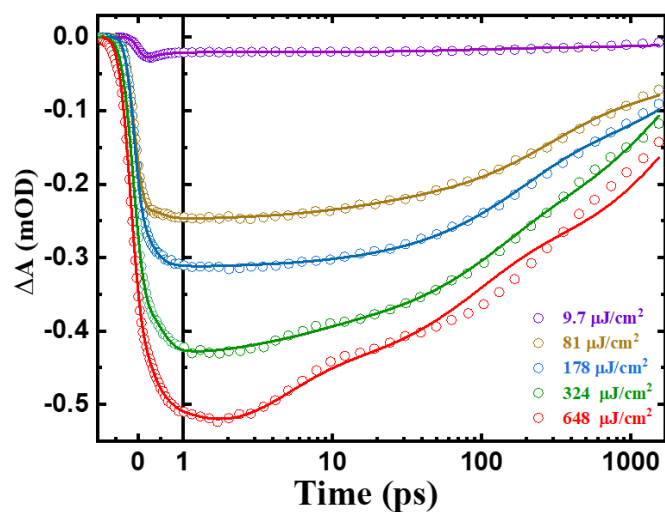


Figure S3. Kinetic profiles of FA/MA film probed at 530 nm at various pump intensities from 9.7 to 648  $\mu\text{J}/\text{cm}^2$ .

Table S1. Time constants in ps resulting from the global fit analysis for different powers of FA/MA thin films on glass.

Power	$\tau_1$ (ps)	$\tau_2$ (ps)	$\tau_3$ (ps)	$\tau_4$ (ps)
9.7 $\mu\text{J}/\text{cm}^2$	0.20	40	500	inf
81 $\mu\text{J}/\text{cm}^2$	0.27	11.08	182	inf
178 $\mu\text{J}/\text{cm}^2$	0.3	10.18	135	inf
324 $\mu\text{J}/\text{cm}^2$	0.35	5.9	100	inf
648 $\mu\text{J}/\text{cm}^2$	0.84	3.65	85	inf

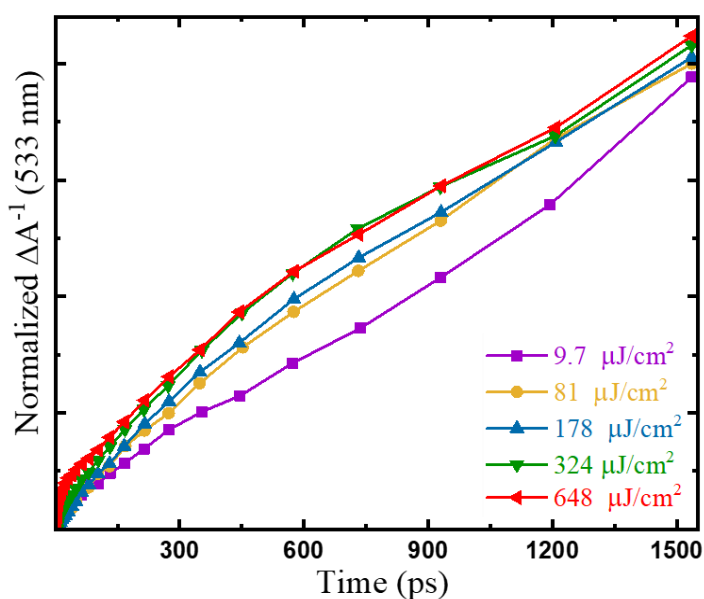


Figure S4. Reciprocal of kinetic traces on FA/MA film up to 1.5 ns at 533 nm for different powers: (a) 9.7, (b) 81, (c) 178, (d) 324 and (e) 648  $\mu\text{J}/\text{cm}^2$  normalized at the maximum bleach (minimum  $\Delta A^{-1}$ ).

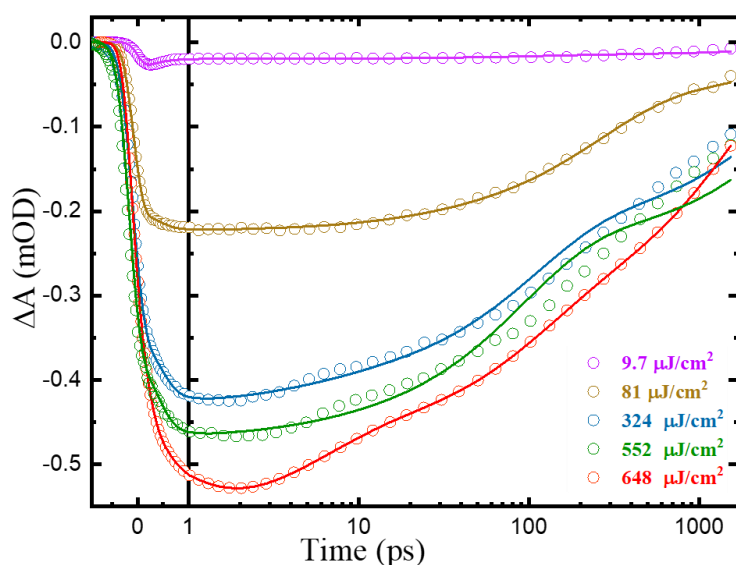


Figure S5. Kinetic profiles of Cs/FA/MA film probed at 530 nm at various pump intensities.

Table S2. Time constants in ps resulting from the global fit analysis for different powers of Cs/FA/MA thin films on glass.

Power	$\tau_1$ (ps)	$\tau_2$ (ps)	$\tau_3$ (ps)	$\tau_4$ (ps)
$9.7 \mu\text{J}/\text{cm}^2$	0.21	71	905	inf
$81 \mu\text{J}/\text{cm}^2$	0.29	18	190	inf
$324 \mu\text{J}/\text{cm}^2$	0.43	6.4	166	inf
$552 \mu\text{J}/\text{cm}^2$	0.71	6.5	148	inf
$648 \mu\text{J}/\text{cm}^2$	0.91	4.66	124	inf

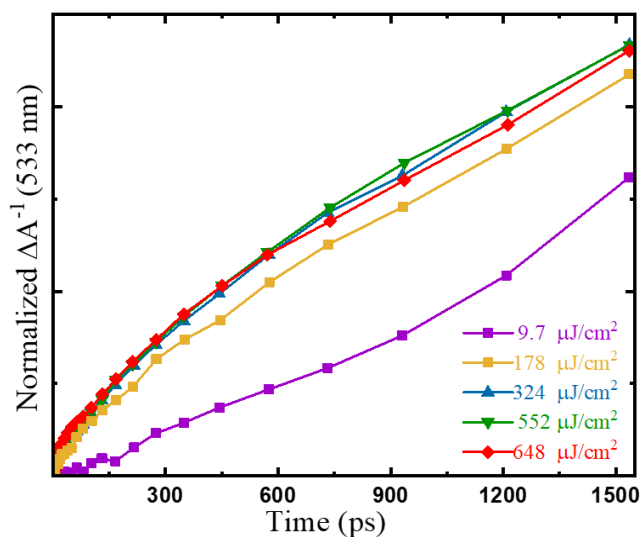


Figure S6. Reciprocal of kinetic traces on Cs/FA/MA film up to 1.5 ns at 533 nm for different powers: (a) 9.7, (b) 81, (c) 324, (d) 552 and (e) 648  $\mu\text{J}/\text{cm}^2$  normalized at the maximum bleach (minimum  $\Delta A^{-1}$ ).

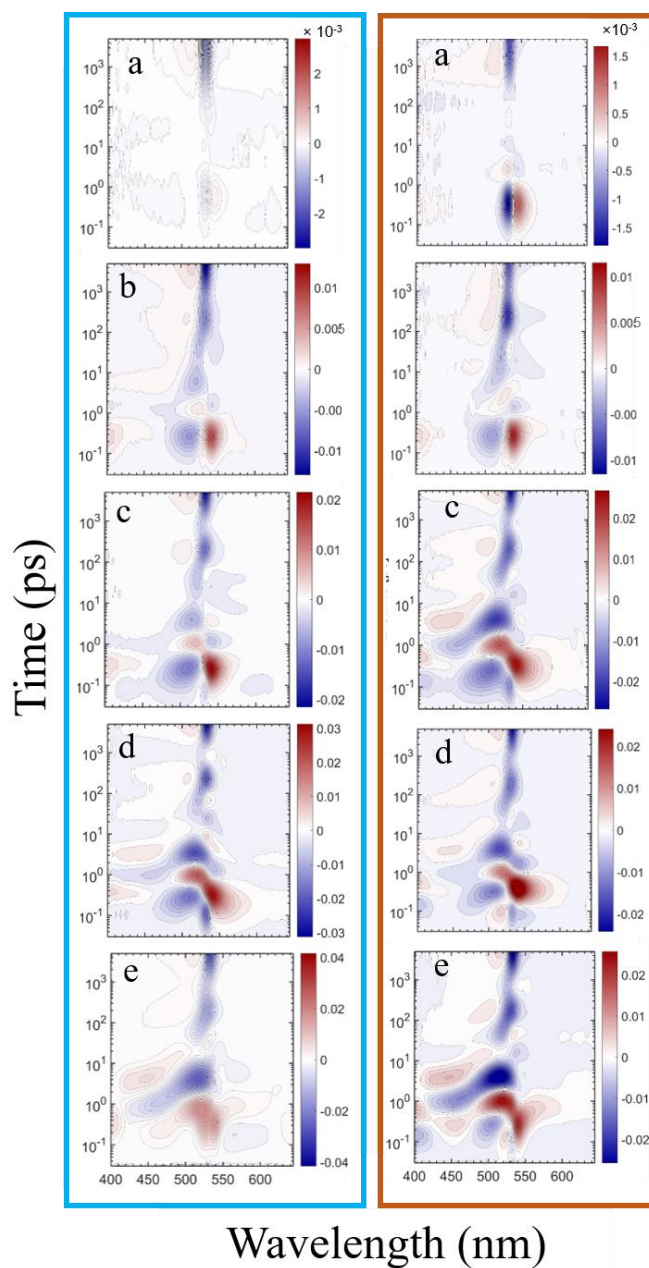


Figure S7. (left panel) Lifetime density maps of FA/MA film up to 1.5 ns at different powers: (a) 9.7, (b) 81, (c) 178, (d) 324 and (e) 648  $\mu\text{J}/\text{cm}^2$ . (right panel) lifetime density maps of Cs/FA/MA film up to 1.5 ns at different powers: (a) 9.7, (b) 81, (c) 324, (d) 552 and (e) 648  $\mu\text{J}/\text{cm}^2$ .

## 7.4 Soliman et al., ACS Omega 2022, 7

### Base-Free Synthesis and Photophysical Properties of New Schiff Bases Containing Indole Moiety

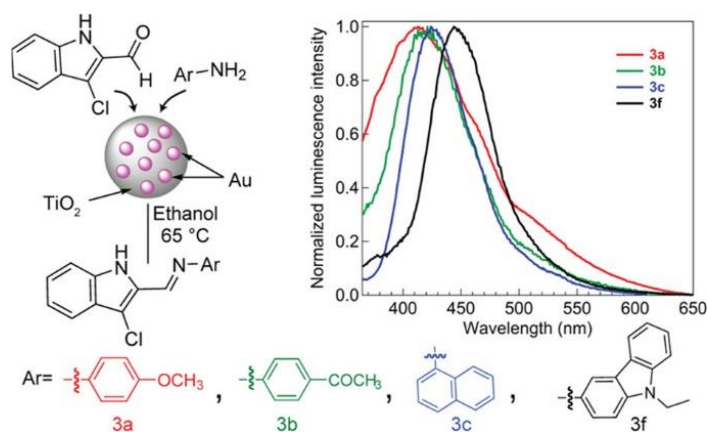
Ahmed I. A. Soliman\*<sup>#</sup>, Mostafa Sayed<sup>#</sup>, **Mahmoud M. Elshanawany<sup>#</sup>**, Osama Younis, Mostafa Ahmed, Adel M. Kamal El-Dean, Aboel-Magd A. Abdel-Wahab, Josef Wachtveitl, Markus Braun\*, Pedram Fatehi, and Mahmoud S. Tolba

ACS Omega **2022**, 7, 12, 10178–10186

**Publication Date:** March 16, 2022

**DOI:** 10.1021/acsomega.1c06636

Reprinted with permission from the American Chemical Society



# Base-Free Synthesis and Photophysical Properties of New Schiff Bases Containing Indole Moiety

Ahmed I. A. Soliman,<sup>\*,#</sup> Mostafa Sayed,<sup>#</sup> Mahmoud M. Elshanawany,<sup>#</sup> Osama Younis, Mostafa Ahmed, Adel M. Kamal El-Dean, Aboel-Magd A. Abdel-Wahab, Josef Wachtveitl, Markus Braun,<sup>\*</sup> Pedram Fatehi, and Mahmoud S. Tolba



Cite This: *ACS Omega* 2022, 7, 10178–10186



Read Online

ACCESS |



Metrics & More

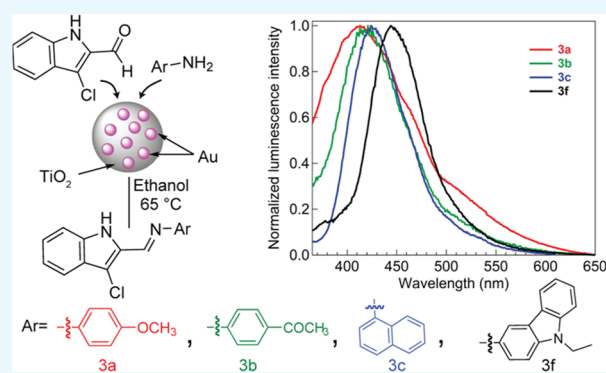


Article Recommendations



Supporting Information

**ABSTRACT:** Schiff bases represent an essential class in organic chemistry with antitumor, antiviral, antifungal, and antibacterial activities. The synthesis of Schiff bases requires the presence of an organic base as a catalyst such as piperidine. Base-free synthesis of organic compounds using a heterogeneous catalyst has recently attracted more interest due to the facile procedure, high yield, and reusability of the used catalyst. Herein, we present a comparative study to synthesize new Schiff bases containing indole moieties using piperidine as an organic base catalyst and Au@TiO<sub>2</sub> as a heterogeneous catalyst. In both methods, the products were isolated in high yields and fully characterized using different spectral analysis techniques. The catalyst was reusable four times, and the activity was slightly decreased. The presence of Au increases the number of acidic sites of TiO<sub>2</sub>, resulting in C=O polarization. Yields of the prepared Schiff bases in the presence of Au@TiO<sub>2</sub> and piperidine were comparable. However, Au@TiO<sub>2</sub> is an easily separable and recyclable catalyst, which would facilitate the synthesis of organic compounds without applying any hazardous materials. Furthermore, the luminescence behavior of the synthesized Schiff bases exhibited spectral shape dependence on the substituent group. Interestingly, the compounds also displayed deep-blue fluorescence with Commission Internationale de l'Éclairage (CIE) coordinates of  $\gamma < 0.1$ . Thus, these materials may contribute to decreasing the energy consumption of the emitting devices.



## 1. INTRODUCTION

Schiff bases, synthesized through the condensation reactions between primary amines with ketones or aldehydes under optimized conditions, are widely used as antitumor, antiviral, antifungal, and antibacterial active substances.<sup>1–5</sup> For instance, Schiff bases derived from indole-3-carboxaldehyde showed antimicrobial and antitumor activities.<sup>5–7</sup> They are commonly used for stabilizing metal cations, resulting in enhancing their catalytic, industrial, and biological applications.<sup>7–10</sup> The synthesis of these bases can be performed in the presence of homogeneous or heterogeneous catalysts. Homogeneous catalysts, such as organic bases, inorganic bases, and Lewis acids, are not recoverable and require careful disposal to avoid environmental hazards. Therefore, the use of recoverable catalysts acquired much interest.

Recently, the use of heterogeneous catalysts received attention in the organic synthesis field due to their high efficiency and ease of recovery.<sup>11–15</sup> The use of these recoverable heterogeneous catalysts reduces the environmental risks that can arise from the use of nonrecoverable homogeneous catalysts without a significant reduction in the yield of synthesized compounds.<sup>16</sup> In the presence of UV light,

FeCu@N-doped carbon is an efficient catalyst that can be applied for converting amines with alcohols into Schiff bases.<sup>17</sup> Also, bifunctionalized cobalt/zinc-incorporated mesoporous silica nanoparticles were used for synthesis of Schiff bases from aryl amine and benzyl alcohol, and the reaction was performed at 120 °C for 3 h in the presence of airflow.<sup>18</sup> The mixture of P<sub>2</sub>O<sub>5</sub> and Al<sub>2</sub>O<sub>3</sub> was used to catalyze the synthesis of Schiff bases from the carbonyl compounds and primary amines in the absence of a solvent.<sup>19</sup> Co nanoparticles embedded in mesoporous nitrogen-doped carbon were found effective in converting nitro groups into amino groups followed by coupling with carbonyl compounds in the presence of formic acid at 190 °C.<sup>20</sup>

On the other hand, Schiff bases are perfect candidates for photovoltaic solar cell, sensor, and organic light-emitting diode

**Received:** November 23, 2021

**Accepted:** February 17, 2022

**Published:** March 16, 2022



(OLED) applications; they can emit in a specific range.<sup>21,22</sup> Recently, we have reported some simple Schiff bases as luminescent coatings with white luminescence from a single chromophore.<sup>23</sup> Moreover, studying the excited state and its correlation with the molecular structure or molecular aggregation can help us to specify the optical properties of the organic materials.<sup>24–29</sup> Some indole derivatives and other heterocyclic compounds have been designed and showed aggregation-induced emission properties.<sup>22,30–32</sup> Thus, Schiff bases with indole moieties may have some interesting optical properties. However, limited studies have exclusively examined such materials.

In this work, Au@TiO<sub>2</sub> was utilized as a base-free catalyst in the synthesis of six new Schiff bases derived from indole, and the product yields were compared with the yields obtained from the use of piperidine. The developed catalyst was characterized by X-ray diffraction analysis (XRD), infrared spectroscopy (IR), X-ray photoelectron spectroscopy (XPS), transmission electron microscopy (TEM), and energy-dispersive X-ray spectroscopy (EDX). The synthesized Schiff bases were characterized by different spectral analyses such as IR, <sup>1</sup>H NMR, <sup>13</sup>C NMR, mass spectrometry, UV–Vis absorption, PL, and TCSPC. The recovery and reusability of the catalyst were investigated for four cycles. Also, the photophysical properties of the synthesized Schiff bases were studied.

## 2. RESULTS AND DISCUSSION

**2.1. Catalyst Characterization.** For the hydrothermal development of Au@TiO<sub>2</sub>, TiO<sub>2</sub> and the Au precursor (HAuCl<sub>4</sub>·3H<sub>2</sub>O) were heated in a Teflon autoclave at 180 °C in the presence of ethanol. Figure 1a shows the XRD

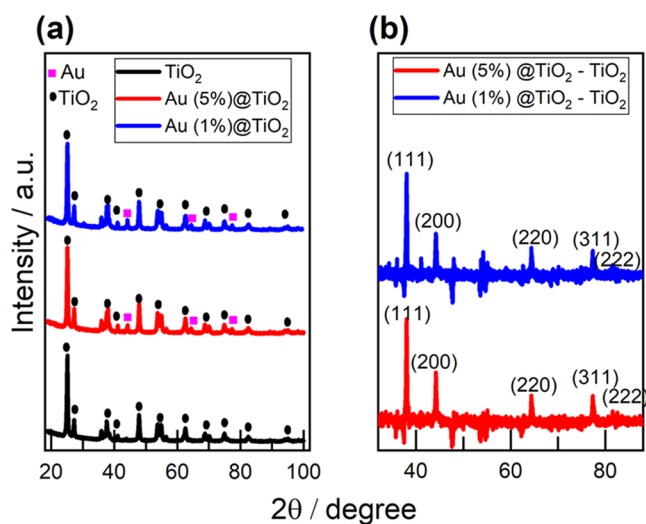


**Figure 1.** XRD patterns of (a) TiO<sub>2</sub> and Au@TiO<sub>2</sub> and (b) Au@TiO<sub>2</sub> after subtracting TiO<sub>2</sub> patterns.

patterns of TiO<sub>2</sub> (P25) before and after Au loading. Characteristic diffraction peaks located at 27.3, 35.9, 41.1, 54.9, 56.5, 68.9, and 70.0° are indexed to (110), (101), (111), (211), (220), (301), and (112) crystallographic planes for rutile TiO<sub>2</sub>, respectively.<sup>33–36</sup> Peaks at 25.1, 37.6, 47.8, 53.7, 62.7, 75.0, and 82.5° were equivalent to the planes (101), (004), (200), (105), (204), (215), and (303), respectively, indicating the tetragonal structure of anatase TiO<sub>2</sub>.<sup>33,34,37,38</sup>

Additional XRD peaks at 44.2, 64.4, and 77.3° were observed, which are indexed to the (200), (220), and (311) crystallographic planes of Au, respectively.<sup>39</sup> When the XRD spectra of TiO<sub>2</sub> were subtracted from the spectra of Au@TiO<sub>2</sub> as illustrated in Figure 1b, the overlap between these spectra was deconvoluted, resulting in new peaks at 38.0 and 81.5°, which are indexed to the crystallographic planes (111) and (222) of Au, respectively.<sup>39,40</sup> From the XRD data, the loading of Au on TiO<sub>2</sub> was successfully achieved without observing changes in the phases of TiO<sub>2</sub>. At the same time, the deposited Au nanoparticles had a face-centered cubic (fcc) structure.<sup>39,40</sup>

Figure S1a,b shows the TEM images of TiO<sub>2</sub>(p25), where the size of TiO<sub>2</sub> particles was <30 nm. Figure S1c illustrates the selected area electron diffraction (SAED) patterns, which indicates the polycrystallinity of TiO<sub>2</sub> (P25) due to the presence of both anatase and rutile TiO<sub>2</sub> nanoparticles. Figure S1d shows the high-resolution (HR)-TEM data that the interlayer distance between the lattice fringes was 0.34 nm, which is close to the d-spacing of the (101) plane in anatase TiO<sub>2</sub>. After deposition of Au (1%) on TiO<sub>2</sub>, Au nanoparticles with a size of <10 nm were observed, as shown in Figure 2a,b. The polycrystallinity of the developed Au@TiO<sub>2</sub> is concluded from the SEAD image (Figure 2c), where the estimated d-spacing values indicate the presence of anatase TiO<sub>2</sub>, rutile TiO<sub>2</sub>, and Au nanoparticles. The HR-TEM image (Figure 2d) illustrates the lattice fringes with a d-spacing of 0.22 nm, corresponding to the (111) plane of the Au fcc structure.<sup>41,42</sup>

Figure S2a shows the EDX spectrum of Au(1%)@TiO<sub>2</sub>, which indicates the presence of Au with a percentage of 1.2%. The TEM image of Au(5%)@TiO<sub>2</sub> is illustrated in Figure S2b. These results indicated that the grafting of Au@TiO<sub>2</sub> through the hydrothermal method was successfully performed, and the size of Au was <10 nm. EDX mapping of Au(1%)@TiO<sub>2</sub> (Figure S3) illustrates the dispersion of Au nanoparticles on TiO<sub>2</sub>. From these results, TiO<sub>2</sub> worked as a support, where the Au ions were dispersed. The FTIR spectrum of Au@TiO<sub>2</sub> (Figure S4) shows absorption bands at 1345–1625 and 3342 cm<sup>-1</sup>, which are ascribed to Ti-OH and the absorbed water, respectively.<sup>43–46</sup> Also, the absorption bands at 400–700 cm<sup>-1</sup> were ascribed to TiO<sub>2</sub>.<sup>43–46</sup> Figure S5 shows the chemical compositions of the Au(1%)@TiO<sub>2</sub> composite investigated by XPS. In the Ti2p spectrum (Figure S5a), two peaks were observed at 464.5 and 459.0 eV, which are attributed to Ti2p<sup>1/2</sup> and Ti2p<sup>3/2</sup>, respectively.<sup>47</sup> The XPS O1s spectrum (Figure S5b) shows a peak at 529.9, which is attributed to titanium oxide.<sup>47</sup> Figure S5c shows the Au4f spectrum, where two peaks are shown at 83.5 and 87.3 eV, which are attributed to Au(0)4f<sup>5/4</sup> and Au(0)4f<sup>7/2</sup> nanoparticles, respectively. From the abovementioned results, the hydrothermal treatment induced the reduction of the dispersed Au ions into Au(0) nanoparticles without changing the morphology and crystallinity of TiO<sub>2</sub>.<sup>48,49</sup>

**2.2. Synthesis of Schiff Bases.** As shown in Scheme 1, the starting material 3-chloro-1H-indole-2-carbaldehyde (1) was prepared according to the previously published procedure,<sup>50</sup> which then was allowed to react with different aromatic amines represented in 4-anisidine, 4-aminoacetophenone, 1-naphthyl amine, and 6-aminonaphthalene-2-sulfonic acid in the presence of piperidine as a homogeneous catalyst. The reaction mixture was refluxed for ≥ 4 h, and the used solvent was ethanol. All products (3a–3d) were isolated in high yields (85–90%). Besides, heterocyclic amines including 6-methoxy-2-amino-benzothiazole and N-ethyl-9-aminocarbazole have been

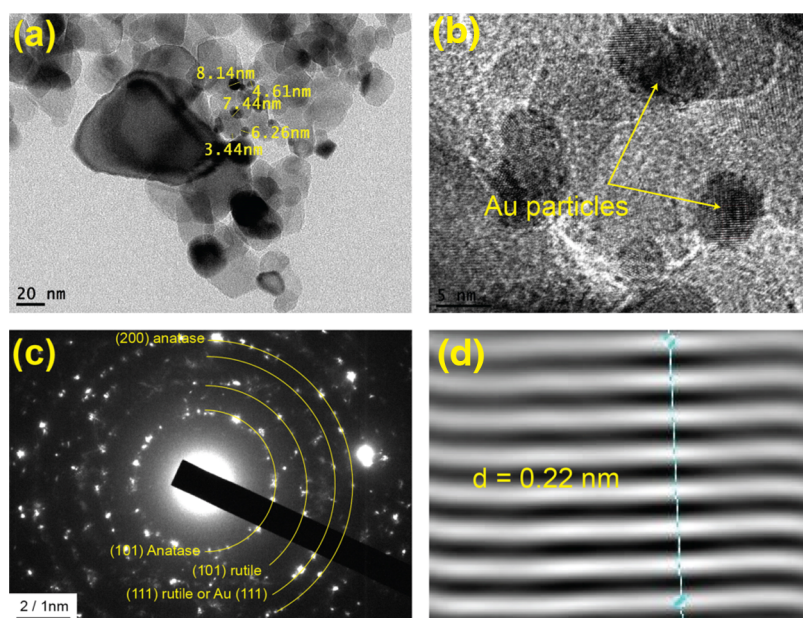
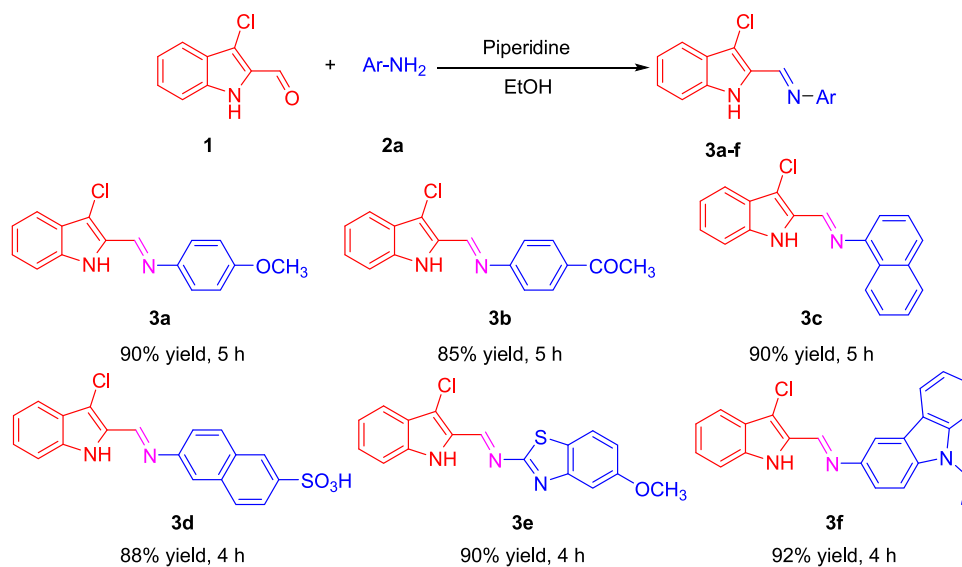


Figure 2. (a, b) TEM, (c) SAED pattern, and (d) HR-TEM images of Au(1%)/TiO<sub>2</sub>.

### Scheme 1. Substrate Scope for Amines<sup>a</sup>



<sup>a</sup>Unless noted otherwise, the reaction of **1** (6 mmol) and **2a** (1 equiv) was carried out with piperidine (5 drops) in EtOH at 90 °C for the mentioned time.

tolerated in this transformation, which efficiently delivered the products (**3e**, **3f**) in high yields (90–92%). The six new Schiff bases were successfully characterized using different spectral analysis techniques. The IR spectra (Figure 3) exhibited new bands around 1620 cm<sup>-1</sup>, characteristic for the CH=N group. Also, the absorption band at 1661 cm<sup>-1</sup>, which was attributed to the stretching absorption bands of the C=O group in the starting aldehyde **1** as previously reported, disappeared, indicating the occurrence of condensation between the C=O group of aldehyde and NH<sub>2</sub> groups of amines.<sup>51</sup> Moreover, the <sup>1</sup>H-NMR analysis revealed new signals in the region 8–9 ppm corresponding to the CH=N protons for all products.

Based on the abovementioned advantages of heterogeneous catalysis in organic synthesis, the base-free alternative way was used to synthesize the six Schiff bases in Scheme 1. To the best

of our knowledge, the use of Au@TiO<sub>2</sub> as a catalyst for the synthesis of these Schiff bases has not been reported before. To begin this study, aniline **2** was used as the model amine substrate for the reaction with 3-chloro-1H-indole-2-carbaldehyde (**1**) and EtOH as a solvent. No products were detected in the absence of catalysts even if the reaction temperature was increased to 65 °C (Table 1). Adding TiO<sub>2</sub> only delivered product (**3**) in traces with 10% yield when the reaction continued for 1 h in ethanol (entry 2). To our delight, the Schiff base product was obtained in 60% yield using the Ag@TiO<sub>2</sub> catalyst in ethanol when the reaction was conducted for 1 h (entry 3), which suggests that the Ag particles have a considerable effect on the polarization of the carbonyl group, which in turn favors the condensation reaction.<sup>52,53</sup> The Au(5%)/TiO<sub>2</sub> and Au(1%)/TiO<sub>2</sub> catalysts interestingly

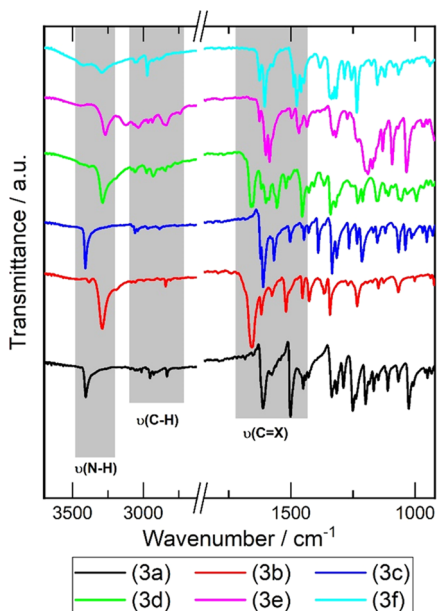
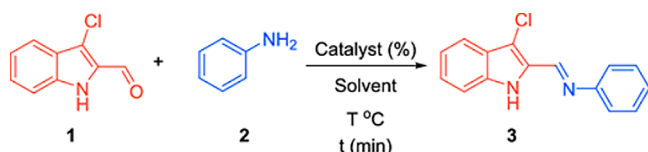


Figure 3. IR spectra of the synthesized Schiff bases.

Table 1. Reaction Optimization<sup>a</sup>



entry	catalyst	load (%)	solvent	T (°C)	t (h)	yield (%)
1			EtOH	65	1	
2	TiO <sub>2</sub>	10	EtOH	65	1	10
3	Ag(5%)@TiO <sub>2</sub>	10	EtOH	65	1	60
4	Au(5%)@TiO <sub>2</sub>	10	EtOH	65	1	72
5	Au(1%)@TiO <sub>2</sub>	10	EtOH	65	1	70
6	Au(1%)@TiO <sub>2</sub>	10	EtOH	65	2	75
7	Au(1%)@TiO <sub>2</sub>	10	EtOH	65	3	85
8	Au(1%)@TiO <sub>2</sub>	10	H <sub>2</sub> O	65	3	30
9	Au(1%)@TiO <sub>2</sub>	10	CH <sub>2</sub> Cl <sub>2</sub>	65	3	traces
10	Au(1%)@TiO <sub>2</sub>	10	CH <sub>3</sub> CN	65	3	25
11	Au(1%)@TiO <sub>2</sub>	0.5	EtOH	65	3	traces
12	Au(1%)@TiO <sub>2</sub>	5	EtOH	65	3	30
13	Au(1%)@TiO <sub>2</sub>	20	EtOH	65	3	85
14	piperidine	5 drops	EtOH	65	3	50
15	piperidine	5 drops	EtOH	reflux	5	85

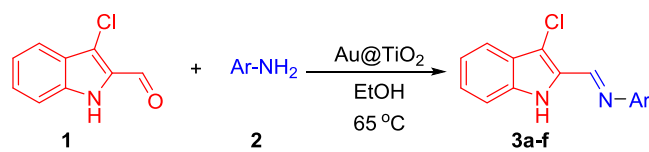
<sup>a</sup>Unless noted otherwise, the reactions of **1** (3 mmol) and aniline (1 equiv) were carried out with Au@TiO<sub>2</sub> in 10 mL of solvent and at 65 °C for the mentioned time (*t*) in hours.

delivered the Schiff base product in 72% and 70% yield (entries 4 and 5), respectively. Carrying out the reaction for a longer time boosted the reaction yield, where the product was isolated in 75% and 85% yield after 2 and 3 h, respectively (entries 6 and 7). Moreover, the examination of other solvents illustrated that EtOH allowed the reaction to give the highest yield, while the reaction gave only a 30% yield in H<sub>2</sub>O (entry 8). Trace amounts of Schiff bases were synthesized in the presence of CH<sub>2</sub>Cl<sub>2</sub> and CH<sub>3</sub>CN as solvents (entries 9 and 10, respectively). Furthermore, the catalyst load was also investigated, where the amount of Au catalyst has a considerable effect on the product yield. We found that

lowering the loading of the catalyst to 0.5 and 5% led to a diminished yield (entries 11 and 12). However, increasing the catalyst load to 20% did not significantly increase the reaction yield (entry 13). Keeping all reaction conditions unchanged and using piperidine as a homogeneous catalyst instead of Au@TiO<sub>2</sub> led to the formation of **3** in 50% yield (entry 14). Using piperidine as an organic catalyst under reflux in ethanol for 5 h delivered the product in 85% yield (entry 15). These findings indicated that the optimized procedures for the synthesis of Schiff bases performed the reaction in ethanol at 65 °C in the presence of Au(1%)@TiO<sub>2</sub> with a load of 10%.

The substrate scope for the Schiff base formation was explored (Table 2) using the optimized procedures. Aryl

Table 2. Substrate Scope for Amines<sup>a</sup>



entry	product	t (h)	yield (%)
1	3a	3	85
2	3b	4	80
3	3c	3	88
4	3d	3	85
5	3e	2	90
6	3f	2	90

<sup>a</sup>Unless noted otherwise, the reactions of **1** (3 mmol) and **2** (1 equiv) were carried out with a 10% load of Au(1%)@TiO<sub>2</sub> in EtOH at 65 °C for 3 h.

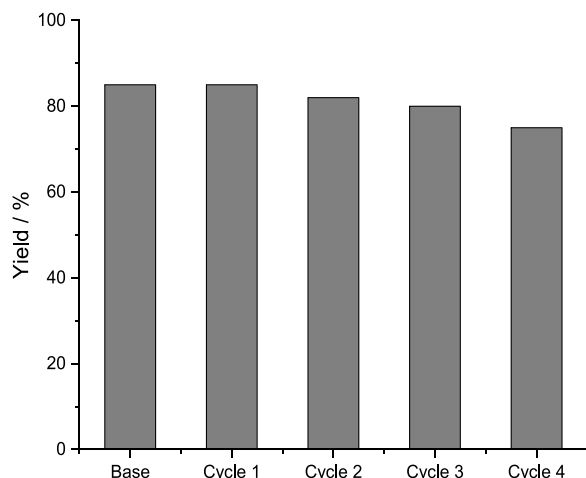
substituents, including electronically rich or poor ones, have been efficiently tolerated in this transformation to afford Schiff base products in high yields. Aromatic amines with the electron-donating group *p*-anisidine gave the corresponding Schiff base product **3a** in a very good yield (85%). Aromatic amines containing an electron-withdrawing group (4-aminoacetophenone) provided the Schiff base product **3b** only without detecting the chalcone byproduct, and the reaction needed a longer time to complete. Furthermore, the scope of substrates containing more substituted arenes with a naphthalene ring has been successfully examined, and the desired products **3c** and **3d** were synthesized in high yields (88 and 85%, respectively). Finally, the substrate of heterocyclic amine was also tolerated in this transformation to give the Schiff bases in high yields. Both **3e** and **3f** Schiff bases obtained from benzothiazole and carbazole substrates were isolated in 90% yield.

Comparing the results obtained by the two methods, it is obvious that the base-free method is a promising alternative route and gave a comparable yield with the conventional method using an organic base (such as piperidine). This strategy is beneficial for the synthesis of different kinds of Schiff bases and may be extended to include the design of new reactions that need organic bases such as Knoevenagel condensation or aldol condensation.

The catalyst was easily separated by dissolving the synthesized Schiff bases, followed by filtration, washing, and drying at 80 °C for 3 h. The catalyst was effective for synthesizing compound **3** for four cycles without a significant decrease in the separated yield as shown in Figure 4a. Comparing the applied conditions during the use of Au(1%)@



### (a) Recycling efficiency



### (b) Mechanism

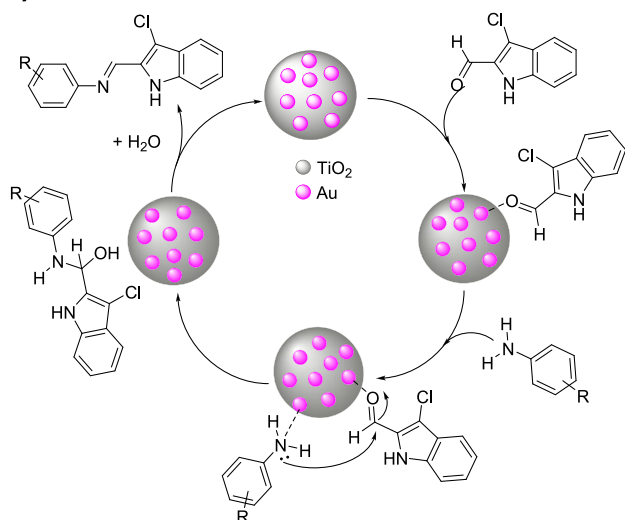


**Figure 4.** (a) Reuse of Au(1%)/TiO<sub>2</sub> in the synthesis of **3** compared to the use of piperidine as a base. (b) Plausible synthetic routes of Schiff bases on Au(1%)/TiO<sub>2</sub>.

TiO<sub>2</sub> to those during the use of base illustrates the mild conditions during the use of Au@TiO<sub>2</sub> with effective catalytic activity and recyclable usage. Also, the Schiff base can be synthesized in water (Table 1), which is considered a green approach. Figure 4b illustrates the plausible mechanistic routes of Schiff's bases on Au@TiO<sub>2</sub>, where the presence of Au(0) in the catalyst would presumably facilitate the coordination with the oxygen of the carbonyl groups of indole-aldehyde or amino groups of amines.<sup>52–56</sup> TiO<sub>2</sub> is considered a weak acid support, and the deposition of Au(0) would enhance the reactivity toward Schiff base synthesis by increasing the number of Lewis acid and Bronsted acid sites. The CHO groups would be polarized due to the presence of acidic sites. Subsequently, amino groups of amines nucleophilically attacked the polarized CHO groups, resulting in the formation of N–C bonds. Then, rearrangements occurred to form OH, which would be elaborated from the compounds with the H atom as H<sub>2</sub>O to give Schiff bases.<sup>52–56</sup> Also, the amino groups have an affinity to bond with Au atoms through the donation–backdonation mechanism, which might facilitate their reaction with formyl groups.<sup>57,58</sup> No changes were observed in the FTIR spectrum

of recycled Au@TiO<sub>2</sub> (Figure S6), which could refer to the stability and reusability of Au@TiO<sub>2</sub> after the synthesis of Schiff bases. The characteristic diffraction peaks of Au NPs and TiO<sub>2</sub> (anatase and rutile) were observed in the XRD spectrum of the recycled Au@TiO<sub>2</sub> (Figure S7). No changes in the XPS Au 4f, Ti 2p, and O 1s spectra of the recycled Au(1%)/TiO<sub>2</sub> catalyst were observed as illustrated in Figure S8. Also, the XPS N 1s spectra of the as-prepared and the recycled Au(1%)/TiO<sub>2</sub> are shown in Figure S9, where nitrogen did not exist on the catalyst. Namely, the recycled catalyst after regeneration was clean without contaminating it with the Schiff base. The content of Au(0) in the catalyst decreased to 70% after recycling, which could describe a slight decrease in the reactivity of the catalyst.

**2.3. Photophysical Behavior.** The photophysical behavior of the selected Schiff bases has been studied in the solution state using DMSO as a solvent. The UV–Vis absorption spectra of the solutions ( $1 \times 10^{-7}$  mol L<sup>-1</sup> for **3b**,  $1 \times 10^{-9}$  mol L<sup>-1</sup> for **3a**, **3c**, and **3f**) are displayed in Figure 5a. Due to the weak absorption of **3b**, its spectrum is presented separately as an inset of Figure 5a. The studied compounds showed absorption bands in the region of 290–440 nm with peaks at  $\lambda_{\text{max}}$  around 365 nm for **3a** and **3c**, 315 nm for **3b**, and 395 nm for **3f**. These absorption peaks can be ascribed to the  $\pi \rightarrow \pi^*$  transitions. The peaks at 280–320 nm have resulted from the  $\pi \rightarrow \pi^*$  transitions of the aromatic core. The bands at the range of 300–360 nm involve  $\pi \rightarrow \pi^*$  transitions of the C=N groups. The longer wavelength absorptions reflect the extended conjugation in the whole molecule. On the other hand, these materials are transparent in the region of 450–700 nm. The different absorption spectra of these Schiff bases suggest different ground states of their solutions due to having different substituents.

Furthermore, the emission spectra of the studied compounds have been measured as illustrated in Figure 5b. It has been reported that inserting electron-donating or electron-withdrawing groups into Schiff bases can decrease or increase the energy gap ( $E_{\text{gap}}$ ) between the lowest unoccupied molecular orbital (LUMO) and the highest occupied molecular orbital (HOMO) to cause a red or blue shift, respectively.<sup>59</sup> However, there is no significant change in  $\lambda_{\text{max}}$  of the emission spectra for **3a** and **3b** (about 415 nm for both) with the electron-donating (methoxy) and -withdrawing (acetyl) groups, respectively.  $E_{\text{gap}}$  of the gaseous state could be different from that of the solution or solid states because some interactions disturb the electronic distribution around the molecule and subsequently change the  $E_{\text{gap}}$ . Therefore, we speculate that attaching these groups to the phenyl ring does not affect  $E_{\text{gap}}$  of these Schiff bases due to the interaction of these polar molecules with the solvent molecules (DMSO). On the other hand, replacing the phenyl ring of **3a** and **3b** with naphthyl and carbazolyl rings in **3c** and **3f** red-shifted the emission  $\lambda_{\text{max}}$  to 430 and 450 nm, respectively. This result implies the ability of the substituent groups to increase  $E_{\text{HOMO}}$  in the order carbazolyl > naphthyl > phenyl. The emission colors were determined quantitatively using a Commission Internationale de l'Éclairage (CIE) chromaticity diagram, Figure 5c. CIE of **3a** showed light-blue emission with coordinates of (0.17, 0.15), while **3b**, **3c**, and **3f** gave deep-blue emission with coordinates of (0.16, 0.09), (0.16, 0.07), and (0.15, 0.09), respectively. Blue light-emitting dyes are basic for realizing the full-color display in OLEDs.<sup>60</sup>

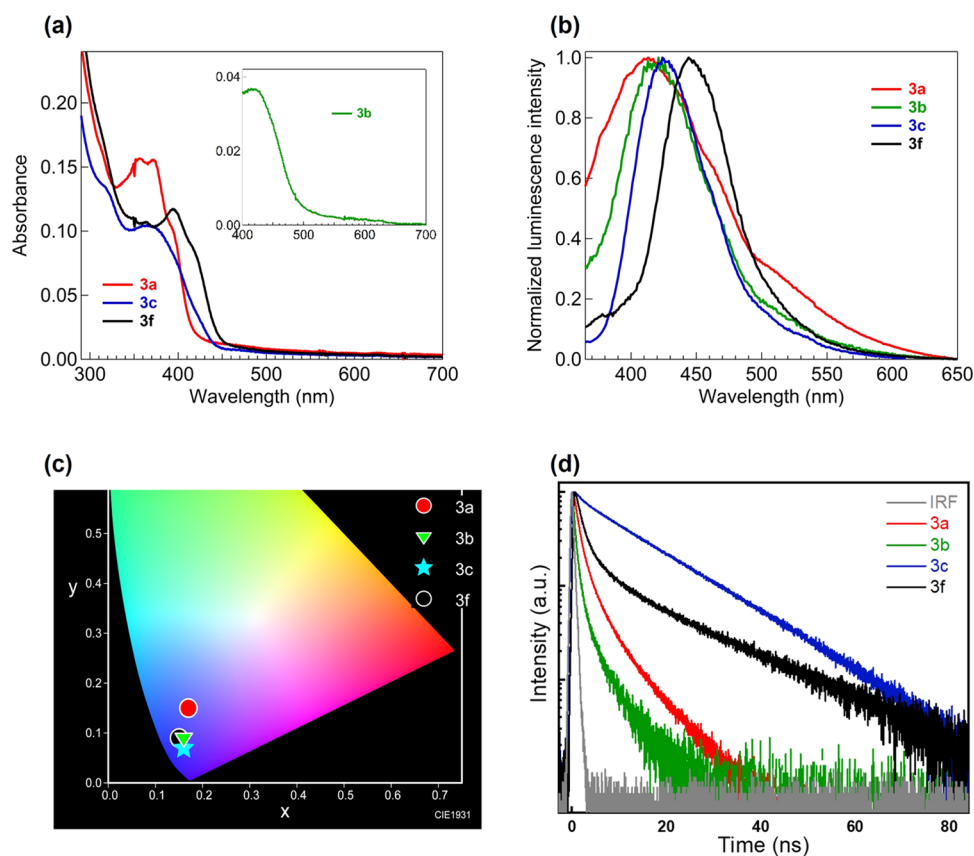


**Figure 5.** Photophysical behavior of DMSO solutions of **3a**, **3b**, **3c**, and **3f** at room temperature: (a) UV-vis absorption spectra ( $1 \times 10^{-7}$  mol L $^{-1}$  for **3b** and  $1 \times 10^{-9}$  mol L $^{-1}$  for **3a**, **3c**, and **3f**). (b) Emission spectra with excitation at 320 nm ( $1 \times 10^{-7}$  mol L $^{-1}$ ). (c) CIE chromaticity diagram of the emission colors. (d) Photoluminescence decay profiles with excitation at 320 nm.

Additionally, the smaller the CIE coordinates of the blue light, the less the power consumption of OLEDs, where it has been reported that deeper blue emitters are predicted to boost white OLED performance due to the fact that power consumption diminishes as blue saturation increases.<sup>61–64</sup> The photoluminescence lifetime of the examined compounds was also estimated in the solution state. Figure 5d displays the logarithmic graph of the emission decay curve. Despite having different spectral shapes owing to the different molecular structures, the studied Schiff bases showed similar biexponential decay profiles with emission lifetimes on the order of nanoseconds. Thus, the emission of the materials can be assigned as fluorescence emitted from singlet excited states. This fluorescence was also confirmed from the close  $\lambda_{\text{max}}$  of both the absorption and emission spectra given in Figure 5a,b. The compounds displayed similar decay profiles because their luminescent centers are comparable. The detailed parameters with the corresponding relative amplitudes ( $A_i$ ) are summarized in Table S1.

### 3. CONCLUSIONS

In this report, new Schiff bases have been synthesized for the first time on the Au@TiO $_2$  heterogeneous catalyst under mild conditions. The optimal procedures for accomplishing the synthesis of Schiff bases were mixing the aldehydes and amines in ethanol as a solvent at 65 °C for 3 h in the presence of Au(1%)@TiO $_2$ . In water, the isolated yield of Schiff base was 30%, which is considered a green approach for synthesizing Schiff bases. The catalyst was easily recycled from the reaction

mixture and showed reusability for four cycles without a significant decrease in the isolated yield. Additionally, the synthesized Schiff bases demonstrated some interesting luminescence behaviors, such as the dependence of the spectral shape on the substituent group and the emission of deep-blue fluorescence with CIE coordinates of  $y < 0.1$ . Therefore, these dyes may help design new OLEDs with reduced energy consumption.

## 4. EXPERIMENTAL SECTION

**4.1. Synthesis of Au@TiO $_2$ .** In total, 1 g of TiO $_2$  (P25, Degussa, 20 nm) was transferred into a Teflon container. Then, 20 mL of water and 20 mL of ethanol were mixed and transferred into the Teflon container. The Teflon container was sonicated for 20 min, and subsequently, the appropriate amount of HAuCl $_4$ ·3H $_2$ O (BDH, 1% w/v) was added into the Teflon container and sonicated for an additional 20 min. The Teflon container closed well in a stainless-steel autoclave and was heated at 180 °C for 12 h. Then, Au@TiO $_2$  was separated through centrifuging at 4000 rpm, washed using deionized water three times, and dried at 80 °C for 8 h. The amount of HAuCl $_4$ ·3H $_2$ O was calculated to prepare Au(1%)@TiO $_2$  and Au(5%)@TiO $_2$ .

**4.2. Synthesis of Schiff Bases.** **4.2.1. Base-Catalyzed Synthesis of the Schiff Bases.** All the Schiff base derivatives were synthesized by refluxing an ethanolic solution of 3-chloro-1H-indole-2-carbaldehyde (**1**) (6 mmol, 0.5 gm) and the corresponding aromatic or heterocyclic amine (6 mmol) in 1:1 stoichiometric ratio for the mentioned time in the presence of

piperidine catalyst (five drops).<sup>22,50,51</sup> The solid precipitate formed after cooling the reaction mixture was filtered off, dried, and recrystallized from ethanol to afford the desired pure compounds.

**4.2.2. Base-Free Synthesis of the Schiff Bases.** In a typical reaction procedure, 3-chloro-1H-indole-2-carbaldehyde **1** (0.5 gm, 3 mmol), aniline (0.28 gm, 3 mmol), ethanol (15 mL) as the solvent, and catalyst (50 mg) were added into a 50 mL reaction vessel. The resulting mixture was stirred at 65 °C in an oil bath for 3 h. After confirming the reaction completion using TLC, ethyl acetate was added to the reaction mixture, and the catalyst was filtered. The solvent was evaporated at reduced pressure using a rotary evaporator to give the desired product.

**4.3. Characterization Instruments and Photophysical Measurements.** Structural analysis was studied using a Philips 1700 version diffractometer X-ray powder diffractometer (XRD) equipped with Cu K $\alpha$  radiation. A transmission electron microscope (TEM, JEOL, JEM-2100F, Japan) was used for investigating the morphologies and crystallinity of the developed catalyst, where an accelerating voltage of 200 kV was applied. XPS spectra of samples were collected using a Kratos AXIS Supra, Japan, with the monochromatic AL anode (1486.6 eV). CasaXPS software was utilized for data analysis. All melting points were measured on a Fisher-John apparatus. IR spectra were registered on a Pye-Unicam Sp-100 spectrophotometer utilizing the KBr wafer method. NMR analyses were performed on Bruker BioSpin GmbH (<sup>1</sup>H: 500 MHz, <sup>13</sup>C: 125 MHz) spectrometers using tetramethylsilane (TMS) as an internal standard and DMSO-*d*<sub>6</sub> as a solvent. Analytical TLC was completed on silica gel plates (Fluka 70643-50EA, Sigma-Aldrich, Germany) utilizing UV light. Absorption spectra were recorded with a SPECORD S600 UV/Vis spectrophotometer (Analytik Jena, Jena, Germany). PL spectra were collected using an FP-8500 spectrofluorometer (Jasco, Groß-Umstadt, Germany). The excitation wavelength was 320 nm with a bandwidth of 5 nm. The PMT voltage was set to 580 V. All measurements were performed in ambient air and at room temperature. The sample solution was excited using a pulsed LED PLS320 at 320 nm (Fluo Time 100, PicoQuant, FWHM ~800 ps). For all samples, a long-pass filter at 390 nm was inserted routinely to block stray light of the excitation source.

## ■ ASSOCIATED CONTENT

### SI Supporting Information

The Supporting Information is available free of charge at <https://pubs.acs.org/doi/10.1021/acsomega.1c06636>.

TEM, HR-TEM, SAED, EDX mapping, XPS, and analytical data of Schiff bases (color, melting point, IR, <sup>1</sup>H NMR, <sup>13</sup>C NMR, and MS) (PDF)

## ■ AUTHOR INFORMATION

### Corresponding Authors

**Ahmed I. A. Soliman** – Chemistry Department, Faculty of Science, Assiut University, Assiut 71516, Egypt; Chemical Engineering Department, Lakehead University, Thunder Bay, Ontario P7B 5E1, Canada; [orcid.org/0000-0001-8851-3887](https://orcid.org/0000-0001-8851-3887); Email: [ahmed.soliman.38z@science.aun.edu.eg](mailto:ahmed.soliman.38z@science.aun.edu.eg)

**Markus Braun** – Institute of Physical and Theoretical Chemistry, Goethe University, 60438 Frankfurt am Main, Germany; Email: [braun@theochem.uni-frankfurt.de](mailto:braun@theochem.uni-frankfurt.de)

## Authors

**Mostafa Sayed** – Chemistry Department, Faculty of Science, New Valley University, El-Kharga 72511, Egypt; Hefei National Laboratory for Physical Sciences at the Microscale, Department of Chemistry, University of Science and Technology of China, Hefei 230026, China; [orcid.org/0000-0002-5469-0129](https://orcid.org/0000-0002-5469-0129)

**Mahmoud M. Elshanawany** – Institute of Physical and Theoretical Chemistry, Goethe University, 60438 Frankfurt am Main, Germany

**Osama Younis** – Chemistry Department, Faculty of Science, New Valley University, El-Kharga 72511, Egypt; [orcid.org/0000-0001-9822-0228](https://orcid.org/0000-0001-9822-0228)

**Mostafa Ahmed** – Chemistry Department, Faculty of Science, New Valley University, El-Kharga 72511, Egypt; [orcid.org/0000-0002-3264-9299](https://orcid.org/0000-0002-3264-9299)

**Adel M. Kamal El-Dean** – Chemistry Department, Faculty of Science, Assiut University, Assiut 71516, Egypt

**Aboel-Magd A. Abdel-Wahab** – Chemistry Department, Faculty of Science, Assiut University, Assiut 71516, Egypt

**Josef Wachtveitl** – Institute of Physical and Theoretical Chemistry, Goethe University, 60438 Frankfurt am Main, Germany; [orcid.org/0000-0002-8496-8240](https://orcid.org/0000-0002-8496-8240)

**Pedram Fatehi** – Chemical Engineering Department, Lakehead University, Thunder Bay, Ontario P7B 5E1, Canada; [orcid.org/0000-0002-3874-5089](https://orcid.org/0000-0002-3874-5089)

**Mahmoud S. Tolba** – Chemistry Department, Faculty of Science, New Valley University, El-Kharga 72511, Egypt; [orcid.org/0000-0002-4794-6130](https://orcid.org/0000-0002-4794-6130)

Complete contact information is available at:

<https://pubs.acs.org/doi/10.1021/acsomega.1c06636>

## Author Contributions

\*A.I.A.S., M.S., and M.M.E. contributed equally to this work.

## Notes

The authors declare no competing financial interest.

## ■ ACKNOWLEDGMENTS

M.M.E., M.B., and J.W. acknowledge funding from the German Research Foundation DFG (WA 1850/6-2). Deep thanks to Dr. Isam Elamri and Sina Roth (Goethe University) for helpful discussions.

## ■ REFERENCES

- (1) Hamed, A. A.; Abdelhamid, I. A.; Saad, G. R.; Elkady, N. A.; Elsabee, M. Z. Synthesis, Characterization and Antimicrobial Activity of a Novel Chitosan Schiff Bases Based on Heterocyclic Moieties. *Int. J. Biol. Macromol.* **2020**, *153*, 492–501.
- (2) Erturk, A. G. Synthesis, Structural Identifications of Bioactive Two Novel Schiff Bases. *J. Mol. Struct.* **2020**, *1202*, 127299.
- (3) Bhagat, S.; Sharma, N.; Chundawat, T. S. Synthesis of Some Salicylaldehyde-Based Schiff Bases in Aqueous Media. *J. Chem.* **2013**, *2013*, 1–4.
- (4) Mladenova, R.; Ignatova, M.; Manolova, N.; Petrova, T.; Rashkov, I. Preparation, Characterization and Biological Activity of Schiff Base Compounds Derived from 8-Hydroxyquinoline-2-Carboxaldehyde and Jeffamines ED. *Eur. Polym. J.* **2002**, *38*, 989–999.
- (5) Sinha, D.; Tiwari, A. K.; Singh, S.; Shukla, G.; Mishra, P.; Chandra, H.; Mishra, A. K. Synthesis, Characterization and Biological Activity of Schiff Base Analogues of Indole-3-Carboxaldehyde. *Eur. J. Med. Chem.* **2008**, *43*, 160–165.
- (6) Singh, G.; Kalra, P.; Arora, A.; Singh, A.; Sharma, G.; Sanchita; Maurya, I. K.; Dutta, S.; Munshi, P.; Verma, V. Acetylenic Indole-Encapsulated Schiff Bases: Synthesis, In Silico Studies as Potent

- Antimicrobial Agents, Cytotoxic Evaluation and Synergistic Effects. *ChemistrySelect* **2018**, *3*, 2366–2375.
- (7) Reshma, R.; Joseyphus, R. S.; Dasan, A.; John, L. Synthesis and Spectral Characterization of Metal Complexes of Schiff Base Derived from Indole-3-Carboxaldehyde and L-Histidine as Potent Biocides. *J. Coord. Chem.* **2019**, *72*, 3326–3337.
- (8) Malik, M. A.; Dar, O. A.; Gull, P.; Wani, M. Y.; Hashmi, A. A. Heterocyclic Schiff Base Transition Metal Complexes in Antimicrobial and Anticancer Chemotherapy. *MedChemComm* **2018**, *9*, 409–436.
- (9) Pan, C.; Wang, K.; Ji, S.; Wang, H.; Li, Z.; He, H.; Huo, Y. Schiff Base Derived Fe<sup>3+</sup>-Selective Fluorescence Turn-off Chemosensors Based on Triphenylamine and Indole: Synthesis, Properties and Application in Living Cells. *RSC Adv.* **2017**, *7*, 36007–36014.
- (10) Abu-Dief, A. M.; Mohamed, I. M. A. A Review on Versatile Applications of Transition Metal Complexes Incorporating Schiff Bases. *Beni-Suef Univ. J. Basic Appl. Sci.* **2015**, *4*, 119–133.
- (11) Aqeel Ashraf, M.; Liu, Z.; Li, Y. Y.; Li, C.; Zhang, D. Zinc Nanomagnetic Catalysts in Organic Synthesis. *Synth. Commun.* **2021**, *51*, 37–56.
- (12) He, R.; Zhou, J.; Mao, W. The Application of MNPs-Ag Catalysts in Organic Synthesis. *Synth. Commun.* **2021**, *1*, 1478–1495.
- (13) Gisbertz, S.; Pieber, B. Heterogeneous Photocatalysis in Organic Synthesis. *ChemPhotoChem* **2020**, *4*, 456–475.
- (14) Bai, Y.; Chen, J.; Zimmerman, S. C. Designed Transition Metal Catalysts for Intracellular Organic Synthesis. *Chem. Soc. Rev.* **2018**, *47*, 1811–1821.
- (15) Afewerki, S.; Córdova, A. Combinations of Aminocatalysts and Metal Catalysts: A Powerful Cooperative Approach in Selective Organic Synthesis. *Chem. Rev.* **2016**, *116*, 13512–13570.
- (16) Appaturi, J. N.; Ratti, R.; Phoon, B. L.; Batagarawa, S. M.; Din, I. U.; Selvaraj, M.; Ramalingam, R. J. A Review of the Recent Progress on Heterogeneous Catalysts for Knoevenagel Condensation. *Dalton Trans.* **2021**, *50*, 4445–4469.
- (17) Wang, K.; Gao, W.; Jiang, P.; Lan, K.; Yang, M.; Huang, X.; Ma, L.; Niu, F.; Li, R. Bi-Functional Catalyst of Porous N-Doped Carbon with Bimetallic FeCu for Solvent-Free Resultant Imines and Hydrogenation of Nitroarenes. *Mol. Catal.* **2019**, *465*, 43–53.
- (18) Tayefe, H. C.; Sazegar, M. R.; Mahmoudi, A.; Jadidi, K. Catalyzed Schiff Base Synthesis over Bifunctionalized Cobalt/Zinc-Incorporated Mesoporous Silica Nanoparticles under UV Irradiation. *J. Nanostruct.* **2019**, *9*, 712–722.
- (19) Naeimi, H.; Salimi, F.; Rabiei, K. Mild and Convenient One Pot Synthesis of Schiff Bases in the Presence of P<sub>2</sub>O<sub>5</sub>/Al<sub>2</sub>O<sub>3</sub> as New Catalyst under Solvent-Free Conditions. *J. Mol. Catal., A* **2006**, *260*, 100–104.
- (20) Fei, H.; Yang, Y.; Peng, Z.; Ruan, G.; Zhong, Q.; Li, L.; Samuel, E. L. G.; Tour, J. M. Cobalt Nanoparticles Embedded in Nitrogen-Doped Carbon for the Hydrogen Evolution Reaction. *ACS Appl. Mater. Interfaces* **2015**, *7*, 8083–8087.
- (21) Gomha, S. M.; Ahmed, H. A.; Shaban, M.; Abolibda, T. Z.; Khushaim, M. S.; Alharbi, K. A. Synthesis, Optical Characterizations and Solar Energy Applications of New Schiff Base Materials. *Materials* **2021**, *14*, 3718.
- (22) Younis, O.; Orabi, E. A.; Kamal, A. M.; Sayed, M.; Hassanien, R.; Davis, R. L.; Tsutsumi, O.; Ahmed, M. Aggregation-Induced Emission with White, Green, or Blue Luminescence from Biologically-Active Indole Derivatives. *Opt. Mater.* **2020**, *100*, 109713.
- (23) Younis, O.; El-Katori, E. E.; Hassanien, R.; Abousalem, A. S.; Tsutsumi, O. Luminescent Coatings: White-Color Luminescence from a Simple and Single Chromophore with High Anticorrosion Efficiency. *Dyes Pigm.* **2020**, *175*, 108146.
- (24) Younis, O.; Sami, H.; Maruoka, Y.; Hisano, K.; Tsutsumi, O. Fascinating Phenomena towards Single-Component White-Light Emission through Luminescent Thermochromism. *Dyes Pigm.* **2021**, *194*, 109621.
- (25) Younis, O.; Rokusha, Y.; Sugimoto, N.; Fujisawa, K.; Yamada, S.; Tsutsumi, O. Effects of Molecular Structure and Aggregated Structure on Photoluminescence Properties of Liquid-Crystalline Gold(I) Complexes with Various Aromatic Rings. *Mol. Cryst. Liq. Cryst.* **2015**, *617*, 21–31.
- (26) Younis, O.; Abdel-Hakim, M.; Sayed, M. M.; Tsutsumi, O.; Aly, K. I. Liquid Crystal Polymers as Luminescent Coatings: Single-Component White-Light Photoluminescence and Corrosion Inhibition. *J. Lumin.* **2021**, *239*, 118361.
- (27) Aly, K. I.; Younis, O.; Mahross, M. H.; Tsutsumi, O.; Mohamed, M. G.; Sayed, M. M. Novel Conducting Polymeric Nanocomposites Embedded with Nanoclay: Synthesis, Photoluminescence, and Corrosion Protection Performance. *Polym. J.* **2019**, *51*, 77–90.
- (28) Younis, O.; Tsutsumi, O. Single-Component White-Color Photoluminescence from Liquid Crystal Polymers: Color Tuning by a Combination of Luminescence Thermo- and Mechanochromism. *Dyes Pigm.* **2021**, *188*, 109189.
- (29) Elshanawany, M. M.; Ricciardulli, A. G.; Saliba, M.; Wachtveitl, J.; Braun, M. Mechanism of Ultrafast Energy Transfer between the Organic-Inorganic Layers in Multiple-Ring Aromatic Spacers for 2D Perovskites. *Nanoscale* **2021**, *13*, 15668–15676.
- (30) Sayed, M.; Younis, O.; Hassanien, R.; Ahmed, M.; Mohammed, A. A. K.; Kamal, A. M.; Tsutsumi, O. Design and Synthesis of Novel Indole Derivatives with Aggregation-Induced Emission and Antimicrobial Activity. *J. Photochem. Photobiol. A* **2019**, *383*, 111969.
- (31) Ahmed, M.; Younis, O.; Orabi, E. A.; Sayed, A. M.; Kamal El-Dean, A. M.; Hassanien, R.; Davis, R. L.; Tsutsumi, O.; Tolba, M. S. Synthesis of Novel Biocompatible Thienopyrimidine Chromophores with Aggregation-Induced Emission Sensitive to Molecular Aggregation. *ACS Omega* **2020**, *5*, 29988–30000.
- (32) Younis, O.; Tolba, M. S.; Orabi, E. A.; Kamal, A. M.; Hassanien, R.; Tsutsumi, O.; Ahmed, M. Biologically-Active Heterocyclic Molecules with Aggregation-Induced Blue-Shifted Emission and Efficient Luminescence Both in Solution and Solid States. *J. Photochem. Photobiol. A* **2020**, *400*, 112642.
- (33) Phomma, S.; Wutikhun, T.; Kasamechonchung, P.; Eksangsri, T.; Saphcharoenkun, C. Effect of Calcination Temperature on Photocatalytic Activity of Synthesized TiO<sub>2</sub> Nanoparticles via Wet Ball Milling Sol-Gel Method. *Appl. Sci.* **2020**, *10*, 993.
- (34) He, J.; Du, Y.; Bai, Y.; An, J.; Cai, X.; Chen, Y.; Wang, P.; Yang, X.; Feng, Q. Facile Formation of Anatase/Rutile TiO<sub>2</sub> Nanocomposites with Enhanced Photocatalytic Activity. *Molecules* **2019**, *24*, 2996.
- (35) Almarshori, K.; Ali, T. T.; Saeed, A.; Alwafi, R.; Aly, M.; Al-Hazmi, F. E. Antibacterial and Photocatalytic Activities of Controllable (Anatase/Rutile) Mixed Phase TiO<sub>2</sub> Nanophotocatalysts Synthesized: Via a Microwave-Assisted Sol-Gel Method. *New J. Chem.* **2020**, *44*, 562–570.
- (36) Haque, F. Z.; Nandanwar, R.; Singh, P. Evaluating Photodegradation Properties of Anatase and Rutile TiO<sub>2</sub> Nanoparticles for Organic Compounds. *Optik* **2017**, *128*, 191–200.
- (37) Abazari, R.; Mahjoub, A. R.; Sanati, S. A Facile and Efficient Preparation of Anatase Titania Nanoparticles in Micelle Nano-reactors: Morphology, Structure, and Their High Photocatalytic Activity under UV Light Illumination. *RSC Adv.* **2014**, *4*, 56406–56414.
- (38) Muniandy, S. S.; Mohd Kaus, N. H.; Jiang, Z. T.; Altarawneh, M.; Lee, H. L. Green Synthesis of Mesoporous Anatase TiO<sub>2</sub> Nanoparticles and Their Photocatalytic Activities. *RSC Adv.* **2017**, *7*, 48083–48094.
- (39) Rodríguez-Martínez, C.; García-Domínguez, ÁE.; Guerrero-Robles, F.; Saavedra-Díaz, R. O.; Torres-Torres, G.; Felipe, C.; Ojedalópez, R.; Silahua-Pavón, A.; Cervantes-Urbe, A. Synthesis of Supported Metal Nanoparticles (Au/TiO<sub>2</sub>) by the Suspension Impregnation Method. *J. Compos. Sci.* **2020**, *4*, 89.
- (40) Nguyen, V. N.; Nguyen, M. V.; Nguyen, T. H. T.; Doan, M. T.; Ngoc, L. L. T.; Janssens, E.; Yadav, A.; Lin, P.-C.; Nguyen, M. S.; Hoang, N. H. Surface-Modified Titanium Dioxide Nanofibers with Gold Nanoparticles for Enhanced Photoelectrochemical Water Splitting. *Catalysts* **2020**, *10*, 261.

- (41) Krupski, K.; Moors, M.; Kobiela, T.; Krupski, A. Structure Determination of Au on Pt(111) Surface: LEED, STM and DFT Study. *Materials* **2015**, *111*, 2935–2952.
- (42) Li, Y.; Wang, H.; Feng, Q.; Zhou, G.; Wang, Z. S. Gold Nanoparticles Inlaid TiO<sub>2</sub> Photoanodes: A Superior Candidate for High-Efficiency Dye-Sensitized Solar Cells. *Energy Environ. Sci.* **2013**, *6*, 2156–2165.
- (43) Arockia Jency, D.; Parimaladevi, R.; Umadevi, M. Au–TiO<sub>2</sub> Core Shell Motif Scavenger: Facile Synthesis, High SERS Effect, Synergistic Photocatalytic Activity. *J. Cluster Sci.* **2018**, *29*, 793–804.
- (44) Deng, Y.; Chen, M.; Chen, G.; Zou, W.; Zhao, Y.; Zhang, H.; Zhao, Q. Visible-Ultraviolet Upconversion Carbon Quantum Dots for Enhancement of the Photocatalytic Activity of Titanium Dioxide. *ACS Omega* **2021**, *6*, 4247–4254.
- (45) Powell, C. D.; Daigh, A. W.; Pollock, M. N.; Chandler, B. D.; Pursell, C. J. Co Adsorption on Au/TiO<sub>2</sub> Catalysts: Observations, Quantification, and Explanation of a Broad-Band Infrared Signal. *J. Phys. Chem. C* **2017**, *121*, 24541–24547.
- (46) Ren, Y.; Xing, S.; Wang, J.; Liang, Y.; Zhao, D.; Wang, H.; Wang, N.; Jiang, W.; Wu, S.; Liu, S.; Liu, C.; Ding, W.; Zhang, Z.; Pang, J.; Dong, C. Weak-Light-Driven Ag–TiO<sub>2</sub> Photocatalyst and Bactericide Prepared by Coprecipitation with Effective Ag Doping and Deposition. *Opt. Mater.* **2022**, *124*, 111993.
- (47) Wu, C.; Soliman, A. I. A.; Tu, Y.; Utsunomiya, T.; Ichii, T.; Sugimura, H. Fabrication of TiO<sub>2</sub> Micropatterns on Flexible Substrates by Vacuum-Ultraviolet Photochemical Treatments. *Adv. Mater. Interfaces* **2020**, *7*, 1901634.
- (48) Oi, L. E.; Choo, M. Y.; Lee, H. V.; Ong, H. C.; Hamid, S. B. A.; Juan, J. C. Recent Advances of Titanium Dioxide (TiO<sub>2</sub>) for Green Organic Synthesis. *RSC Adv.* **2016**, *6*, 108741–108754.
- (49) Lakshminarayana, B.; Satyanarayana, G.; Subrahmanyam, C. Bimetallic Pd-Au/TiO<sub>2</sub> Nanoparticles: An Efficient and Sustainable Heterogeneous Catalyst for Rapid Catalytic Hydrogen Transfer Reduction of Nitroarenes. *ACS Omega* **2018**, *3*, 13065–13072.
- (50) Sayed, M.; Kamal Eldean, A. M.; Ahmed, M. M.; Hassanien, R. Synthesis Of Some New Heterocyclic Compounds Containing Indole Moeity. *Eur. Chem. Bull.* **2017**, *6*, 171.
- (51) Sayed, M.; Kamal El-Dean, A. M.; Ahmed, M.; Hassanien, R. Synthesis of Some Heterocyclic Compounds Derived from Indole as Antimicrobial Agents. *Synth. Commun.* **2018**, *48*, 413–421.
- (52) Maleki, B.; Baghayeri, M.; Vahdat, S. M.; Mohammadzadeh, A.; Akhoondi, S. Ag@TiO<sub>2</sub> Nanocomposite; Synthesis, Characterization and Its Application as a Novel and Recyclable Catalyst for the One-Pot Synthesis of Benzoxazole Derivatives in Aqueous Media. *RSC Adv.* **2015**, *5*, 46545–46551.
- (53) Fatahpour, M.; Noori Sadeh, F.; Hazeri, N.; Maghsoodlou, M. T.; Hadavi, M. S.; Mahnaei, S. Ag/TiO<sub>2</sub> Nano-Thin Films as Robust Heterogeneous Catalyst for One-Pot, Multi-Component Synthesis of Bis (Pyrazol-5-Ol) and Dihydropyrano[2,3-c]Pyrazole Analogs. *J. Saudi Chem. Soc.* **2017**, *21*, 998–1006.
- (54) Mondal, R. K.; Riyajuddin, S.; Ghosh, A.; Ghosh, S.; Ghosh, K.; Islam, S. M. Polymer Immobilized [Mg@PS-Anthra] Complex: An Efficient Recyclable Heterogeneous Catalyst for the Incorporation of Carbon Dioxide into Oxiranes at Atmospheric Pressure and Knoevenagel Condensation Reaction under Solvent Free Condition. *J. Organomet. Chem.* **2019**, *880*, 322–332.
- (55) Ameer, N.; Ferouani, G.; Belkadi, Z.; Bachir, R.; Calvino, J. J.; Hakkoum, A. A Novel Approach for the Preparation of Silver Nanoparticles Supported on Titanate Nanotubes and Bentonite-Application in the Synthesis of Heterocyclic Compound Derivatives. *Mater. Res. Express* **2019**, *6*, 125051.
- (56) Puthiaraj, P.; Yu, K.; Baeck, S. H.; Ahn, W. S. Cascade Knoevenagel Condensation-Chemosselective Transfer Hydrogenation Catalyzed by Pd Nanoparticles Stabilized on Amine-Functionalized Aromatic Porous Polymer. *Catal. Today* **2020**, *352*, 298–307.
- (57) Hoft, R. C.; Ford, M. J.; McDonagh, A. M.; Cortie, M. B. Adsorption of Amine Compounds on the Au(111) Surface: A Density Functional Study. *J. Phys. Chem. C* **2007**, *111*, 13886–13891.
- (58) Naya, S.; Kimura, K.; Tada, H. One-Step Selective Aerobic Oxidation of Amines to Imines by Gold Nanoparticle-Loaded Rutile Titanium(IV) Oxide Plasmon Photocatalyst. *ACS Catal.* **2013**, *3*, 10–13.
- (59) Wang, K.; Su, H.; Wang, P.; Wang, W.; Li, H. The Enhancement of the D-A Effect of an Asymmetric Schiff Base by Introducing Acetyl Groups into Diaminomaleonitrile: Synthesis, Red Fluorescence and Crystal Structure. *RSC Adv.* **2019**, *9*, 14268–14275.
- (60) Gao, Z. Q.; Li, Z. H.; Xia, P. F.; Wong, M. S.; Cheah, K. W.; Chen, C. H. Efficient Deep-Blue Organic Light-Emitting Diodes: Arylamine-Substituted Oligofluorenes. *Adv. Funct. Mater.* **2007**, *17*, 3194–3199.
- (61) Tung, Y.-J.; Ngo, T.; Hack, M.; Brown, J.; Koide, N.; Nagara, Y.; Kato, Y.; Ito, H. A High Efficiency Phosphorescent White OLED for LCD Backlight and Display Applications. *SID Symp. Dig. Tech. Pap.* **2004**, *35*, 48.
- (62) Wu, C.-C.; Lin, Y.-T.; Wong, K.-T.; Chen, R.-T.; Chien, Y.-Y. Efficient Organic Blue-Light-Emitting Devices with Double Confinement on Terfluorenes with Ambipolar Carrier Transport Properties. *Adv. Mater.* **2004**, *16*, 61–65.
- (63) Xia, G.; Qu, C.; Zhu, Y.; Ye, J.; Ye, K.; Zhang, Z.; Wang, Y. A TADF Emitter Featuring Linearly Arranged Spiro-Donor and Spiro-Acceptor Groups: Efficient Nondoped and Doped Deep-Blue OLEDs with CIEy <0.1. *Angew. Chem., Int. Ed.* **2021**, *60*, 9598–9603.
- (64) Ahn, D. H.; Kim, S. W.; Lee, H.; Ko, I. J.; Karthik, D.; Lee, J. Y.; Kwon, J. H. Highly Efficient Blue Thermally Activated Delayed Fluorescence Emitters Based on Symmetrical and Rigid Oxygen-Bridged Boron Acceptors. *Nat. Photonics* **2019**, *13*, 540–546.

## Recommended by ACS

### Substituted 2,4-Di(pyridin-2-yl)pyrimidine-Based Ruthenium Photosensitizers for Hydrogen Photoevolution under Red Light

Mira T. Rupp, Dirk G. Kurth, *et al.*

DECEMBER 15, 2020  
INORGANIC CHEMISTRY

READ 

### Designing a New Efficient Photocatalyst Based on Functionalization of Zn-Infinite Coordination Polymer with Ru(acac)<sub>3</sub> Complex for Dye Degradation in Aq...

Nazanin Mosleh, Majid Masteri-Farahani, *et al.*

NOVEMBER 17, 2020  
LANGMUIR

READ 

### Selective Extraction, Recovery, and Sensing of Hydroquinone Mediated by a Supramolecular Pillar[5]quinone Quinhydrone Charge-Transfer Com...

Puttipong Pananusorn, Thanthapatra Bunchuay, *et al.*

JANUARY 30, 2022  
ACS APPLIED MATERIALS & INTERFACES

READ 

### Metal-Free Organic Optoelectronic Molecule as a Highly Efficient Photocatalyst for the Degradation of Organic Pollutants

Xinyu Zhang, Rong Xing, *et al.*

MARCH 29, 2019  
ACS OMEGA

READ 

Get More Suggestions >

Supporting Information of

# Base-free Synthesis and Photophysical Properties of New Schiff Bases Containing Indole Moiety

*Ahmed I. A. Soliman<sup>a,b,#,\*</sup>, Mostafa Sayed<sup>c,d,#</sup>, Mahmoud M. Elshanawany<sup>e,#</sup>, Osama Younis<sup>c</sup>  
Mostafa Ahmed<sup>c</sup>, Adel M. Kamal El-Dean<sup>a</sup>, Aboel-Magd A. Abdel-Wahab<sup>a</sup>, Josef Wachtveitl<sup>e</sup>,  
Markus Braun<sup>e,\*</sup>, Pedram Fatehi<sup>b</sup>, Mahmoud S. Tolba<sup>c</sup>.*

[a] Chemistry Department, Faculty of Science, Assiut University, Assiut 71516, Egypt

[b] Department of Chemical Engineering, Lakehead University, 955 Oliver Road, Thunder Bay,  
ON, P7B 5E1, Canada

[c] Chemistry Department, Faculty of Science, New Valley University, El-Kharga, 72511,  
Egypt.

[d] Hefei National Laboratory for Physical Sciences at the Microscale, Department of Chemistry,  
Center for Excellence in Molecular Synthesis of CAS, University of Science and Technology of  
China, Tai hu road, Hefei 230026.

[e] Institute of Physical and Theoretical Chemistry, Goethe University, 60438, Frankfurt am Main, Germany.

# These authors contributed equally to this work.

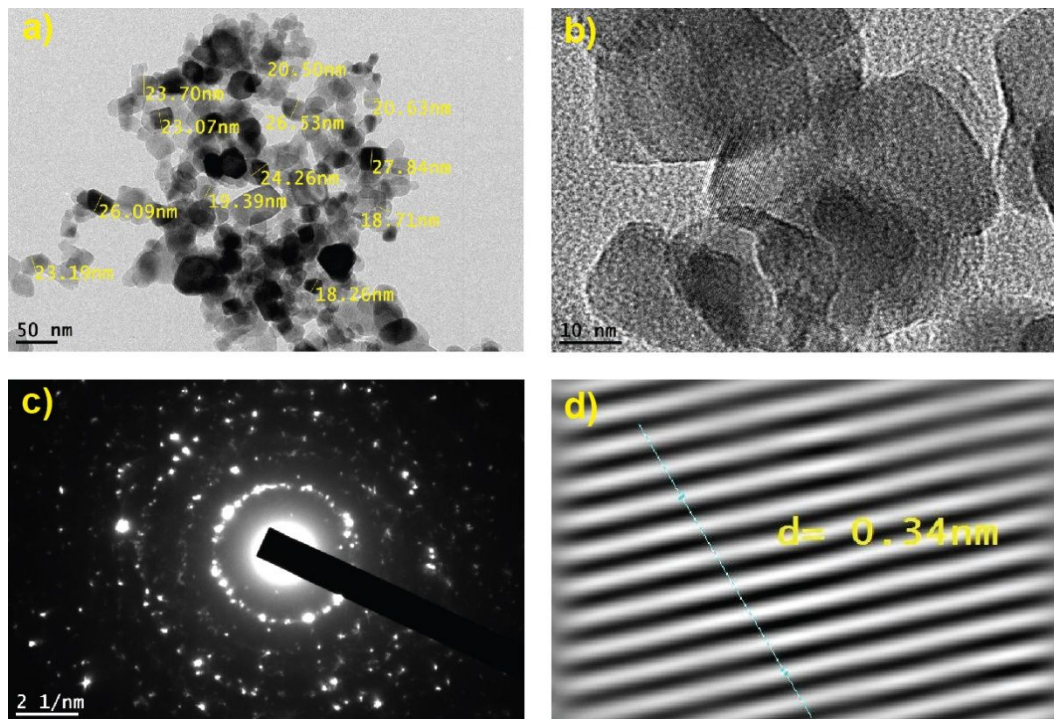


**Figure S1.** (a,b) TEM images, c) SAED patterns, and d) HR-TEM of TiO<sub>2</sub> (P25).

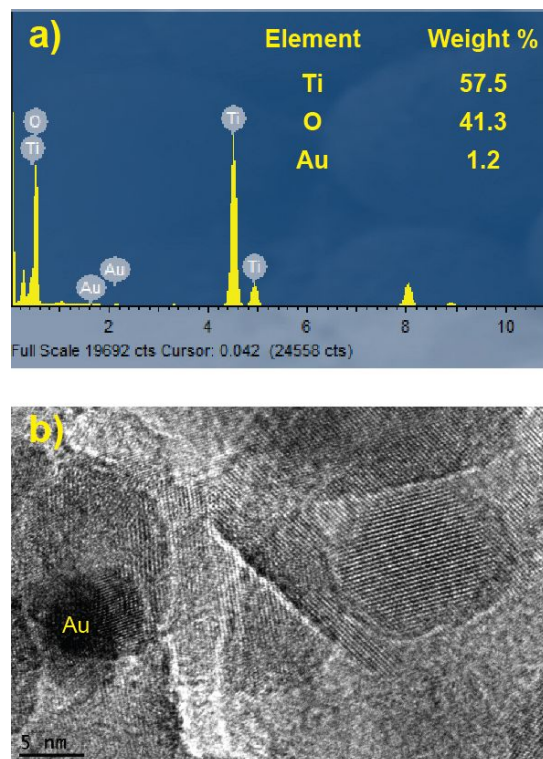


**Figure S2.** a) EDX of Au(1%)@TiO<sub>2</sub>, and b) HR-TEM images of Au(5%)@TiO<sub>2</sub>.

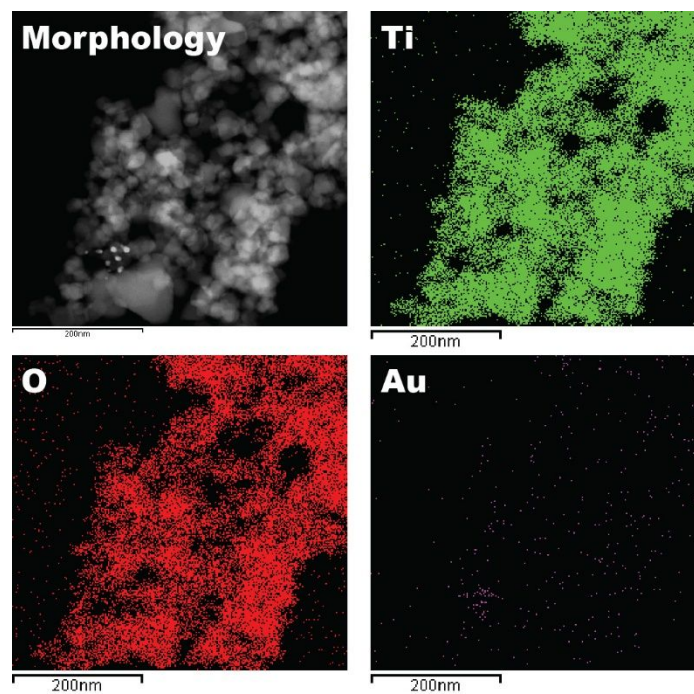


**Figure S3.** Morphology and EDX-mapping titanium, oxygen, and gold of Au(1%)@TiO<sub>2</sub>.



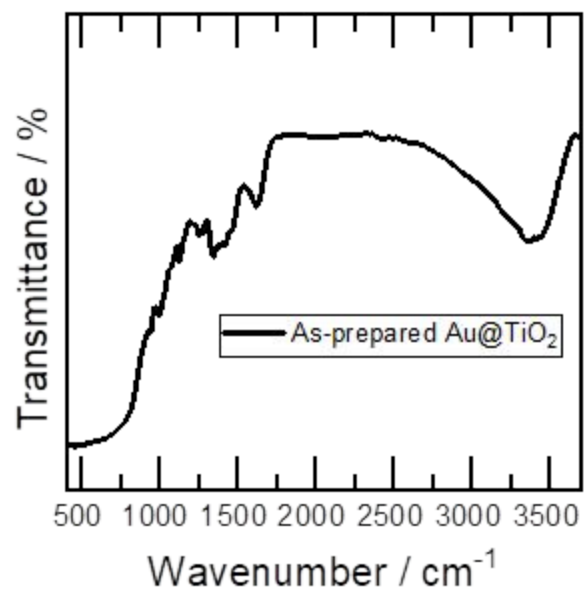


**Figure S4.** FTIR spectra of the as-prepared Au(1%)@TiO<sub>2</sub>.

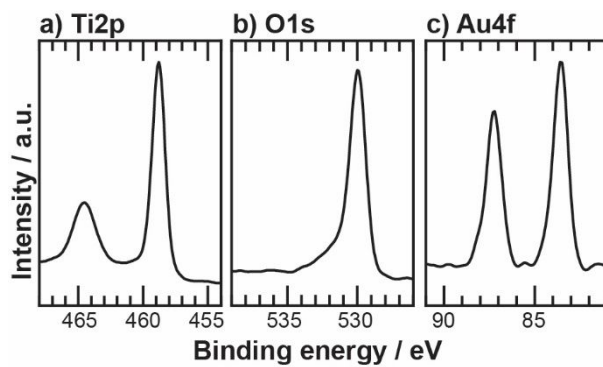


**Figure S5.** XPS (a) Ti2p, (b) O1s and (c) Au4f spectra of the as-prepared Au(1%)@TiO<sub>2</sub>.

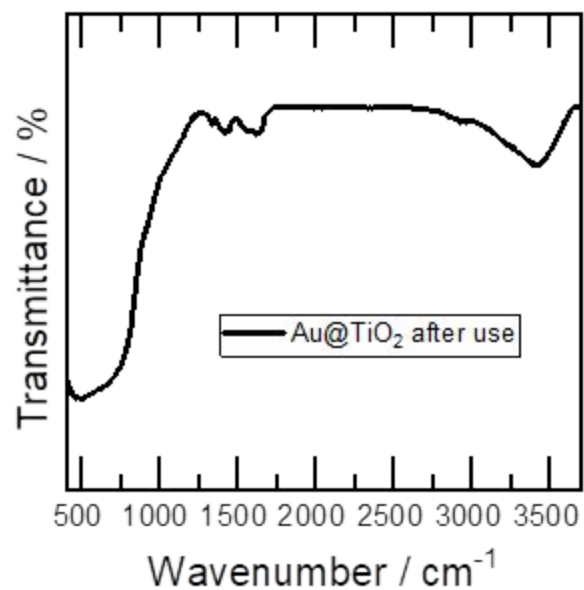


**Figure S6.** FTIR spectra of the recycled Au@TiO<sub>2</sub>.

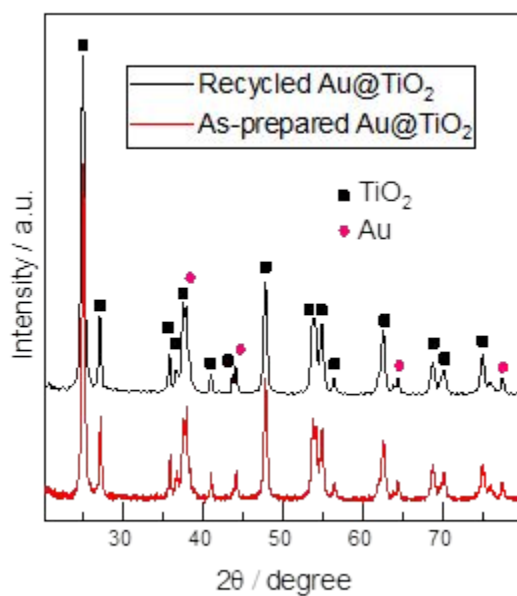


**Figure S7.** XRD spectra of the as-prepared and the recycled Au(1%)@TiO<sub>2</sub>.

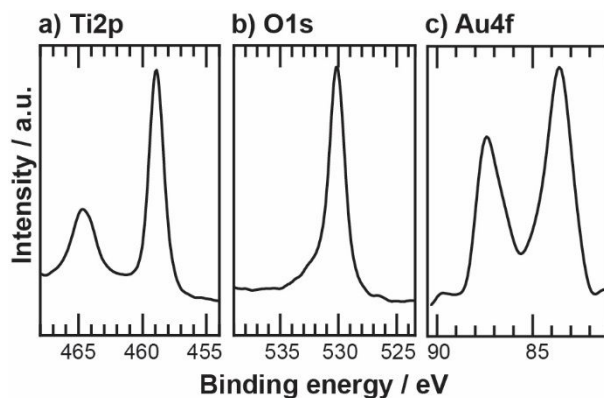


**Figure S8.** XPS (a) Ti2p, (b) O1s and (c) Au4f spectra of the recycled Au(1%)@TiO<sub>2</sub>.

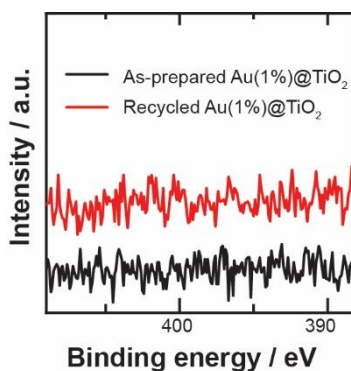


**Figure S9.** XPS of N1s of the as-prepared and the recycled Au(1%)@TiO<sub>2</sub>.

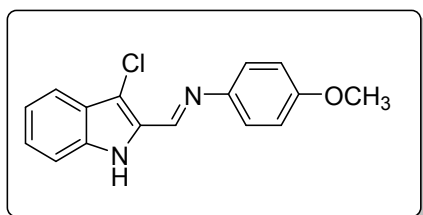
#### General data:

All melting points were measured on a Fisher-John apparatus. IR spectra were registered on a Pye-Unicam Sp-100 spectrophotometer utilizing the KBr wafer method. NMR analyses were performed at Bruker BioSpin GmbH (1H: 500 MHz, 13C: 125 MHz) spectrometers utilizing tetramethylsilane (TMS) as an internal standard DMSO-d<sub>6</sub> as a solvent. Analytical TLC was completed on silica gel plates (Fluka 70643-50EA, SIGMA-ALDRICH, Germany) utilizing UV

light. Mass spectra were recorded on a Thermo LTQ Orbitrap XL (ESI+) or a P-SIMS-Gly of Bruker Daltonics Inc (EI+). All used chemicals were purchased from SIGMA and used without further purification. Compound 1 was prepared according to the reported procedure<sup>1</sup>.

### Analytical Data for the Products:

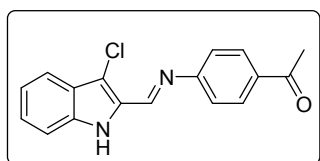
#### (*E*)-1-(3-chloro-1*H*-indol-2-yl)-*N*-(4-methoxyphenyl)methanimine (3a)



Yellow crystals, m.p. 220-222 °C. IR (KBr pellets, cm<sup>-1</sup>)  $\nu$ : 3406, 3013, 2952, 2927, 2832, 1611. <sup>1</sup>H NMR (500 MHz,

DMSO)  $\delta$  2.99 (s, 3H), 7.59 (d,  $J$  = 8.0 Hz, 1H), 7.50 (d,  $J$  = 8.3 Hz, 1H), 7.41 – 7.36 (m, 2H), 7.32 (ddd,  $J$  = 8.2, 7.0, 1.1 Hz, 1H), 7.16 (ddd,  $J$  = 8.0, 7.1, 0.9 Hz, 1H), 7.06 – 6.97 (m, 2H), 8.65 (s, 1H), 11.98 (s, 1H). <sup>13</sup>C NMR (126 MHz, DMSO)  $\delta$  158.71, 145.87, 144.26, 136.58, 131.34, 125.86, 125.47, 122.95, 121.04, 118.61, 115.07, 113.22, 110.03, 55.80. Ms [EI<sup>+</sup>] Calculated for C<sub>16</sub>H<sub>13</sub>ClN<sub>2</sub>O 284.07, Found 284.1.

#### (*E*)-1-(4-(((3-chloro-1*H*-indol-2-yl)methylene)amino)phenyl)ethan-1-one (3b)

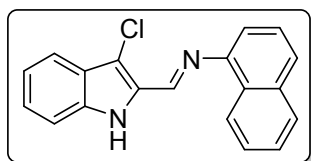


Yellow crystals, m.p. 175-176 °C. IR (KBr pellets, cm<sup>-1</sup>)  $\nu$ : 3290, 2842, 1654, 1618. <sup>1</sup>H NMR (500 MHz, DMSO)  $\delta$  12.15 (s, 1H), 8.66

(s, 1H), 8.06 – 8.01 (m, 1H), 7.62 (d,  $J$  = 8.1 Hz, 1H), 7.51 (d,  $J$  = 8.3 Hz, 1H), 7.46 – 7.41 (m,

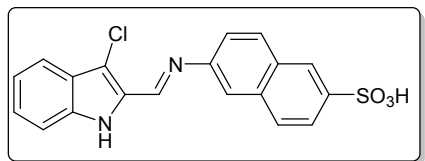
1H), 7.36 (ddd,  $J = 8.3, 7.0, 1.1$  Hz, 1H), 7.18 (ddd,  $J = 8.0, 7.0, 0.9$  Hz, 1H), 2.60 (s, 1H).  $^{13}\text{C}$  NMR (126 MHz, DMSO)  $\delta$  197.43, 155.62, 149.80, 136.95, 134.89, 130.81, 130.23, 126.58, 125.35, 121.68, 121.31, 118.96, 113.39, 111.89, 27.14.

**(E)-1-(3-chloro-1H-indol-2-yl)-N-(naphthalen-1-yl)methanimine (3c)**



Brown crystals, m.p. 148-150 °C. IR (KBr pellets,  $\text{cm}^{-1}$ )  $\nu$ : 3409, 3058, 1622, 1611.  $^1\text{H}$  NMR (500 MHz, DMSO)  $\delta$  12.18 (s, 1H), 8.77 (s, 1H), 8.52 (dd,  $J = 5.5, 3.1$  Hz, 1H), 7.96 (dd,  $J = 5.5, 2.8$  Hz, 1H), 7.84 (d,  $J = 8.1$  Hz, 1H), 7.69 – 7.51 (m, 5H), 7.38 (d,  $J = 5.1$  Hz, 2H), 7.20 (t,  $J = 7.4$  Hz, 1H).  $^{13}\text{C}$  NMR (126 MHz, DMSO)  $\delta$  148.21, 148.15, 136.82, 134.12, 131.29, 129.13, 128.13, 127.03, 126.88, 126.62, 126.32, 125.48, 124.28, 121.25, 118.89, 113.48, 113.33, 110.87. Ms [EI $^+$ ] Calculated for  $\text{C}_{19}\text{H}_{13}\text{ClN}_2$  304.07, Found 304.02.

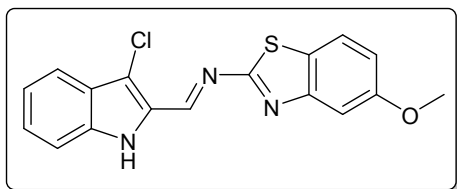
**(E)-6-(((3-chloro-1H-indol-2-yl)methylene)amino)naphthalene-2-sulfonic acid (3d)**



Yellow crystals, m.p. 270-272 °C. IR (KBr pellets,  $\text{cm}^{-1}$ )  $\nu$ : 3267, 3124, 3036, 2966, 2935, 2841, 2592, 1626, 1600.  $^1\text{H}$  NMR (500 MHz, DMSO)  $\delta$  12.14 (s, 1H), 8.81 (s, 1H), 8.11 – 7.92 (m, 2H), 7.87 – 7.74 (m, 2H), 7.62 (dd,  $J = 8.0, 2.9$  Hz, 2H), 7.53 (d,  $J = 8.3$  Hz, 1H), 7.35 (dd,  $J = 8.0, 7.3$  Hz, 1H), 7.19 (dd,  $J = 7.8, 7.2$  Hz, 2H).  $^{13}\text{C}$  NMR (126 MHz, DMSO)  $\delta$  149.66,

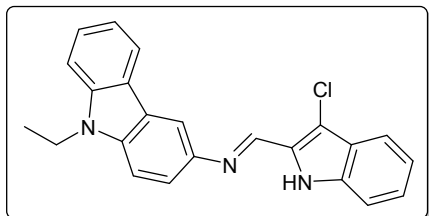
148.57, 145.52, 136.81, 134.06, 131.29, 131.16, 130.27, 128.12, 126.28, 125.44, 124.97, 124.51, 122.13, 121.21, 118.82, 118.24, 113.36, 111.09.

**(E)-1-(3-chloro-1H-indol-2-yl)-N-(5-methoxybenzo[d]thiazol-2-yl)methanimine (3e)**



Orange crystals, m.p. 210-212 °C. IR (KBr pellets,  $\text{cm}^{-1}$ )  $\nu$ : 3287, 3060, 2976, 2931, 2843, 1618.  $^1\text{H}$  NMR (500 MHz, DMSO)  $\delta$  12.38 (s, 1H), 9.13 (s, 1H), 8.15 (d,  $J = 8.4$  Hz, 1H), 8.15 (d,  $J = 8.4$  Hz, 1H), 7.99 (dd,  $J = 8.4, 4.1$  Hz, 1H), 7.87 (d,  $J = 8.9$  Hz, 1H), 7.65 (dd,  $J = 5.6, 3.0$  Hz, 1H), 7.41 (ddd,  $J = 8.2, 6.9, 1.1$  Hz, 1H), 7.13 (dd,  $J = 8.9, 2.6$  Hz, 1H), 3.85 (s, 3H).  $^{13}\text{C}$  NMR (126 MHz, DMSO)  $\delta$  169.12, 162.92, 157.75, 155.69, 151.47, 137.88, 136.23, 129.97, 127.70, 125.46, 123.83, 121.73, 119.31, 116.40, 113.59, 105.55, 56.13.

**(E)-1-(3-chloro-1H-indol-2-yl)-N-(9-ethyl-9H-carbazol-3-yl)methanimine (3f)**



Yellow crystals, m.p. 130-132 °C. IR (KBr pellets,  $\text{cm}^{-1}$ )  $\nu$ : 3294, 3059, 2971, 1625, 1605.  $^1\text{H}$  NMR (500 MHz, DMSO)  $\delta$  12.03 (s, 1H), 8.86 (s, 1H), 8.27 (dd,  $J = 10.1, 4.7$  Hz, 2H), 7.68 – 7.58 (m, 4H), 7.56 – 7.45 (m, 2H), 7.33 (t,  $J = 7.6$  Hz, 1H), 7.20 (dt,  $J = 23.4, 7.4$  Hz, 2H), 4.46 (q,  $J = 7.1$  Hz, 2H), 1.34 (t,  $J = 7.1$  Hz, 3H).  $^{13}\text{C}$  NMR (126 MHz, DMSO)  $\delta$  145.35, 143.28, 140.65, 139.06, 136.57, 131.67, 126.54, 125.76, 125.57, 123.38, 122.86, 121.28, 121.11, 121.03, 119.33, 118.57, 113.22, 112.80, 110.09, 109.79, 109.68, 37.60, 14.21.

**Table S1.** Photoluminescence (PL) Decay Time Coefficients of all samples.

$\tau_1(A_1) / \text{ns}$

$\tau_2(A_2) / \text{ns}$

<b>3a</b>	1.2 (0.85)	5.44 (0.15)
<b>3b</b>	0.58 (0.90)	3.2 (0.10)
<b>3c</b>	1.9 (0.12)	14.3 (0.88)
<b>3f</b>	1.5 (0.81)	14.5 (0.19)

$\tau_1$  is the fitted time coefficients and  $A_i$  is the corresponding amplitudes of each component.

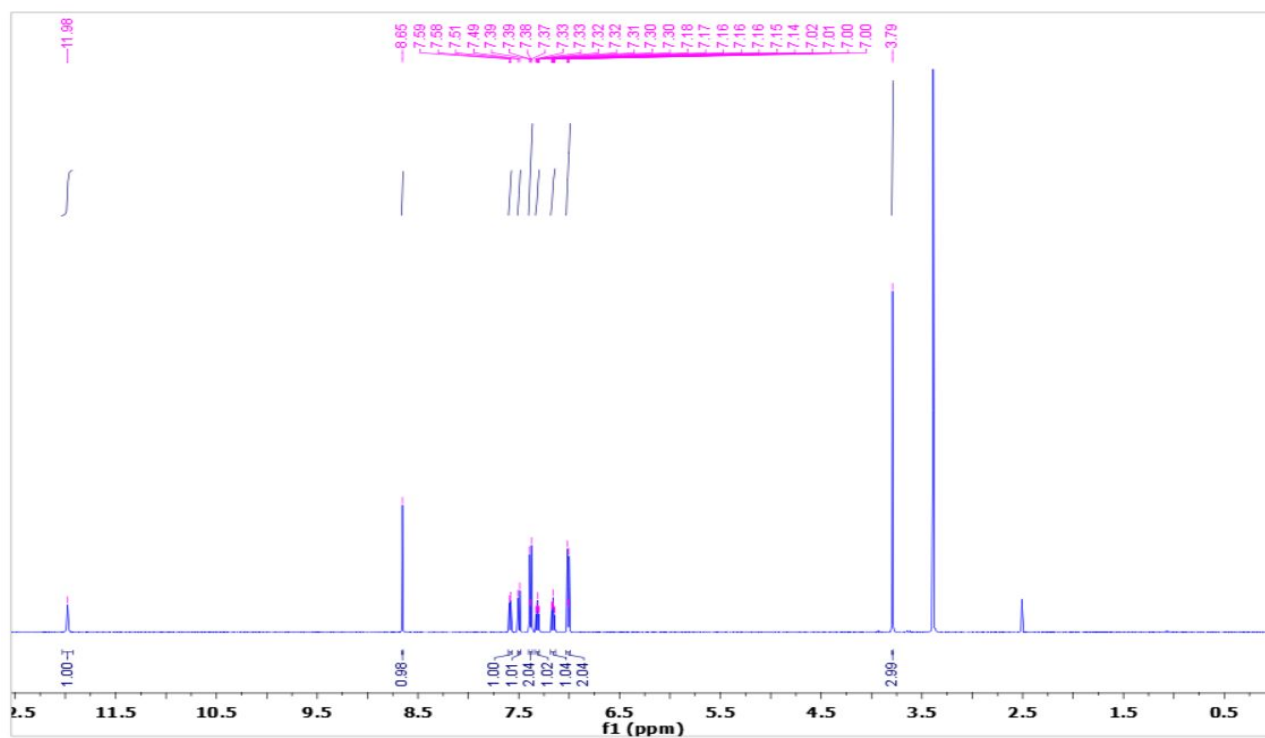
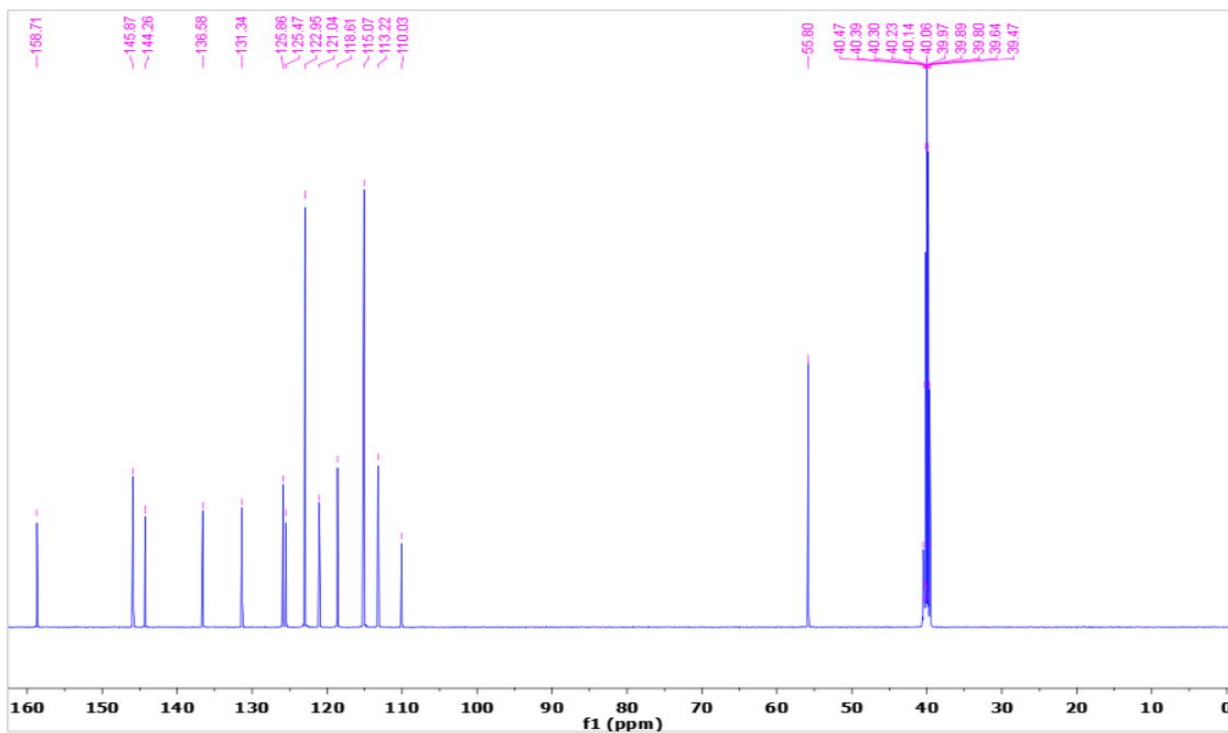
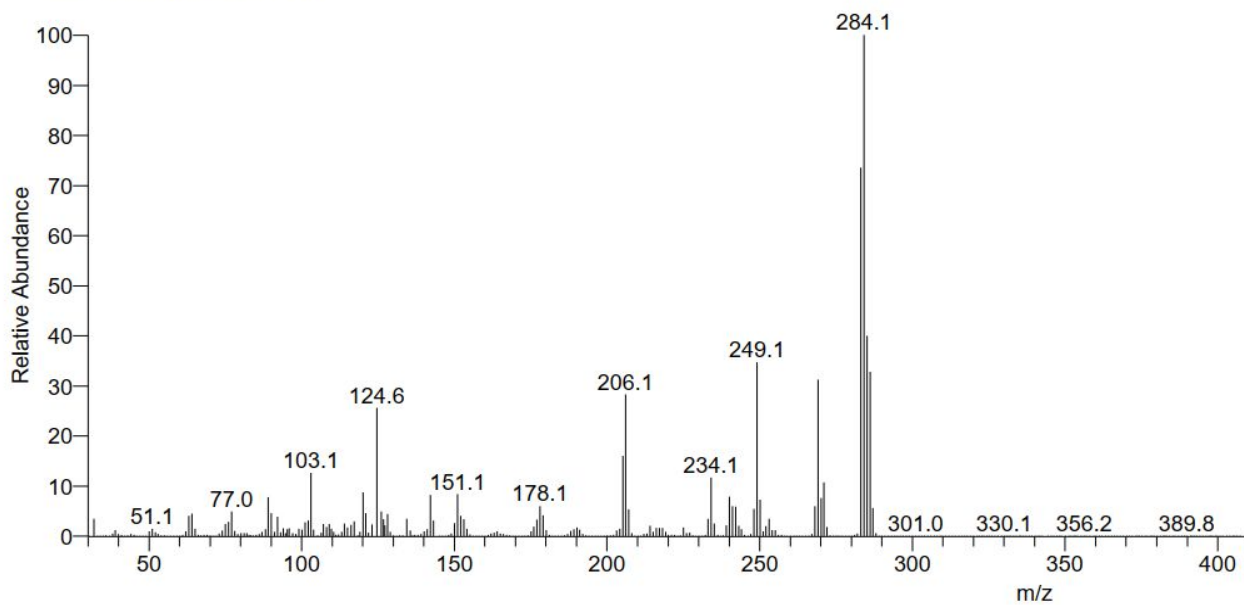


Figure S10. <sup>1</sup>H-NMR Spectrum of Compound 3a.



**Figure S11.**  $^{13}\text{C}$ -NMR Spectrum of Compound **3a**.

sample1 #4014 RT: 13.68 AV: 1 NL: 2.95E8  
T: + c EI Full ms [30.00-650.00]



**Figure S12.** Mass Spectrum of Compound **3a**.



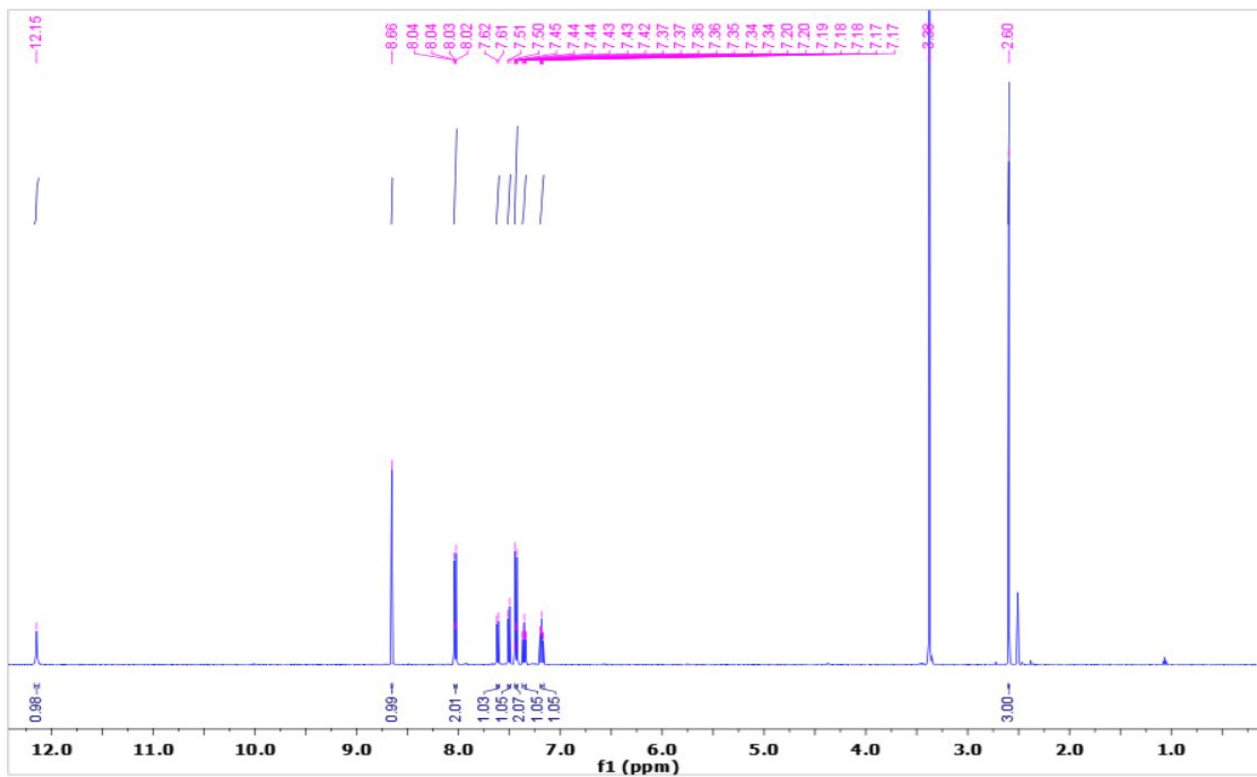


Figure S13. <sup>1</sup>H-NMR spectrum of compound **3b**.

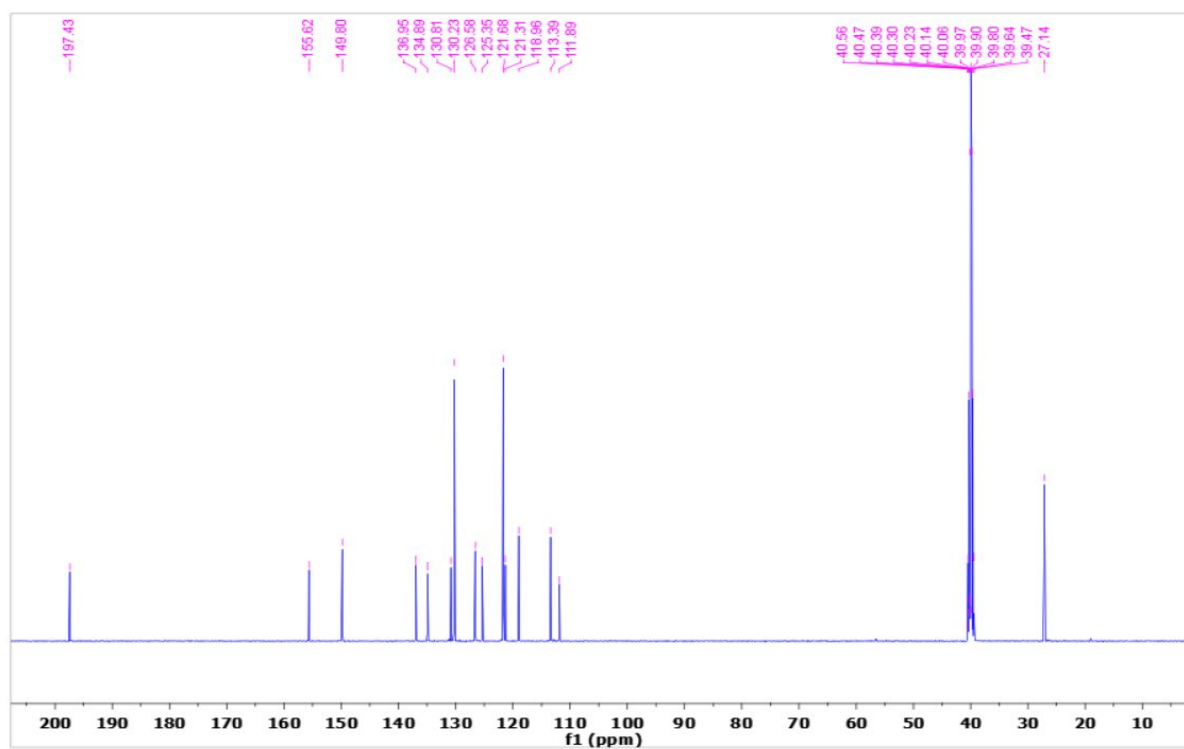


Figure S14. <sup>13</sup>C-NMR Spectrum of Compound 3b.

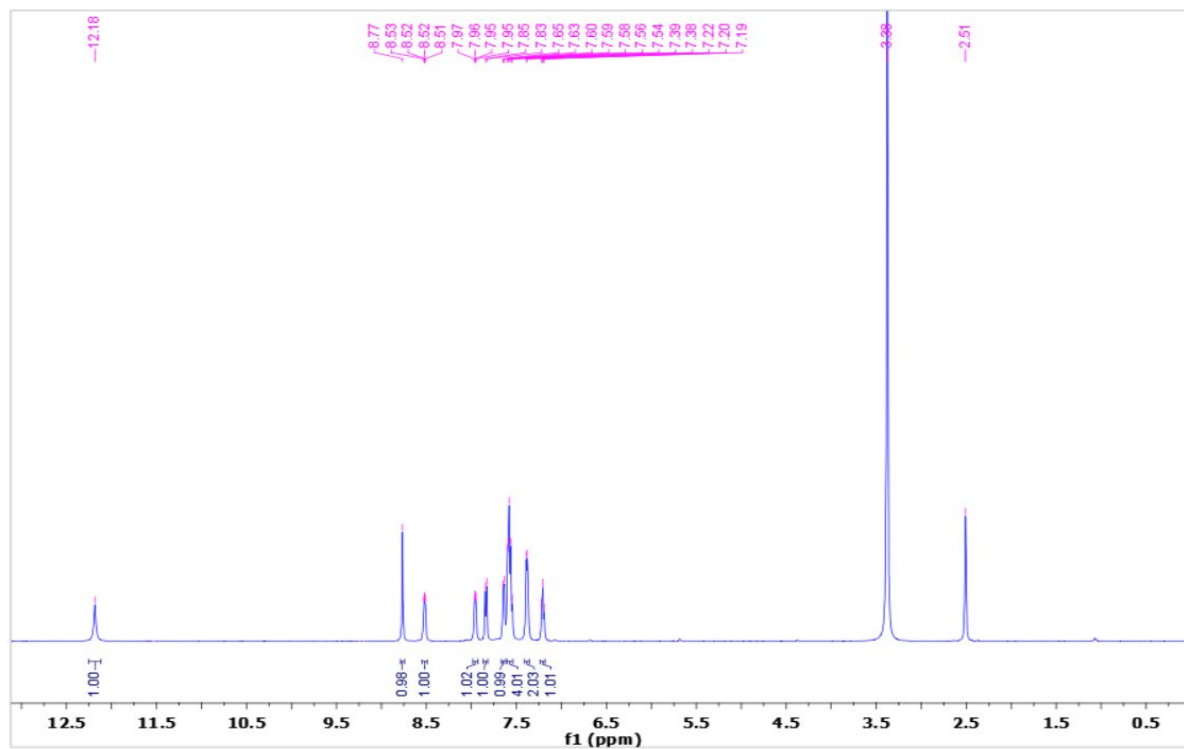


Figure S15. <sup>1</sup>H-NMR Spectrum of Compound 3c.

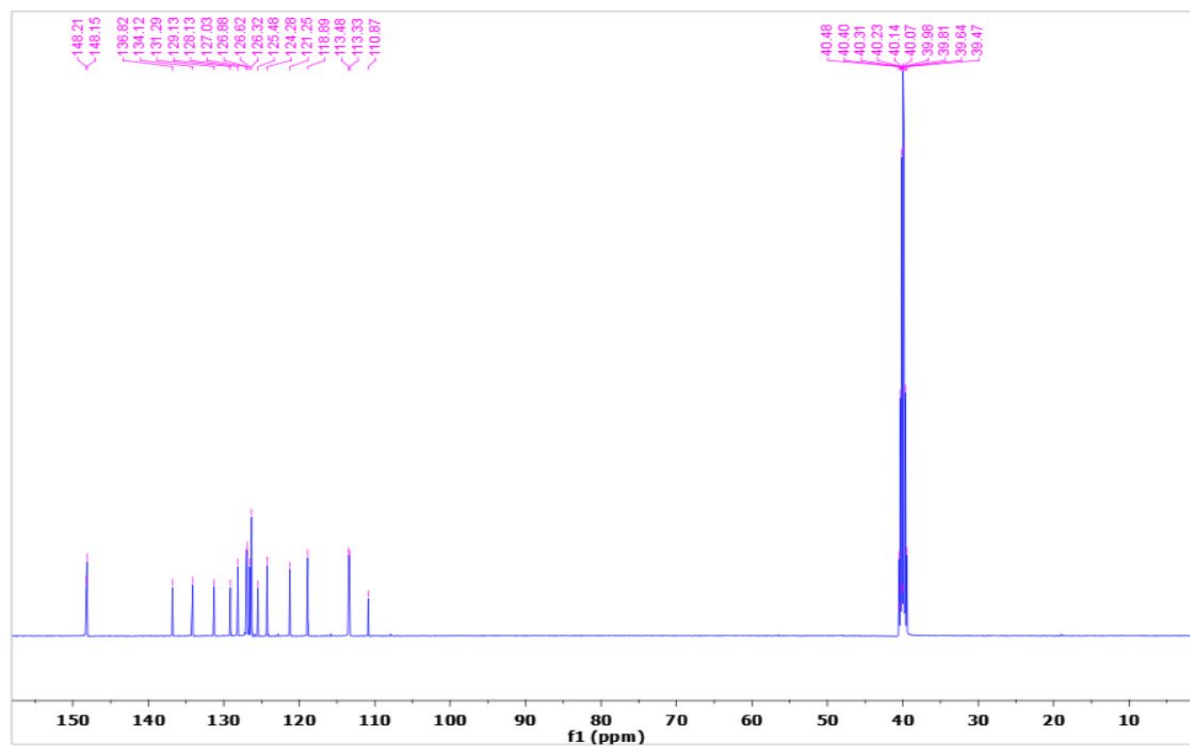


Figure S16. <sup>1</sup>H-NMR Spectrum of Compound 3c.

sample3 #3825 RT: 13.04 AV: 1 NL: 5.84E8  
 T: + c EI Full ms [30.00-650.00]

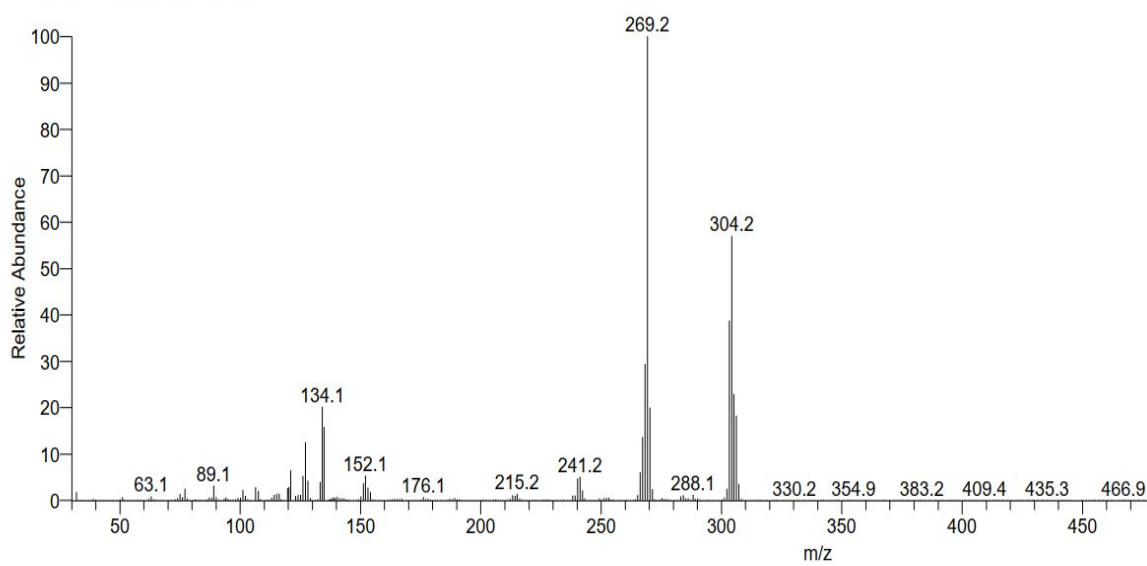


Figure S17. Mass Spectrum of Compound 3c.

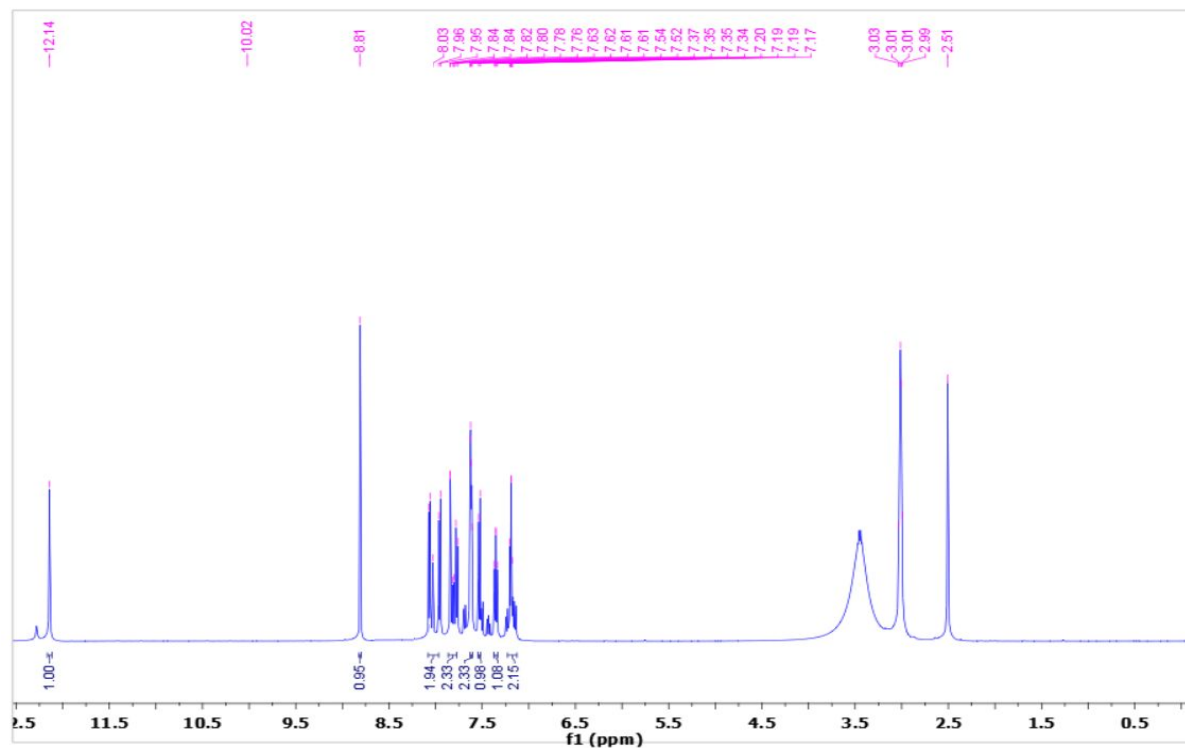


Figure S18. <sup>1</sup>H-NMR Spectrum of Compound 3d.

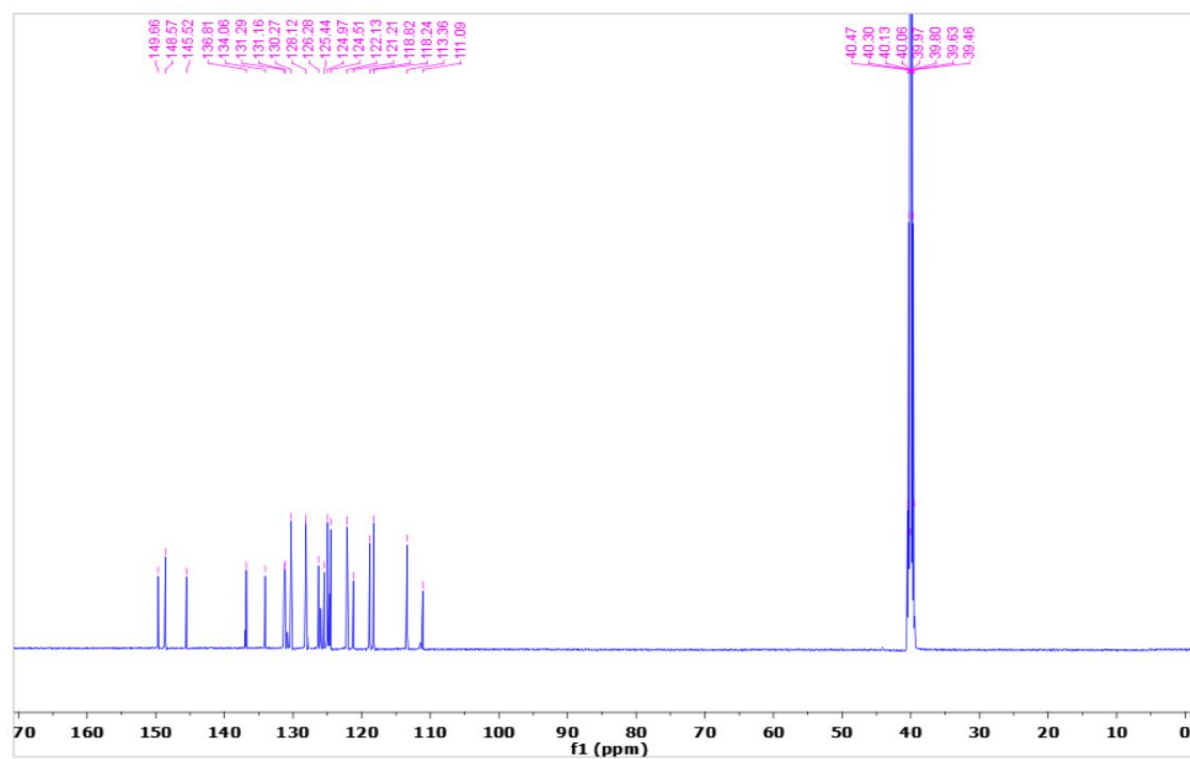


Figure S19. <sup>13</sup>C-NMR Spectrum of Compound 3d.

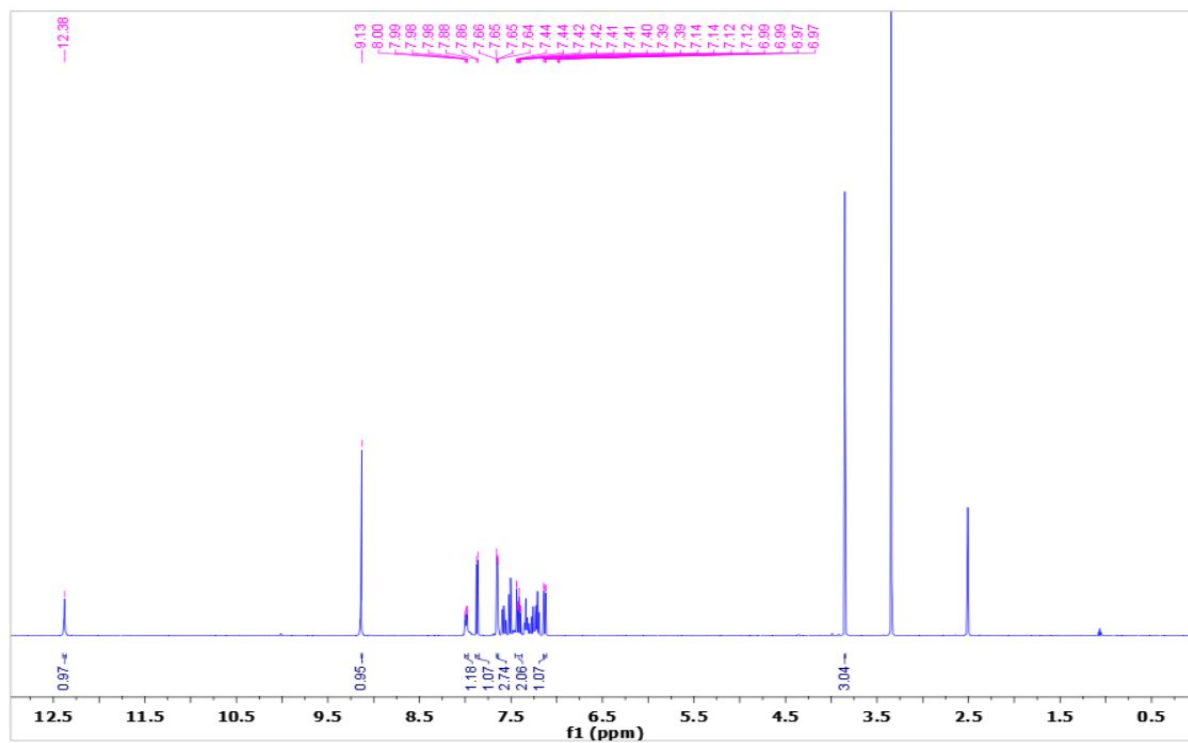


Figure S20. <sup>1</sup>H-NMR Spectrum of Compound 3e.

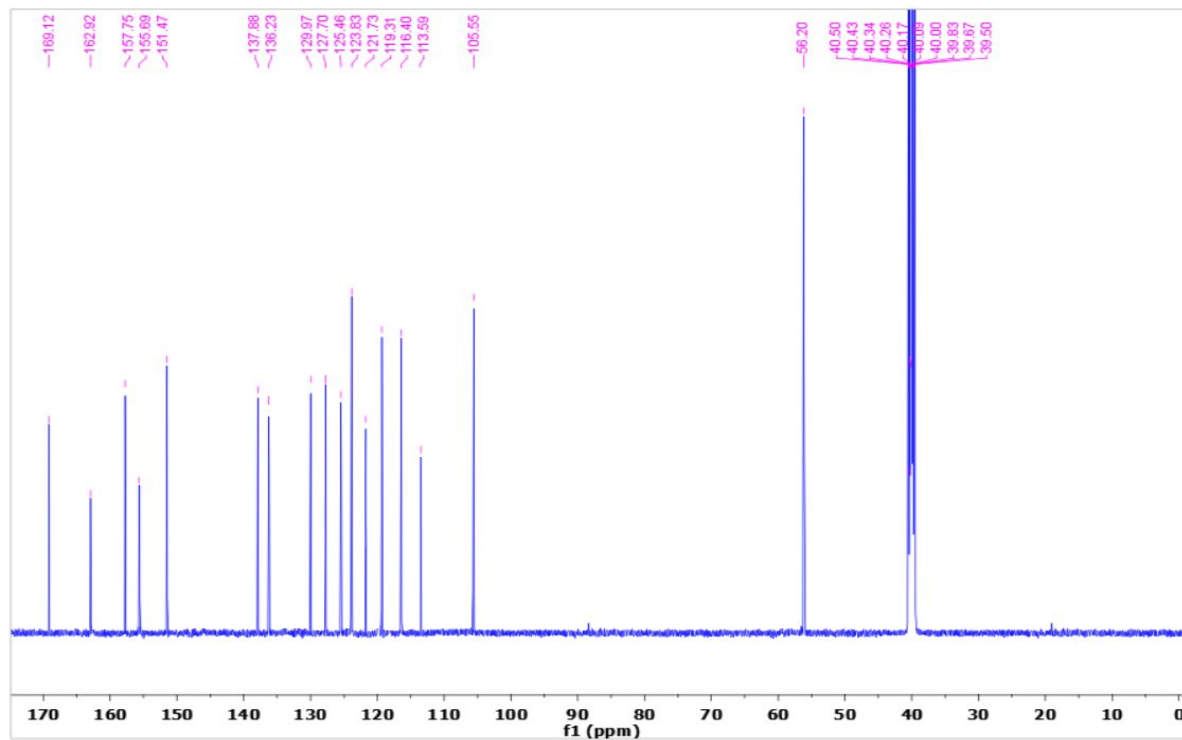


Figure S21. <sup>13</sup>C-NMR Spectrum of Compound 3e.

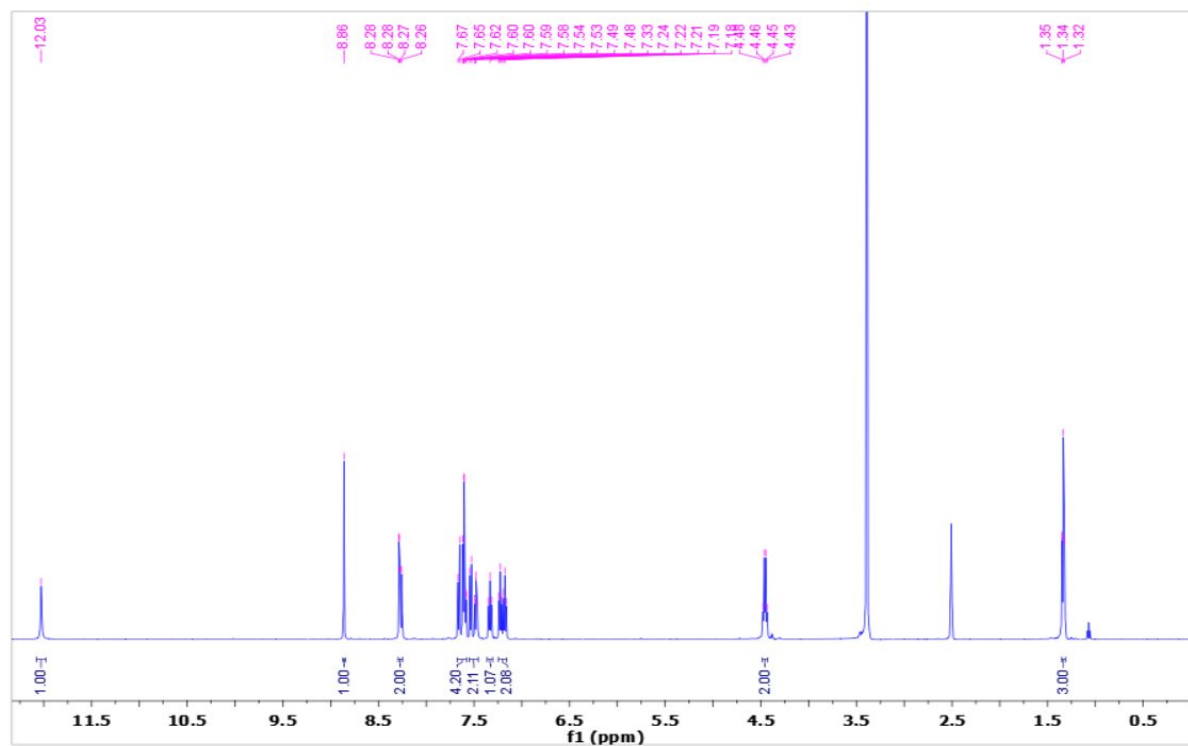


Figure S22. <sup>1</sup>H-NMR Spectrum of Compound 3f.

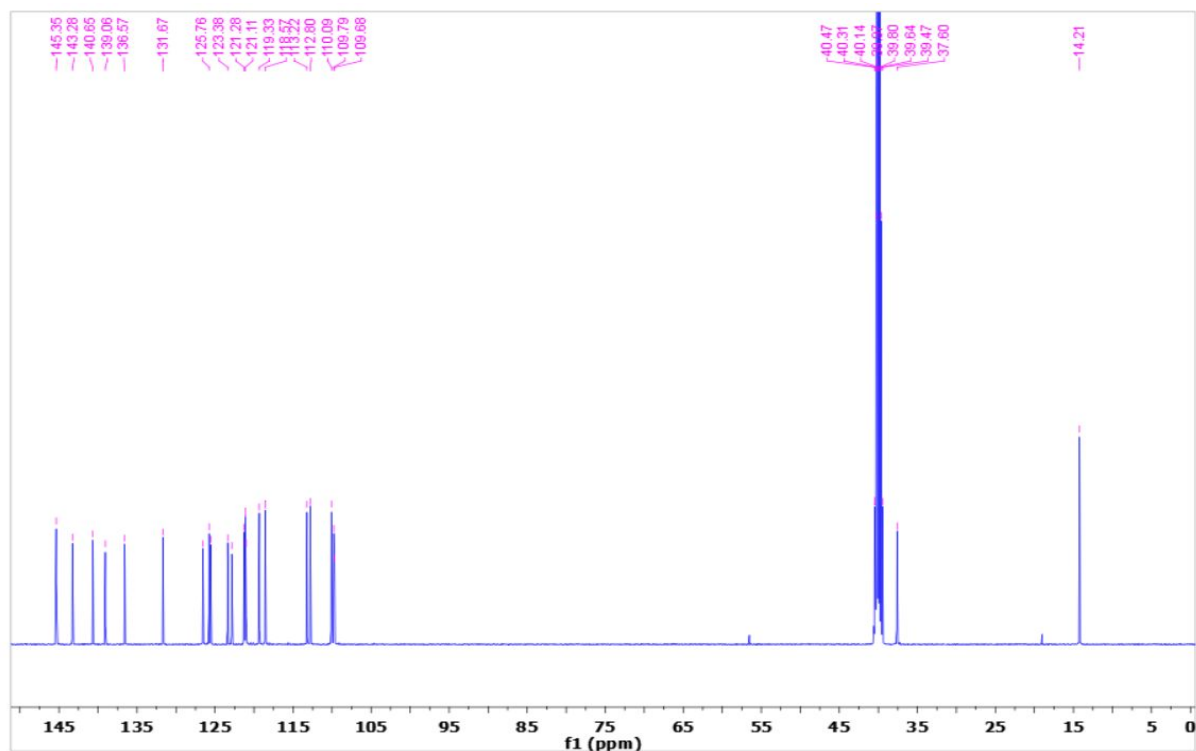


Figure S23. <sup>13</sup>C-NMR Spectrum of Compound 3f.

## References

- 1 N. J. Parmar, H. A. Barad, B. R. Pansuriya and N. P. Talpada, *RSC Adv.*, 2013, **3**, 8064–8070.





# Abbreviations

<b>PSK</b> perovskite	<b>ISC</b> intersystem crossing
<b>2D</b> two-dimensional	<b>IC</b> internal conversion
<b>3D</b> three-dimensional	<b>IVR</b> intramolecular vibrational relaxation
<b>LD</b> low-dimensional	<b>DFG</b> difference frequency generation
<b>PCE</b> power conversion efficiency	<b>KTP</b> potassium titanyl phosphate
<b>PV</b> photovoltaic	<b>LBO</b> lithium triborate
<b>FA</b> formamidinium	<b>KDP</b> potassium dihydrogen phosphate
<b>MA</b> methylammonium	<b>PD Ti:Sa</b> titanium-doped sapphire crystal photodiode
<b>Cs</b> cesium	<b>PMT</b> photomultiplier tube
<b>BA</b> benzyl ammonium	<b>LED</b> light emitting diode
<b>NMA</b> naphthyl-methyl ammonium	<b>Nd:YAG</b> neodymium-doped yttrium
<b>PMA</b> pyrene-methyl ammonium	<b>SCG</b> supercontinuum generation
<b>DMF</b> dimethylformamide	<b>SPM</b> self-phase modulation
<b>DMSO</b> dimethyl sulfoxide	<b>SHG</b> second harmonic generation
<b>VB</b> valence band	<b>NLO</b> non-linear optics
<b>CB</b> conduction band	<b>OD</b> optical density
<b>LUMO</b> lowest unoccupied molecular orbital	<b>UV</b> ultraviolet
<b>HOMO</b> highest occupied criterion molecular orbital	<b>Vis</b> visible
<b>PLQY</b> photoluminescence quantum yield	<b>Abs</b> Absorption
<b>FRET</b> Förster resonance energy transfer	<b>PL</b> photoluminescence
<b>GaAs</b> gallium arsenide	<b>TCSPC</b> time-correlated single photon counting
<b>LASER</b> light amplification by stimulated emission of radiation	<b>TAS</b> transient absorption spectroscopy
<b>BBO</b> $\beta$ -Barium borate	<b>fs</b> femtosecond
<b>IR</b> infrared	<b>ps</b> picosecond

**ESA** excited state absorption

**GSB** ground-state bleach

**SE** stimulated emission

**IRF** instrumental response

**DAS** decay-associated spectrum function

**LDM** lifetime density map

**GLA** global lifetime analysis

**BGR** bandgap renormalization

**NMR** nuclear magnetic resonance

**SEM** scanning electron microscope

**XRD** X-ray diffraction

**DOI** digital object identifier

# Acknowledgements

[Redacted text block containing multiple lines of blacked-out content]

|

[Redacted text block consisting of 18 horizontal black bars of varying lengths]

|

*Mahmoud Hassan*

*Frankfurt am Main 2022*





# Curriculum Vitae

---

*Mahmoud Hassan*

*(Scientific Name: Mahmoud M. Elshanawany)*

---

**Date of birth:** [REDACTED]

**Place of birth:** Manfalout / Asuit

**Nationality:** Egyptian

**Marital status:** [REDACTED]



## Education and Work Experience:

- **Doctor of Natural Sciences** [07/2019 – 10/2022]  
Institute of Physical and Theoretical Chemistry, Goethe University, Frankfurt am Main  
Work Group: Prof. Dr. Josef Wachtveitl  
**Title:** Ultrafast Dynamics in Wide-bandgap (2D & 3D) Perovskite Semiconductor Thin Films
- **Doctoral Researcher** [07/2018 – 06/2019]  
Institute of Physical Chemistry, Christian-Albrechts-Universität zu Kiel  
Work Group: Prof. Dr. Friedrich Temps
- **Master of Science** [02/2016 – 03/2018]  
Department of Applied Chemistry, National Chiao Tung University, Hsinchu, Taiwan  
Work Group: Prof. Dr. Eric Diau  
**Title:** Femtosecond Transient Absorption Spectral Studies of the Carrier Relaxation Dynamics of Formamidinium Tin Iodide Thin films and the Effects of Varied Additives
- **Working in Industry (Egypt)** [09/2011 – 01/2016]
- **Bachelor of Science** [09/2006 – 06/2011]  
Department of Chemistry, Assuit University, Egypt  
Work Group: Prof. Dr. Zienab Hozien
- **Secondary School** [09/2003 – 06/2006]  
Elmanfalouti Secondary School, Manfalout, Asuit, Egypt
- **Preparatory School** [09/2000 – 06/2003]  
Moheb-Ayoub Preparatory School, Manfalout, Asuit, Egypt